Cite as: E. Chioccarelli, F. De Luca, I. Iervolino (2012), *Preliminary study of Emilia (May 20th 2012) earthquake ground motion records V2.1*, available at http://www.reluis.it.

PRELIMINARY STUDY OF EMILIA (MAY 20th 2012) EARTHQUAKE GROUND MOTION RECORDS V2.1

Eugenio Chioccarelli, Flavia De Luca, and Iunio Iervolino.

eugenio.chioccarelli@unina.it; flavia.deluca@unina.it; iunio.iervolino@unina.it

Dipartimento di Ingegneria Strutturale, Università degli Studi di Napoli Federico II.

Index

1. What's new

This report may be subjected to editing and revisions, check www.reluis.it for updates

New elements of version 2.0 are all referred to records from the station within the epicental distance of 70km. They are:

- **Plots of epsilon values estimated in accordance with Bindi et al. (2011) for geometrical mean of horizontal components and for vertical components (Section 7);**
- **Elastic displacements (Sd_{el}), inelastic displacements ($Sd_{R\mu=i}$) and equivalent number of cycles ($N_{e,\ R\mu=i}$) provided for the horizontal components of the registered signals. These are also compared with the predictions attenuation models of De Luca (2011) and De Luca et al. (2012) based on the Italian data (Section 11).**

New element of version 2.1 is:

- **Comparison between Italian code design spectra and records from the eleven stations closer to the epicenter (Section 9);**
- **Brief comments on forward directivity effects (Section 10);**
- **Geometric mean of the horizontal components of elastic displacements (Sd_{el}), inelastic displacements ($Sd_{R\mu=i}$) and equivalent number of cycles ($N_{e,\ R\mu=i}$) provided for <u>all</u> the registered signals, (Section 11). These are compared with the predictions attenuation models of De Luca (2011) and De Luca et al. (2012) based on the Italian data and computed for soil type A in analogy with the plot shown in section 5 in the case of the attenuation model by Bindi et al. (Section 12).**

2. Introduction

On the 20th of May 2012, at 02:03:53 (UTC), (04:03:53 Italian time), Emilia region (Northern Italy) was struck by a Magnitude, M_L 5.9 (INGV), M_w 6.0 (USGS) earthquake, (lat 44.89, long 11.23, depth 6.3 km). The mainshock was preceded by a M_L 4.1 event on the 19th of May and followed by relevant aftershocks. (Report 1, Dolce et al, 2012) The seismic sequence covered a large area between the provinces of Modena, Ferrara, Rovigo and Mantova. The number of daily earthquakes registered between the 16th of May and the 1st of June is shown in Figure 1 (http://www.ingv.it/primo-piano/comunicazione/2012/05200508/).

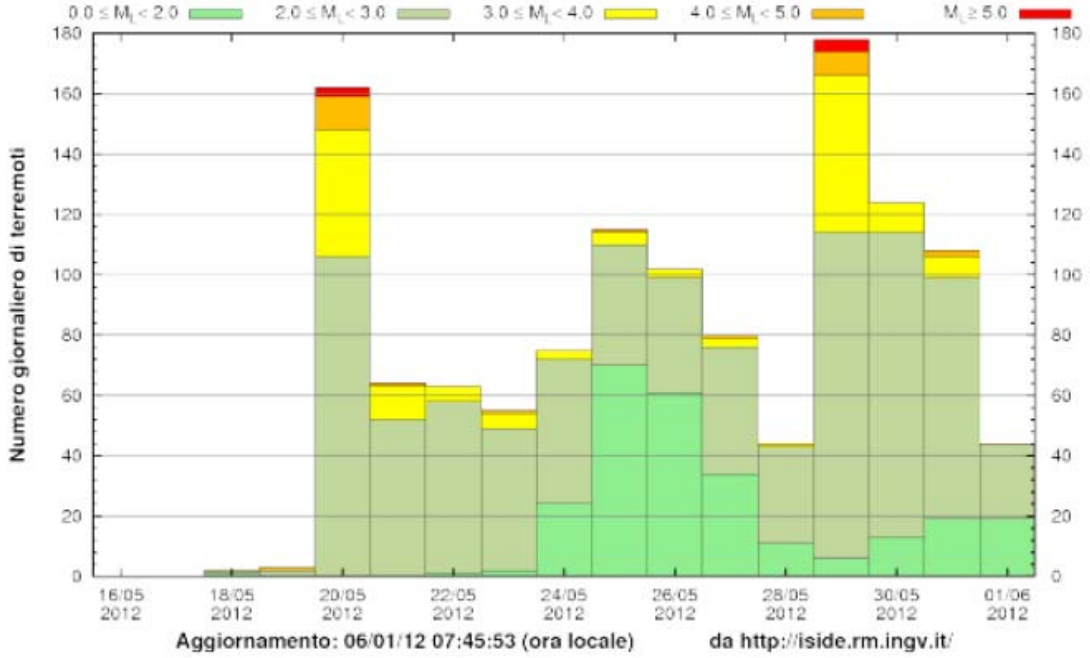

Figure 1. Number of daily earthquakes, update 06/01 (8.00, Italian time), [http://www.ingv.it/primo-piano/comunicazione/2012/05200508/].

The mainshock was registered by 139 stations of the Italian strong motion network (RAN), managed by the National Civil Protection, ranging from 16 km up to 650 km epicentral distance.

In the following a preliminary overview of peak and integral parameters at each station is provided. Waveforms have not been processed with any further data treatment respect to what provided by National Civil Protection (Report 1, Dolce et al, 2012). *Peak Ground Acceleration* (PGA), *Peak Ground Velocity* (PGV) are calculated for the two horizontal direction (East-West and North-South, as recorded) and for the vertical one.

Arias Intensity (I_A), *Cosenza and Manfredi Index* (I_D), evaluated according to Cosenza et al. (1993), and *Housner Intensity* (H_{50}) are the integral parameters computed for each waveform. Housner intensity (H_{50}) is evaluated as the integral of the pseudo-velocity spectrum in the range 0.2-2.0 seconds. Durations computed for each record are: *Significant Duration* (Sd) and *Bracketed Duration* (Bd); the former estimated between 5% and 95% of the I_A, the latter assuming 0.05 PGA as reference value.

The analysis of peak and integral values is made by a comparison with different ground motion attenuation relationships (GMPE). Bindi et al. (2011) GMPE was employed for the comparison in term of PGA, PGV and elastic spectral acceleration at given spectral ordinates, Sa(T). I_A attenuation relationship by Sabetta and Pugliese (1996) and Iervolino et al. (2010) attenuation law in term of I_D have been employed. Sabetta and Pugliese (1996) and Iervolino et al. (2010) GMPEs are based on epicentral distance (R_{epi}) as distance measure, while Bindi et al. (2011) GMPE employs the

epicentral distance (R_{epi}), for M_w < 5.5 events, and the closest distance to fault projection or *Joyner and Boore distance*, R_{jb} (Joyner and Boore, 1981), for stronger earthquakes. Given the lack of information on the fault, at the moment, an approximate conversion law was employed to switch form the distance data in terms of R_{epi} to that in terms of R_{jb}. Equation (1) shows the expression used for the conversion according to (Gruppo di Lavoro INGV, 2004).

$$R_{jb} = -3.5525 + 0.8845 \cdot R_{epi} \geq 1 \quad \left(R^2 = 0.95\right) \tag{1}$$

3. Geographic Information

In Table 1 is possible to relate station IDs, geographic coordinates of the stations, and station names. These data are a gentle concession of the Department of Civil Protection. Figure 2 shows the map of the stations within 200 km while in Figure 3 and Figure 4 map of horizontal (geometrical mean of two direction) and vertical PGA (PGA_h and PGA_h) and PGV (PGV_h and PGV_v) are shown, respectively.

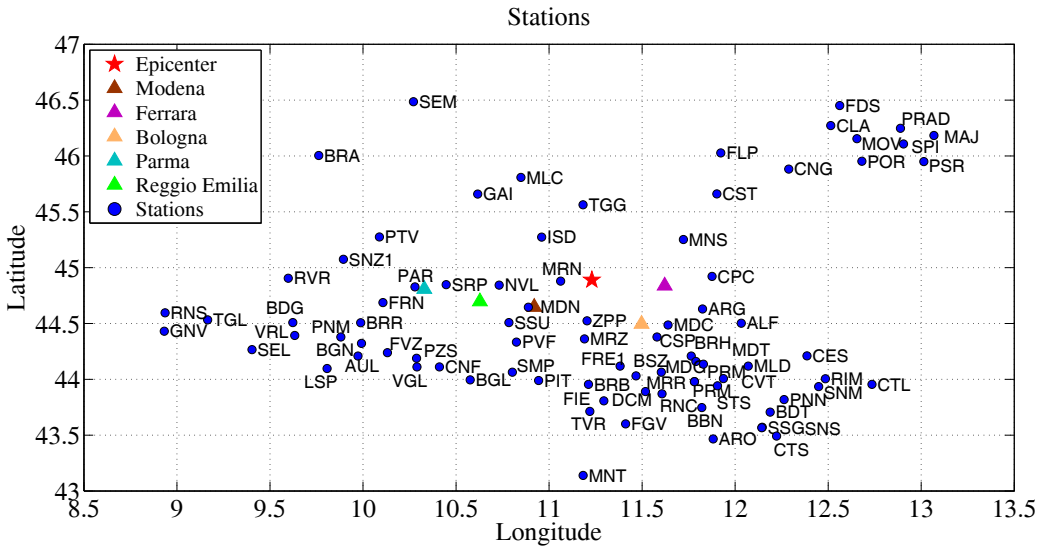

Figure 2. Map of the stations within 200 km from the epicentre.

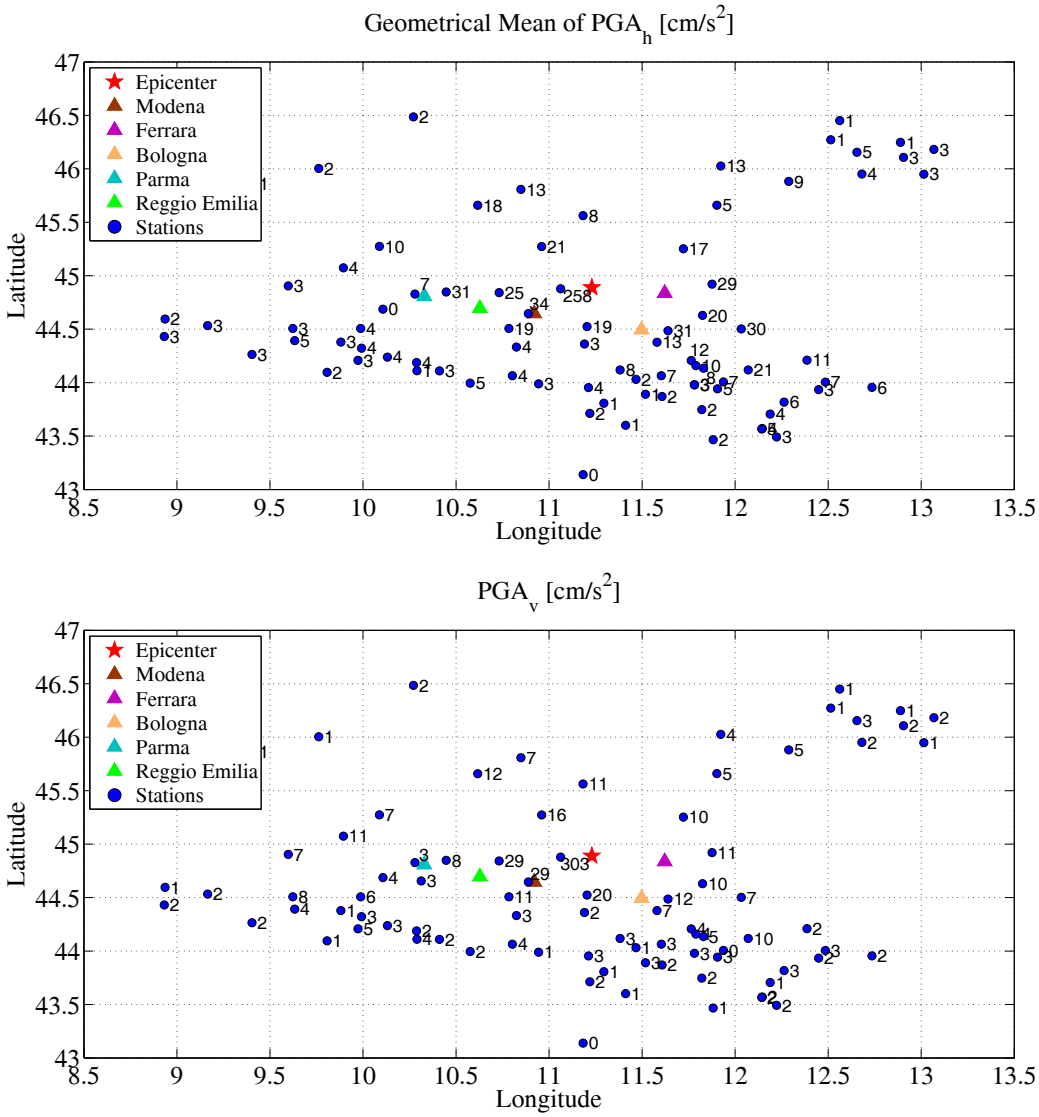

Figure 3. Peak Ground Acceleration (PGA) maps at the stations within 200 km. PGA_h is the geometrical mean of the registered horizontal components, PGA_v is the vertical component.

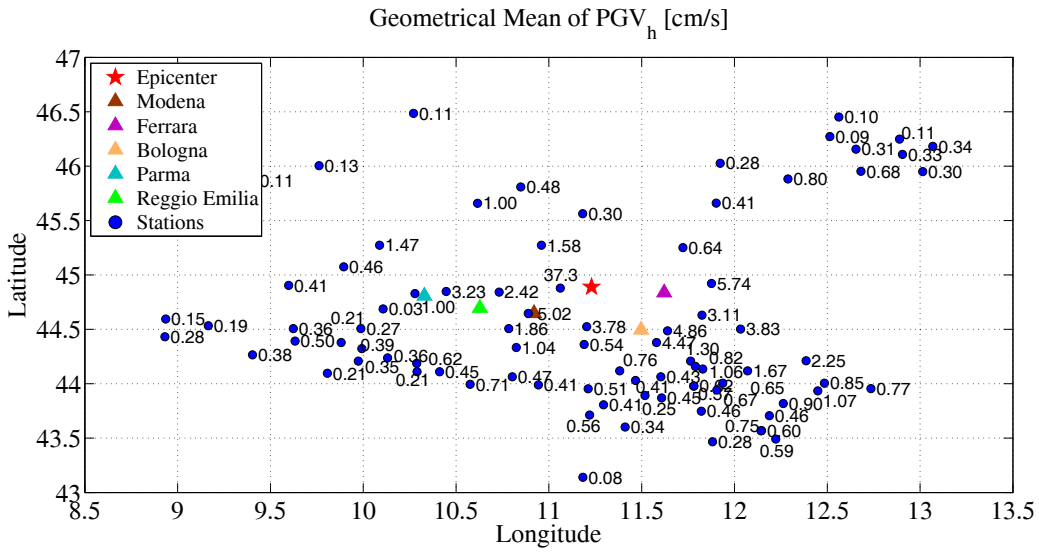

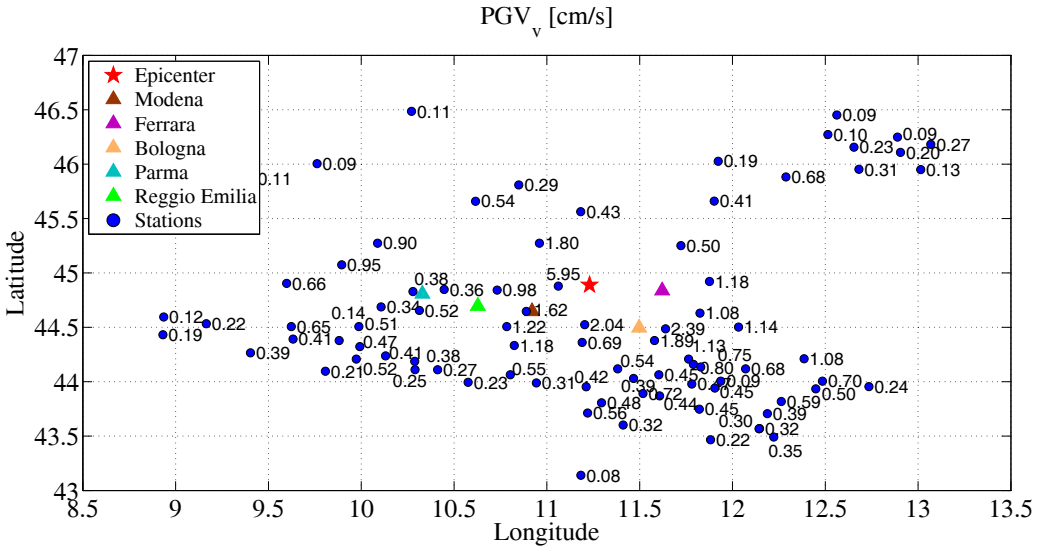

Figure 4. Peak Ground Velocity (PGV) maps at the stations within 200 km. PGV_h is the geometrical mean of the registered horizontal components, PGV_v is the vertical component.

Table 1. Station ID, geographic coordinates, and station names.

Station ID	Lat	Lon	elevation	R_{epi}	Station Name
			[km]	[km]	
MRN	44.8782	11.0617	0.015	16	Mirandola
MDN	44.646	10.889	0.08	41	Modena
NVL	44.843	10.732	0.022	42	Novellara
ZPP	44.524	11.204	0.069	43	Zola_Pedrosa_Piana
ISD	45.273	10.96	0.04	47	Isola_Della_Scala
CPC	44.921	11.876	0.008	49	Copparo_Coccanile
MNS	45.2517	11.7221	0.014	53	Monselice
ARG	44.63	11.825	0.045	54	Argenta
MDC	44.486	11.64	0.026	56	Medicina
SSU	44.507	10.784	0.448	58	Sassuolo
MRZ	44.3614	11.1901	0.456	61	Marzabotto
CSP	44.3784	11.5801	0.088	64	CastelSanPietroTerme
SRP	44.848	10.447	0.032	64	Sorbolo
PVF	44.333	10.825	0.743	72	Pavullo_del_Frignano
TGG	45.5621	11.1827	0.762	73	Tregnago
ALF	44.502	12.033	0.006	76	Alfonsine
PAR	44.828	10.279	0.091	78	Parma
LNG	44.655	10.313	0.203	80	Langhirano
BRH	44.2076	11.7639	0.149	87	Brisighella
FRE1	44.118	11.382	0.461	88	Firenzuola
MDG	44.159	11.789	0.187	93	Modigliana
FRN	44.6868	10.1072	0.28	94	Fornovo
MDT	44.135	11.8297	0.571	97	Modigliana
MRR	44.064	11.603	0.369	97	Marradi
GAI	45.659	10.616	0.4	98	Gaino
CST	45.66	11.902	0.487	98	Castelfranco_Veneto
BSZ	44.031	11.467	0.685	99	Borgo_San_Lorenzo
SMP	44.064	10.803	1.022	100	San_Marcello_Pistoiese

PTV	45.274	10.088	0.055	101	Pontevico
PIT	43.989	10.944	0.537	105	Pistoia
MLC	45.808	10.849	0.098	105	Malcesine
BRB	43.954	11.212	0.426	106	Barberino_Mugello
SNZ1	45.0742	9.8944	0.042	109	S_Nazzaro1
MLD	44.118	12.071	0.116	109	Meldola
BRR	44.5063	9.9872	0.808	110	Berceto
PZS	44.188	10.288	0.659	111	Piazza_al_Serchio
CNF	44.11	10.411	0.323	111	Castelnuovo_di_Garfagnana
PRM	43.9792	11.7814	0.45	111	Premilcuore
CVT	44.006	11.937	0.228	114	Civitella_Di_Romagna
DCM	43.891	11.518	0.2	115	Dicomano
BGL	43.995	10.576	0.447	115	Bagni_Di_Lucca
FVZ	44.238	10.131	0.428	116	Fivizzano
VGL	44.111	10.29	0.613	117	Vagli_Paese
RNC	43.87	11.607	0.534	118	Rincine_Londa
STS	43.942	11.905	0.268	119	Santa_Sofia
BGN	44.322	9.992	0.304	119	Bagnone
CES	44.21	12.386	0.049	120	Cesenatico
FIE	43.807	11.294	0.348	122	Fiesole
PNM	44.379	9.881	0.339	124	Pontremoli
AUL	44.208	9.973	0.177	128	Aulla
RVR	44.9044	9.5981	0.237	131	Rivergaro
TVR	43.712	11.219	0.083	133	Tavarnuzze_Impruneta
CNG	45.882	12.288	0.066	134	Conegliano_Veneto
FLP	46.027	11.923	0.294	135	Feltre_Pasquer
BBN	43.747	11.821	0.471	136	Bibbiena
BDG	44.507	9.623	0.537	137	Bedonia_Gallareto
VRL	44.392	9.633	0.804	141	Varese_Ligure
RIM	44.005	12.485	0.185	142	Rimini
FGV	43.601	11.411	0.344	145	Figline_Valdarno
SNM	43.934	12.449	0.742	146	San_Marino
LSP	44.096	9.807	0.107	146	La_Spezia
PNN	43.818	12.263	0.525	146	Pennabilli
BDT	43.706	12.188	0.795	154	Badia_Tebalda
POR	45.952	12.681	0.022	158	Pordenone
CTL	43.955	12.735	0.062	161	Cattolica
SEL	44.265	9.403	0.076	163	Sestri_Levante
SSG	43.57	12.146	0.347	165	Sansepolcro_Citta
SNS	43.567	12.143	0.377	165	San_Sepolcro
ARO	43.466	11.882	0.353	168	Arezzo
BRA	46.004	9.762	0.815	169	Branzi
TGL	44.533	9.165	1.035	171	Torriglia
MOV	46.155	12.655	0.373	174	Montereale_Valcellina
PSR	45.9493	13.0141	0.08	176	Passariano_Villa_Manin
CTS	43.492	12.223	0.303	176	Citta_Di_Castello
CLA	46.2713	12.5141	0.68	178	Claut
LEC	45.861	9.412	0.231	179	Lecco
SPI	46.108	12.905	0.18	182	Spilimbergo
RNS	44.595	8.936	0.437	187	Ronco_Scrivia

SEM	46.485	10.271	1.466	192	Semogo
GNV	44.431	8.932	0.419	192	Genova
PRAD	46.2481	12.8888	0.52	192	Pradis
MAJ	46.1822	13.0689	0.223	196	Majano_casa_di_riposo
MNT	43.14	11.183	0.371	196	Monticiano
FDS	46.451	12.562	1.795	197	ForniDiSopra
UMB	43.254	12.256	0.628	202	Umbertide
AVS	46.2946	13.0497	0.256	204	Avasinis
GEDE	46.254	13.1243	0.232	204	Gemona_Depuratore
GESC	46.282	13.1404	0.32	207	Gemona_Scugelars
TLM2	46.3814	12.9839	5190	208	Tolmezzo 2
OVD	44.636	8.642	0.235	209	Ovada
CESC	46.3565	13.0572	0.355	209	Cesclans
CVF	46.092	13.429	0.135	210	Cividale_del_Friuli
CARC	45.6527	13.77	0	210	Palazzo Carciotti Trieste
TRI	45.709	13.7642	0.161	212	Trieste station
DST2	45.6587	13.8013	0.08	212	DST Trieste station
VINO	46.256	13.281	0.608	213	Villanova
MASA	46.177	13.4323	0.64	216	Masarolis
SDV	45.628	13.897	0.488	218	San_Dorligo_Della_Valle
MOGG	46.4056	13.1893	0.387	220	Moggio
SAS	44.483	8.486	0.415	224	Sassello
STOL	46.3614	13.3554	0.57	225	Stolvizza
DRN	46.166	13.641	0.784	227	Drenchia
AUP	46.5064	13.2563	0.905	231	Aupa
ANB	43.592	13.507	0.056	237	Ancona2
TLN	43.215	13.258	0.412	252	Tolentino
MCT	43.292	13.418	0.349	255	Macerata
TNS	45.03	7.684	0.408	282	Torino_Superga
CSC	42.719	13.012	0.683	286	Cascia
TNO	45.1	7.633	0.324	286	Torino
RQT	42.813	13.311	1.188	291	Arquata_Del_Tronto
PNR	44.876	7.344	0.372	309	Pinerolo
SBT	42.933	13.86	0.287	311	S_Benedetto_del_Tronto
SDM	42.29	13.558	0.666	353	San_Demetrio_Ne_Vestini
MTC	41.491	13.815	0.507	442	Montecassino
SNN	41.832	15.571	0.216	503	San_Nicandro_Garganico
BENI	41.1298	14.7716	0.075	521	Universita_Del_Sannio
NAPI	40.84	14.18	0.12	522	Complesso_Universitario_Monte_Sant_Angelo
SSB3	41.0785	15.2292	0.724	549	San_Sossio_Baronia
RSF3	40.9643	15.176	0.865	557	Rocca_San_Felice
MNT3	40.837	15.0067	0.866	560	Montella
LIO3	40.8969	15.1804	0.737	564	Lioni
NSC3	40.8468	15.1222	1.3	565	Nusco
AND3	40.9298	15.3331	0.905	568	Andretta
CLT3	40.903	15.4043	0.525	575	Calitri
SNR3	40.7357	15.1927	1.009	579	Senerchia
CMP3	40.6519	15.0802	0.958	582	Campagna
RDM3	40.8755	15.5361	0.784	584	Ruvo_Del_Monte
VDS3	40.7408	15.427	1.154	591	Muro_Lucano_(Varco_Staccarino)

COL3	40.6871	15.3304	1.026	591	Colliano
SFL3	40.7889	15.5782	1.062	594	San_Fele
PST3	40.5609	15.2433	0.762	598	Postiglione
BEL3	40.7153	15.6369	0.758	604	Bella
AVG3	40.7619	15.7251	1.213	605	Avigliano
CGG3	40.542	15.5225	1.067	614	Caggiano
SRN3	40.4861	15.458	1.067	616	Sant_Arsenio
STN3	40.53	15.6515	0.832	622	Satriano
PGN3	40.5722	15.7967	0.882	626	Pignola
MRN3	40.4256	15.7296	0.772	636	Marsico_Nuovo_(PZ)
VGG3	40.336	15.901	0.882	653	Viggiano_(Prot.Civ.Gr.Lucano)

4. Peak and integral parameters of the uncorrected waveforms

Peak and integral parameters defined in Section 1 are computed for the uncorrected waveforms for the two horizontal components (N-S, E-W) and for the vertical component (Z). The result are shown in Table A1, A2, and A3 in the Appendix.

From Figure 5 to Figure 11 several intensity measures (IMs) computed from the geometrical mean of the horizontal components and the vertical components are shown as function of the epicentral distance (R_{epi}). Peak ground acceleration (PGA), peak ground velocity (PGV), Arias intensity (I_A), and Housner intensity (H_{50}) are characterized by a strict attenuation after 20km, unfortunately the only registration available in this range is MRN station. On the other hand such a result find confirmation in the fact that the event was quite superficial (depth 6.3 km).

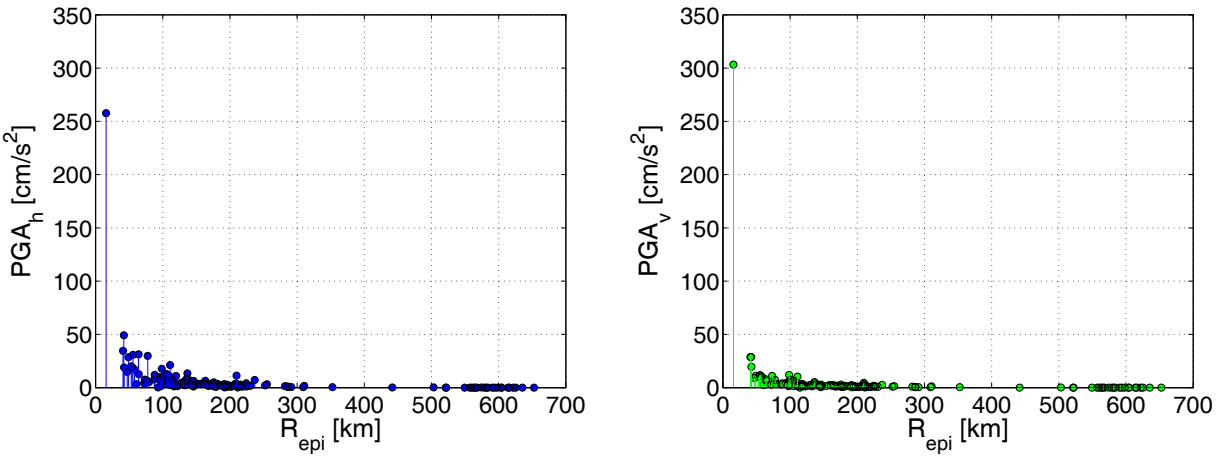

Figure 5. PGA values: geometrical mean of the horizontal components, PGA_h (on the left), and vertical component PGA_v (on the left).

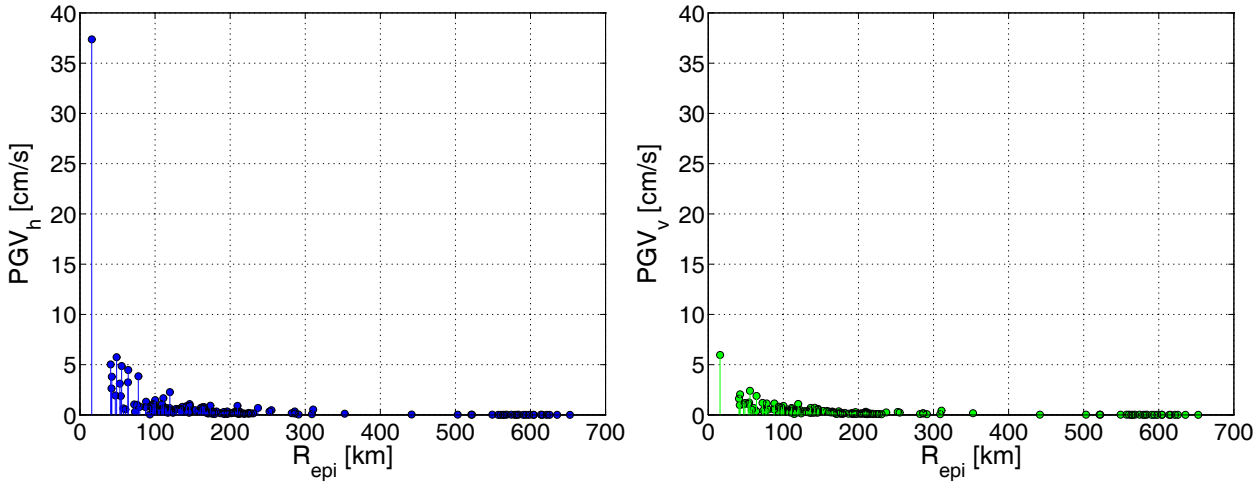

Figure 6. PGV values: geometrical mean of the horizontal components, PGV_h (on the left), and vertical component PGV_v (on the left).

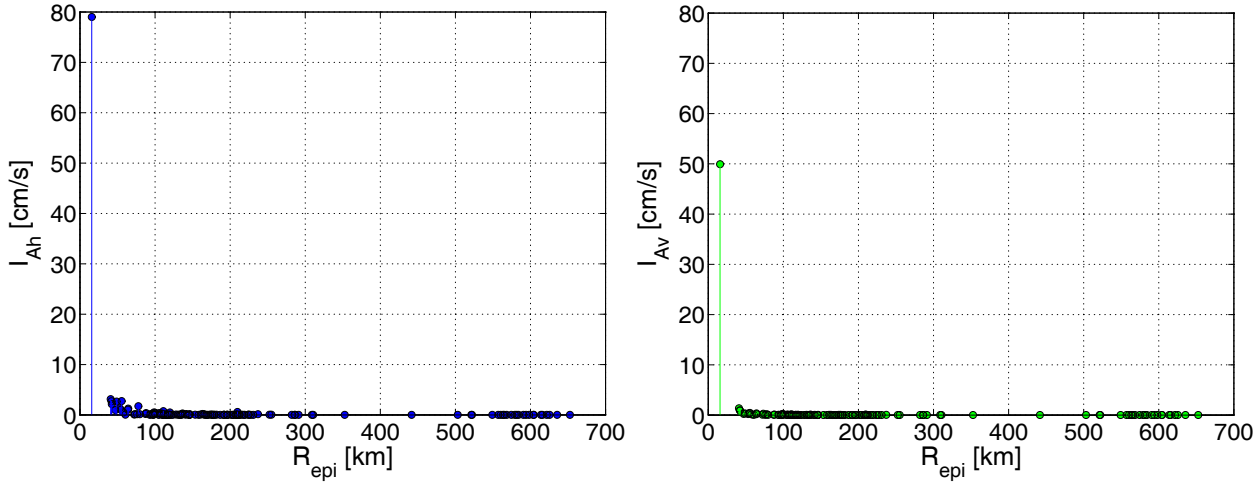

Figure 7. I_A values: geometrical mean of the horizontal components, I_{Ah} (on the left), and vertical component I_{Av} (on the left).

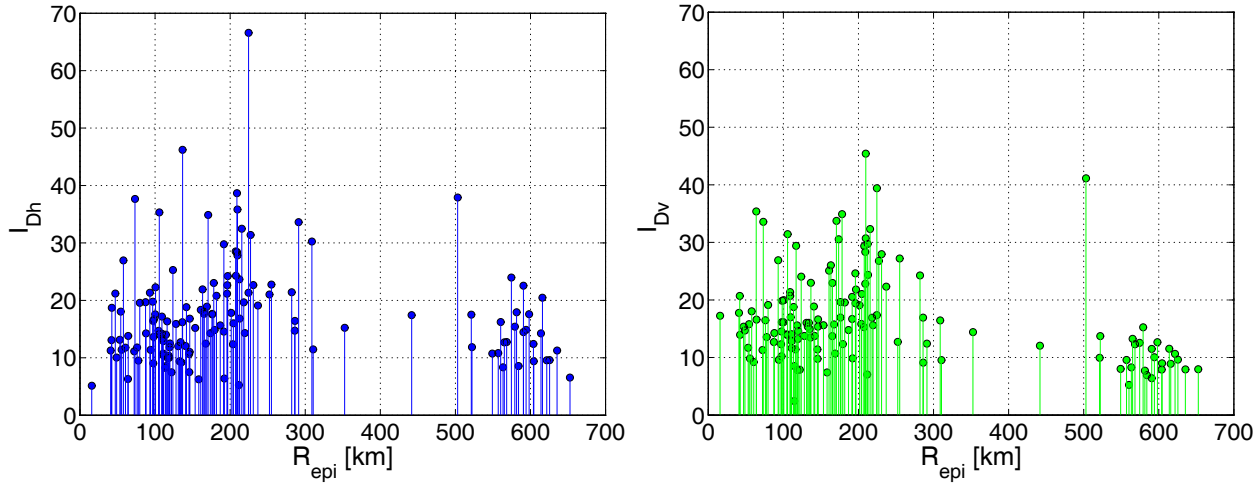

Figure 8. I_D values: geometrical mean of the horizontal components, I_{Dh} (on the left), and vertical component I_{Dv} (on the left).

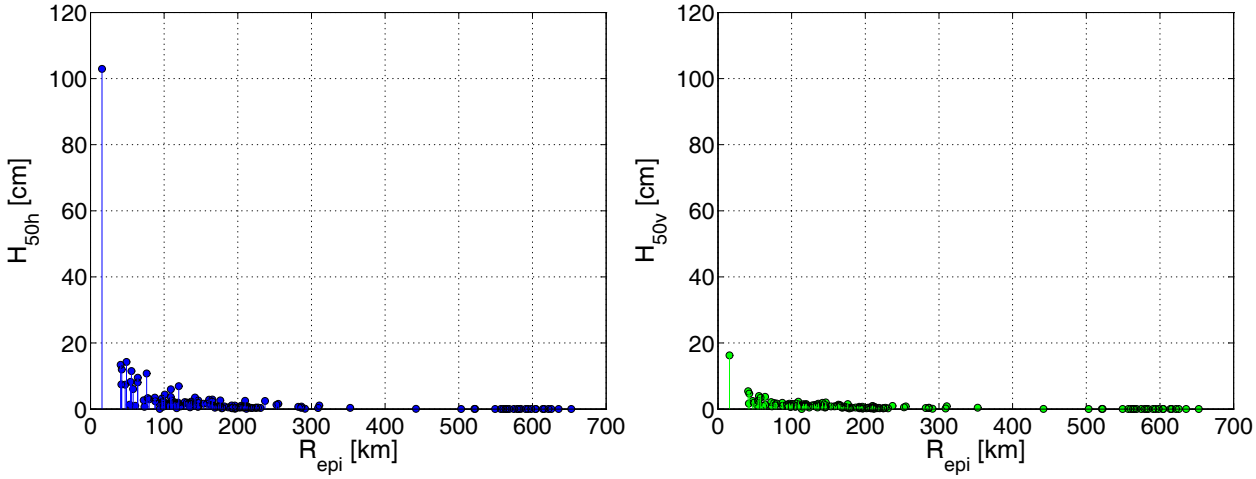

Figure 9. H_{50} values: geometrical mean of the horizontal components, H_{50h} (on the left), and vertical component H_{50v} (on the left).

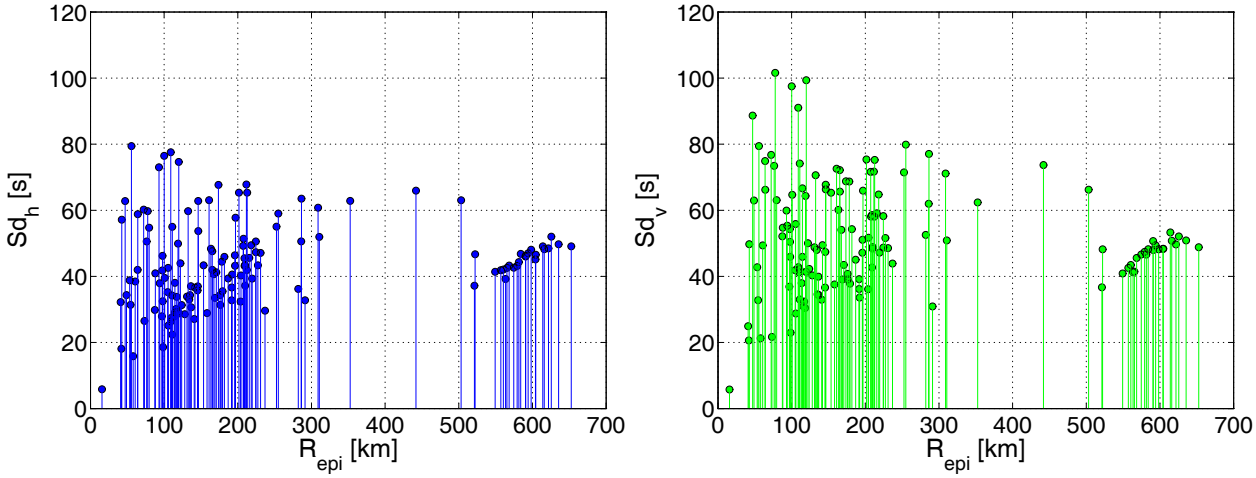

Figure 10. Sd values: geometrical mean of the horizontal components, Sd_h (on the left), and vertical component Sd_v (on the left).

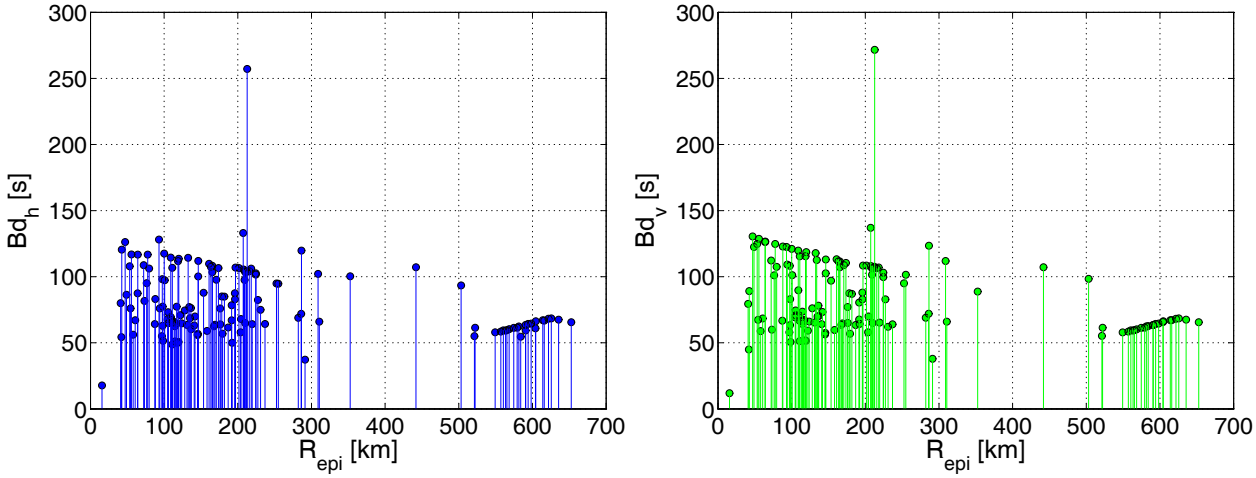

Figure 11. Bd values: geometrical mean of the horizontal components, Bd_h (on the left), and vertical component Bd_v (on the left).

5. Comparison of the data with Bindi et al. GMPE predictions, PGA, PGV and Sa(T).

In the following preliminary comparisons of the registered data with Bindi et al. (2011) GMPE median predictions and their uncertainties bands (represented by the median plus and median minus one total standard deviation, $Median + \sigma$ and $Median - \sigma$, respectively) in terms of PGA, PGV, Sa(T) are provided. It is worth to note that the range of validity of such GMPE is within 0km up to 200km, thus hereafter the extrapolation of the prediction outside this range is represented by dotted lines. The predictions are made, preliminarily, for A soil class according to Eurocode 8 or EC8, (CEN, 2004), notwithstanding the fact that each station is located on different soil classes and their classification is provided by the Italian Accelerometric Archive (ITACA), http://itaca.mi.ingv.it. A soil class is defined as "rock or other rock-like geological formation, including at most 5 m of weaker material at the surface", characterized by an average value of shear wave velocity in the first 30 m, V_{s30}, higher than 800 m/s. Soil class A is characterized by the least soil amplification factor respect to other, softer soil classes (B, C, D, E) and is the richest soil class in Bindi et al. (2011) dataset, with more than 300 waveforms.

Figure 12 show the comparison of the geometrical mean of the registered horizontal components data and the median predictions in term of PGA and PGV. Same plot is shown in Figure 13 for the case of the vertical component. It can be observed that registered data are, in most cases, within the $\pm\sigma$ bands. Figure 14 and Figure 15 show the same comparison in terms of Sa(T) at different periods, for geometrical mean of the horizontal and vertical components, respectively. Such comparison emphasizes how the data exceed the $\pm\sigma$ range in the case of periods higher than 1.75 s even if it should take into account the preliminary approximation that soil amplification was not considered in this case, given the hypothesis of A soil class.

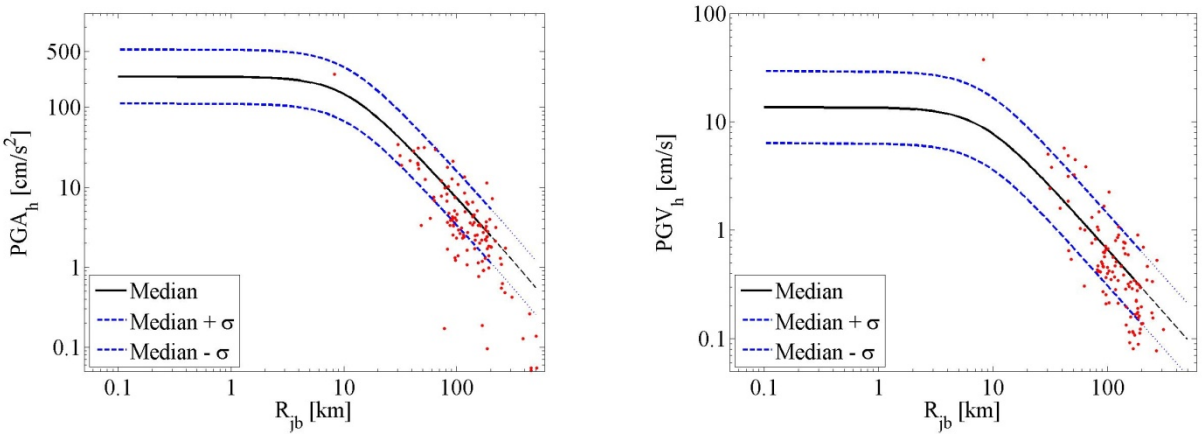

Figure 12. PGA_h and PGV_h comparison of the geometrical mean of the horizontal components of the registered data with the median and $\pm\sigma$ predictions according to Bindi et al. (2011).

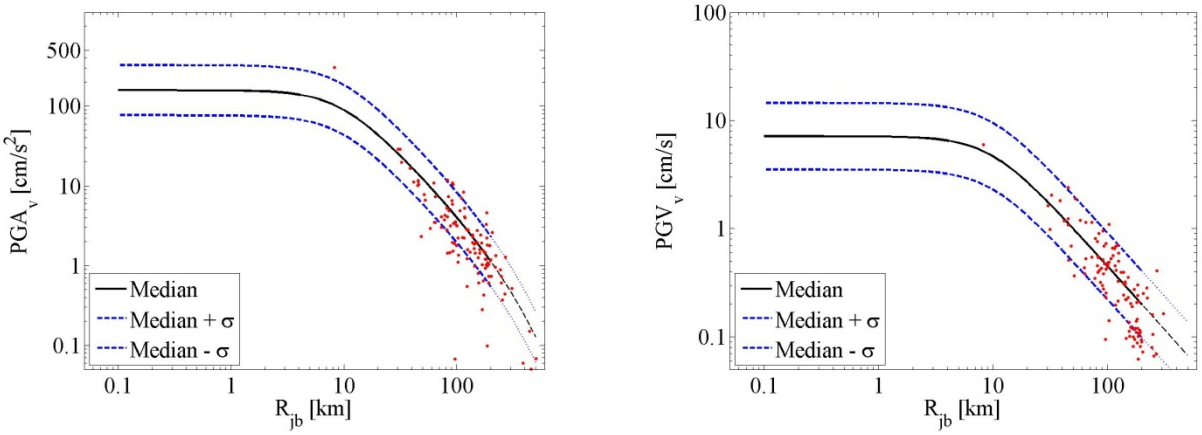

Figure 13. PGA_v and PGV_v comparison of the vertical component of the registered data with the median and $\pm\sigma$ predictions according to Bindi et al. (2011).

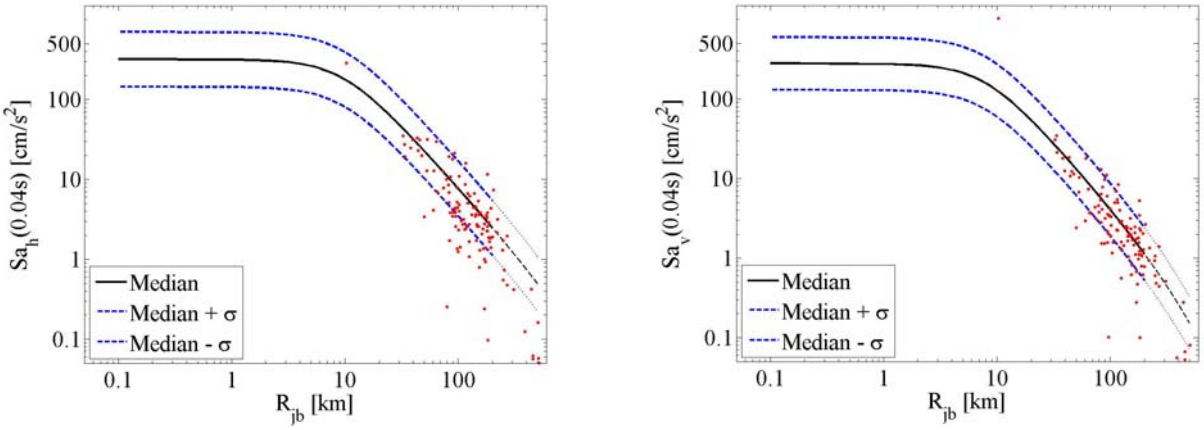

Figure 13. Spectral acceleration comparison of the geometrical mean of the horizontal components $Sa_h(T)$, on the right, and the vertical component $Sa_v(T)$, on the left, of the registered data with the median and $\pm\sigma$ predictions according to Bindi et al. (2011) for T=0.04s.

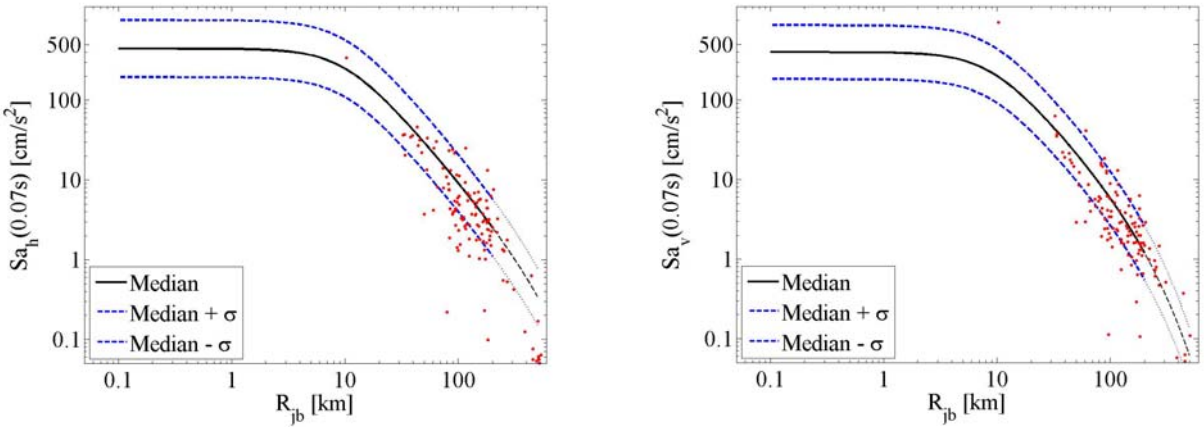

Figure 14. Spectral acceleration comparison of the geometrical mean of the horizontal components $Sa_h(T)$, on the right, and the vertical component $Sa_v(T)$, on the left, of the registered data with the median and $\pm\sigma$ predictions according to Bindi et al. (2011) for T=0.07s.

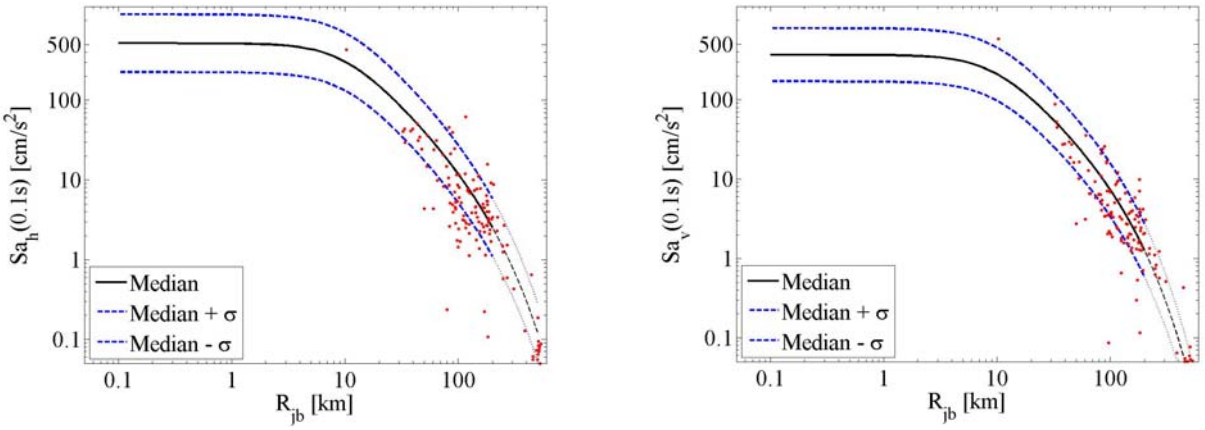

Figure 15. Spectral acceleration comparison of the geometrical mean of the horizontal components $Sa_h(T)$, on the right, and the vertical component $Sa_v(T)$, on the left, of the registered data with the median and $\pm\sigma$ predictions according to Bindi et al. (2011) for T=0.1s.

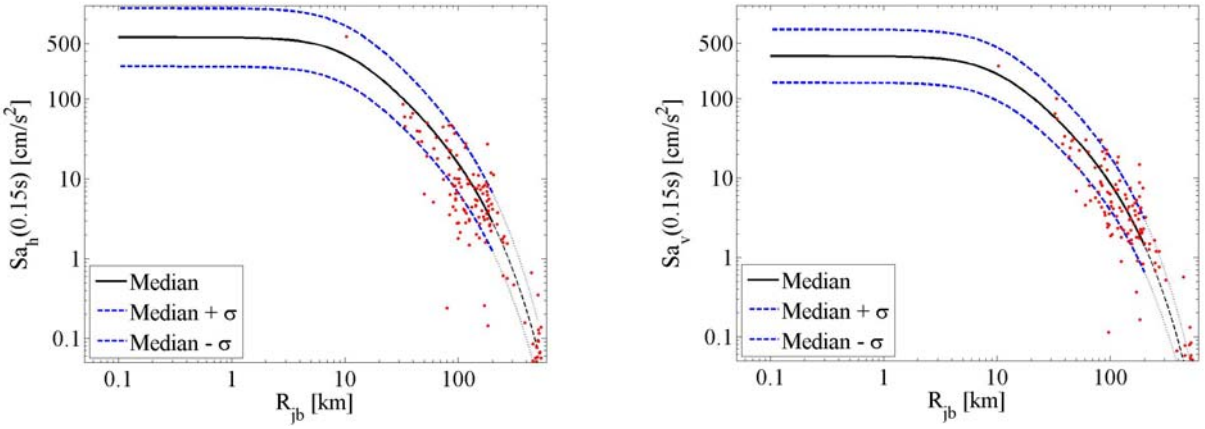

Figure 16. Spectral acceleration comparison of the geometrical mean of the horizontal components $Sa_h(T)$, on the right, and the vertical component $Sa_v(T)$, on the left, of the registered data with the median and $\pm\sigma$ predictions according to Bindi et al. (2011) for T=0.15s.

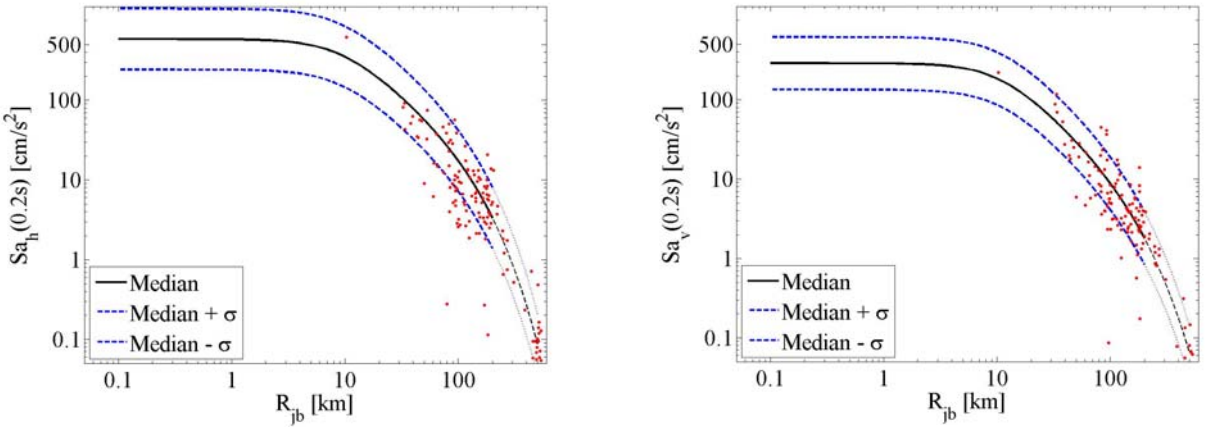

Figure 17. Spectral acceleration comparison of the geometrical mean of the horizontal components $Sa_h(T)$, on the right, and the vertical component $Sa_v(T)$, on the left, of the registered data with the median and $\pm\sigma$ predictions according to Bindi et al. (2011) for T=0.20s.

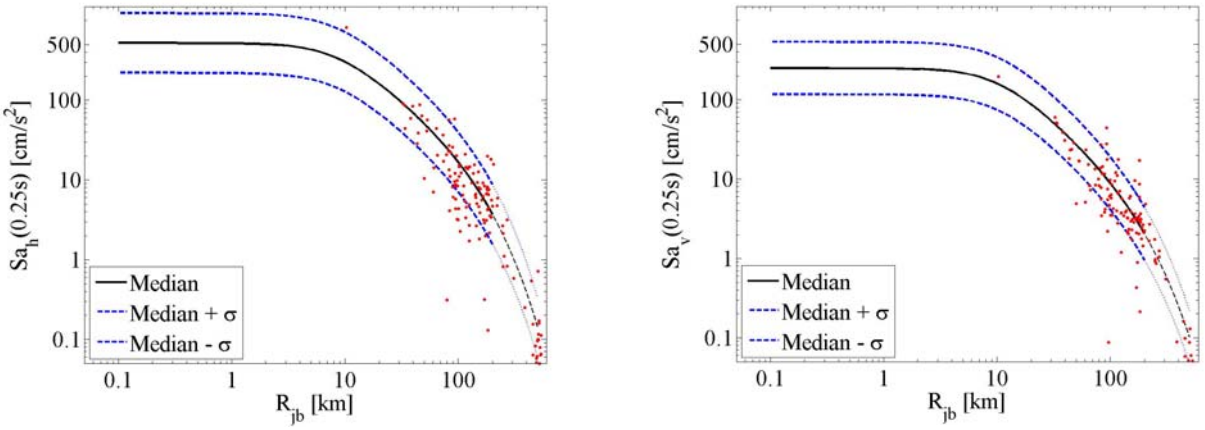

Figure 18. Spectral acceleration comparison of the geometrical mean of the horizontal components $Sa_h(T)$, on the right, and the vertical component $Sa_v(T)$, on the left, of the registered data with the median and $\pm\sigma$ predictions according to Bindi et al. (2011) for T=0.25s.

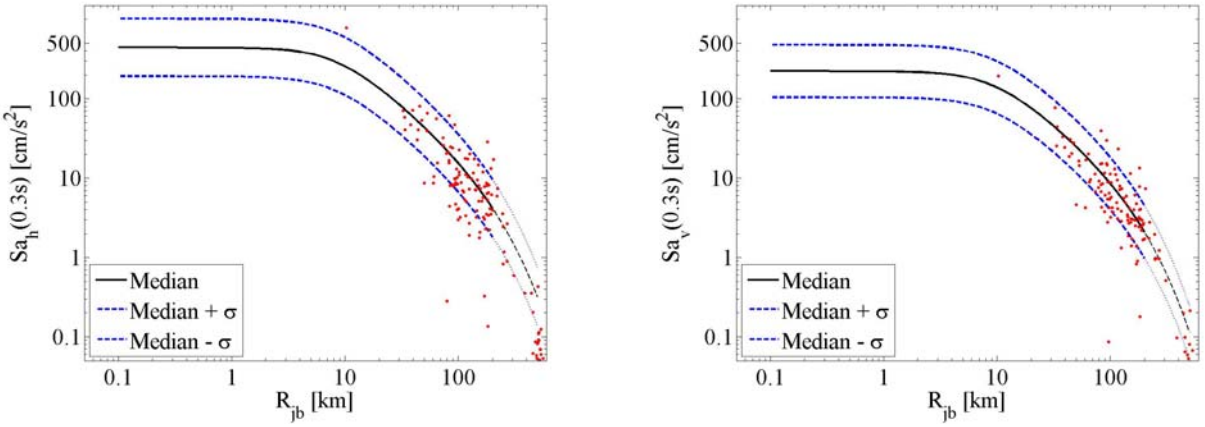

Figure 19. Spectral acceleration comparison of the geometrical mean of the horizontal components $Sa_h(T)$, on the right, and the vertical component $Sa_v(T)$, on the left, of the registered data with the median and $\pm\sigma$ predictions according to Bindi et al. (2011) for T=0.30s.

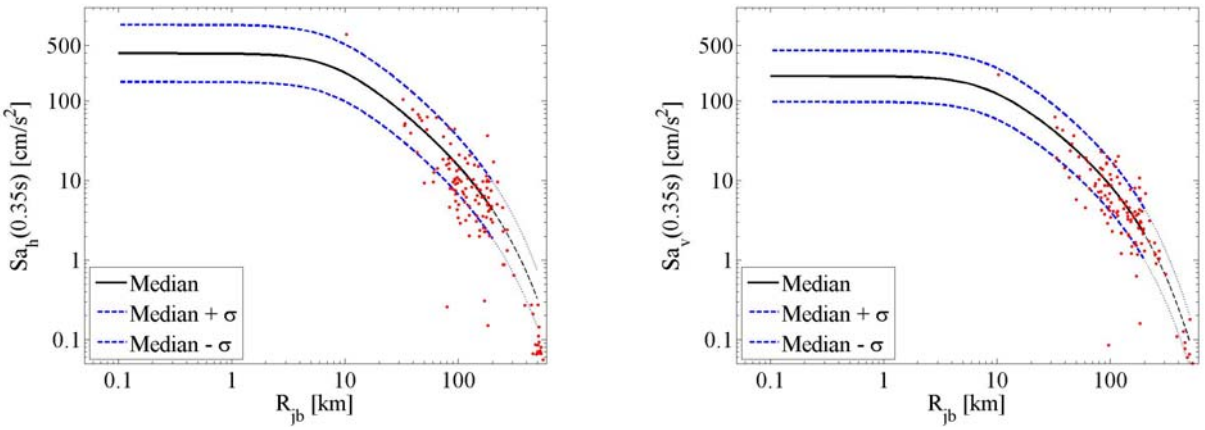

Figure 20. Spectral acceleration comparison of the geometrical mean of the horizontal components $Sa_h(T)$, on the right, and the vertical component $Sa_v(T)$, on the left, of the registered data with the median and $\pm\sigma$ predictions according to Bindi et al. (2011) for T=0.35s.

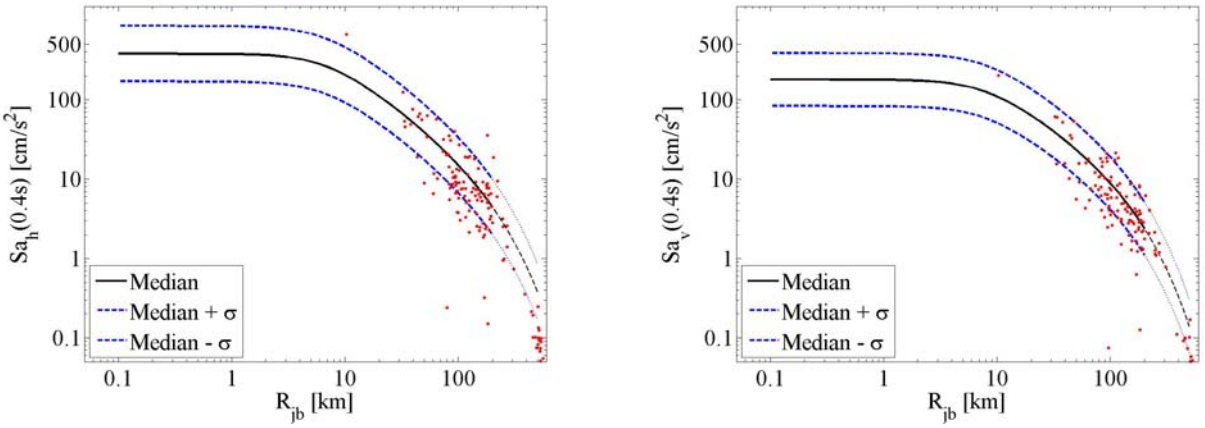

Figure 21. Spectral acceleration comparison of the geometrical mean of the horizontal components $Sa_h(T)$, on the right, and the vertical component $Sa_v(T)$, on the left, of the registered data with the median and $\pm\sigma$ predictions according to Bindi et al. (2011) for T=0.40s.

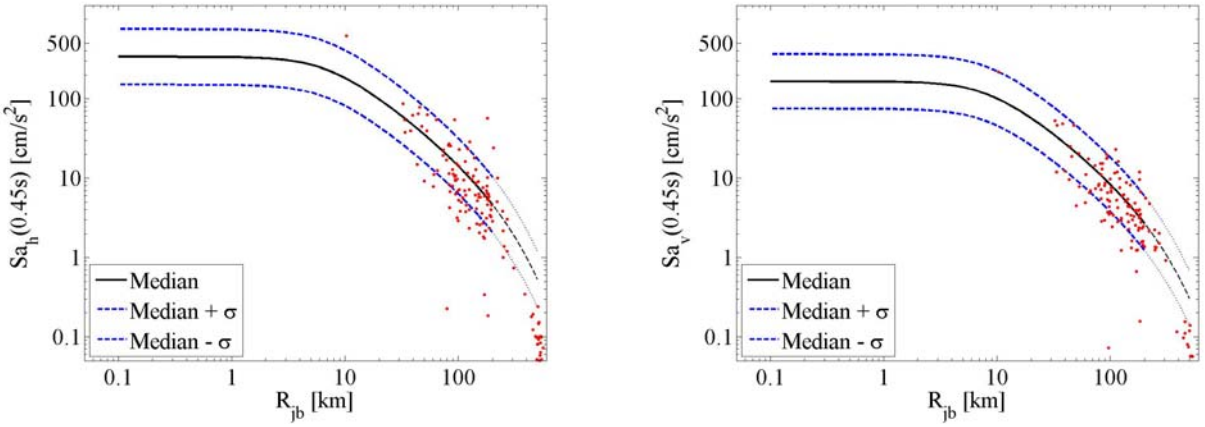

Figure 22. Spectral acceleration comparison of the geometrical mean of the horizontal components $Sa_h(T)$, on the right, and the vertical component $Sa_v(T)$, on the left, of the registered data with the median and $\pm\sigma$ predictions according to Bindi et al. (2011) for T=0.45s.

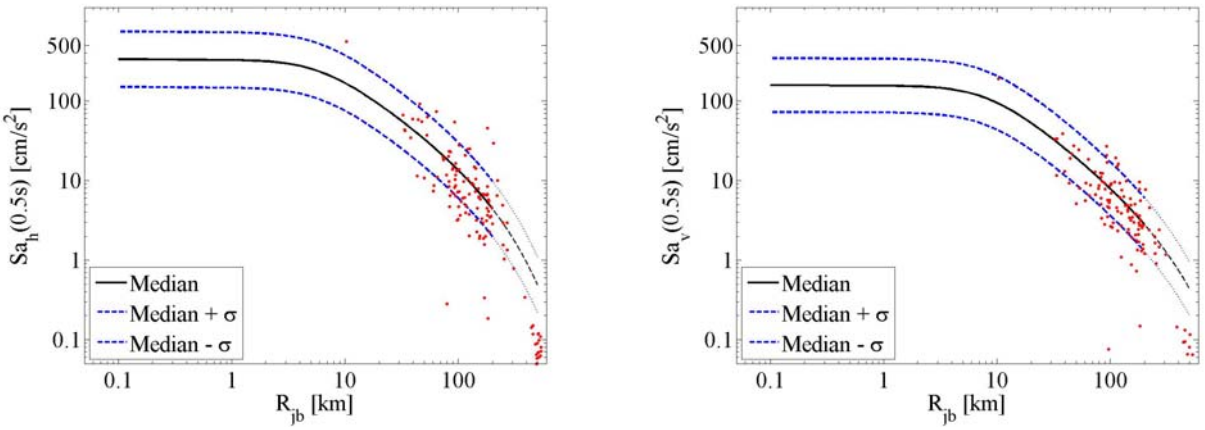

Figure 23. Spectral acceleration comparison of the geometrical mean of the horizontal components $Sa_h(T)$, on the right, and the vertical component $Sa_v(T)$, on the left, of the registered data with the median and $\pm\sigma$ predictions according to Bindi et al. (2011) for T=0.50s.

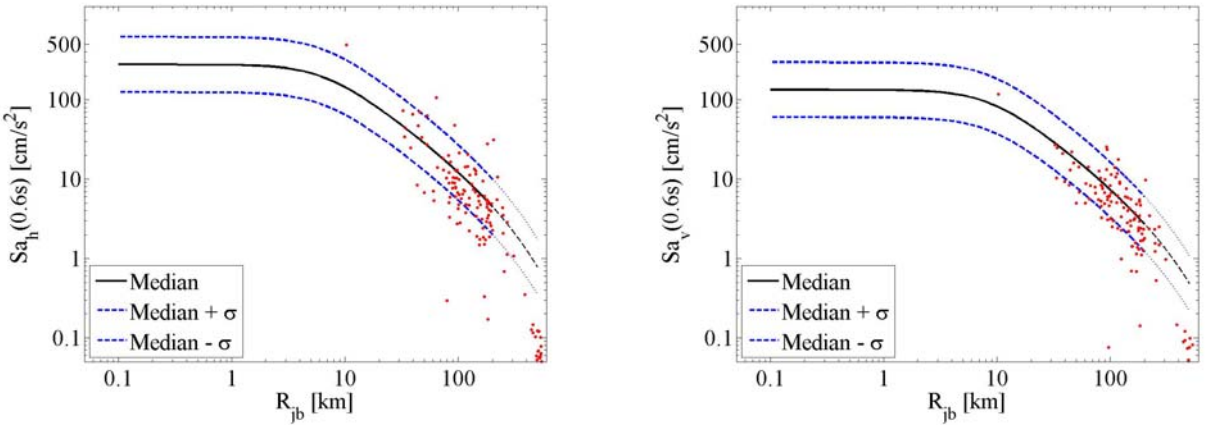

Figure 24. Spectral acceleration comparison of the geometrical mean of the horizontal components $Sa_h(T)$, on the right, and the vertical component $Sa_v(T)$, on the left, of the registered data with the median and $\pm\sigma$ predictions according to Bindi et al. (2011) for T=0.60s.

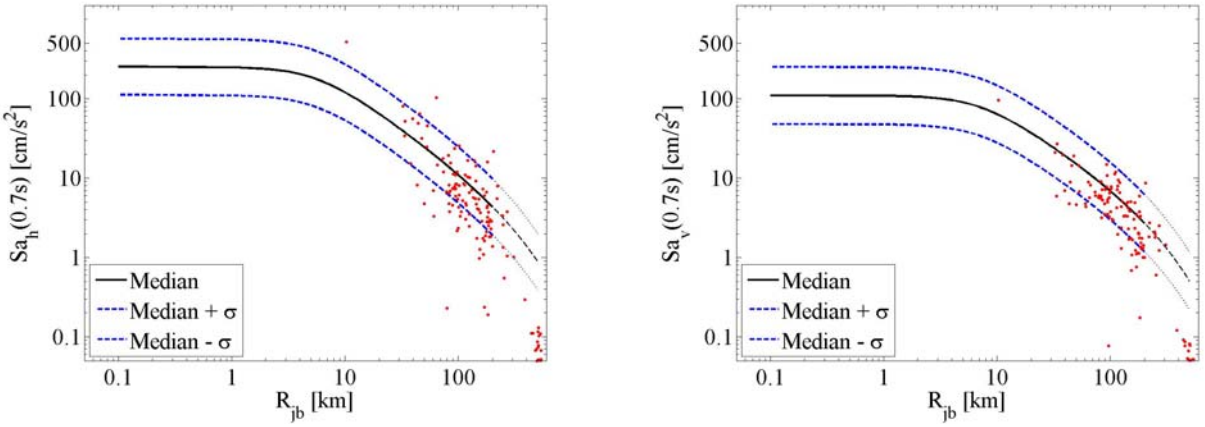

Figure 25. Spectral acceleration comparison of the geometrical mean of the horizontal components $Sa_h(T)$, on the right, and the vertical component $Sa_v(T)$, on the left, of the registered data with the median and $\pm\sigma$ predictions according to Bindi et al. (2011) for T=0.70s.

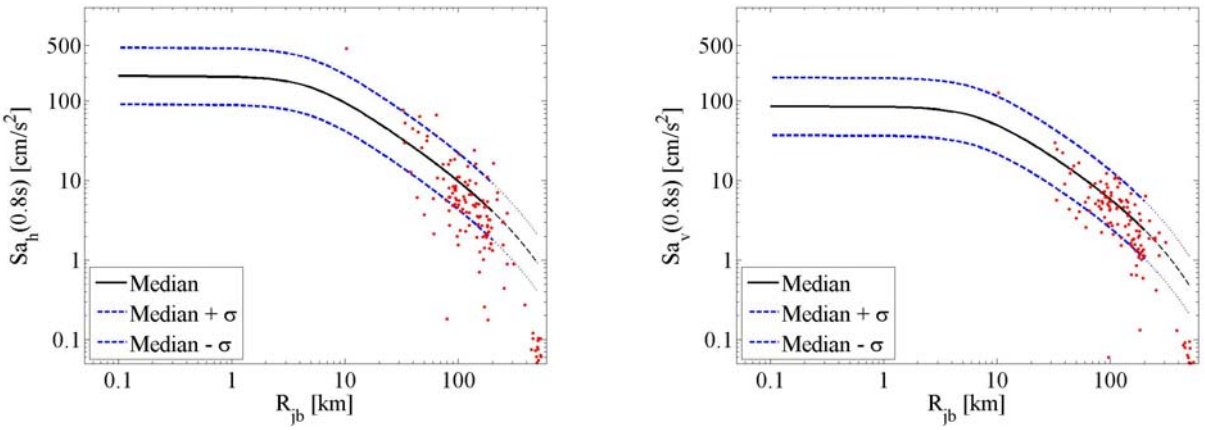

Figure 26. Spectral acceleration comparison of the geometrical mean of the horizontal components $Sa_h(T)$, on the right, and the vertical component $Sa_v(T)$, on the left, of the registered data with the median and $\pm\sigma$ predictions according to Bindi et al. (2011) for T=0.80s.

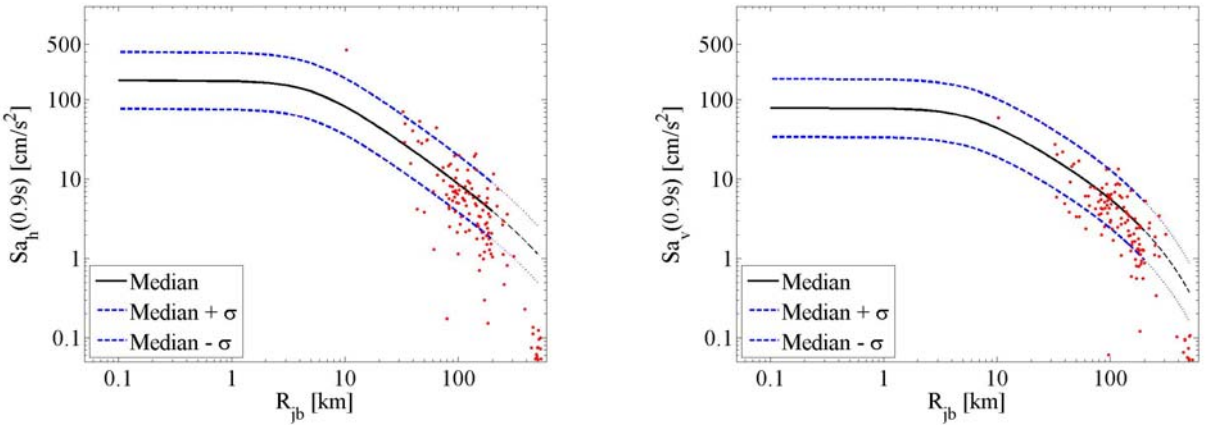

Figure 27. Spectral acceleration comparison of the geometrical mean of the horizontal components $Sa_h(T)$, on the right, and the vertical component $Sa_v(T)$, on the left, of the registered data with the median and $\pm\sigma$ predictions according to Bindi et al. (2011) for T=0.90s.

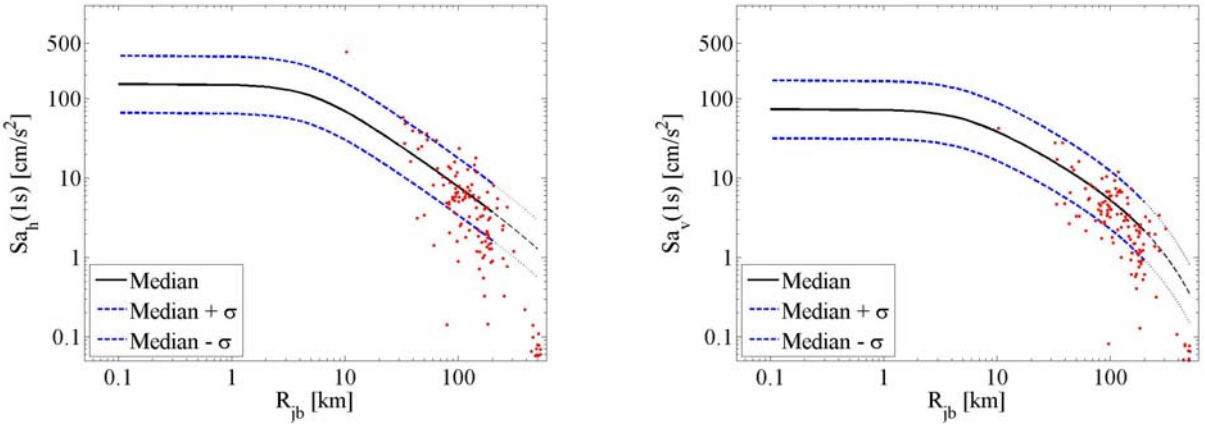

Figure 28. Spectral acceleration comparison of the geometrical mean of the horizontal components $Sa_h(T)$, on the right, and the vertical component $Sa_v(T)$, on the left, of the registered data with the median and $\pm\sigma$ predictions according to Bindi et al. (2011) for T=1.00s.

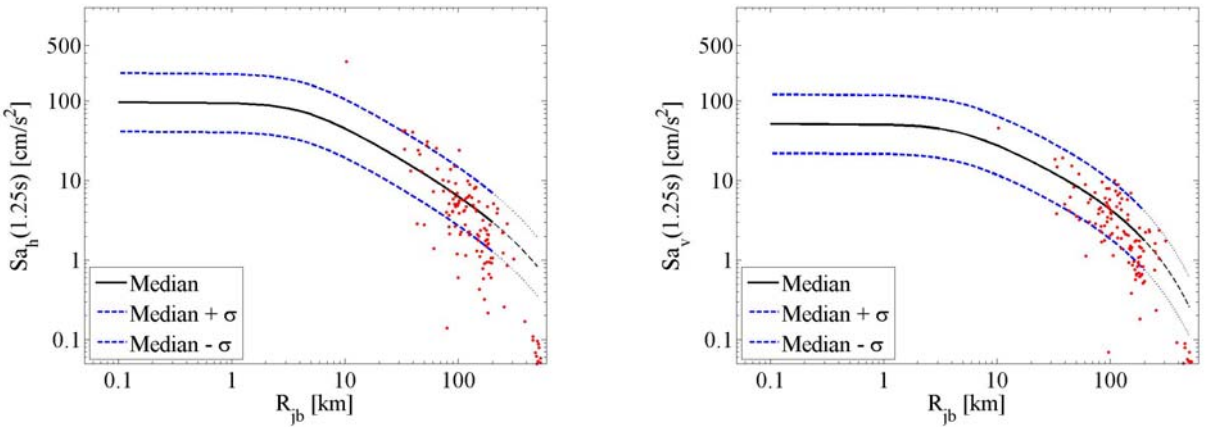

Figure 29. Spectral acceleration comparison of the geometrical mean of the horizontal components $Sa_h(T)$, on the right, and the vertical component $Sa_v(T)$, on the left, of the registered data with the median and $\pm\sigma$ predictions according to Bindi et al. (2011) for T=1.25s.

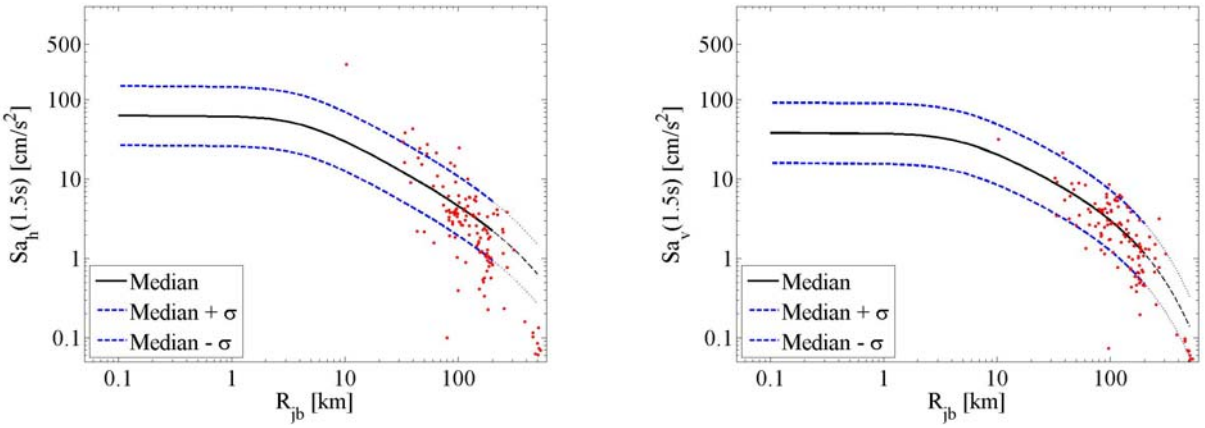

Figure 30. Spectral acceleration comparison of the geometrical mean of the horizontal components $Sa_h(T)$, on the right, and the vertical component $Sa_v(T)$, on the left, of the registered data with the median and $\pm\sigma$ predictions according to Bindi et al. (2011) for T=1.50s.

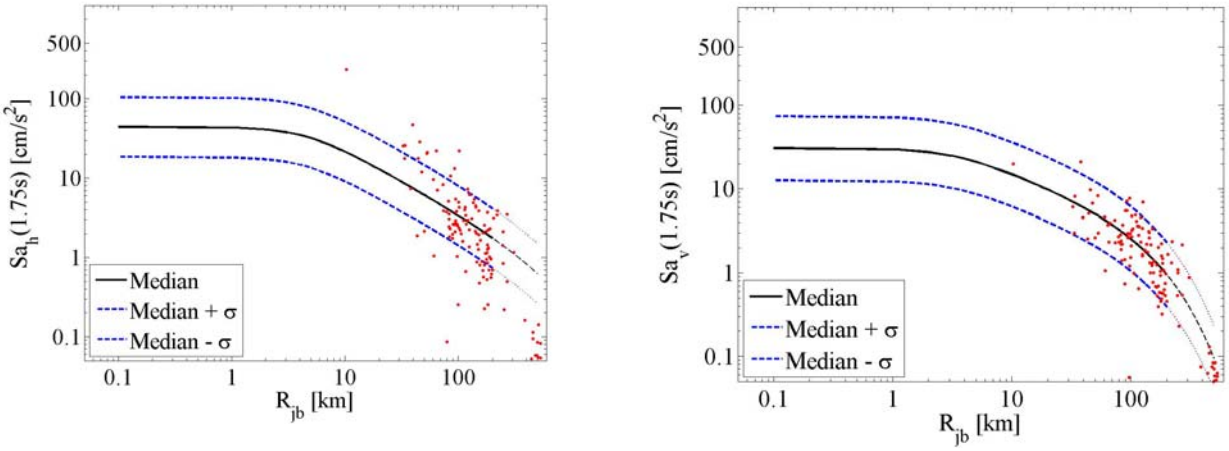

Figure 31. Spectral acceleration comparison of the geometrical mean of the horizontal components $Sa_h(T)$, on the right, and the vertical component $Sa_v(T)$, on the left, of the registered data with the median and $\pm\sigma$ predictions according to Bindi et al. (2011) for T=1.75s.

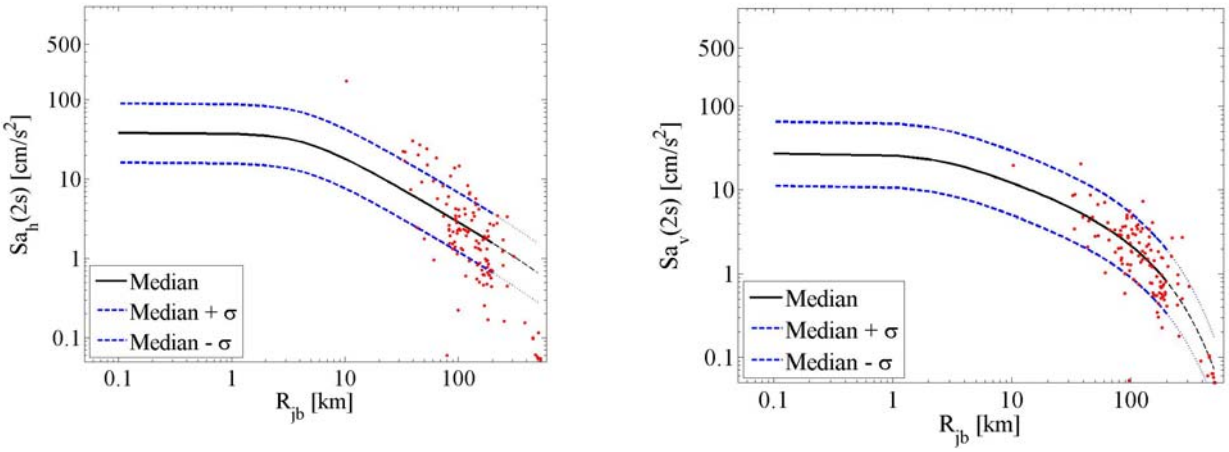

Figure 32. Spectral acceleration comparison of the geometrical mean of the horizontal components $Sa_h(T)$, on the right, and the vertical component $Sa_v(T)$, on the left, of the registered data with the median and $\pm\sigma$ predictions according to Bindi et al. (2011) for T=2.00s.

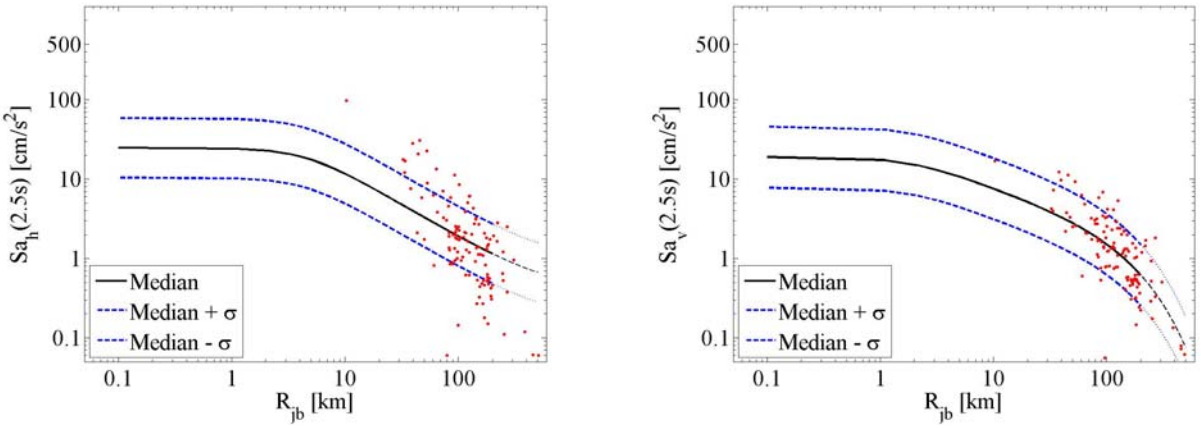

Figure 33. Spectral acceleration comparison of the geometrical mean of the horizontal components $Sa_h(T)$, on the right, and the vertical component $Sa_v(T)$, on the left, of the registered data with the median and $\pm\sigma$ predictions according to Bindi et al. (2011) for T=2.50s.

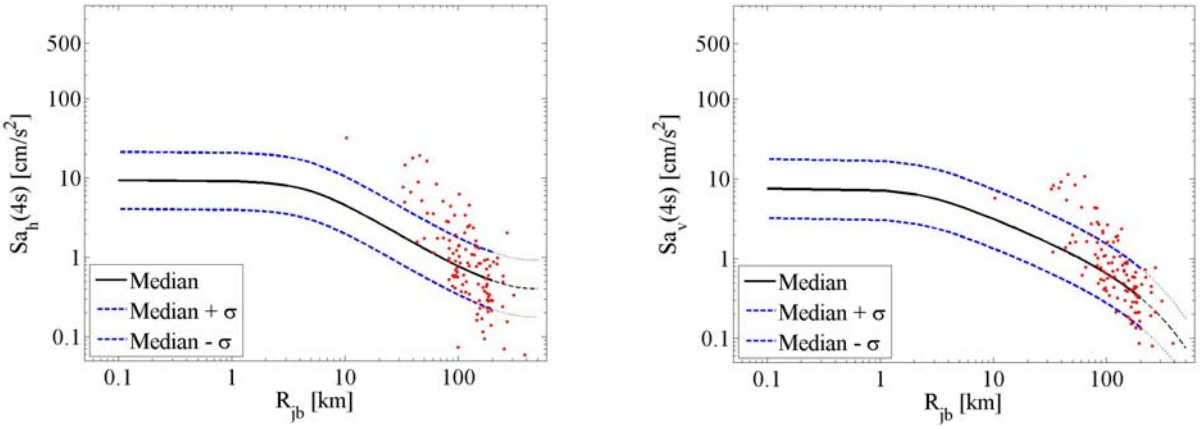

Figure 34. Spectral acceleration comparison of the geometrical mean of the horizontal components $Sa_h(T)$, on the right, and the vertical component $Sa_v(T)$, on the left, of the registered data with the median and $\pm\sigma$ predictions according to Bindi et al. (2011) for T=4.0s.

6. Direct spectral comparison of the data registered within 70km

A direct spectral comparison is made for the signals registered within 70km form the epicenter. For such stations the classification according to the Italian Accelerometric Archive (ITACA) is provided in Table 2. Soil type marked with a star (*) means that the identification is carried out from Italian geological maps (1:100.000 scale). Two stations, ZPP and MRZ were not found in ITACA; thus, in Table 2 they are indicated as “nf”, and for the following direct spectral comparison such stations are considered on soil class A, in analogy with the hypothesis made in the previous section.

In Figure 35 to Figure 47 the direct comparison of the horizontal and vertical component registered spectra with median and bands of Bindi et al. (2011) GMPE is provided. Joyner and Boore distance is evaluated according to the approximate expression in Equation (1). The most of

the registered spectra fall within the $\pm\sigma$ bands. The only exception is found in the closest waveform (MRN) in the N-S component. In this latter case the spectra exceeds the prediction in the medium high-period range (T > 0.5s).

Table 2. Soil classification of the stations within 70 km from the epicentre.

Station ID	R_{epi}	Station Name	soil class
	[km]		
MRN	16	Mirandola	C* (3)
MDN	41	Modena	C (3)
NVL	42	Novellara	C (3)
ZPP	43	Zola_Pedrosa_Piana	nf
ISD	47	Isola_Della_Scala	B*(2)
CPC	49	Copparo_Coccanile	C*(3)
MNS	53	Monselice	C*(3)
ARG	54	Argenta	D (4)
MDC	56	Medicina	C*(3)
SSU	58	Sassuolo	A*(1)
MRZ	61	Marzabotto	nf
CSP	64	CastelSanPietroTerme	B*(2)
SRP	64	Sorbolo	C*(3)

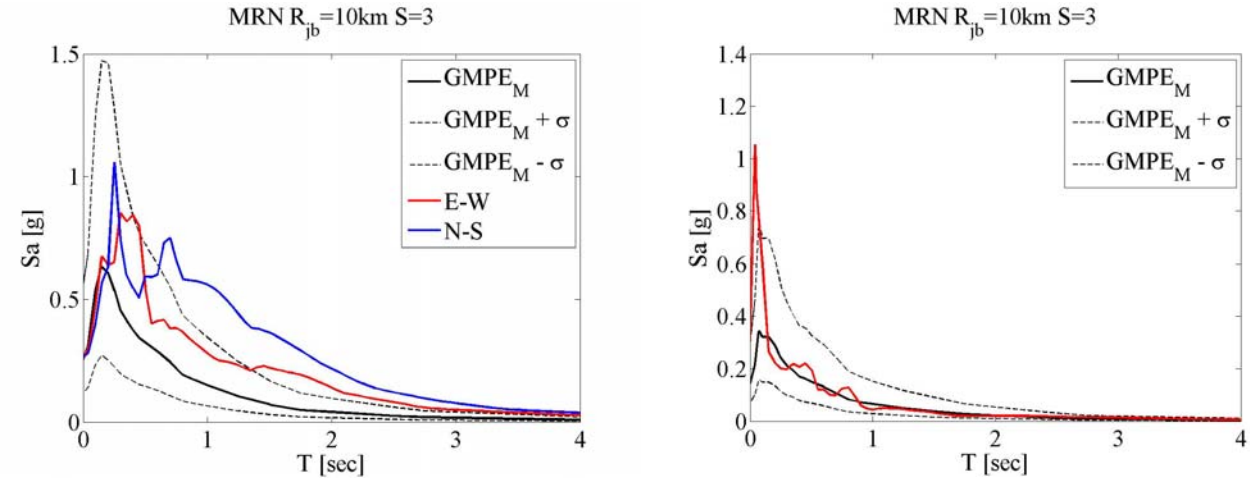

Figure 35. Comparison of the registered spectra at MRN station for E-W and N-S components (on the left) and vertical component (on the right) with the mean $\pm\sigma$ predictions according to Bindi et al. (2011).

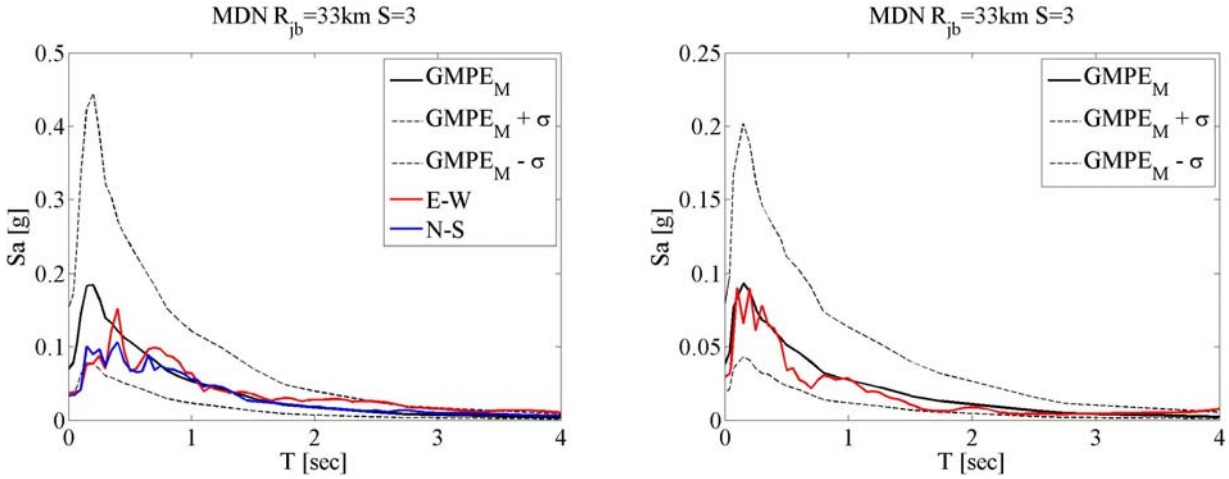

Figure 36. Comparison of the registered spectra at MDN station for E-W and N-S components (on the left) and vertical component (on the right) with the mean $\pm\sigma$ predictions according to Bindi et al. (2011).

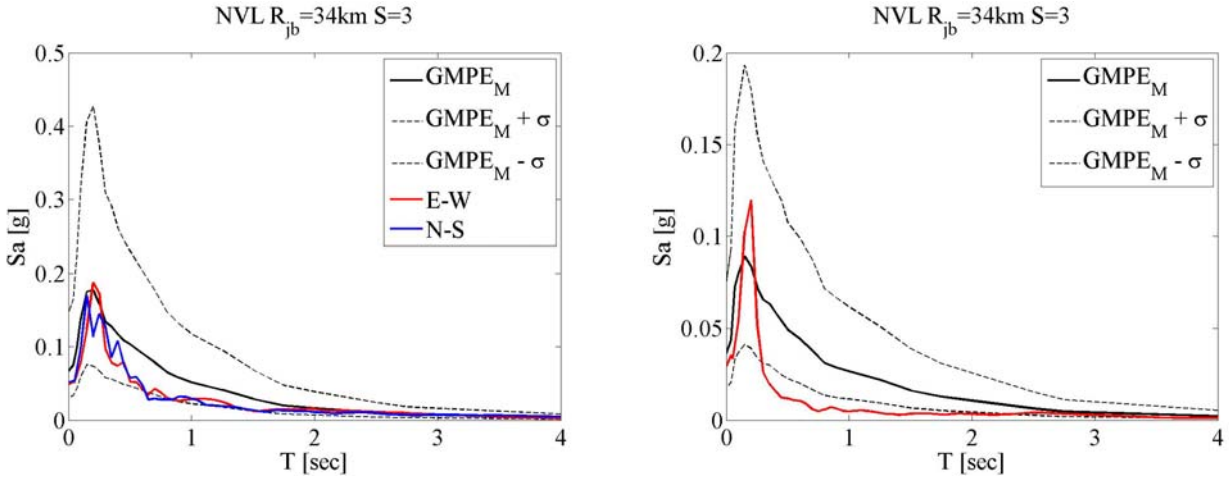

Figure 37. Comparison of the registered spectra at NVL station for E-W and N-S components (on the left) and vertical component (on the right) with the mean $\pm\sigma$ predictions according to Bindi et al. (2011).

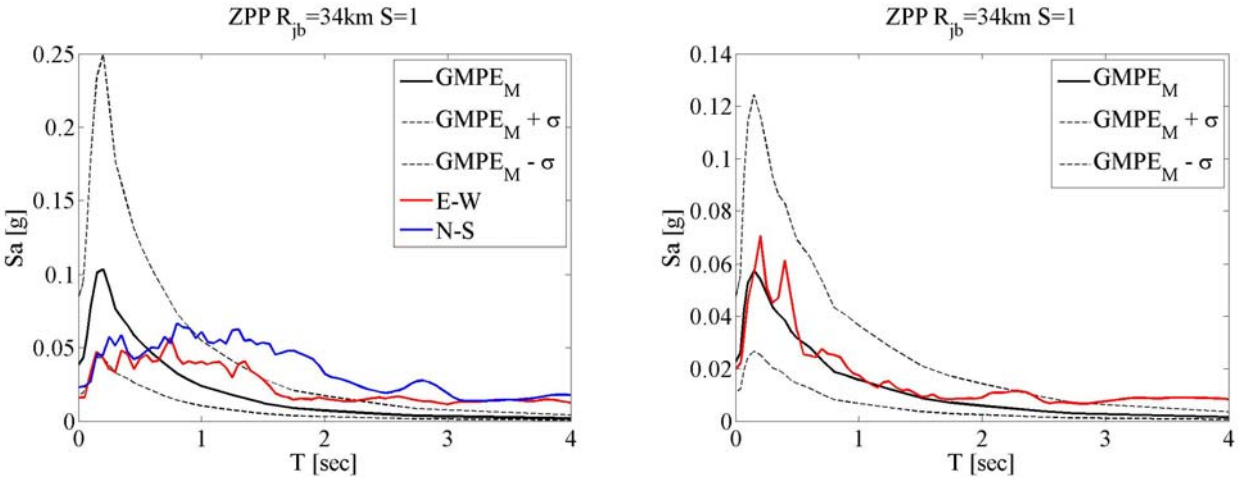

Figure 38. Comparison of the registered spectra at ZPP station for E-W and N-S components (on the left) and vertical component (on the right) with the mean $\pm\sigma$ predictions according to Bindi et al. (2011).

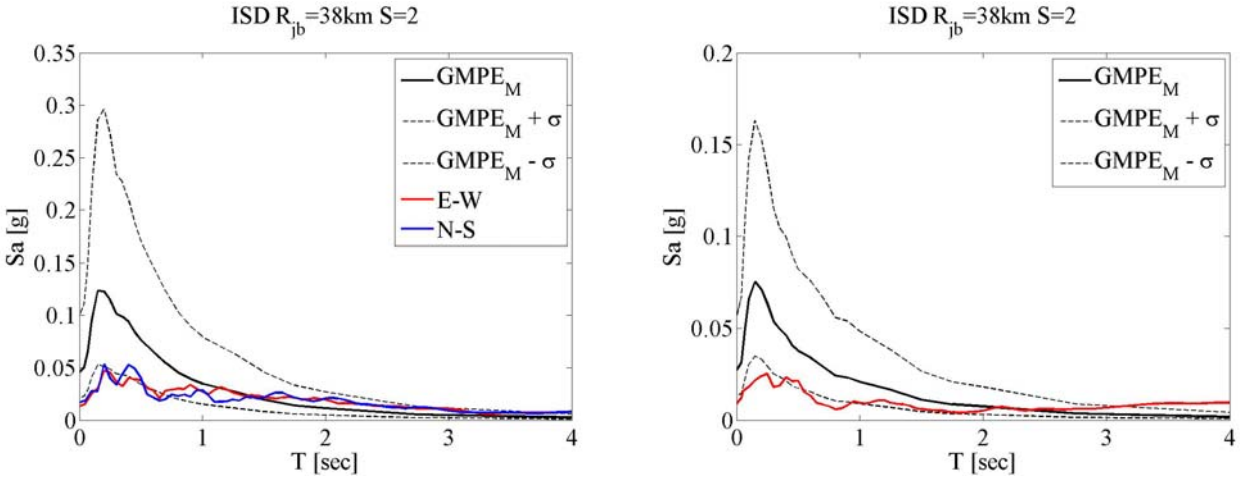

Figure 39. Comparison of the registered spectra at ISD station for E-W and N-S components (on the left) and vertical component (on the right) with the mean $\pm\sigma$ predictions according to Bindi et al. (2011).

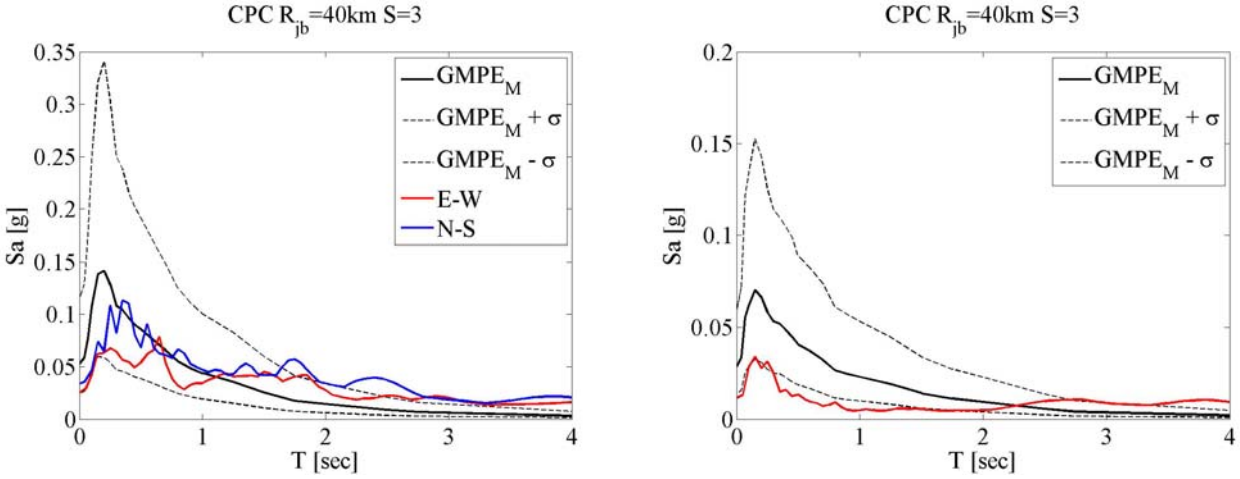

Figure 40. Comparison of the registered spectra at CPC station for E-W and N-S components (on the left) and vertical component (on the right) with the mean $\pm\sigma$ predictions according to Bindi et al. (2011).
ith the mean $\pm\sigma$ predictions according to Bindi et al. (2011).

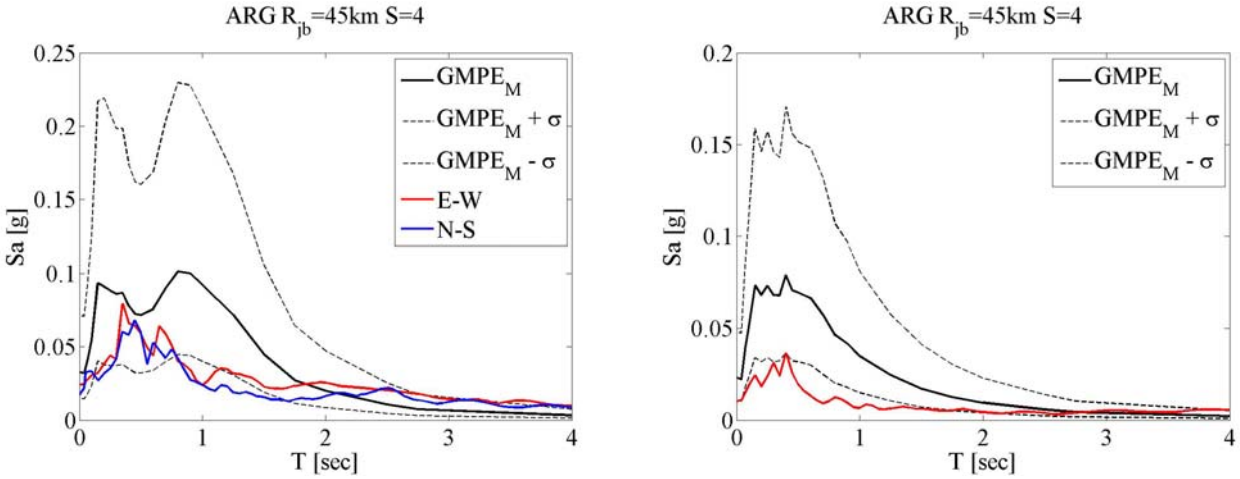

Figure 41. Comparison of the registered spectra at ARG station for E-W and N-S components (on the left) and vertical component (on the right) with the mean $\pm\sigma$ predictions according to Bindi et al. (2011).

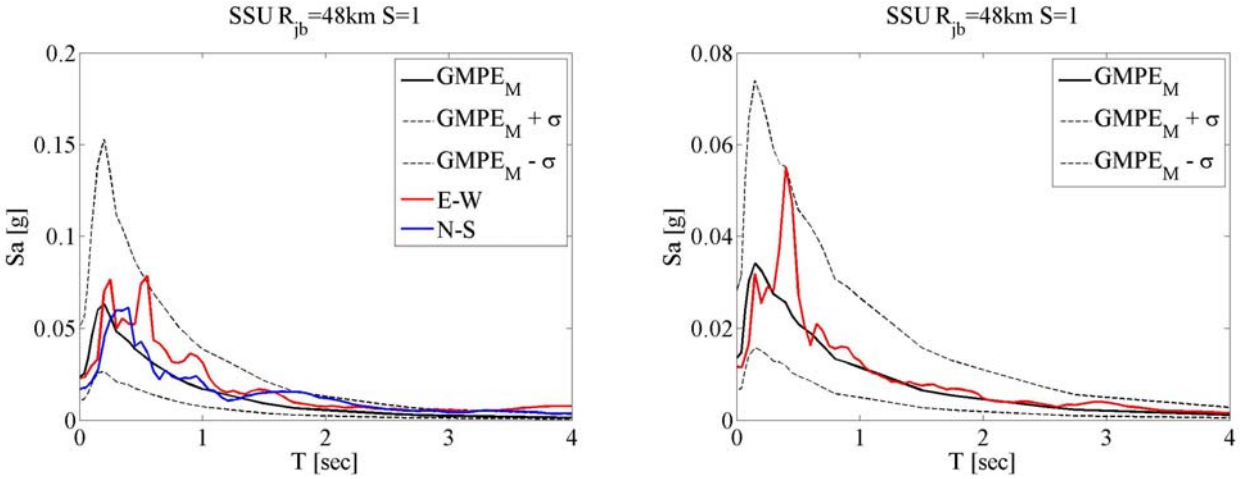

Figure 42. Comparison of the registered spectra at SSU station for E-W and N-S components (on the left) and vertical component (on the right) with the mean $\pm\sigma$ predictions according to Bindi et al. (2011).

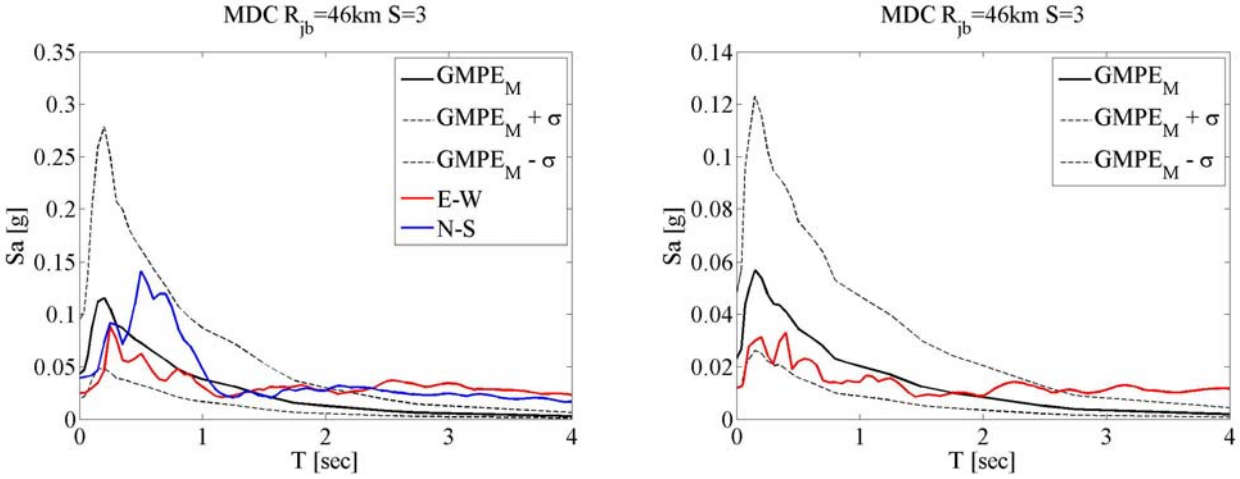

Figure 43. Comparison of the registered spectra at MDC station for E-W and N-S components (on the left) and vertical component (on the right) with the mean $\pm\sigma$ predictions according to Bindi et al. (2011).

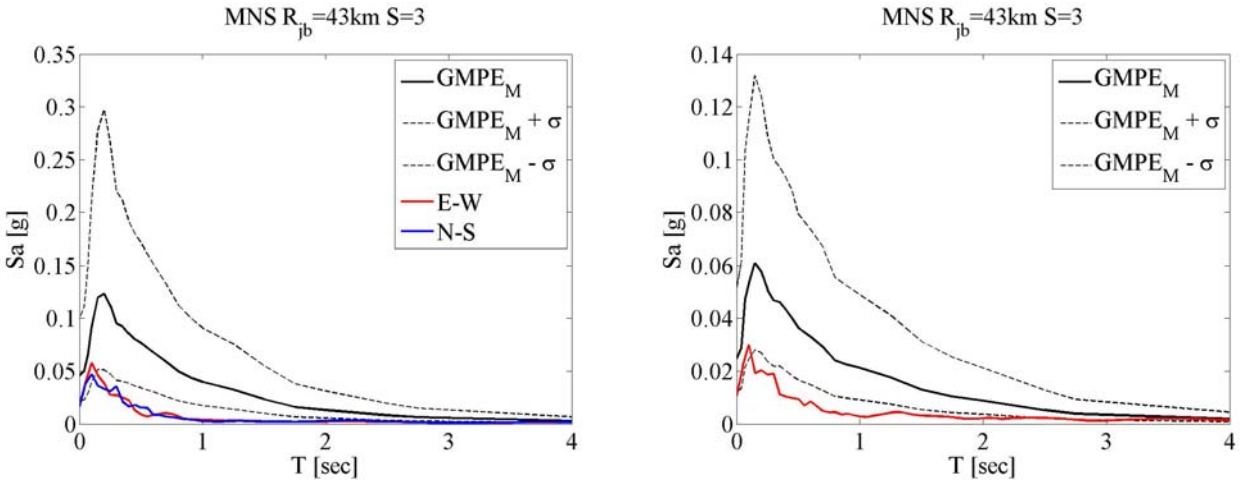

Figure 44. Comparison of the registered spectra at MNS station for E-W and N-S components (on the left) and vertical component (on the right) with the mean $\pm\sigma$ predictions according to Bindi et al. (2011).

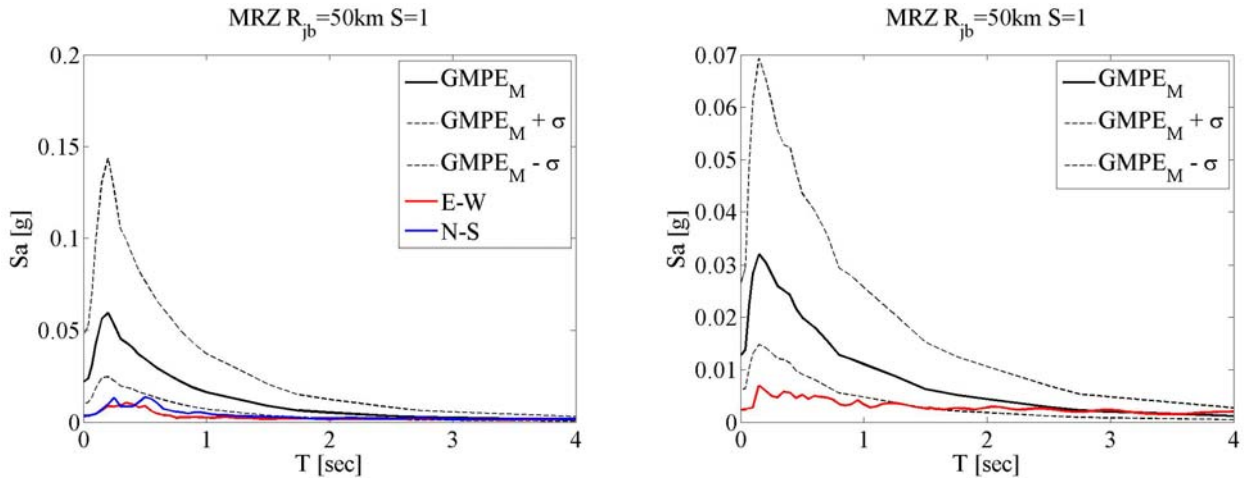

Figure 45. Comparison of the registered spectra at MRZ station for E-W and N-S components (on the left) and vertical component (on the right) with the mean $\pm\sigma$ predictions according to Bindi et al. (2011).

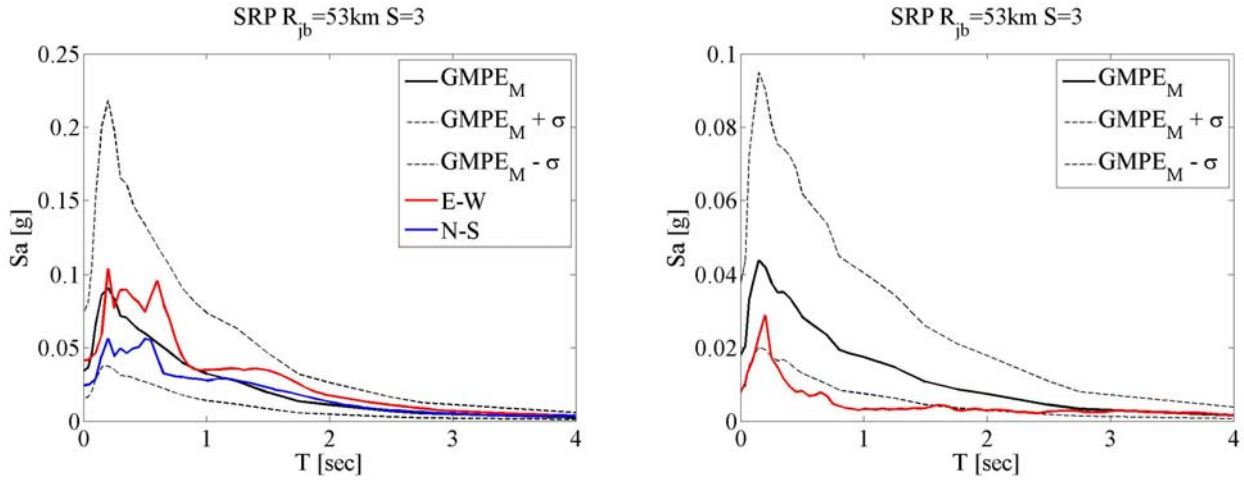

Figure 46. Comparison of the registered spectra at SRP station for E-W and N-S components (on the left) and vertical component (on the right) with the mean $\pm\sigma$ predictions according to Bindi et al. (2011).

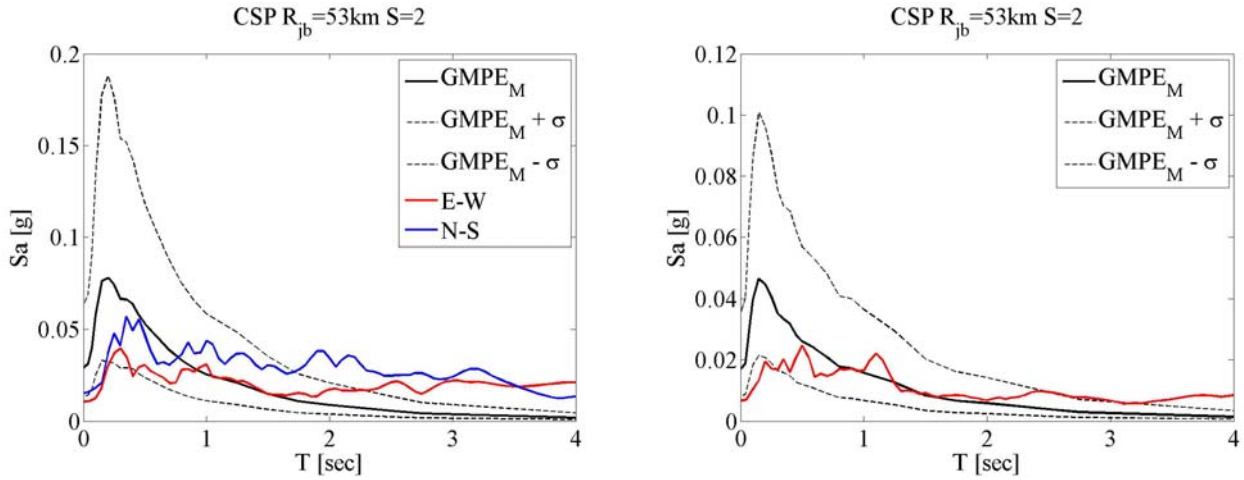

Figure 47. Comparison of the registered spectra at CSP station for E-W and N-S components (on the left) and vertical component (on the right) with the mean $\pm\sigma$ predictions according to Bindi et al. (2011).

7. Epsilon values of the data registered within 70km

In this section, according to the previous one, signals registered within 70km form the epicentre are compared with Bindi et al. (2011) GMPE. Results are reported in terms of epsilon values (ε) which measures the number of total standard deviations $(\sigma_{\log IM})$ by which logarithms of observed intensity measures $(\log IM)$ differs from a its predicted mean $(\mu_{\log IM})$:

$$\varepsilon = \frac{\log IM - \mu_{\log IM}}{\sigma_{\log IM}} \tag{2}$$

Joyner Boore distance is evaluated according to the approximate expression in Equation (1).

In Figure 48 epsilon values of PGA are shown for geometrical mean of horizontal components (in accordance with estimated variable of used GMPE) and for the vertical components. In Figure 49 epsilon values of PGV are shown for geometrical mean of horizontal components and for the vertical components. Figures 50 to 71 show epsilon values of spectral acceleration at a fixed vibration period $\left(\varepsilon_{Sa(T)} = \varepsilon(T)\right)$ of the geometrical mean of horizontal components and the vertical components.

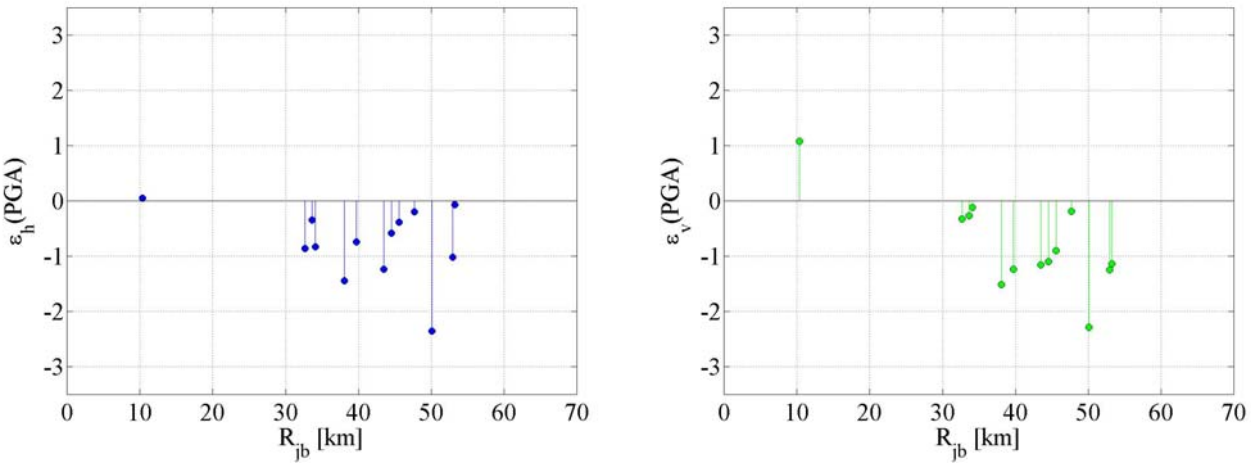

Figure 48. Epsilon values of PGA for geometrical mean of the horizontal components (ε_h) and vertical components (ε_v): left and right, respectively.

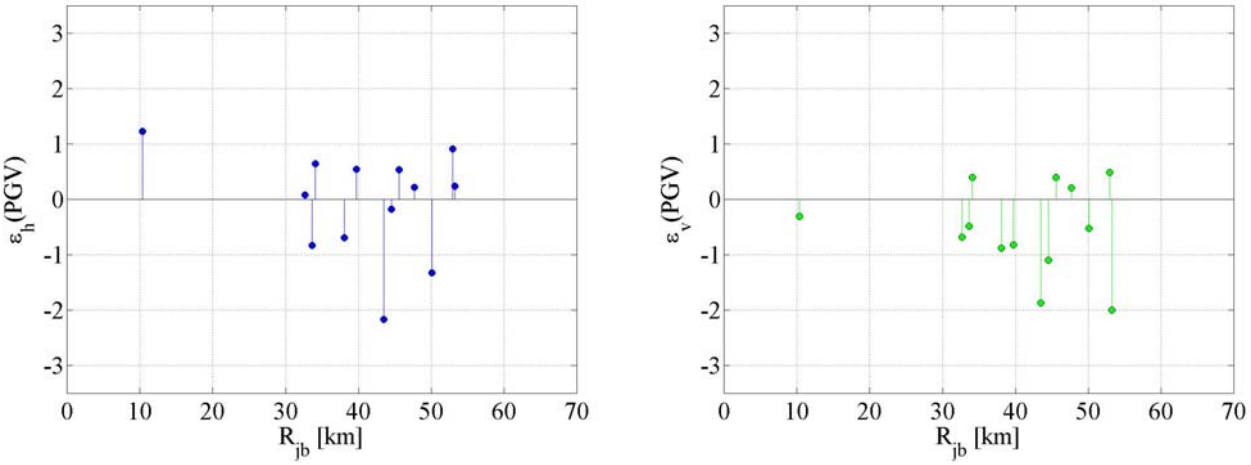

Figure 49. Epsilon values of PGV for geometrical mean of the horizontal components (ε_h) and vertical components (ε_v): left and right, respectively.

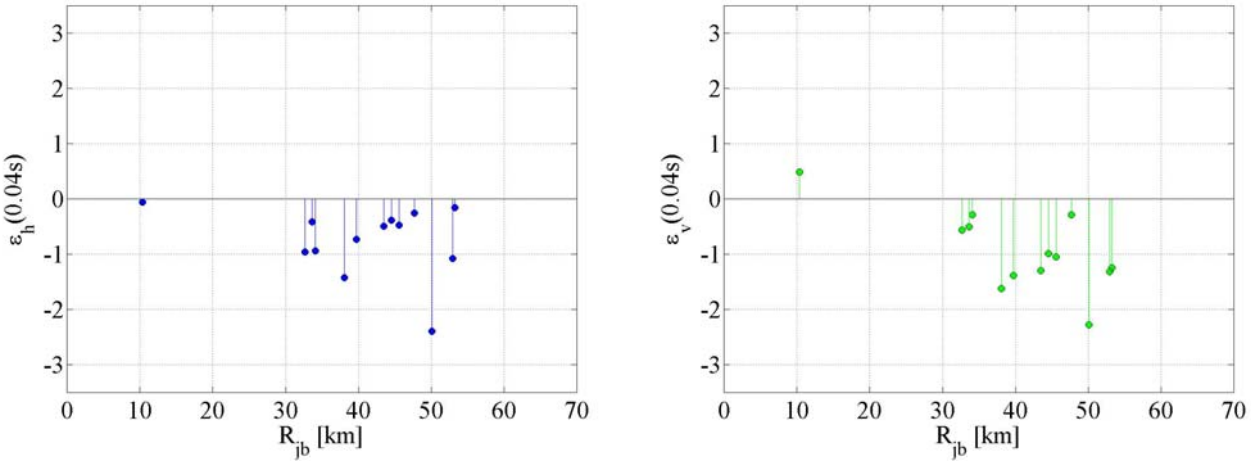

Figure 50. Epsilon values of Sa(T) for geometrical mean of the horizontal components (ε_h) and vertical components (ε_v): left and right, respectively for T equal to 0.04s.

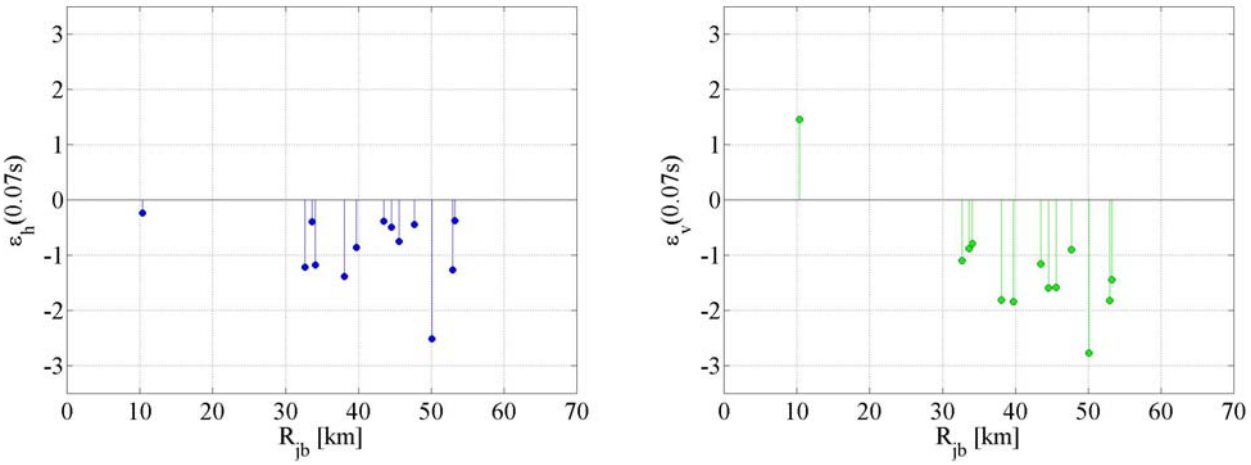

Figure 51. Epsilon values of Sa(T) for geometrical mean of the horizontal components (ε_h) and vertical components (ε_v): left and right, respectively for T equal to 0.07s.

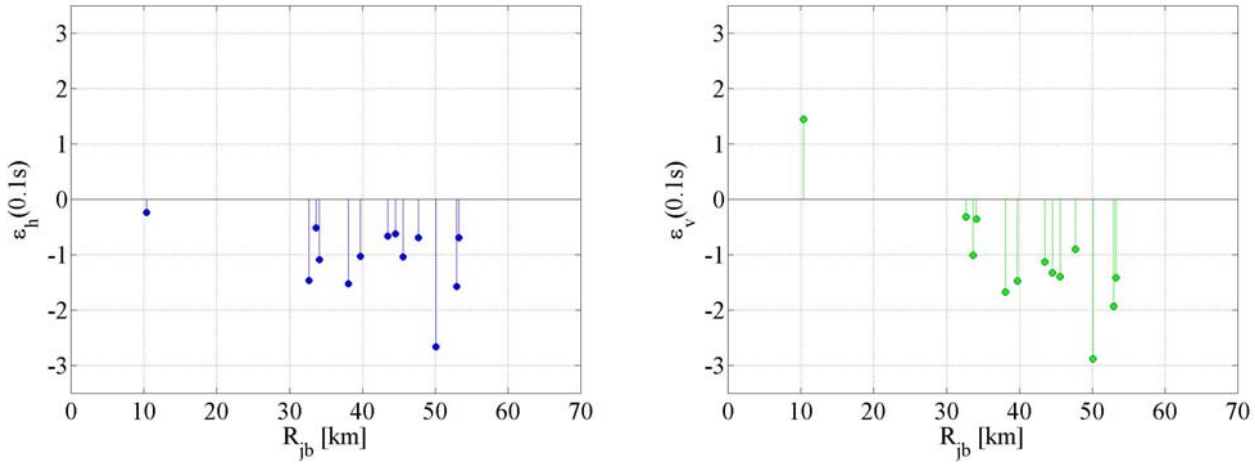

Figure 52. Epsilon values of Sa(T) for geometrical mean of the horizontal components (ε_h) and vertical components (ε_v): left and right, respectively for T equal to 0.1s.

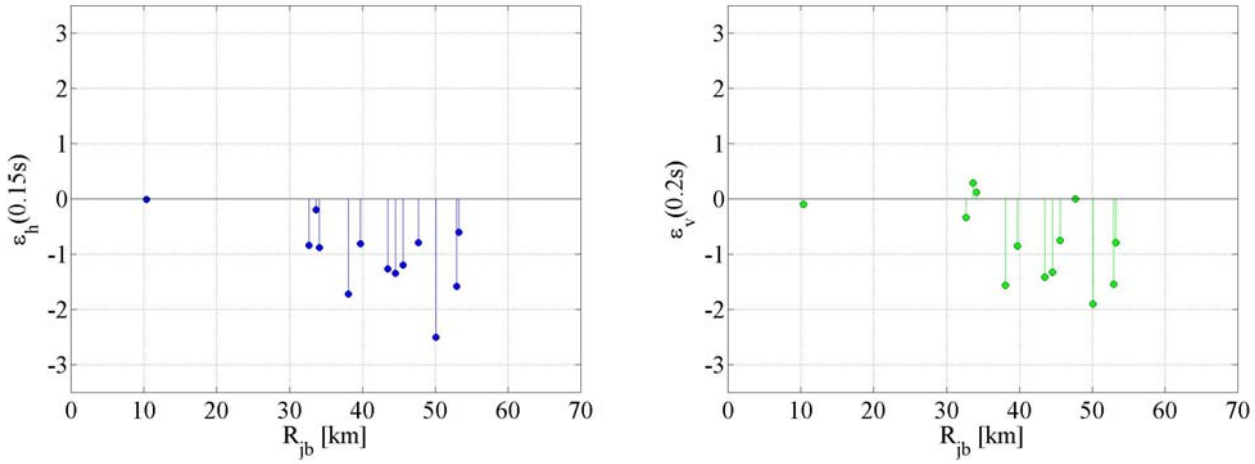

Figure 53. Epsilon values of Sa(T) for geometrical mean of the horizontal components (ε_h) and vertical components (ε_v): left and right, respectively for T equal to 0.15s.

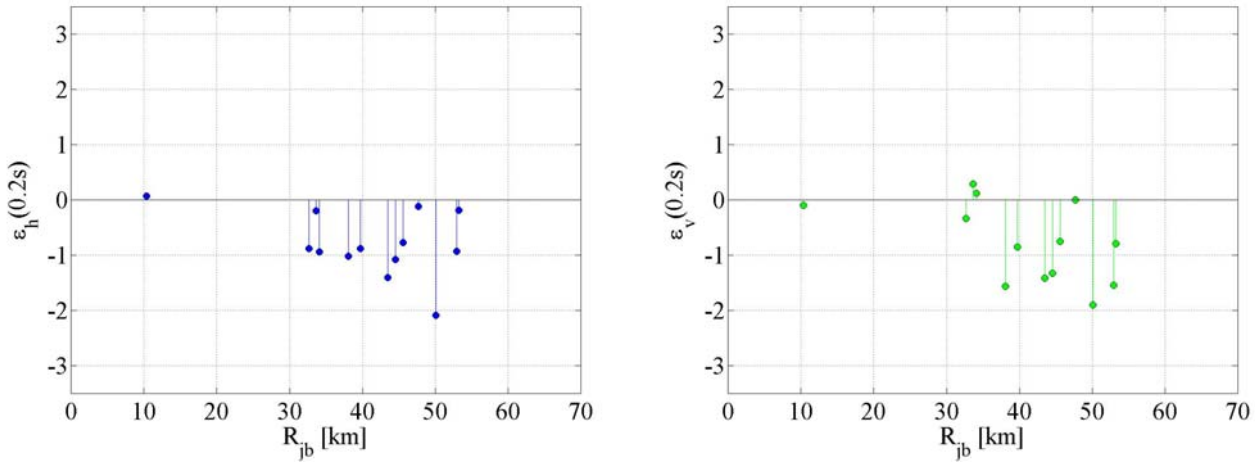

Figure 54. Epsilon values of Sa(T) for geometrical mean of the horizontal components (ε_h) and vertical components (ε_v): left and right, respectively for T equal to 0.20s.

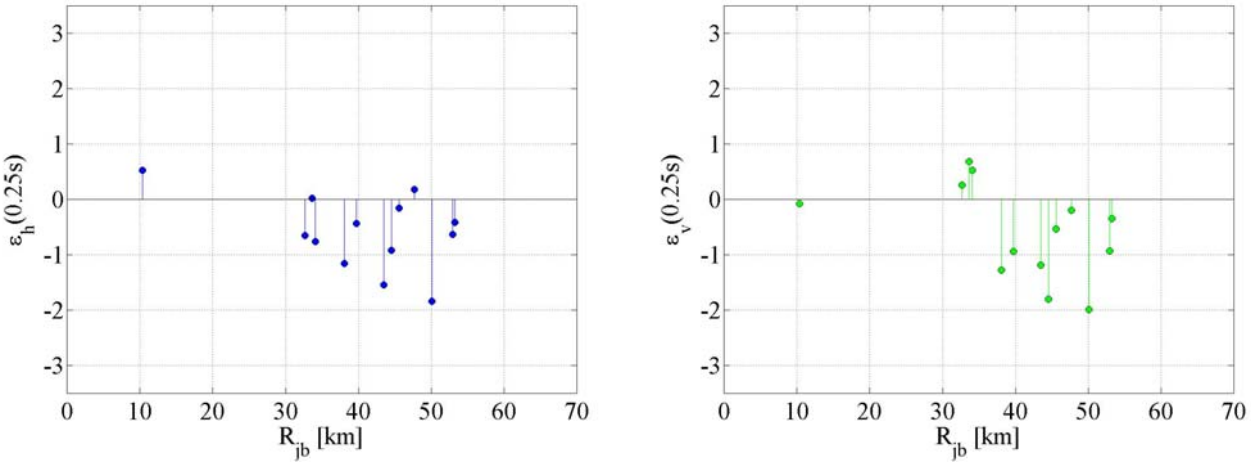

Figure 55. Epsilon values of Sa(T) for geometrical mean of the horizontal components (ε_h) and vertical components (ε_v): left and right, respectively for T equal to 0.25s.

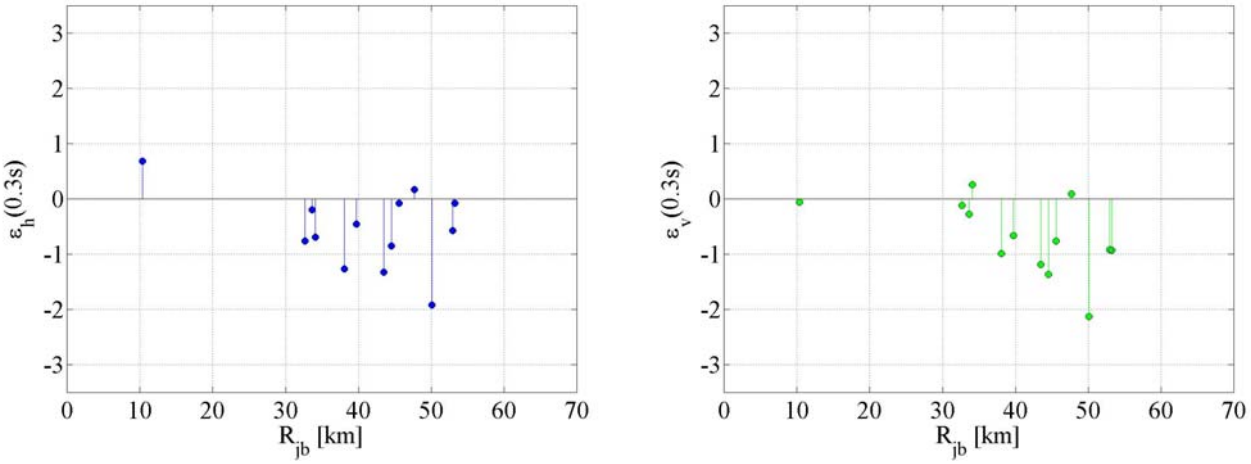

Figure 56. Epsilon values of Sa(T) for geometrical mean of the horizontal components (ε_h) and vertical components (ε_v): left and right, respectively for T equal to 0.30s.

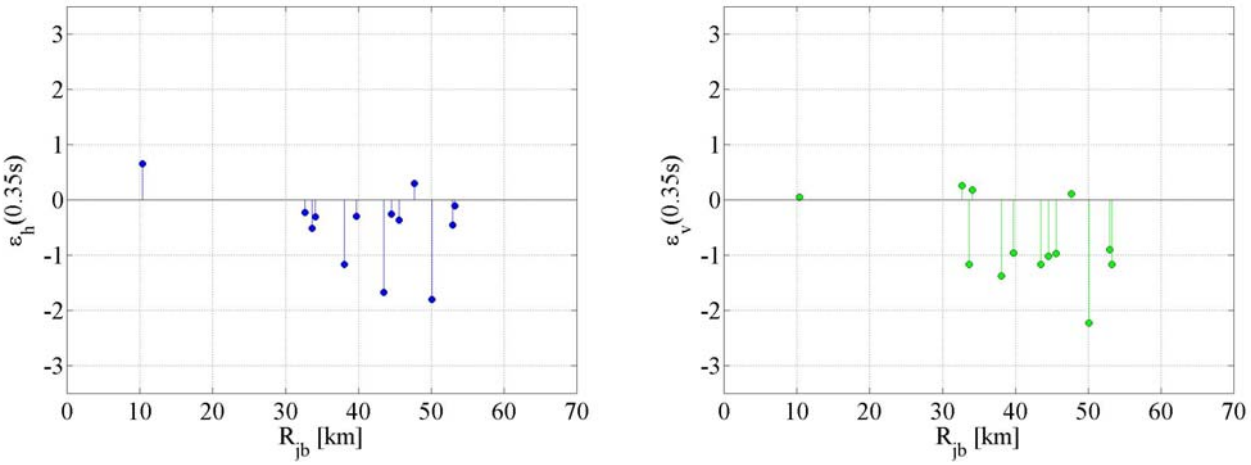

Figure 57. Epsilon values of Sa(T) for geometrical mean of the horizontal components (ε_h) and vertical components (ε_v): left and right, respectively for T equal to 0.35s.

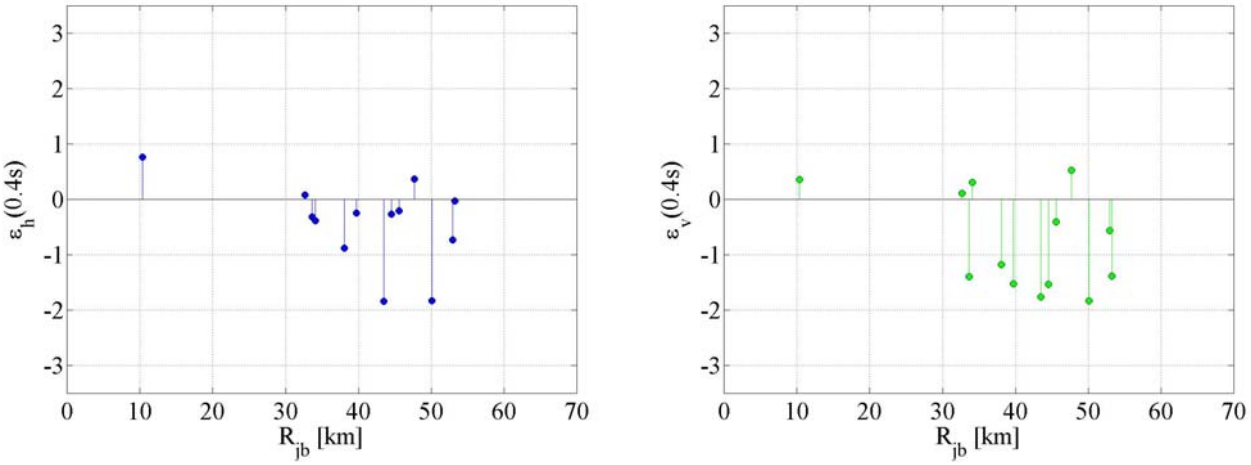

Figure 58. Epsilon values of Sa(T) for geometrical mean of the horizontal components (ε_h) and vertical components (ε_v): left and right, respectively for T equal to 0.40s.

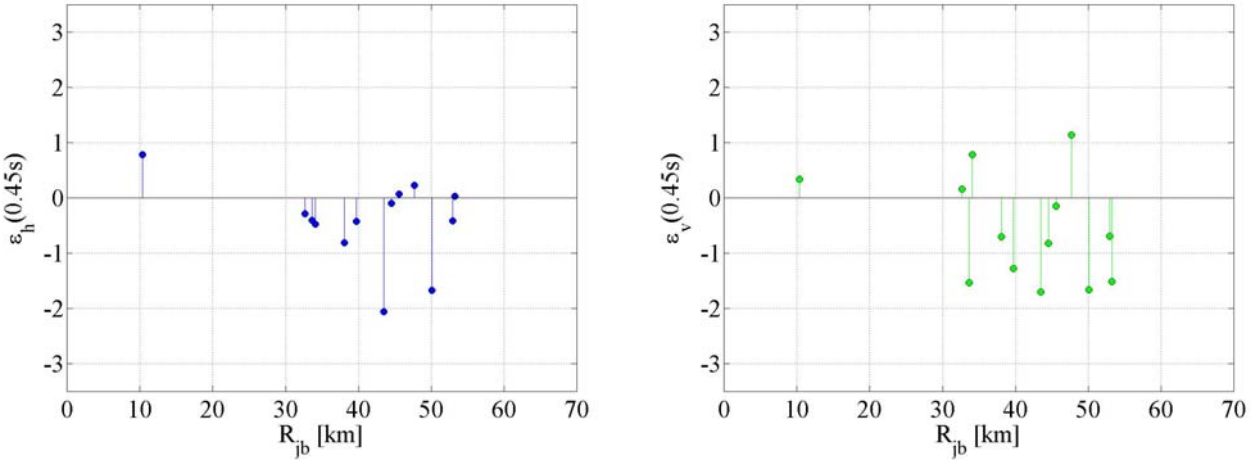

Figure 59. Epsilon values of Sa(T) for geometrical mean of the horizontal components (ε_h) and vertical components (ε_v): left and right, respectively for T equal to 0.45s.

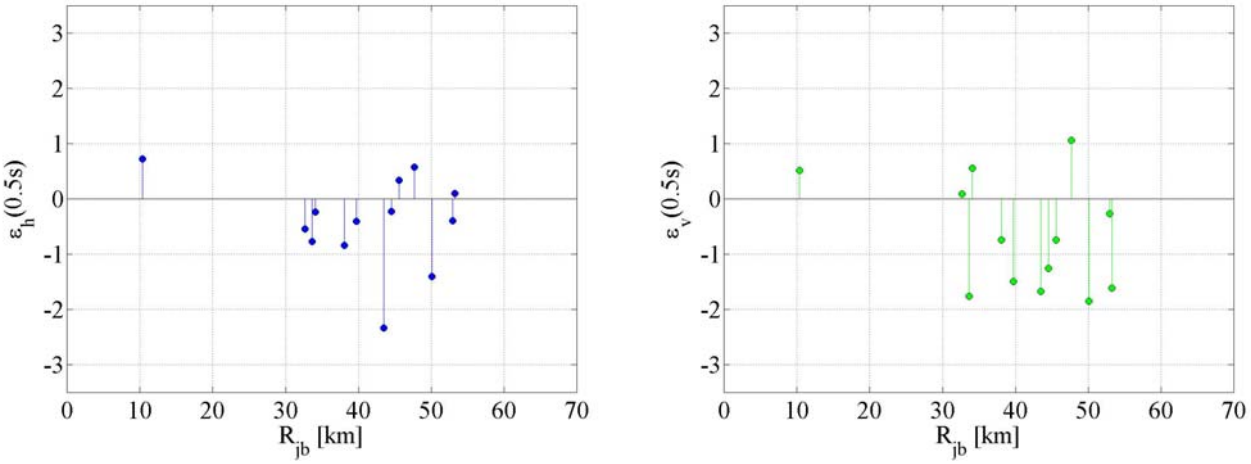

Figure 60. Epsilon values of Sa(T) for geometrical mean of the horizontal components (ε_h) and vertical components (ε_v): left and right, respectively for T equal to 0.50s.

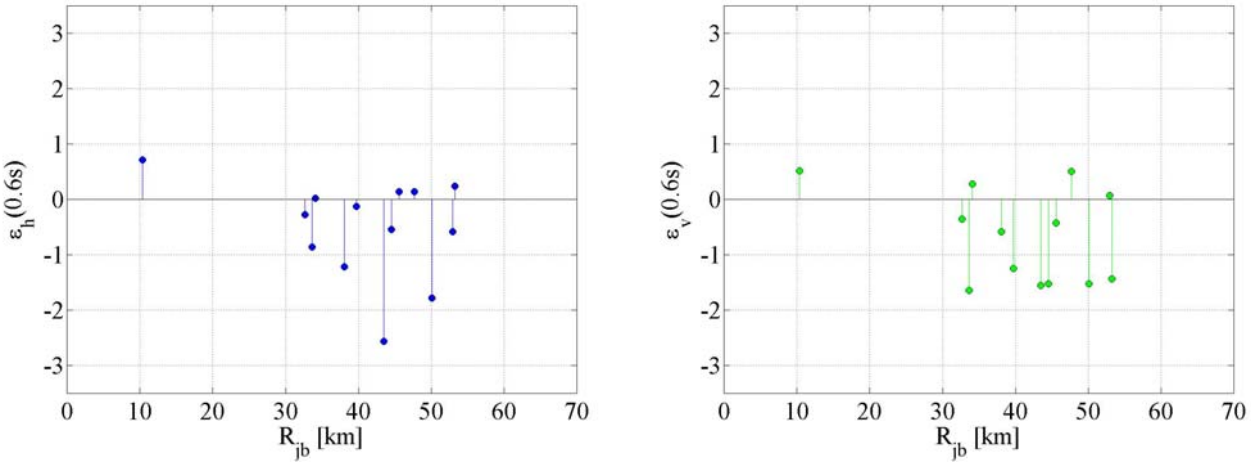

Figure 61. Epsilon values of Sa(T) for geometrical mean of the horizontal components (ε_h) and vertical components (ε_v): left and right, respectively for T equal to 0.60s.

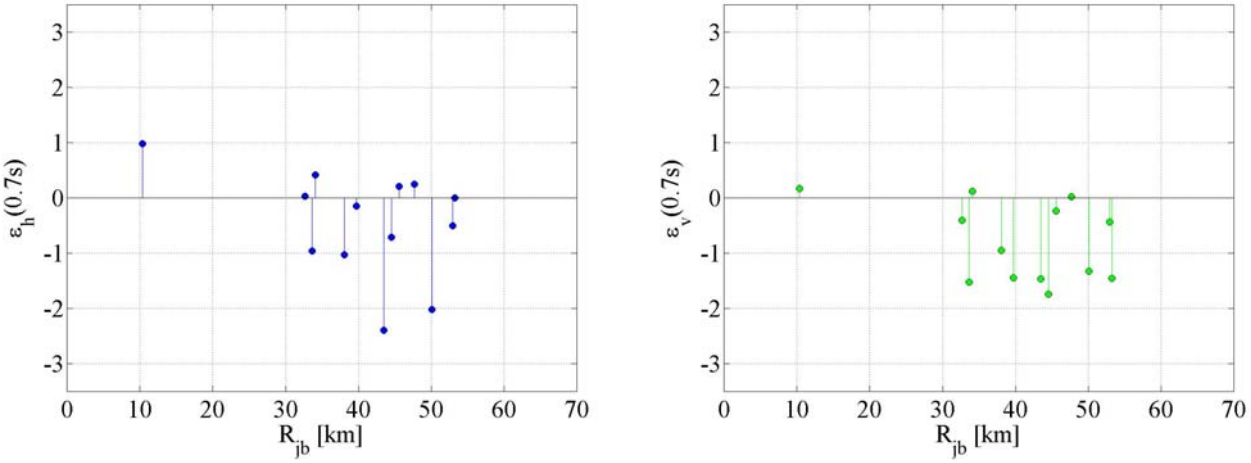

Figure 62. Epsilon values of Sa(T) for geometrical mean of the horizontal components (ε_h) and vertical components (ε_v): left and right, respectively for T equal to 0.70s.

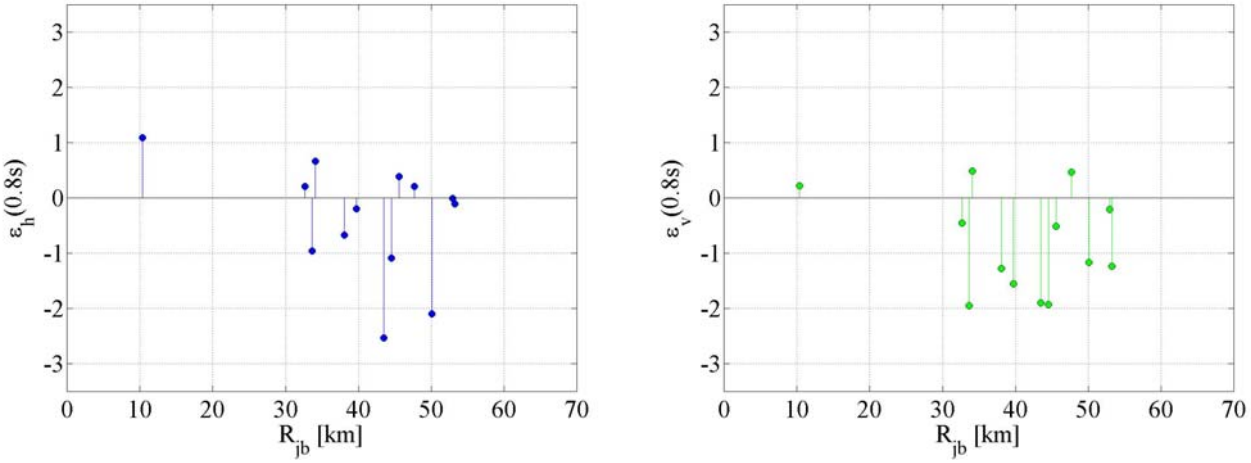

Figure 63. Epsilon values of Sa(T) for geometrical mean of the horizontal components (ε_h) and vertical components (ε_v): left and right, respectively for T equal to 0.80s.

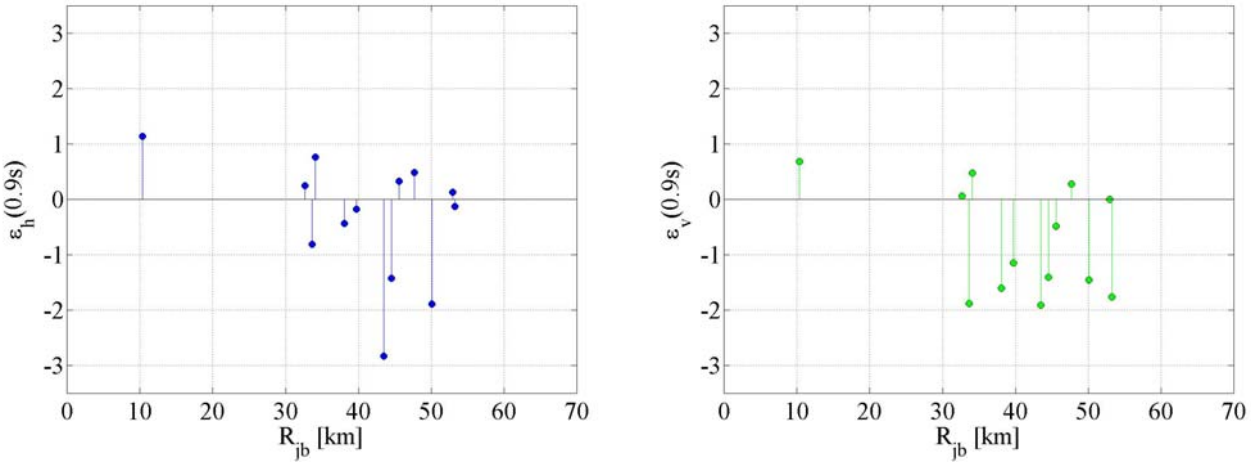

Figure 64. Epsilon values of Sa(T) for geometrical mean of the horizontal components (ε_h) and vertical components (ε_v): left and right, respectively for T equal to 0.90s.

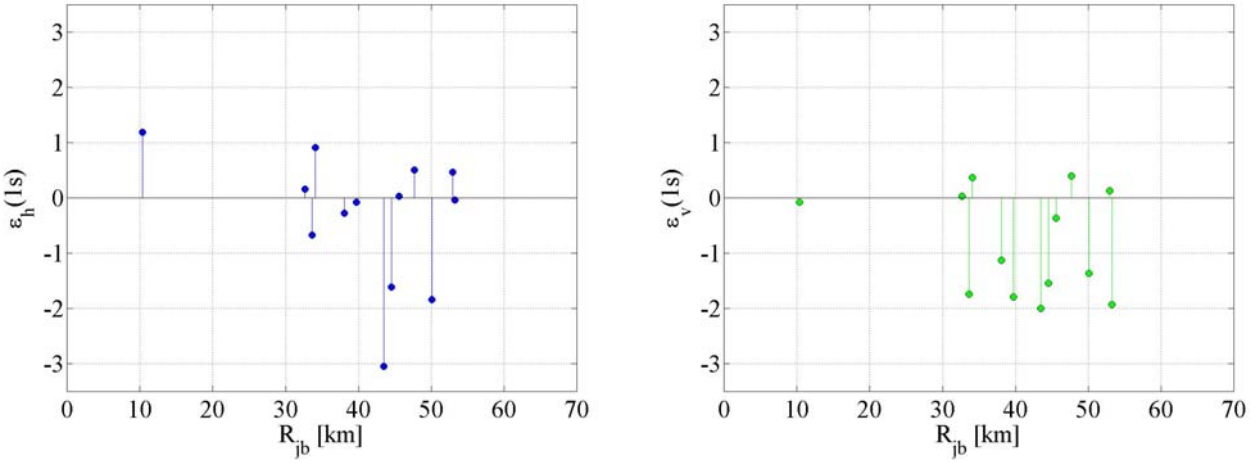

Figure 65. Epsilon values of Sa(T) for geometrical mean of the horizontal components (ε_h) and vertical components (ε_v): left and right, respectively for T equal to 1.00s.

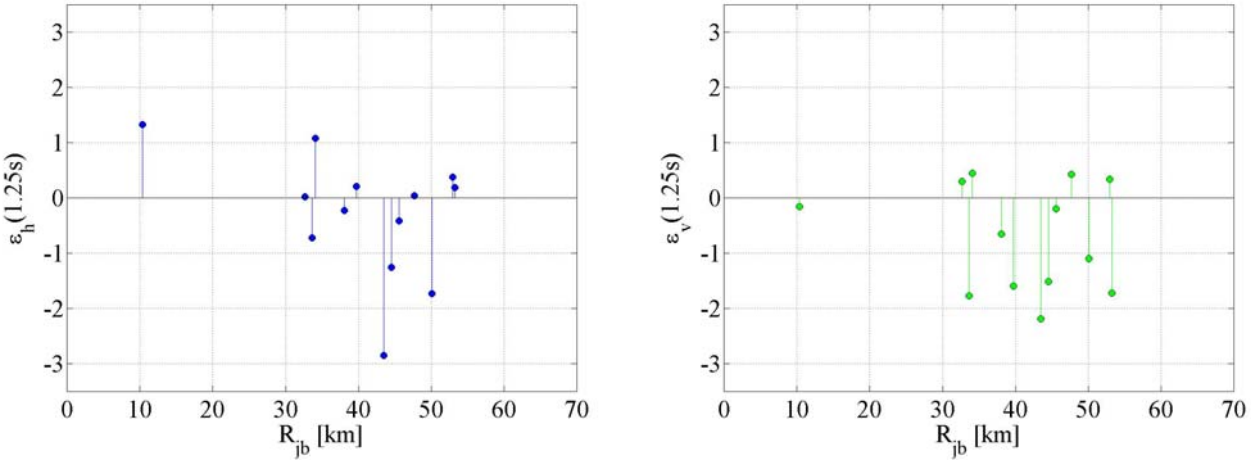

Figure 66. Epsilon values of Sa(T) for geometrical mean of the horizontal components (ε_h) and vertical components (ε_v): left and right, respectively for T equal to 1.25s.

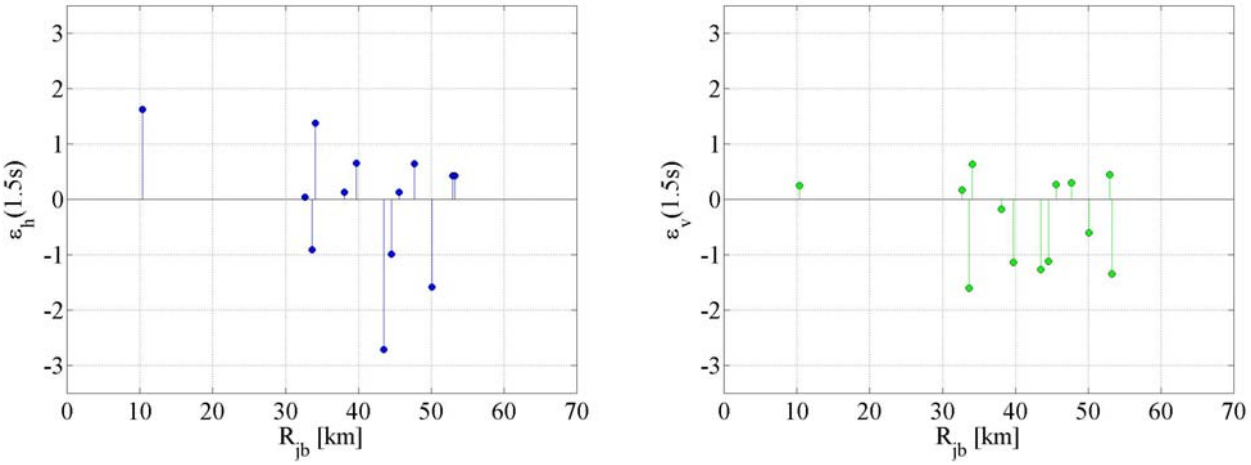

Figure 67. Epsilon values of Sa(T) for geometrical mean of the horizontal components (ε_h) and vertical components (ε_v): left and right, respectively for T equal to 1.50s.

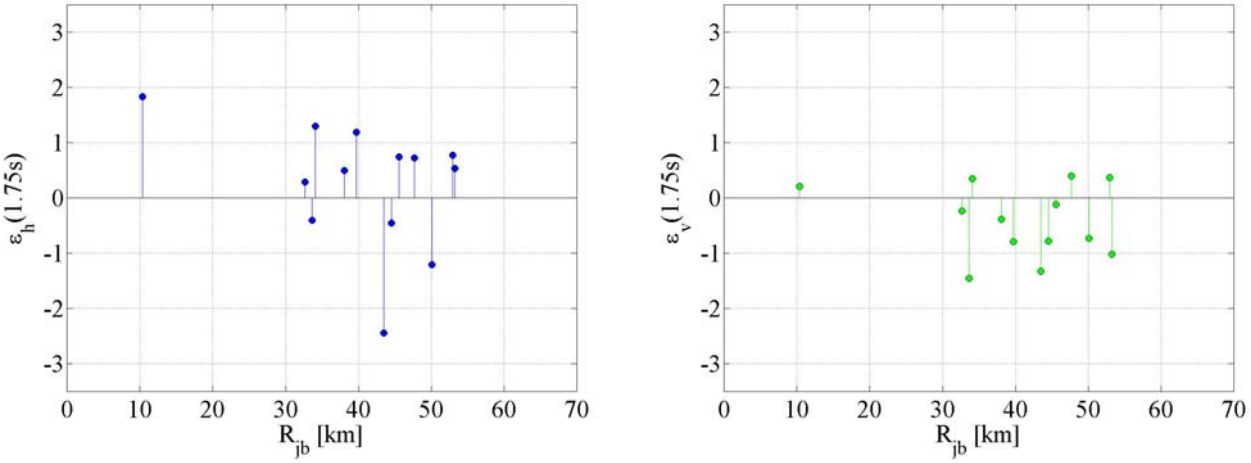

Figure 68. Epsilon values of Sa(T) for geometrical mean of the horizontal components (ε_h) and vertical components (ε_v): left and right, respectively for T equal to 1.75s.

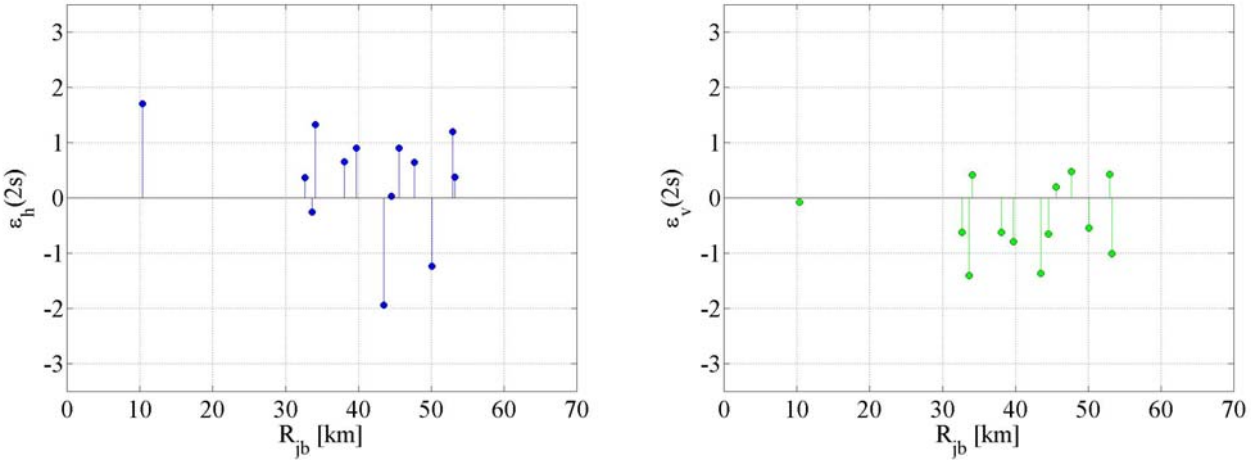

Figure 69. Epsilon values of Sa(T) for geometrical mean of the horizontal components (ε_h) and vertical components (ε_v): left and right, respectively for T equal to 2.00s.

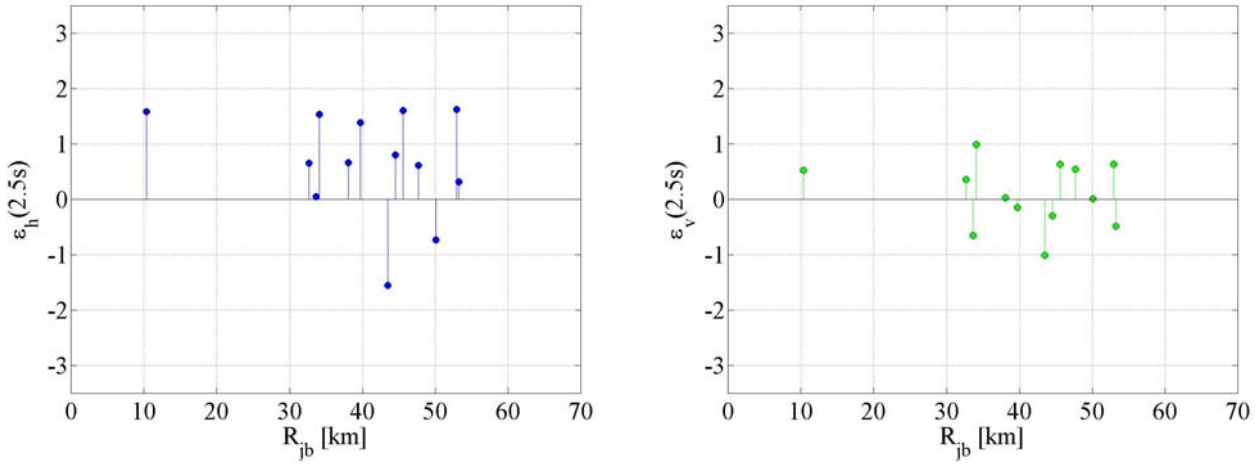

Figure 70. Epsilon values of Sa(T) for geometrical mean of the horizontal components (ε_h) and vertical components (ε_v): left and right, respectively for T equal to 2.50s.

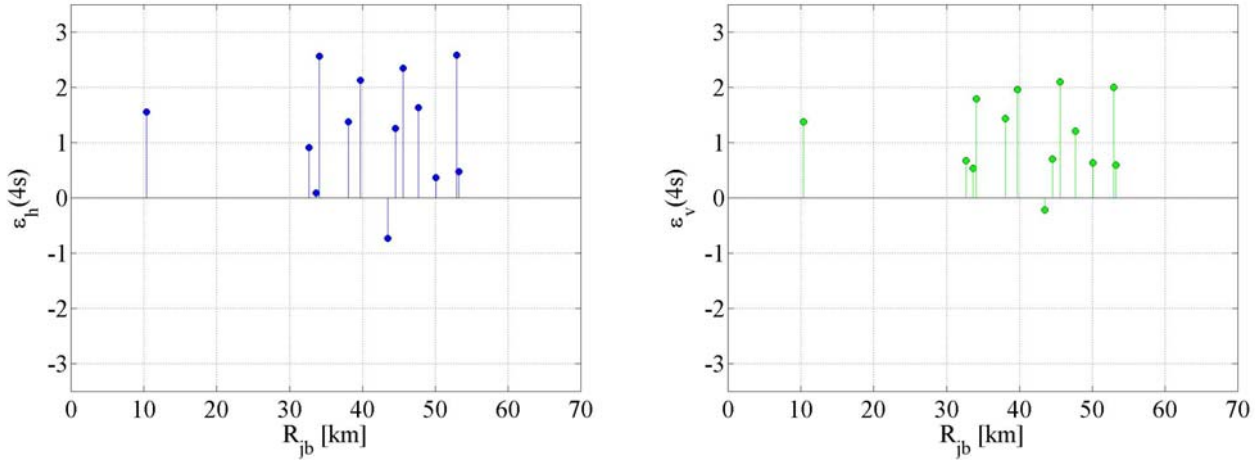

Figure 71. Epsilon values of Sa(T) for geometrical mean of the horizontal components (ε_h) and vertical components (ε_v): left and right, respectively for T equal to 4.00s.

8. Comparison of data with Sabetta and Pugliese (1996) and Iervolino et al. (2010) GMPE predictions, I_A and I_D

The comparison of the registered data with the predictions of GMPEs is made also in term of integral parameters. Figure 72 show the comparison of the registered data with the mean predictions and the $\pm\sigma$ standard deviation bands of Arias intensity (I_A) and Cosenza and Manfredi index (I_D), respectively.

Both these attenuation relationship are valid within 100km and are computed as function of the epicentral distance (R_{epi}); thus, in this case no distance conversion was necessary. It is worth to note that I_A in Figure 72 is expressed in cm^2/s^3, so normalized by the constant factor $\pi/2g$ respect to the values in Table A1 to A3, evaluated according to Equation (2) and expressed in cm/s. The GMPE

employed for I_A is the one by Sabetta and Pugliese (1996), while for I_D Iervolino et al. (2010) GMPE was considered. Both the GMPEs considered provide the prediction of the highest horizontal component; so, in this case, the registered data refer to the maximum between the two registered horizontal components shown in Table A2 and A3.

$$I_A = \frac{\pi}{2 \cdot g} \int_0^{t_E} a^2(t)\, dt \tag{2}$$

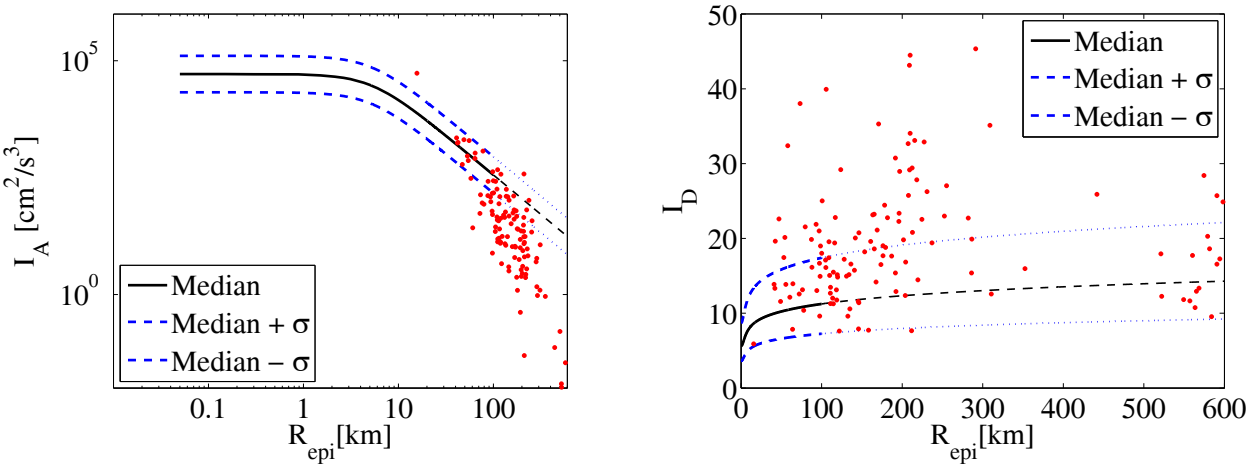

Figure 72. Comparison of the maximum horizontal component of the registered data with the median and $\pm\sigma$ predictions according to Sabetta and Pugliese (1996) and Iervolino et al. (2010) GMPE predictions in terms of I_A and I_D, respectively.

9. Comparison with Italian hazard data

A preliminary comparison of the closest waveform registered MRN station (R_{epi} = 16 km) with Italian code prescription (CS. LL. PP., 2008) at the same site is shown in Figure 73. The N-S and E-W spectra at MRN are compared with code spectra computed for both soil classes A and D for two different return periods (Tr) equal to 475 and 2475 years. The horizontal spectra at the station, (whose soil is classified in ITACA as C) are almost within the code spectra computed according to Italian code (CS. LL. PP., 2008) for soil class D and Tr 475 and 2475. In the medium-high period range (0.5s < T < 2.5s), the N-S component exceeds the band identified by the two D soil spectra at the two different return periods. The spectrum for the vertical component at MRN station exceeds significantly the vertical code spectrum for Tr 2475 years with a peak that exceeds 1g in correspondence of the constant acceleration branch of the code spectrum. According to this latter comparison it seems that the earthquake occurred can be considered within the prediction of the Italian hazard map. Regarding this aspect, two key issues should be observed:

- only after the 2009 L'Aquila earthquake the employment of the new Italian building code and its hazard map have become compulsory for design;
- according to obsolete building code regulations (up to 1980) the area struck by the earthquake was not classified as seismically prone (Lai et al, 2009).

For MRN station geographical coordinates, the hazard disaggregation (Iervolino et al, 2011) was computed for the PGA and Sa(T=1s) for the two Tr (475 and 2475 years) by means of REXEL v 3.3 (Iervolino et al., 2010), as shown in Figure 74 and 75. PGA disaggregations shows single modal values for both considered Tr: modal magnitudes and distances range between 4.8 and 5.3, and 0-20km, respectively with slight differences depending on Tr. Conversely Sa(T=1s) disaggregation at Tr=475 yr seems to suggest a non negligible hazard contribution of more distant (from 50 to 100 km) and stronger (around 6.3 M) second design earthquake. As usually expected such second modal value contribution decreases increasing considered return period and for Tr=2475yr, a single design earthquake can be identified with about 20 km distance and 5.8 magnitude.

Similarly to the case of MRN station, in the following recorded waveforms are compared with design code spectra[1] for the other ten station with R_{epi} lower than 62 km (see Table 1).

Before drawing conclusions from these comparisons, the following should be noted. A probabilistic hazard map, which is at the basis of the code spectra employed in the figures, hardly can be validated by the occurrence of a single earthquake, mainly for the following reasons.

(1) If the map refers to ground motion, which is exceeded on average every 475 yr, at least 5000 yr of records in each site of the map have to be observed to obtain a reliable statistic (e.g., based on 10 observations) of ground motion the map refers for comparison with the predicted values.

(2) This is the most important reason: the ground motion provided by probabilistic hazard assessment averages ground motions from different sources; it is therefore expected that, when an earthquake occurs, the ground motion at the source (e.g., in the epicenter) location is larger than that from the hazard map.

On the other hand, it seems that earthquake magnitude and location are consistent with the ranges considered by the national hazard assessment (i.e., Stucchi et al., 2011), and ground motion values are in general agreement with GMPEs. Therefore, in the opinion of the authors, this kind of earthquake cannot be claimed as not contemplated by that hazard assessment.

[1] Lower differences are expected for design spectra in close sites thus for all the considered stations, design spectra are replaced by the spectra computed for Mirandola.

Having specified that the spectral comparison provided cannot be used to validate the official hazard map, it should be noted that recorded spectra do not exceed code spectra[2] anywhere close to the source, except in the epicentral location where, as discussed above at bullet (2), ground motion is naturally expected to be larger with respect to that predicted by an hazard assessment.

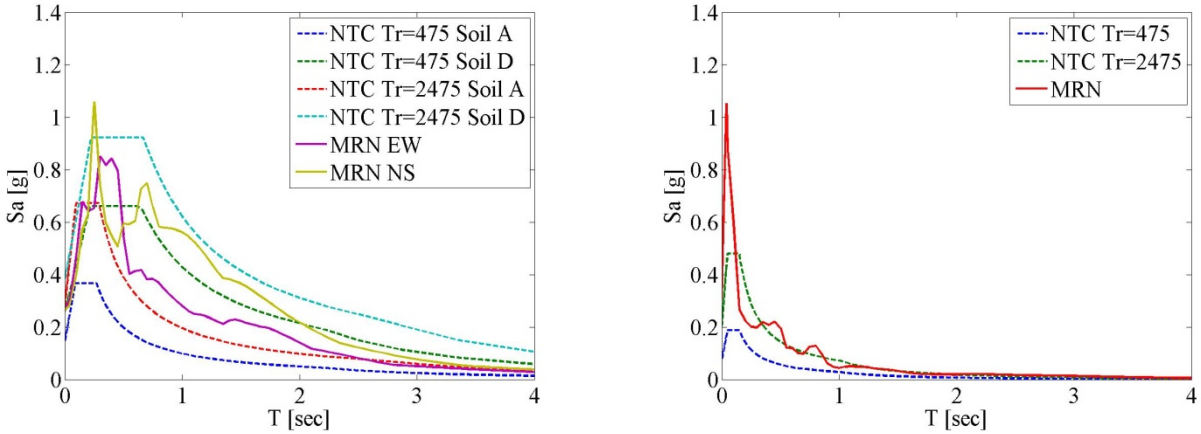

Figure 73. Comparison of the horizontal code spectra for soil classes A and D (on the right) and vertical code spectra (on the left) computed at MRN station (lat 42.87, long 11.06), Mirandola, and the spectra of the waveform registered at MRN station.

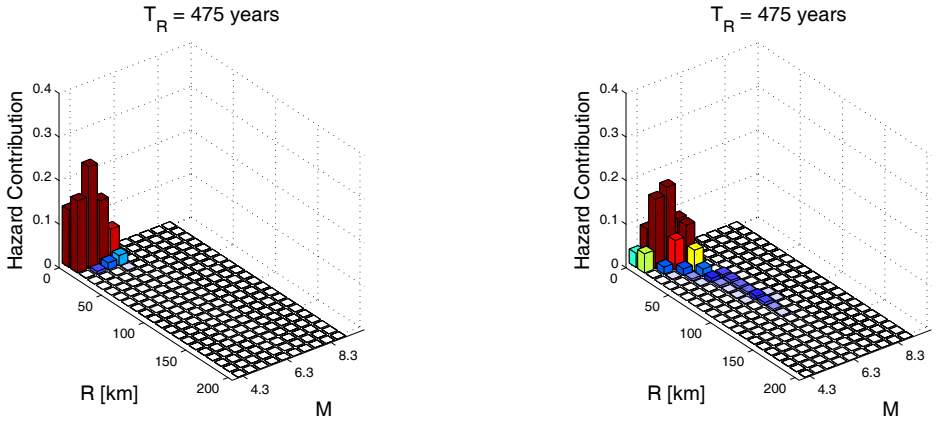

Figure 74. Disaggregation PGA and Sa(1 s) hazard with Tr 475 yr in Mirandola.

[2] In fact, code spectra are uniform hazard spectra (UHS) basically, and it is known that UHSs are not representative of any specific ground motion spectrum, being in fact, "envelopes" of spectra of ground motions corresponding to all magnitude and source-to-site distances considered as possible in the hazard evaluation.

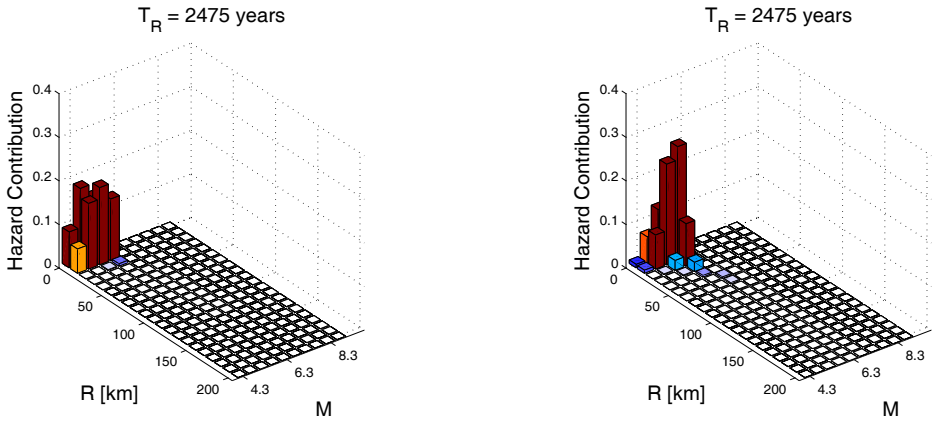

Figure 75. Disaggregation PGA and Sa(1 s) hazard with Tr 2475 yr in Mirandola

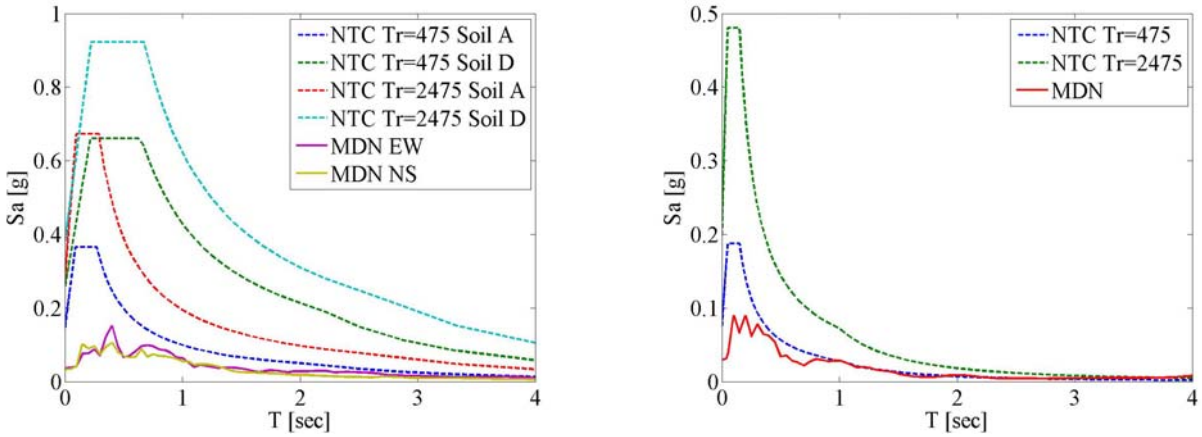

Figure 76. Comparison of the horizontal code spectra for soil classes A and D (on the right) and vertical code spectra (on the left) and the spectra of the waveform registered at MDN station.

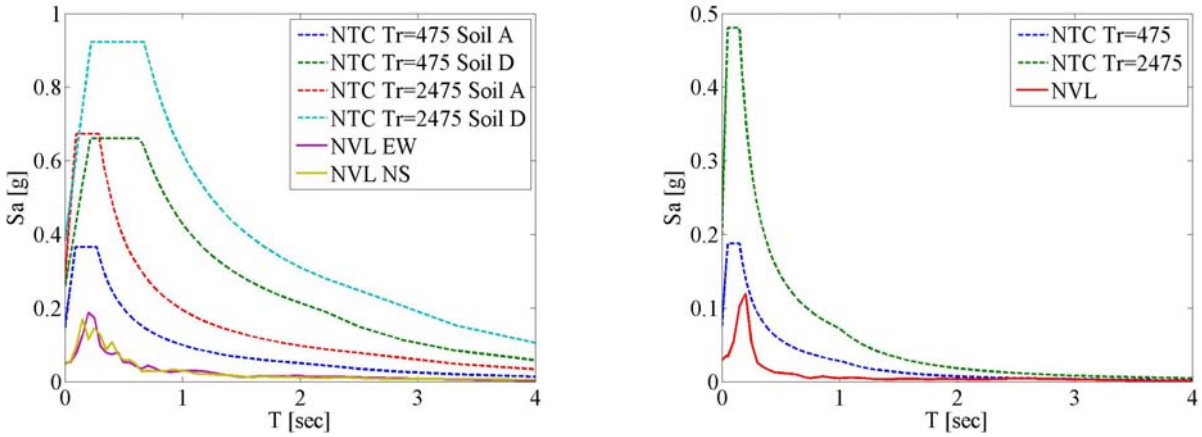

Figure 77. Comparison of the horizontal code spectra for soil classes A and D (on the right) and vertical code spectra (on the left) and the spectra of the waveform registered at NVL station.

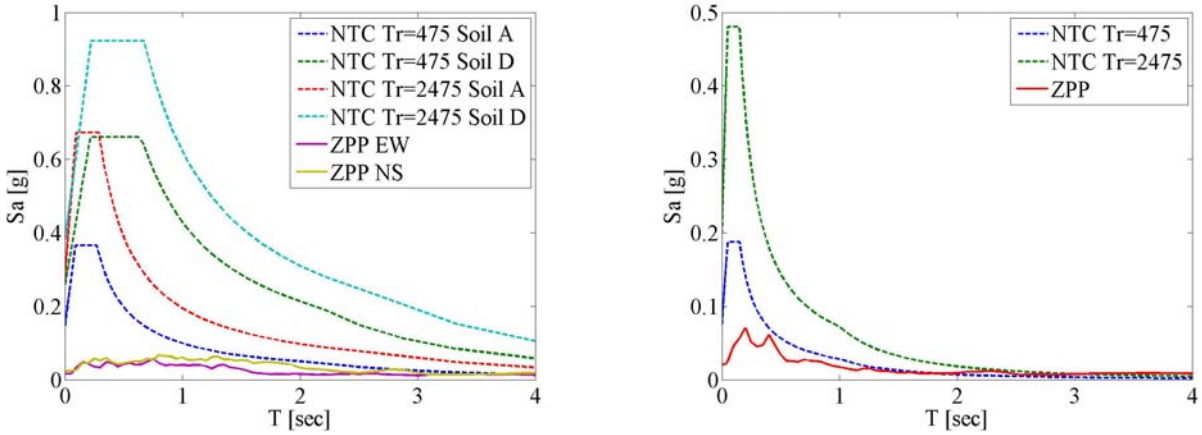

Figure 78. Comparison of the horizontal code spectra for soil classes A and D (on the right) and vertical code spectra (on the left) and the spectra of the waveform registered at ZPP station.

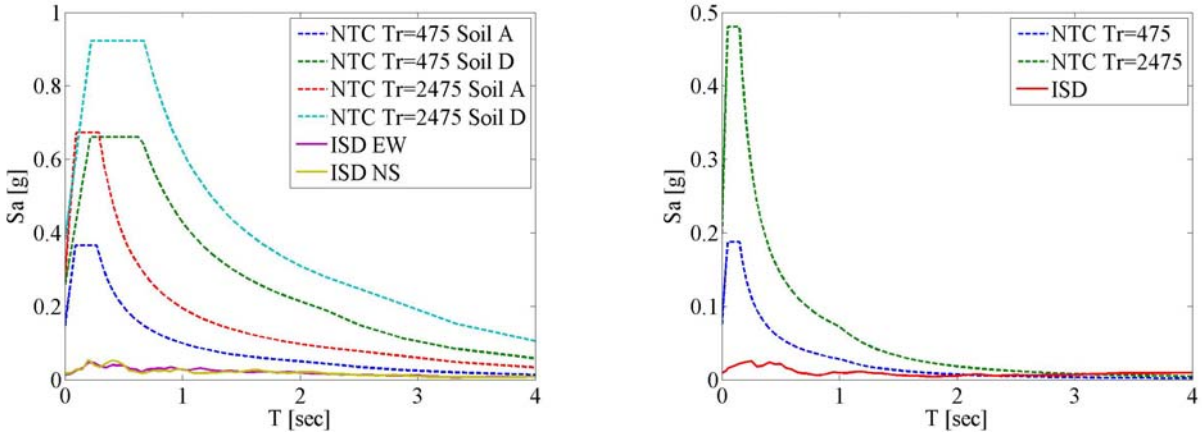

Figure 79. Comparison of the horizontal code spectra for soil classes A and D (on the right) and vertical code spectra (on the left) and the spectra of the waveform registered at ISD station.

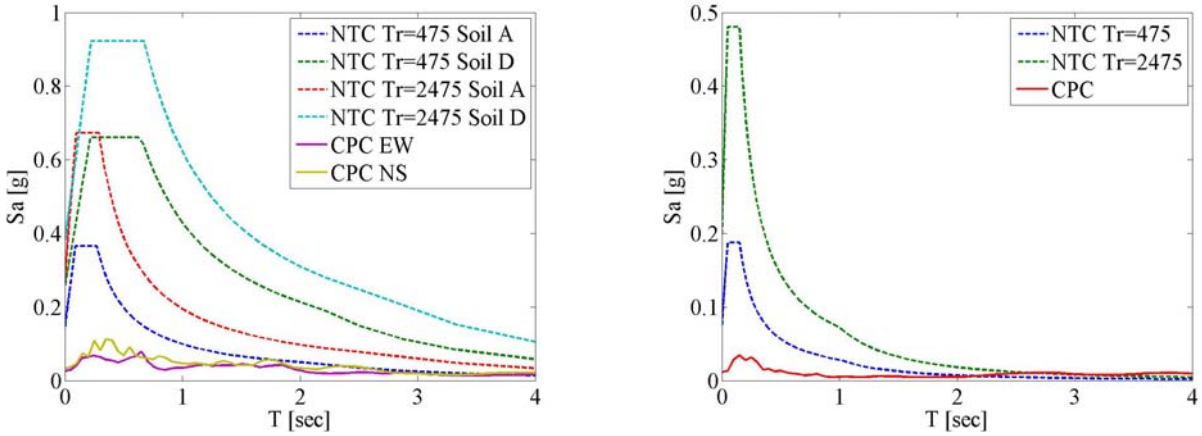

Figure 80. Comparison of the horizontal code spectra for soil classes A and D (on the right) and vertical code spectra (on the left) and the spectra of the waveform registered at CPC station.

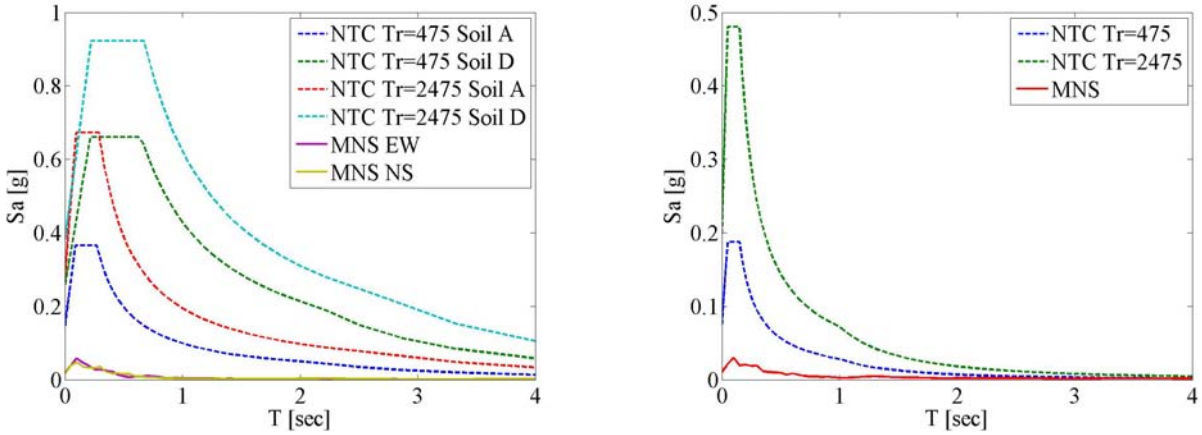

Figure 81 Comparison of the horizontal code spectra for soil classes A and D (on the right) and vertical code spectra (on the left) and the spectra of the waveform registered at MNS station.

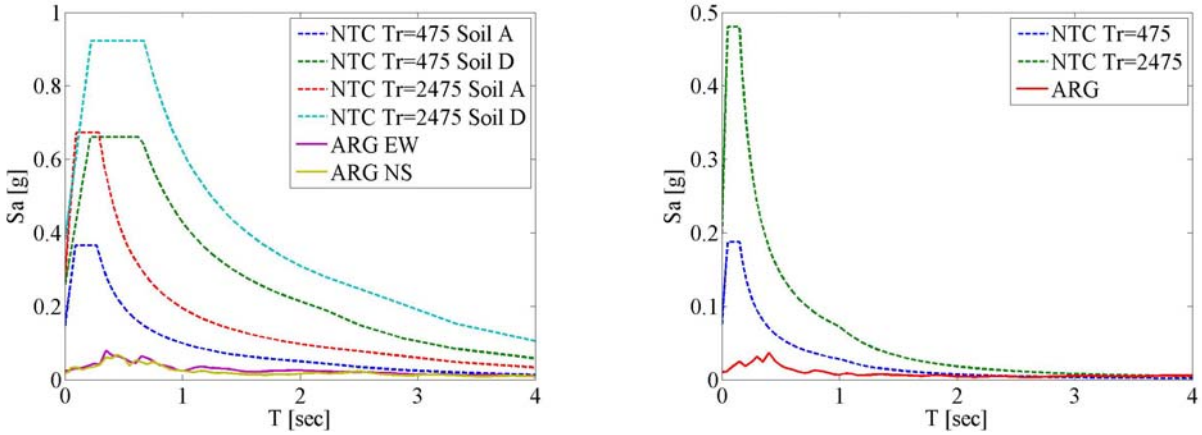

Figure 82 Comparison of the horizontal code spectra for soil classes A and D (on the right) and vertical code spectra (on the left) and the spectra of the waveform registered at ARG station.

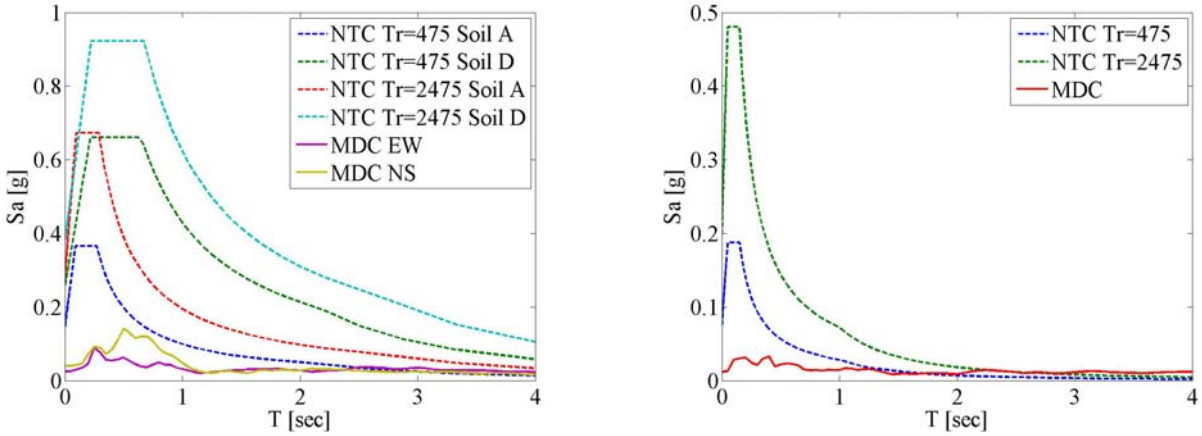

Figure 83 Comparison of the horizontal code spectra for soil classes A and D (on the right) and vertical code spectra (on the left) and the spectra of the waveform registered at MDC station.

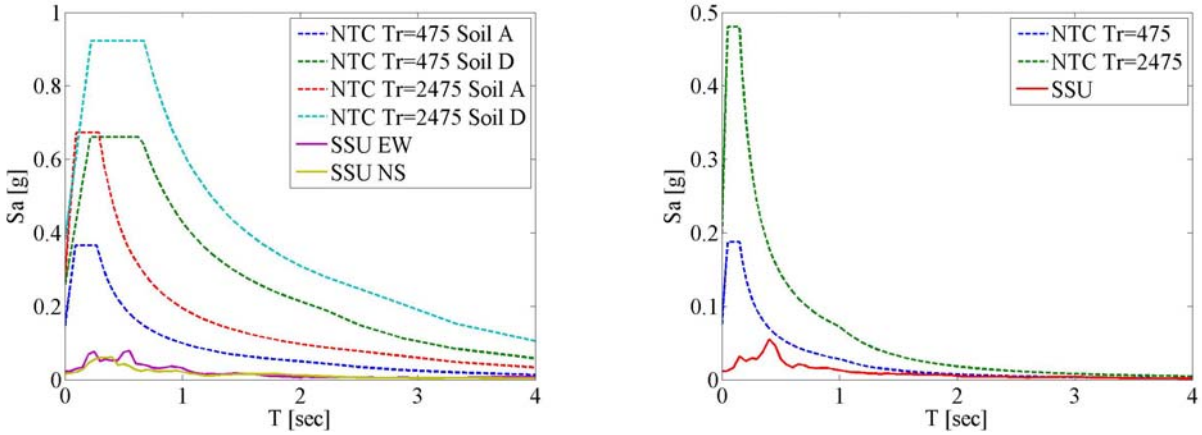

Figure 84 Comparison of the horizontal code spectra for soil classes A and D (on the right) and vertical code spectra (on the left) and the spectra of the waveform registered at SSU station.

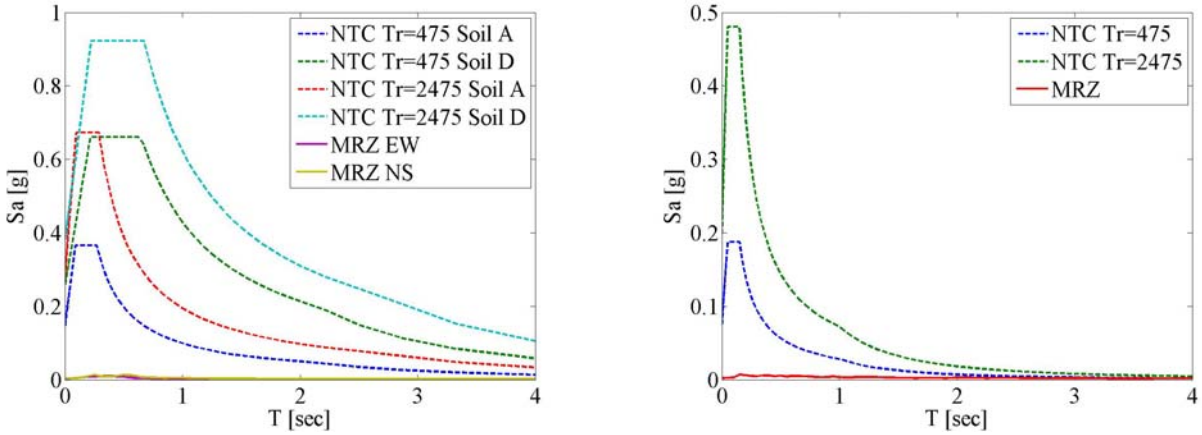

Figure 85 Comparison of the horizontal code spectra for soil classes A and D (on the right) and vertical code spectra (on the left) and the spectra of the waveform registered at MRZ station.

10. Analyses of directivity effects

Recorded ground motions of the station within 60 km from the epicenter were analyzed with respect to possible directivity effects (e.g., Chioccarelli and Iervolino, 2010). In principle directivity effects have to be studied in the horizontal direction orthogonal to the strike of the rupture being the direction of maximum evidence. In this case, the rupture is still unknown to the authors and, for each station, time-history components rotated in all the possible horizontal directions, were studied in accordance with what proposed by Shahi and Baker (2011). However no evidence of significant forward directivity evidence was found.

11. Direct spectral comparison of the data registered within 70km with De Luca et al (2012) inelastic GMPE predictions, Sd_{el}, Sd_{in} and N_E.

In this section elastic displacements (Sd_{el}), inelastic displacements ($Sd_{R\mu=i}$) and equivalent number of cycles ($N_{e,\ R\mu=i}$) are provided for the horizontal components of the registered signals and in term of predictions equations based on the Italian data (De Luca, 2011; De Luca et al., 2012).

$Sd_{R\mu=i}$ and $N_{e,\ R\mu=i}$ are evaluated on a nonlinear SDOF characterized by an elastic-hardening backbone (with the hardening ratio equal to 0.05 of the elastic stiffness) and a pinching hysteresis rule (Clough and Johnston, 1966; Ibarra et al., 2005) with strength reduction factor R_μ equal to 2, 4, 6, and 8, respectively. $N_{e,\ R\mu=i}$ is defined according to Equation (3), given by the cumulative hysteretic energy (E_H), evaluated as the sum of the areas of the hysteretic cycles (without considering the contribution of equivalent viscous damping), normalized with respect to the largest cycle (evaluated as the area underneath the monotonic backbone curve from the yielding displacement to the peak inelastic displacement, or $A_{plastic}$), plus 1.

$$N_e = \frac{E_H}{A_{plastic}} + 1 \qquad (3)$$

In Figure 86 to 150 a comparison between registered horizontal data, within 70km from the epicentre (R_{epi}<70km) and the median estimates $\pm\sigma$ of the prediction equations in terms of Sd_{el}, $Sd_{R\mu=i}$, and $N_{e,\ R\mu=i}$ are provided. The prediction equations are evaluated according to EC8 soil classification of the station provided in Table 2. Registered data, both in term of peak and cyclic inelastic SDOF response are within the standard deviation bands of the predictions equations. Some exceptions can be found at MRN, ZPP, CPC, MDC, and CSP stations. At MRN, the closest triggered station, the peak response (in terms of elastic and inelastic displacements) exceeds strictly the predictions, while cyclic response tends to be systematically lower than the $\pm\sigma$ bands of the N_e prediction equations. The latter observations could have been inferred by the high durations (see Figure 10 and 11) respect to the peak ground motion values (see Table A1 to A3).

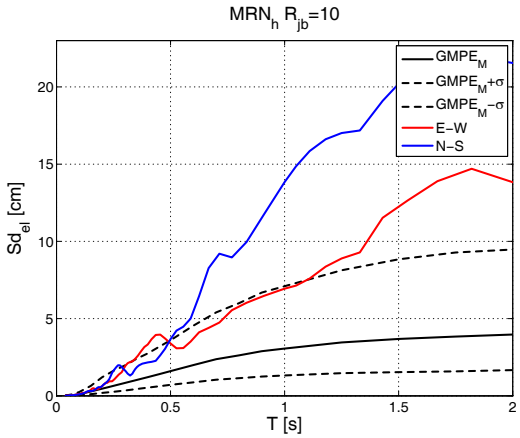

Figure 86. Comparison of the elastic displacement spectra for the horizontal components, Sd_{el}, at MRN station with the median prediction and $\pm\sigma$ bands according to De Luca et al. 2012.

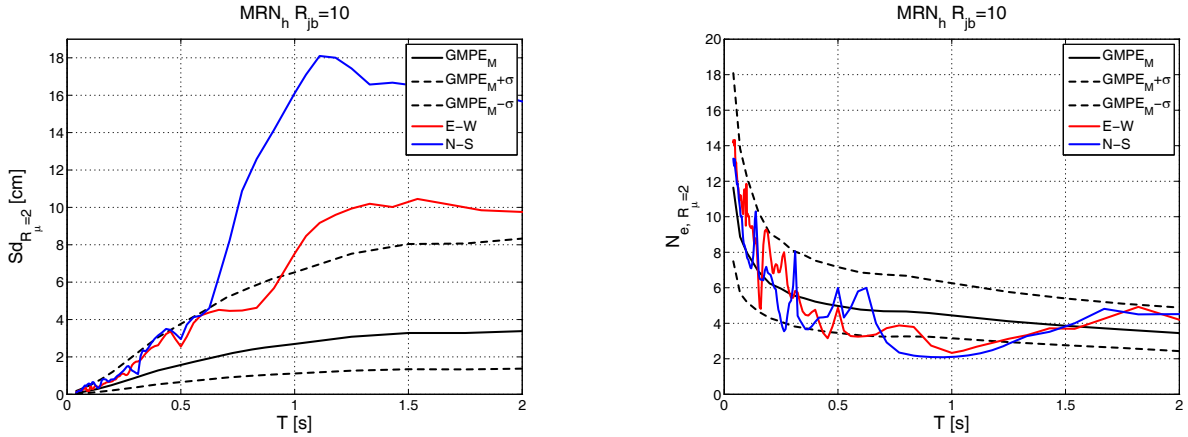

Figure 87. Comparison of the inelastic spectra in terms of displacements, $Sd_{R_\mu=i}$ (on the left) and equivalent number of cycles, $N_{e,\ R_\mu=i}$ (on the left) for R_μ equal to 2, for the horizontal components, at MRN station with the median prediction and $\pm\sigma$ bands according to De Luca et al. 2012.

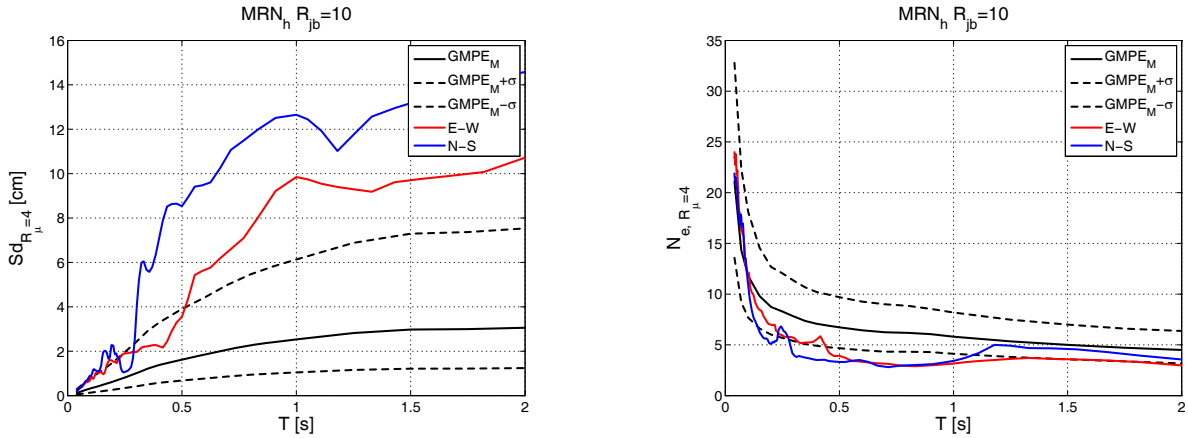

Figure 88. Comparison of the inelastic spectra in terms of displacements, $Sd_{R_\mu=i}$ (on the left) and equivalent number of cycles, $N_{e,\ R_\mu=i}$ (on the left) for R_μ equal to 4, for the horizontal components, at MRN station with the median prediction and $\pm\sigma$ bands according to De Luca et al. 2012.

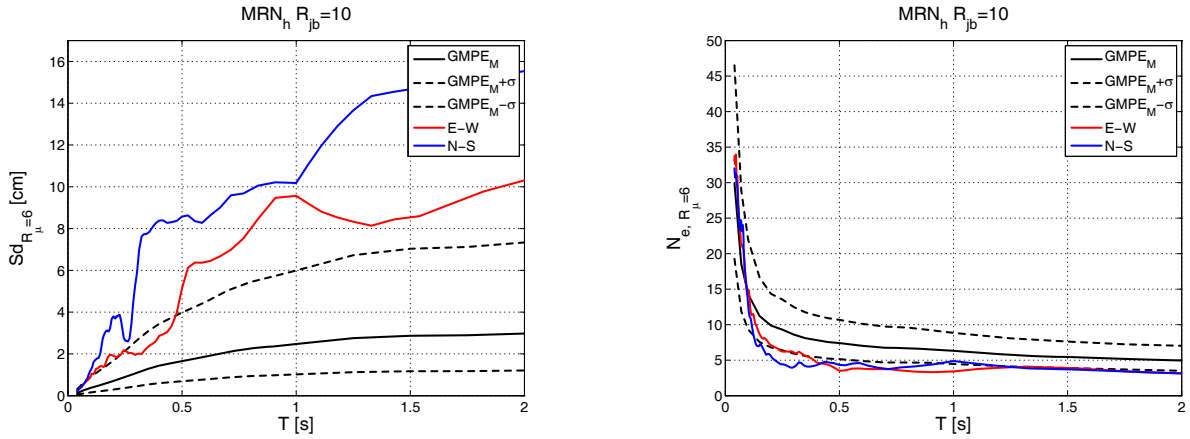

Figure 89. Comparison of the inelastic spectra in terms of displacements, $Sd_{R_\mu=i}$ (on the left) and equivalent number of cycles, $N_{e,\,R_\mu=i}$ (on the left) for R_μ equal to 6, for the horizontal components, at MRN station with the median prediction and $\pm\sigma$ bands according to De Luca et al. 2012.

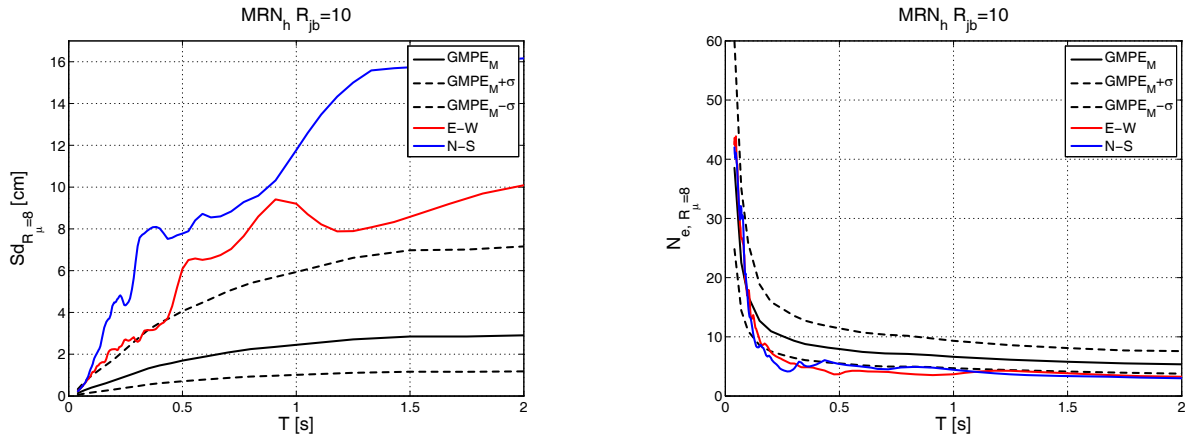

Figure 90. Comparison of the inelastic spectra in terms of displacements, $Sd_{R_\mu=i}$ (on the left) and equivalent number of cycles, $N_{e,\,R_\mu=i}$ (on the left) for R_μ equal to 8, for the horizontal components, at MRN station with the median prediction and $\pm\sigma$ bands according to De Luca et al. 2012.

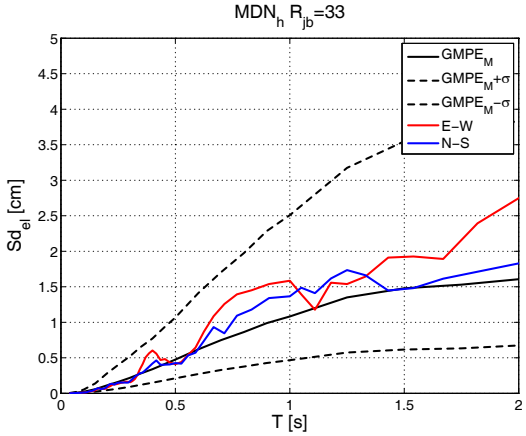

Figure 91. Comparison of the elastic displacement spectra for the horizontal components, Sd_{el}, at MDN station with the median prediction and $\pm\sigma$ bands according to De Luca et al. 2012.

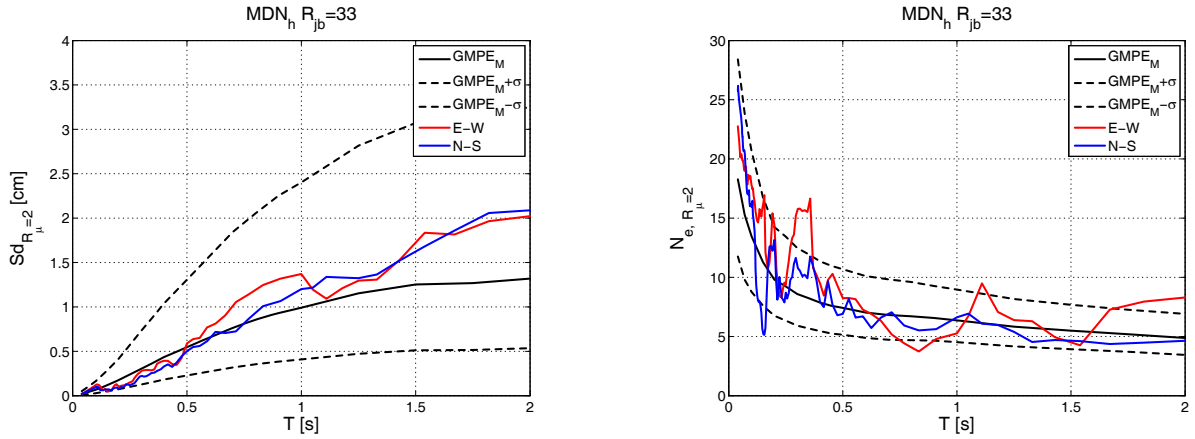

Figure 92. Comparison of the inelastic spectra in terms of displacements, $Sd_{R_\mu=i}$ (on the left) and equivalent number of cycles, $N_{e,\,R_\mu=i}$ (on the left) for R_μ equal to 2, for the horizontal components, at MDN station with the median prediction and $\pm\sigma$ bands according to De Luca et al. 2012.

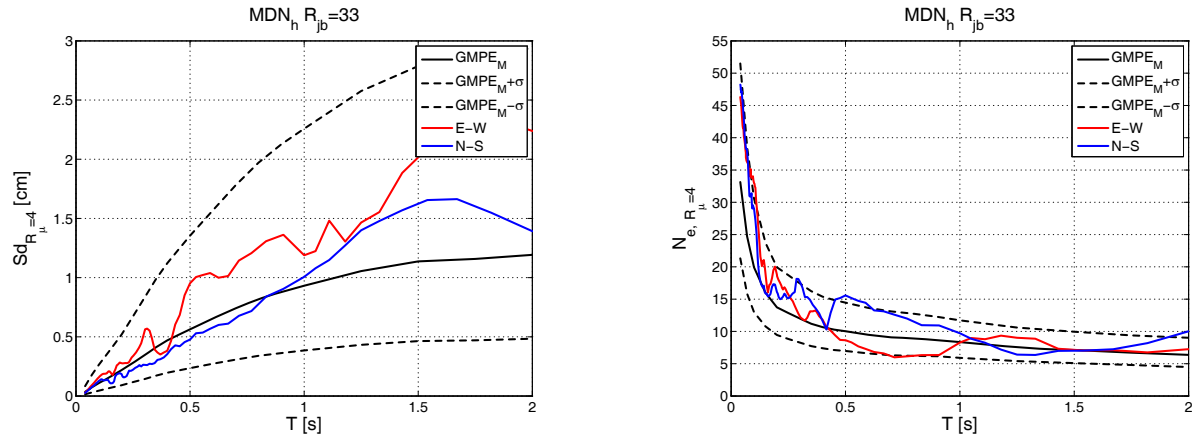

Figure 93. Comparison of the inelastic spectra in terms of displacements, $Sd_{R_\mu=i}$ (on the left) and equivalent number of cycles, $N_{e,\,R_\mu=i}$ (on the left) for R_μ equal to 4, for the horizontal components, at MDN station with the median prediction and $\pm\sigma$ bands according to De Luca et al. 2012.

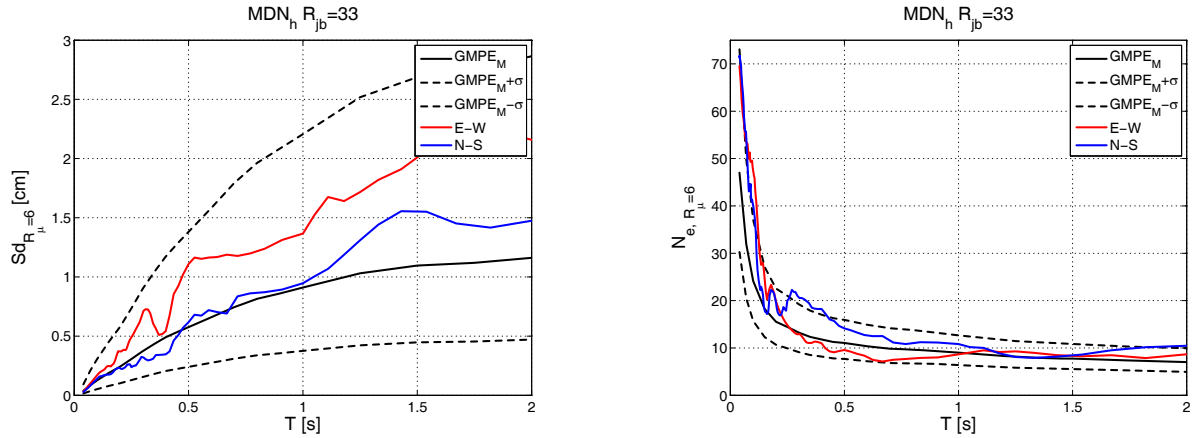

Figure 94. Comparison of the inelastic spectra in terms of displacements, $Sd_{R_\mu=i}$ (on the left) and equivalent number of cycles, $N_{e,\,R_\mu=i}$ (on the left) for R_μ equal to 6, for the horizontal components, at MDN station with the median prediction and $\pm\sigma$ bands according to De Luca et al. 2012.

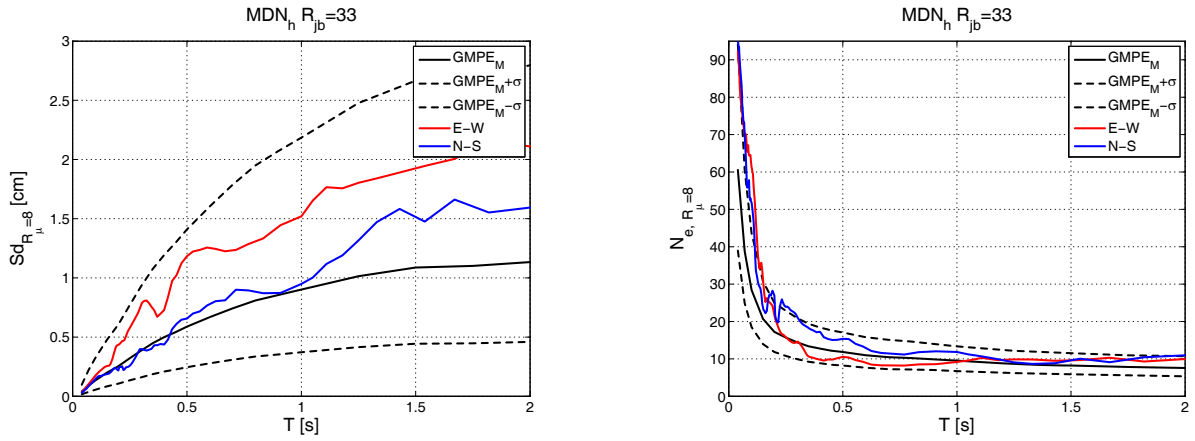

Figure 95. Comparison of the inelastic spectra in terms of displacements, $Sd_{R_\mu=i}$ (on the left) and equivalent number of cycles, $N_{e,R_\mu=i}$ (on the left) for R_μ equal to 8, for the horizontal components, at MDN station with the median prediction and $\pm\sigma$ bands according to De Luca et al. 2012.

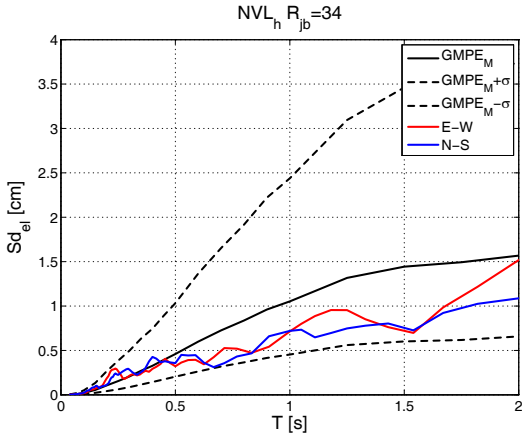

Figure 96. Comparison of the elastic displacement spectra for the horizontal components, Sd_{el}, at NVL station with the median prediction and $\pm\sigma$ bands according to De Luca et al. 2012.

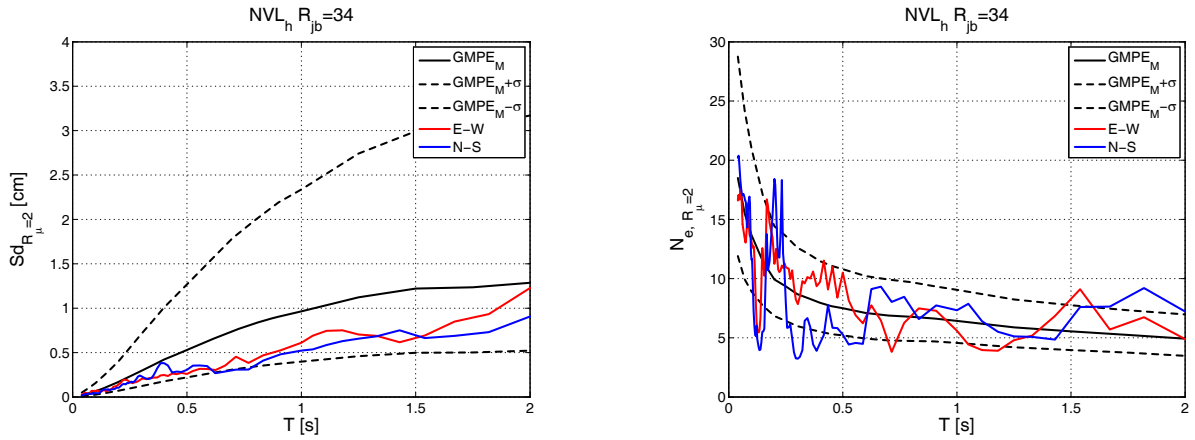

Figure 97. Comparison of the inelastic spectra in terms of displacements, $Sd_{R_\mu=i}$ (on the left) and equivalent number of cycles, $N_{e,R_\mu=i}$ (on the left) for R_μ equal to 2, for the horizontal components, at NVL station with the median prediction and $\pm\sigma$ bands according to De Luca et al. 2012.

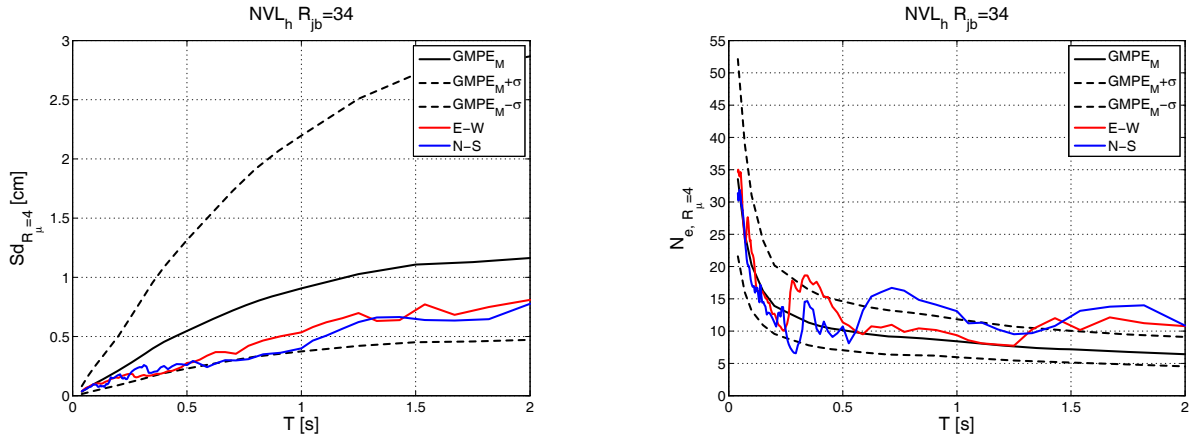

Figure 98. Comparison of the inelastic spectra in terms of displacements, $Sd_{R_\mu=i}$ (on the left) and equivalent number of cycles, $N_{e,R_\mu=i}$ (on the left) for R_μ equal to 4, for the horizontal components, at NVL station with the median prediction and $\pm\sigma$ bands according to De Luca et al. 2012.

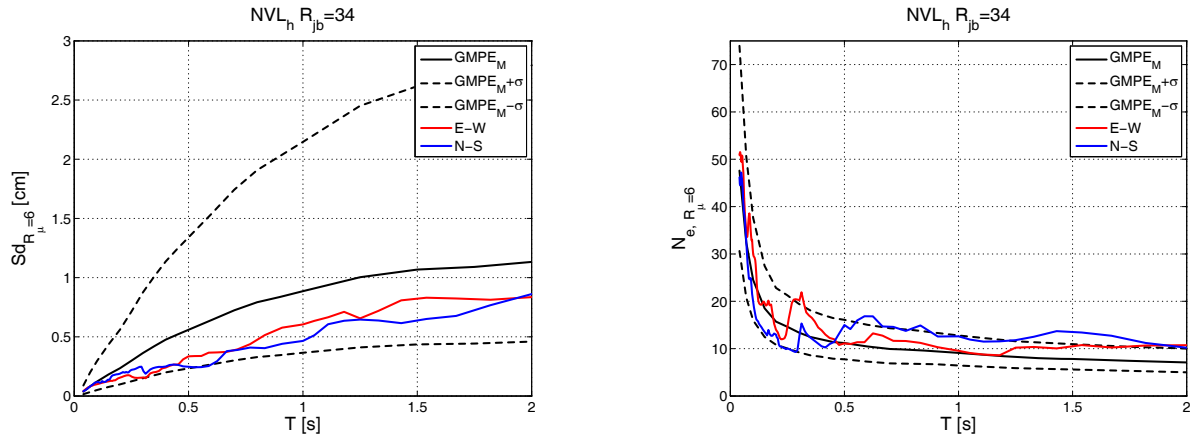

Figure 99. Comparison of the inelastic spectra in terms of displacements, $Sd_{R_\mu=i}$ (on the left) and equivalent number of cycles, $N_{e,R_\mu=i}$ (on the left) for R_μ equal to 6, for the horizontal components, at NVL station with the median prediction and $\pm\sigma$ bands according to De Luca et al. 2012.

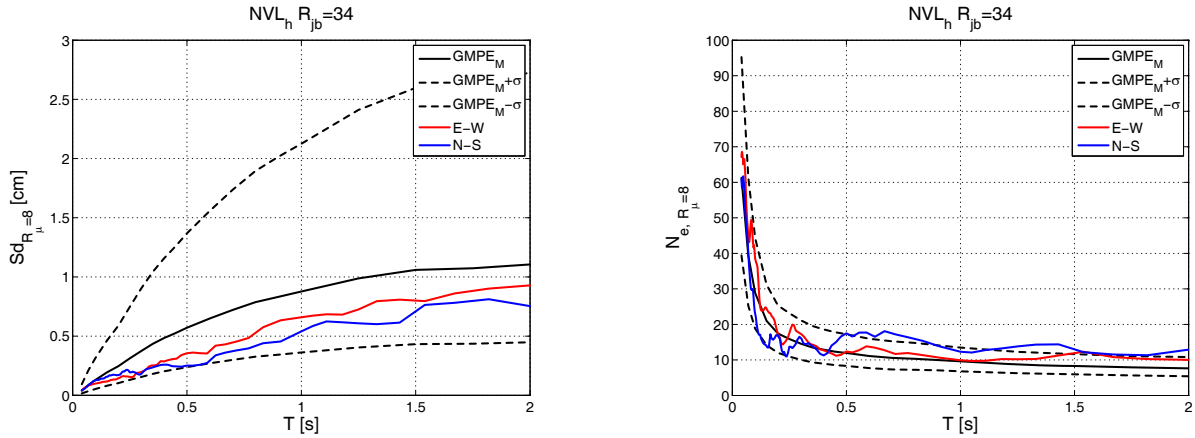

Figure 100. Comparison of the inelastic spectra in terms of displacements, $Sd_{R_\mu=i}$ (on the left) and equivalent number of cycles, $N_{e,R_\mu=i}$ (on the left) for R_μ equal to 8, for the horizontal components, at NVL station with the median prediction and $\pm\sigma$ bands according to De Luca et al. 2012.

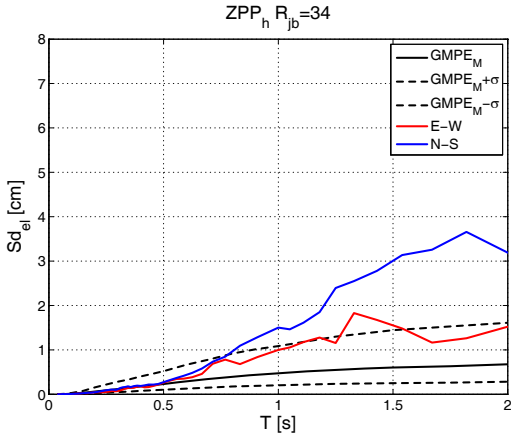

Figure 101. Comparison of the elastic displacement spectra for the horizontal components, Sd_{el}, at ZPP station with the median prediction and $\pm\sigma$ bands according to De Luca et al. 2012.

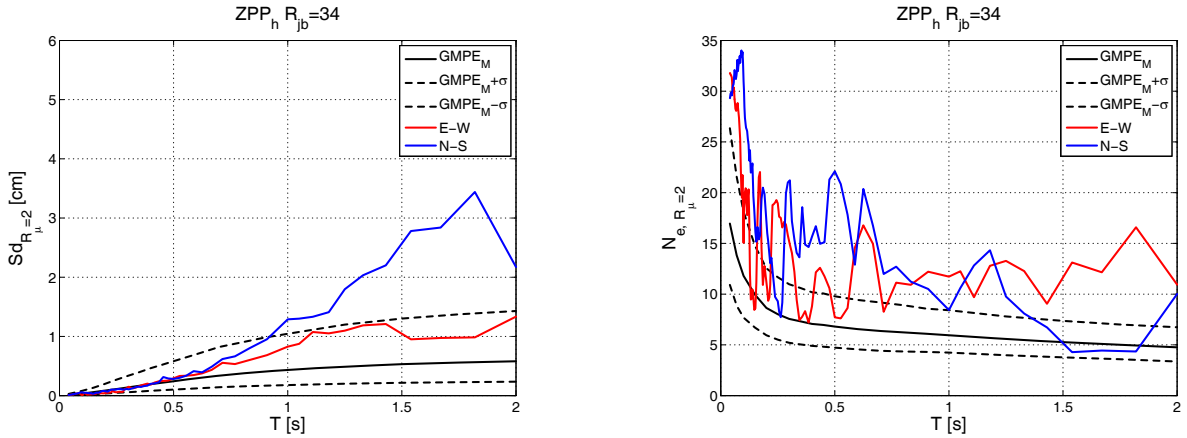

Figure 102. Comparison of the inelastic spectra in terms of displacements, $Sd_{R_\mu=i}$ (on the left) and equivalent number of cycles, $N_{e,R_\mu=i}$ (on the left) for R_μ equal to 2, for the horizontal components, at ZPP station with the median prediction and $\pm\sigma$ bands according to De Luca et al. 2012.

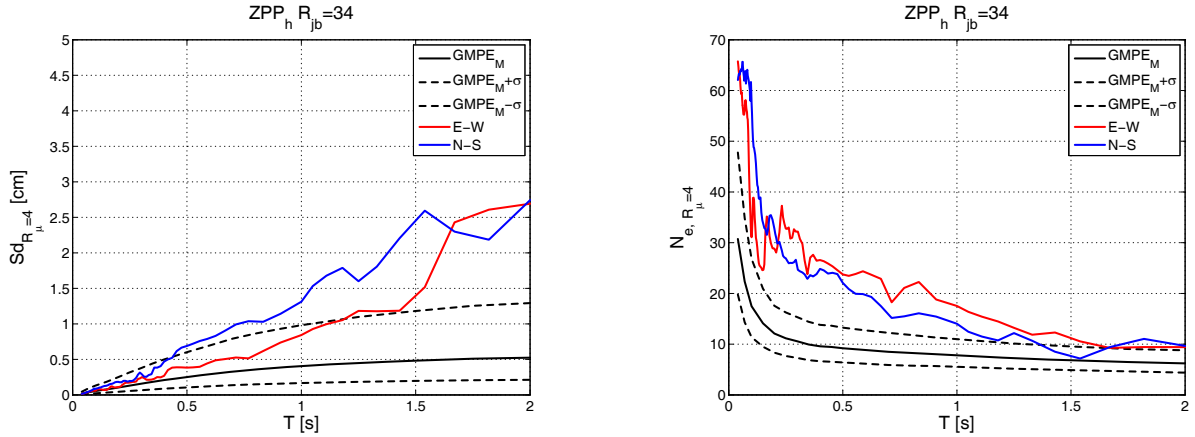

Figure 103. Comparison of the inelastic spectra in terms of displacements, $Sd_{R_\mu=i}$ (on the left) and equivalent number of cycles, $N_{e,R_\mu=i}$ (on the left) for R_μ equal to 4, for the horizontal components, at ZPP station with the median prediction and $\pm\sigma$ bands according to De Luca et al. 2012.

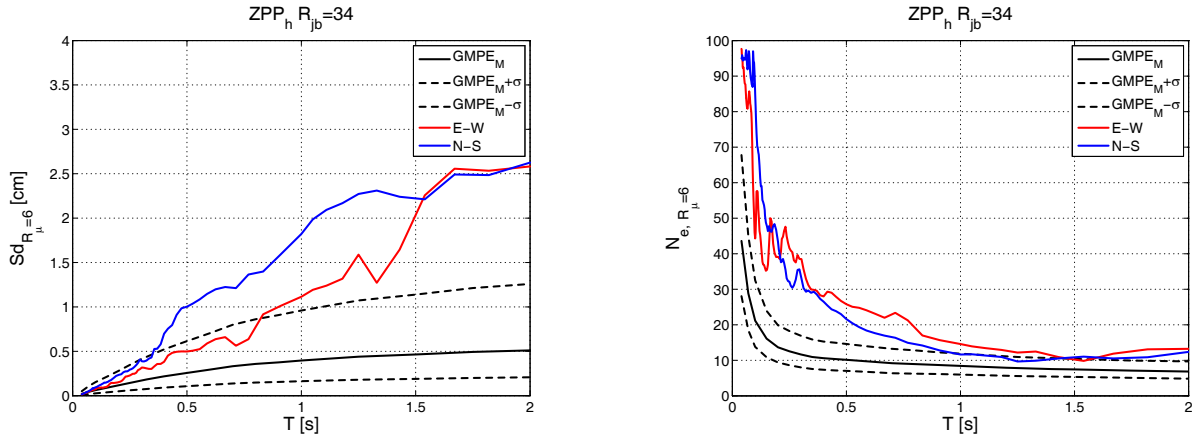

Figure 104. Comparison of the inelastic spectra in terms of displacements, $Sd_{R_\mu=i}$ (on the left) and equivalent number of cycles, $N_{e,R_\mu=i}$ (on the left) for R_μ equal to 6, for the horizontal components, at ZPP station with the median prediction and $\pm\sigma$ bands according to De Luca et al. 2012.

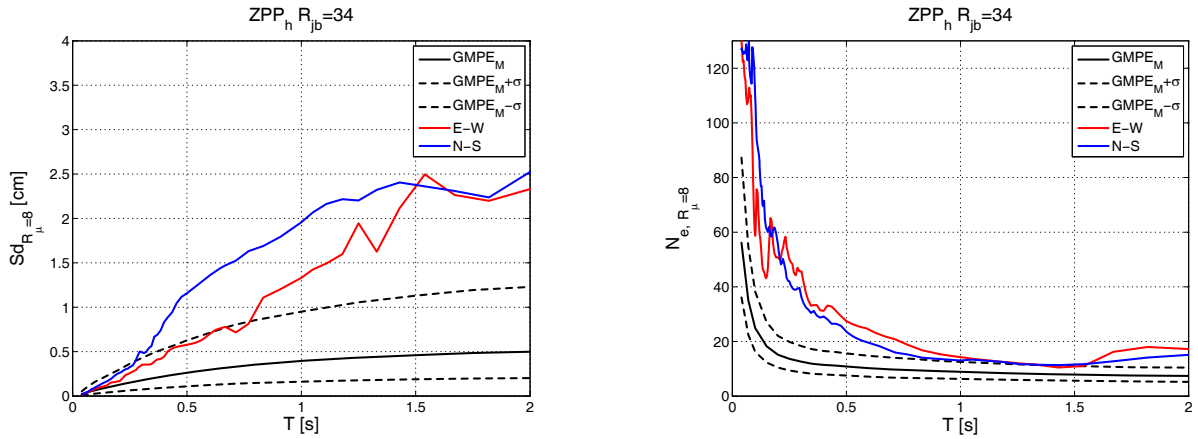

Figure 105. Comparison of the inelastic spectra in terms of displacements, $Sd_{R_\mu=i}$ (on the left) and equivalent number of cycles, $N_{e,R_\mu=i}$ (on the left) for R_μ equal to 8, for the horizontal components, at ZPP station with the median prediction and $\pm\sigma$ bands according to De Luca et al. 2012.

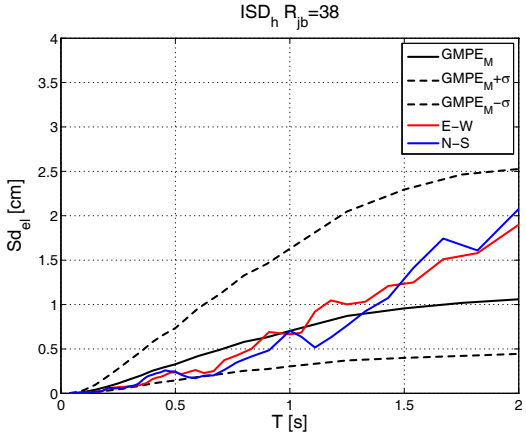

Figure 106. Comparison of the elastic displacement spectra for the horizontal components, Sd_{el}, at ISD station with the median prediction and $\pm\sigma$ bands according to De Luca et al. 2012.

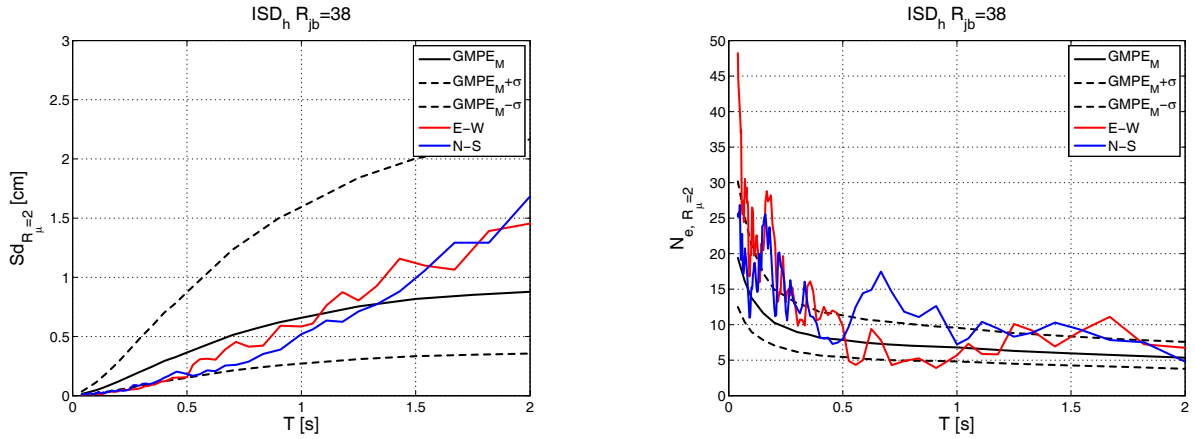

Figure 107. Comparison of the inelastic spectra in terms of displacements, $Sd_{R_\mu=i}$ (on the left) and equivalent number of cycles, $N_{e,\,R_\mu=i}$ (on the left) for R_μ equal to 2, for the horizontal components, at ISD station with the median prediction and $\pm\sigma$ bands according to De Luca et al. 2012.

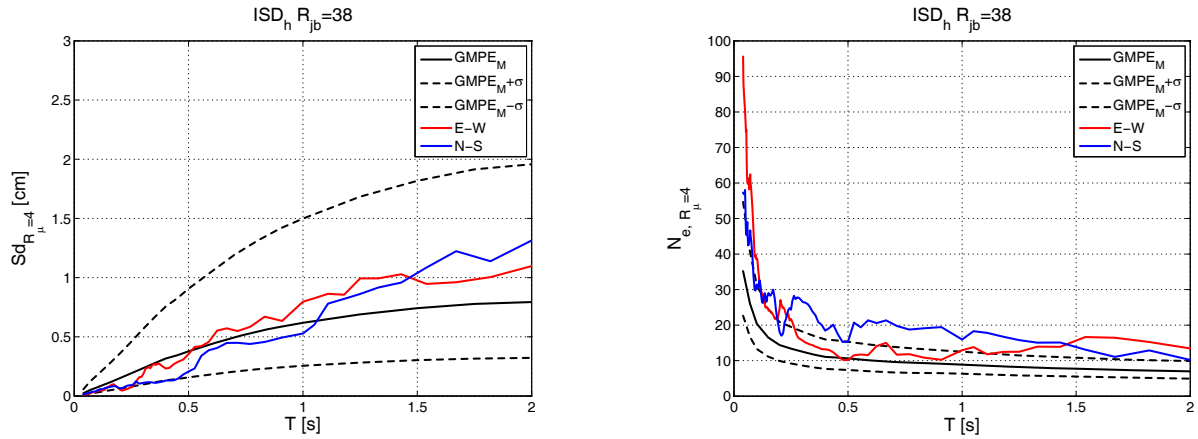

Figure 108. Comparison of the inelastic spectra in terms of displacements, $Sd_{R_\mu=i}$ (on the left) and equivalent number of cycles, $N_{e,\,R_\mu=i}$ (on the left) for R_μ equal to 4, for the horizontal components, at ISD station with the median prediction and $\pm\sigma$ bands according to De Luca et al. 2012.

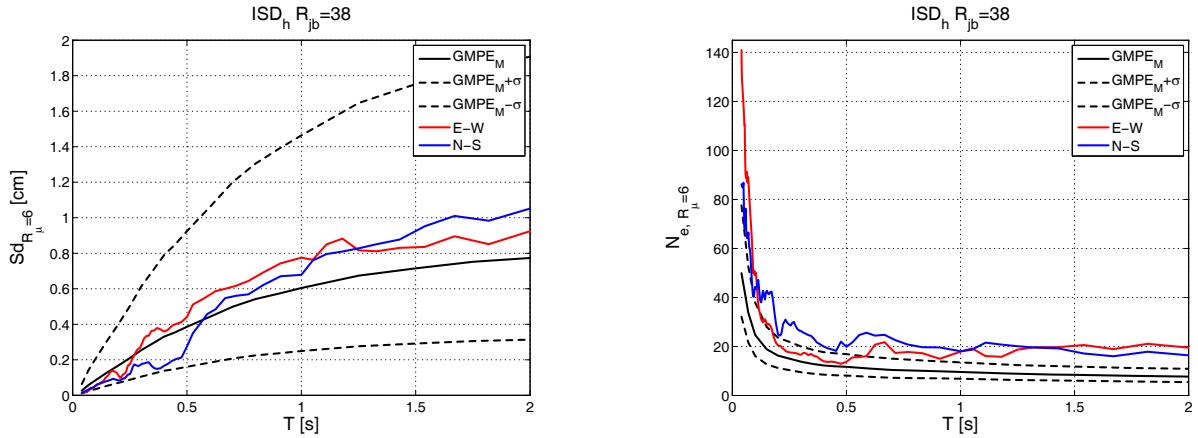

Figure 109. Comparison of the inelastic spectra in terms of displacements, $Sd_{R_\mu=i}$ (on the left) and equivalent number of cycles, $N_{e,\,R_\mu=i}$ (on the left) for R_μ equal to 6, for the horizontal components, at ISD station with the median prediction and $\pm\sigma$ bands according to De Luca et al. 2012.

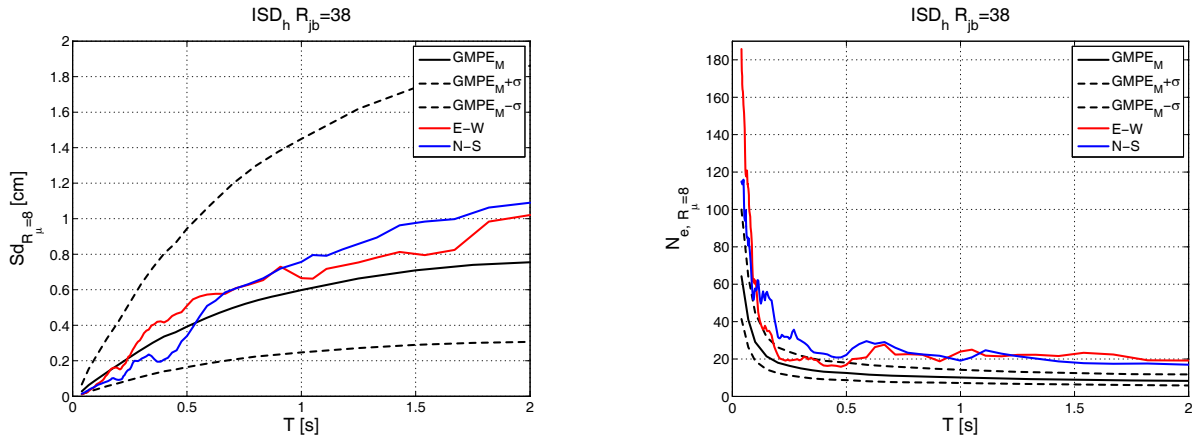

Figure 110. Comparison of the inelastic spectra in terms of displacements, $Sd_{R_\mu=i}$ (on the left) and equivalent number of cycles, $N_{e,\ R_\mu=i}$ (on the left) for R_μ equal to 8, for the horizontal components, at ISD station with the median prediction and $\pm\sigma$ bands according to De Luca et al. 2012.

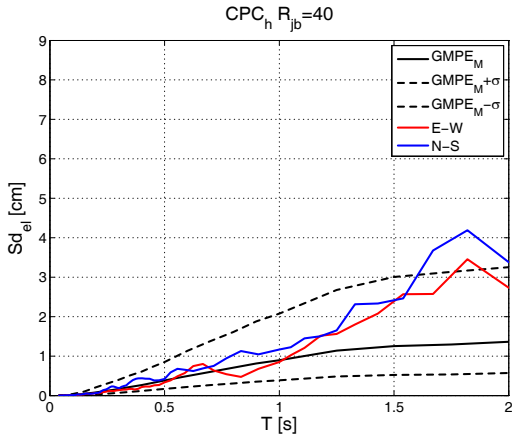

Figure 111. Comparison of the elastic displacement spectra for the horizontal components, Sd_{el}, at CPC station with the median prediction and $\pm\sigma$ bands according to De Luca et al. 2012.

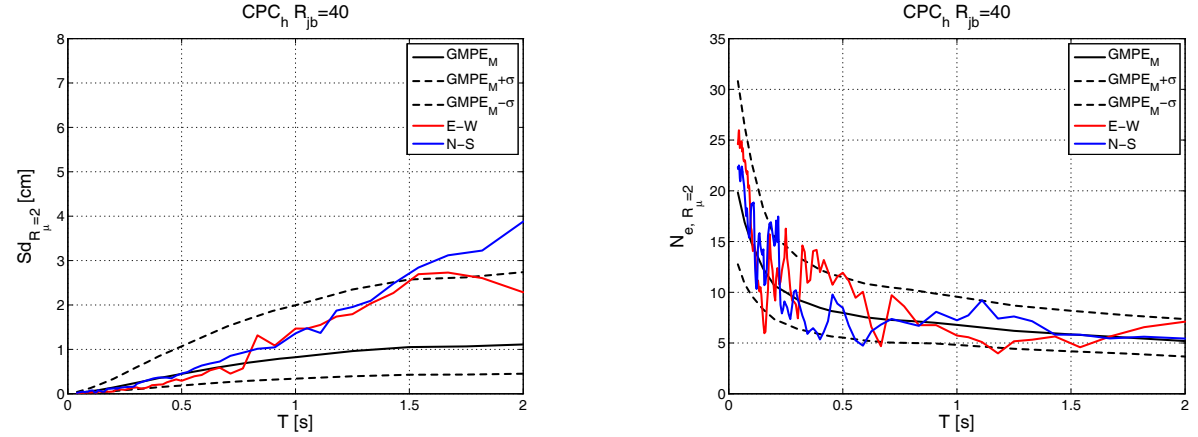

Figure 112. Comparison of the inelastic spectra in terms of displacements, $Sd_{R_\mu=i}$ (on the left) and equivalent number of cycles, $N_{e,\ R_\mu=i}$ (on the left) for R_μ equal to 2, for the horizontal components, at CPC station with the median prediction and $\pm\sigma$ bands according to De Luca et al. 2012.

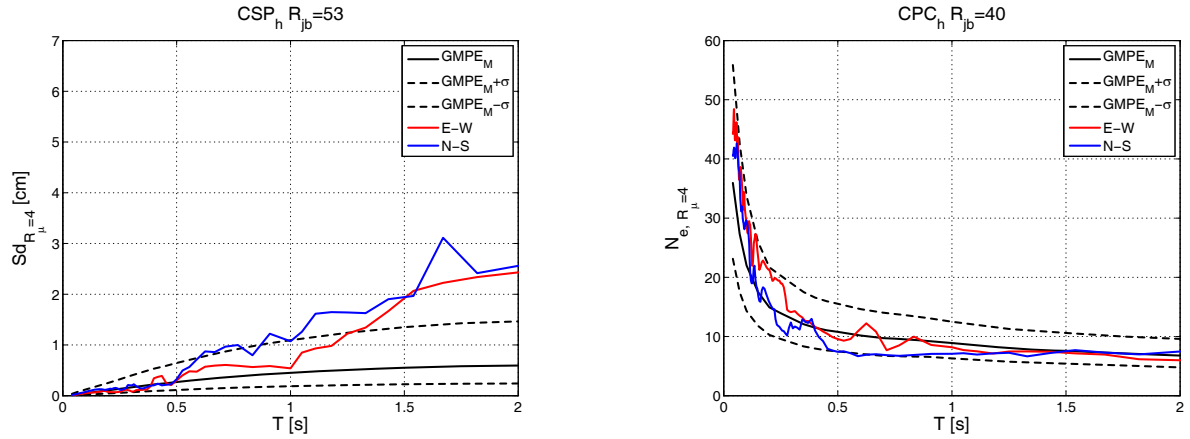

Figure 113. Comparison of the inelastic spectra in terms of displacements, $Sd_{R_\mu=i}$ (on the left) and equivalent number of cycles, $N_{e,R_\mu=i}$ (on the left) for R_μ equal to 4, for the horizontal components, at CPC station with the median prediction and $\pm\sigma$ bands according to De Luca et al. 2012.

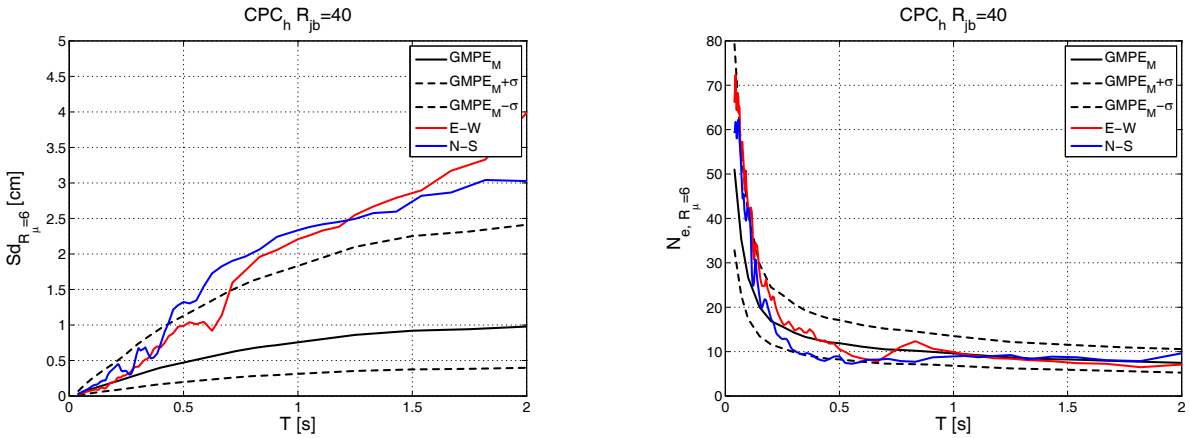

Figure 114. Comparison of the inelastic spectra in terms of displacements, $Sd_{R_\mu=i}$ (on the left) and equivalent number of cycles, $N_{e,R_\mu=i}$ (on the left) for R_μ equal to 6, for the horizontal components, at CPC station with the median prediction and $\pm\sigma$ bands according to De Luca et al. 2012.

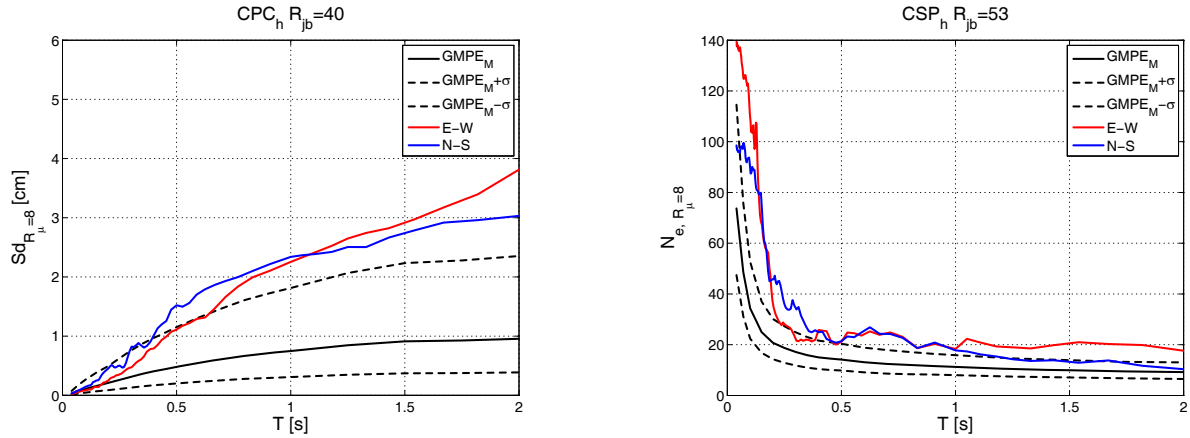

Figure 115. Comparison of the inelastic spectra in terms of displacements, $Sd_{R_\mu=i}$ (on the left) and equivalent number of cycles, $N_{e,R_\mu=i}$ (on the left) for R_μ equal to 8, for the horizontal components, at CPC station with the median prediction and $\pm\sigma$ bands according to De Luca et al. 2012.

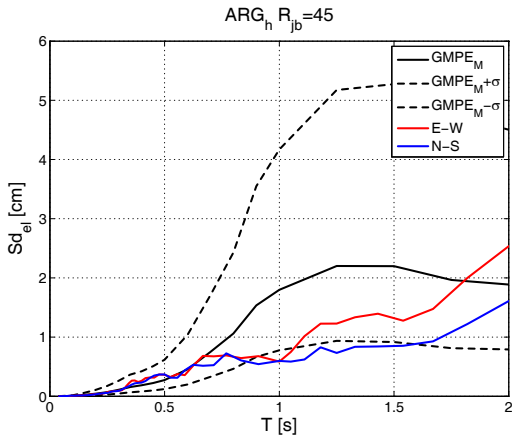

Figure 116. Comparison of the elastic displacement spectra for the horizontal components, Sd_{el}, at ARG station with the median prediction and $\pm\sigma$ bands according to De Luca et al. 2012.

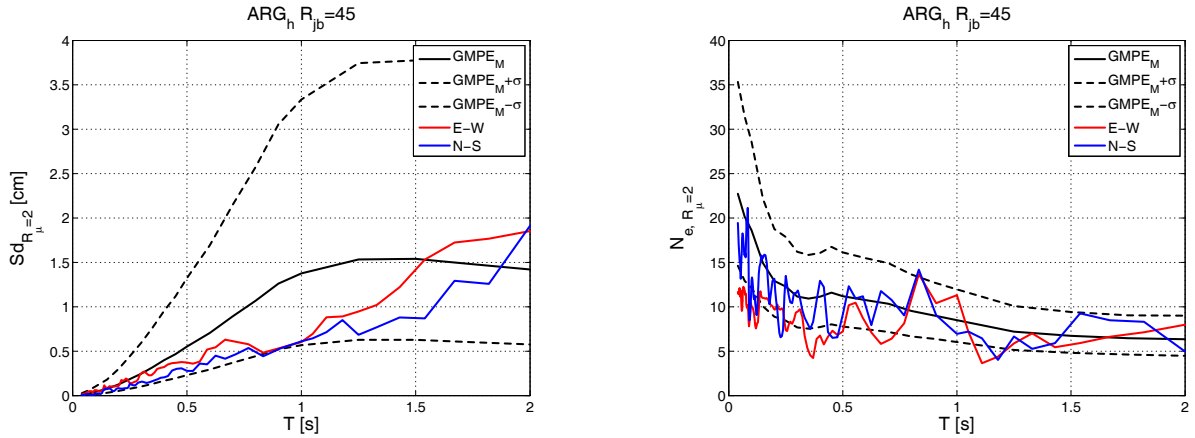

Figure 117. Comparison of the inelastic spectra in terms of displacements, $Sd_{R_\mu=i}$ (on the left) and equivalent number of cycles, $N_{e,\ R_\mu=i}$ (on the left) for R_μ equal to 2, for the horizontal components, at ARG station with the median prediction and $\pm\sigma$ bands according to De Luca et al. 2012.

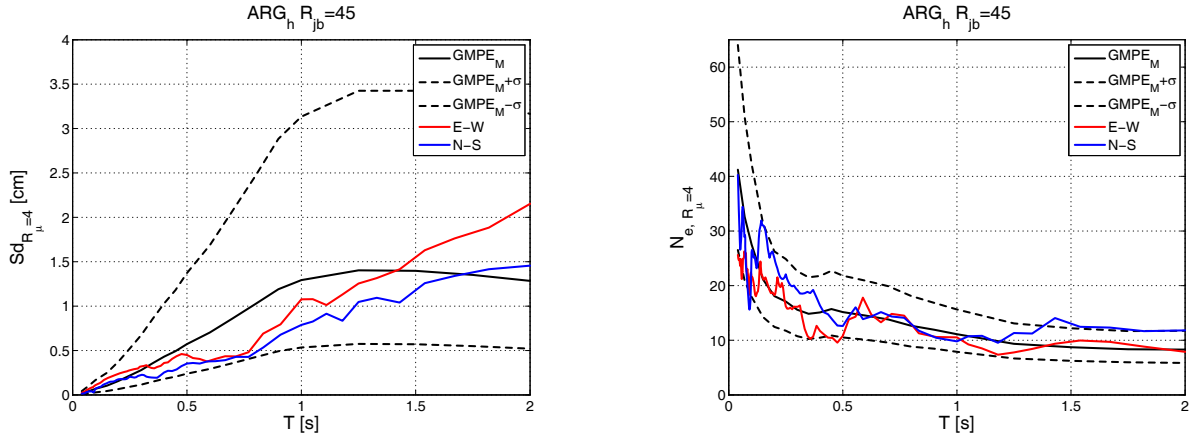

Figure 118. Comparison of the inelastic spectra in terms of displacements, $Sd_{R_\mu=i}$ (on the left) and equivalent number of cycles, $N_{e,\ R_\mu=i}$ (on the left) for R_μ equal to 4, for the horizontal components, at ARG station with the median prediction and $\pm\sigma$ bands according to De Luca et al. 2012.

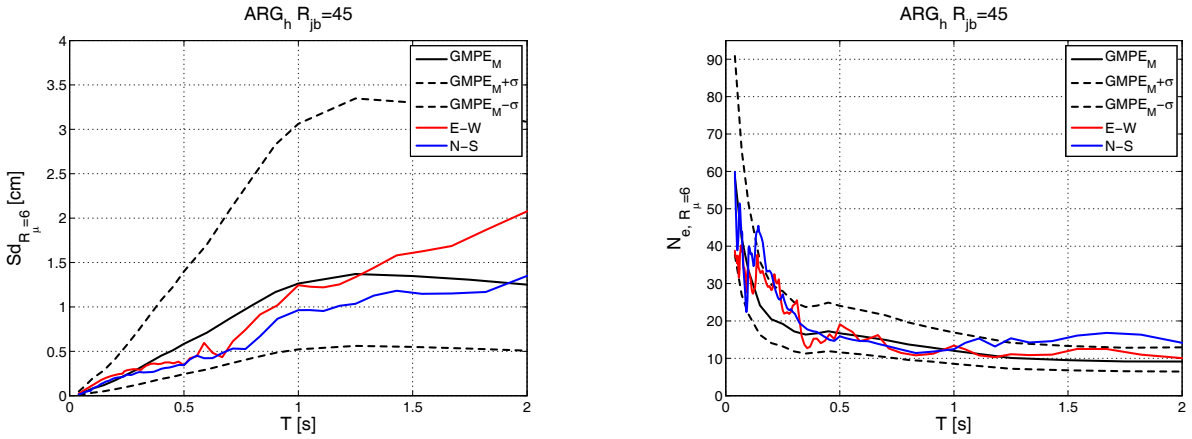

Figure 119. Comparison of the inelastic spectra in terms of displacements, $Sd_{R_\mu=i}$ (on the left) and equivalent number of cycles, $N_{e,R_\mu=i}$ (on the left) for R_μ equal to 6, for the horizontal components, at ARG station with the median prediction and $\pm\sigma$ bands according to De Luca et al. 2012.

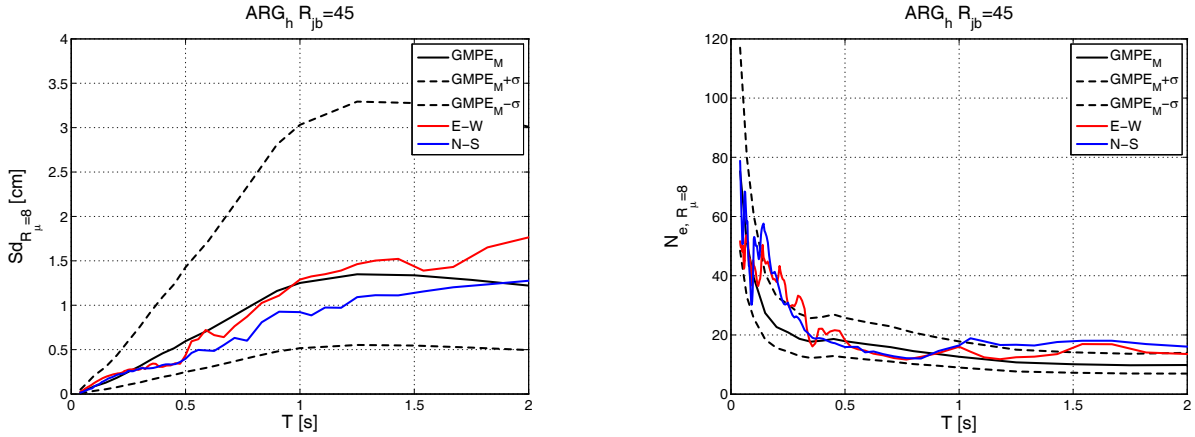

Figure 120. Comparison of the inelastic spectra in terms of displacements, $Sd_{R_\mu=i}$ (on the left) and equivalent number of cycles, $N_{e,R_\mu=i}$ (on the left) for R_μ equal to 8, for the horizontal components, at ARG station with the median prediction and $\pm\sigma$ bands according to De Luca et al. 2012.

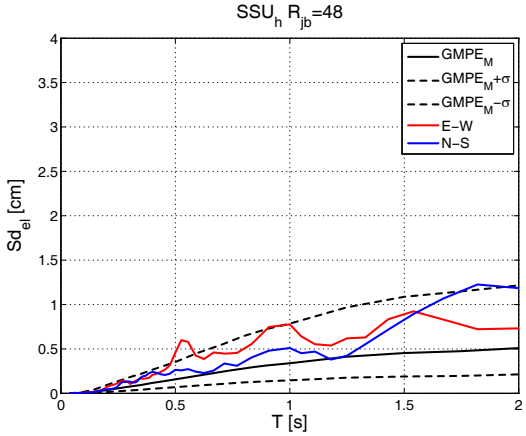

Figure 121. Comparison of the elastic displacement spectra for the horizontal components, Sd_{el}, at SSU station with the median prediction and $\pm\sigma$ bands according to De Luca et al. 2012.

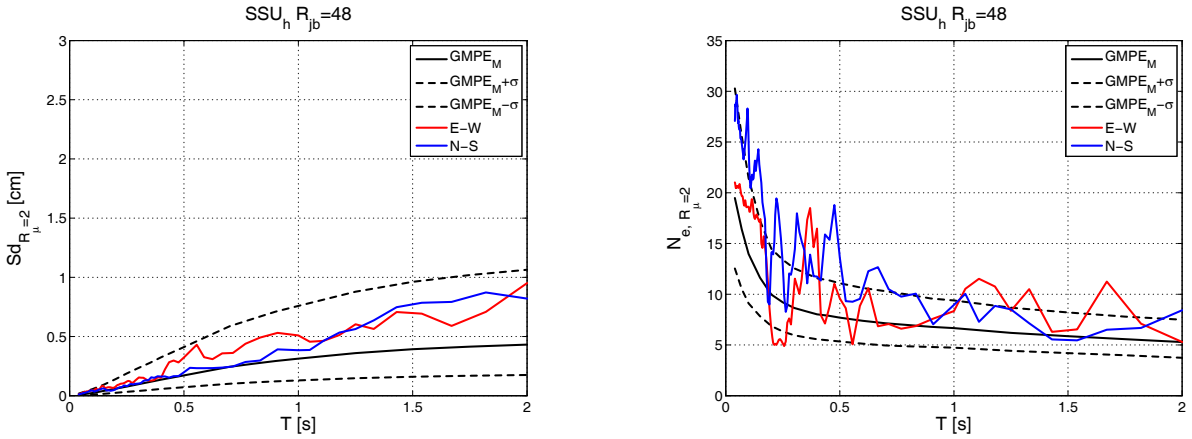

Figure 122. Comparison of the inelastic spectra in terms of displacements, $Sd_{R_\mu=i}$ (on the left) and equivalent number of cycles, $N_{e,R_\mu=i}$ (on the left) for R_μ equal to 2, for the horizontal components, at SSU station with the median prediction and $\pm\sigma$ bands according to De Luca et al. 2012.

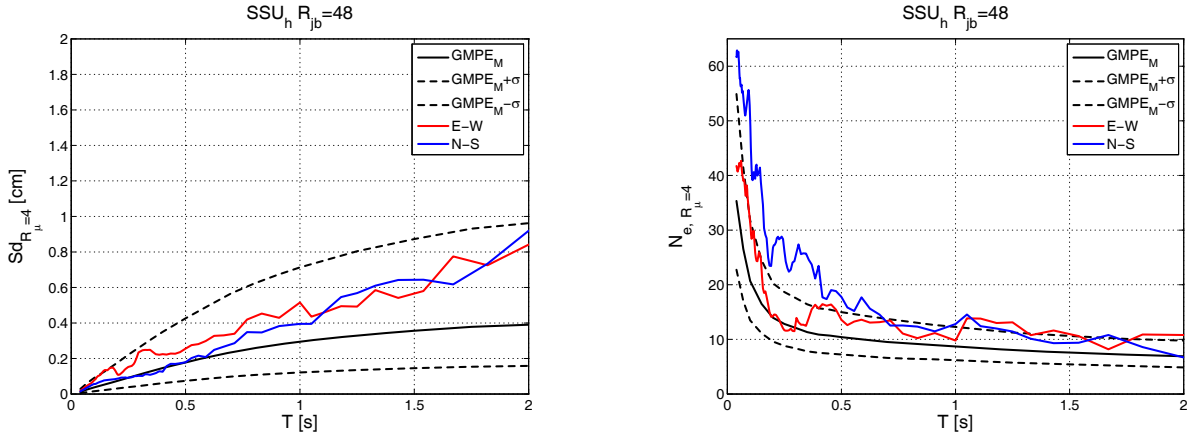

Figure 123. Comparison of the inelastic spectra in terms of displacements, $Sd_{R_\mu=i}$ (on the left) and equivalent number of cycles, $N_{e,R_\mu=i}$ (on the left) for R_μ equal to 4, for the horizontal components, at SSU station with the median prediction and $\pm\sigma$ bands according to De Luca et al. 2012.

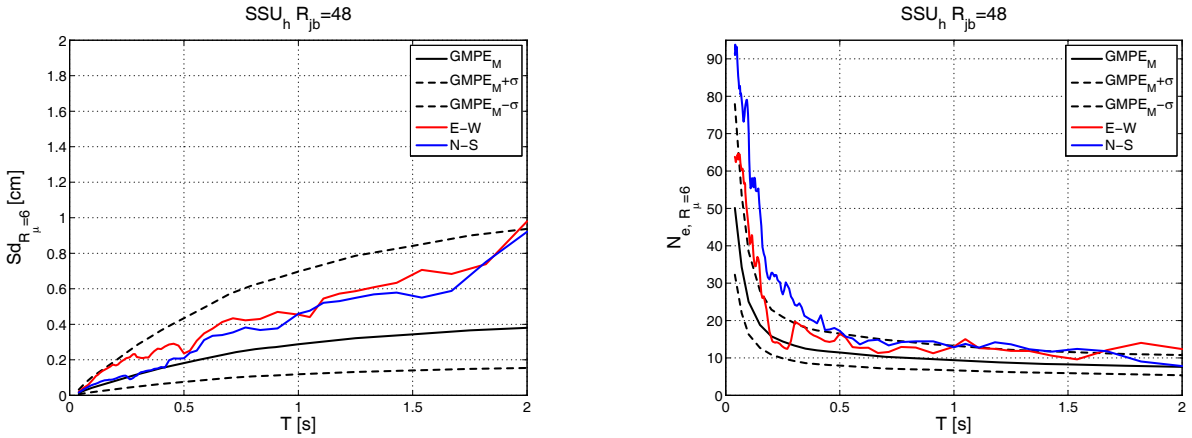

Figure 124. Comparison of the inelastic spectra in terms of displacements, $Sd_{R_\mu=i}$ (on the left) and equivalent number of cycles, $N_{e,R_\mu=i}$ (on the left) for R_μ equal to 6, for the horizontal components, at SSU station with the median prediction and $\pm\sigma$ bands according to De Luca et al. 2012.

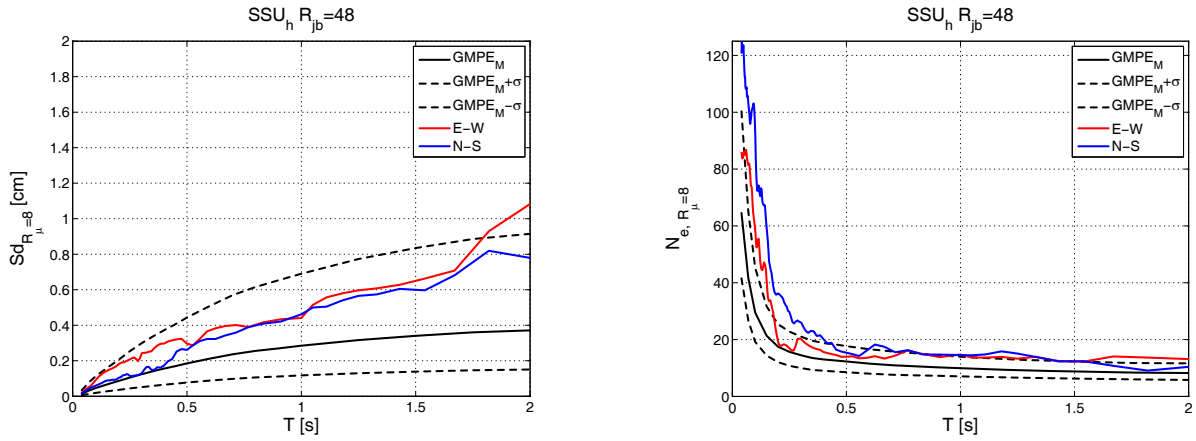

Figure 125. Comparison of the inelastic spectra in terms of displacements, $Sd_{R_\mu=i}$ (on the left) and equivalent number of cycles, $N_{e,\,R_\mu=i}$ (on the left) for R_μ equal to 8, for the horizontal components, at SSU station with the median prediction and $\pm\sigma$ bands according to De Luca et al. 2012.

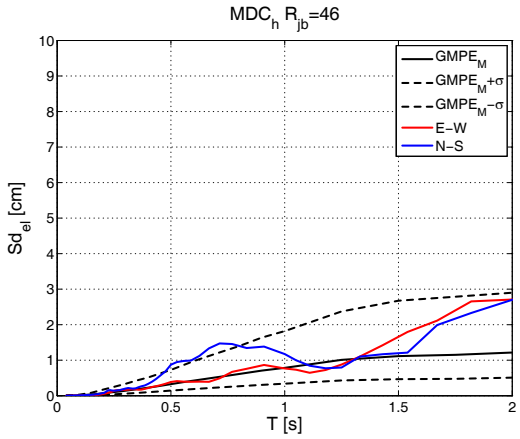

Figure 126. Comparison of the elastic displacement spectra for the horizontal components, Sd_{el}, at MDC station with the median prediction and $\pm\sigma$ bands according to De Luca et al. 2012.

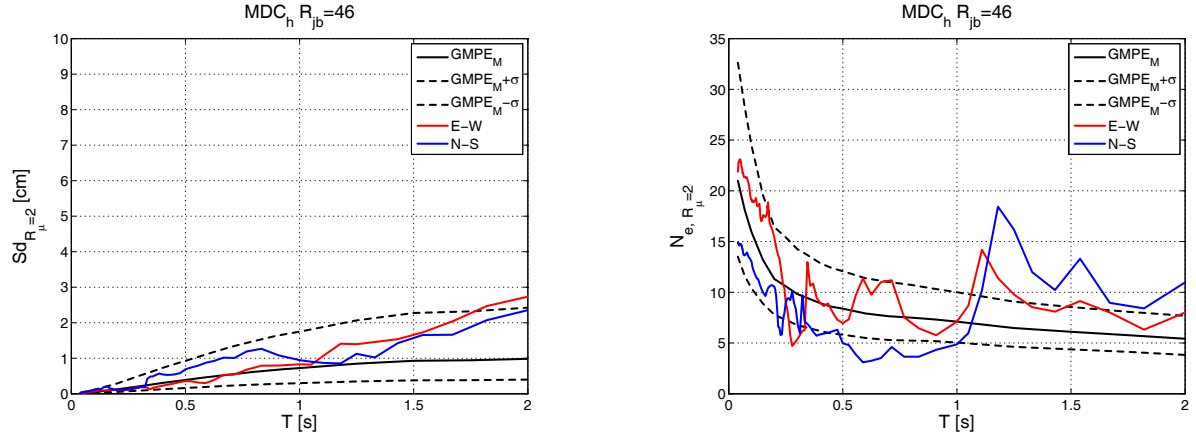

Figure 127. Comparison of the inelastic spectra in terms of displacements, $Sd_{R_\mu=i}$ (on the left) and equivalent number of cycles, $N_{e,\,R_\mu=i}$ (on the left) for R_μ equal to 2, for the horizontal components, at MDC station with the median prediction and $\pm\sigma$ bands according to De Luca et al. 2012.

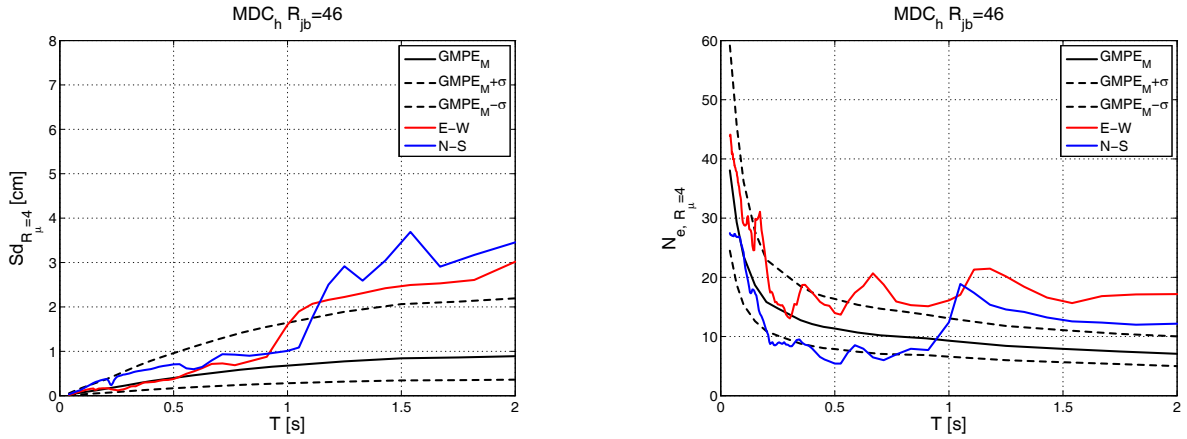

Figure 128. Comparison of the inelastic spectra in terms of displacements, $Sd_{R_\mu=i}$ (on the left) and equivalent number of cycles, $N_{e,\,R_\mu=i}$ (on the left) for R_μ equal to 4, for the horizontal components, at MDC station with the median prediction and $\pm\sigma$ bands according to De Luca et al. 2012.

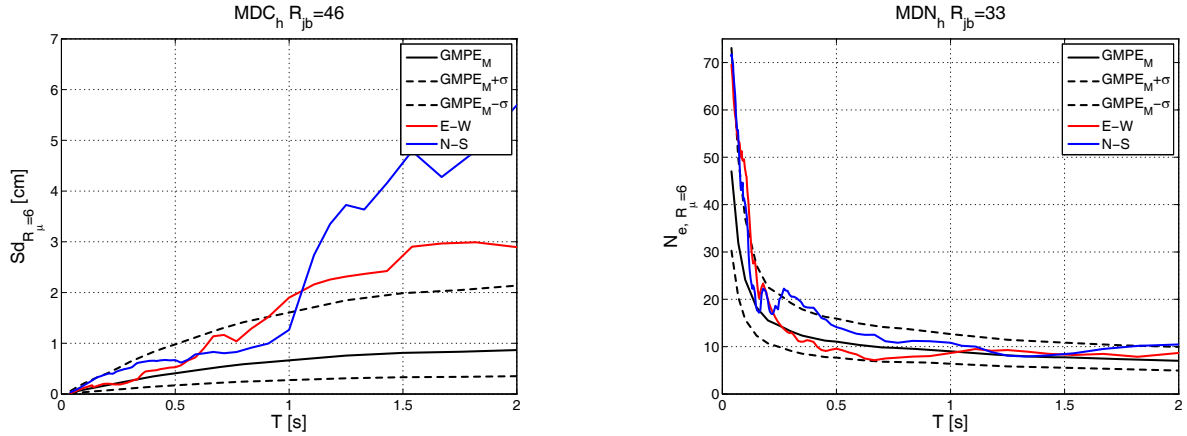

Figure 129. Comparison of the inelastic spectra in terms of displacements, $Sd_{R_\mu=i}$ (on the left) and equivalent number of cycles, $N_{e,\,R_\mu=i}$ (on the left) for R_μ equal to 6, for the horizontal components, at MDC station with the median prediction and $\pm\sigma$ bands according to De Luca et al. 2012.

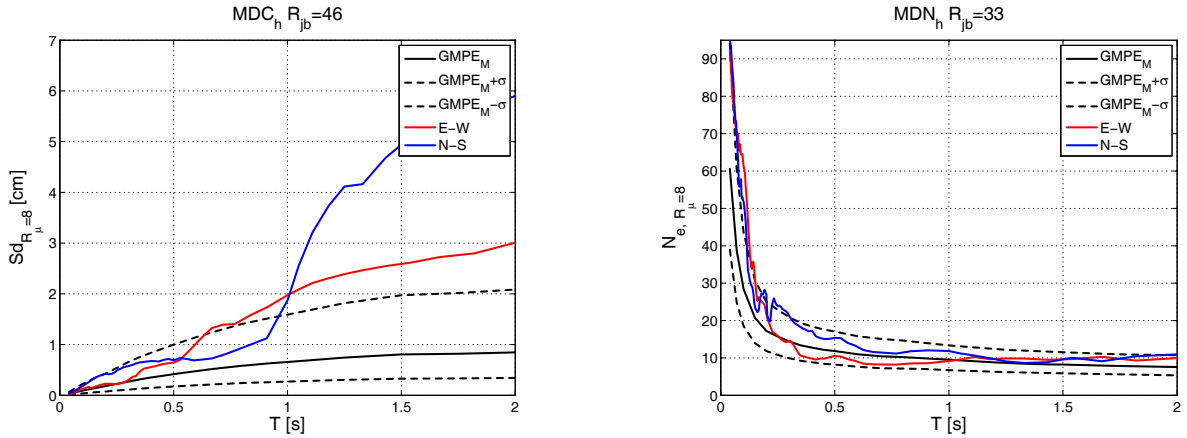

Figure 130. Comparison of the inelastic spectra in terms of displacements, $Sd_{R_\mu=i}$ (on the left) and equivalent number of cycles, $N_{e,\,R_\mu=i}$ (on the left) for R_μ equal to 8, for the horizontal components, at MDC station with the median prediction and $\pm\sigma$ bands according to De Luca et al. 2012.

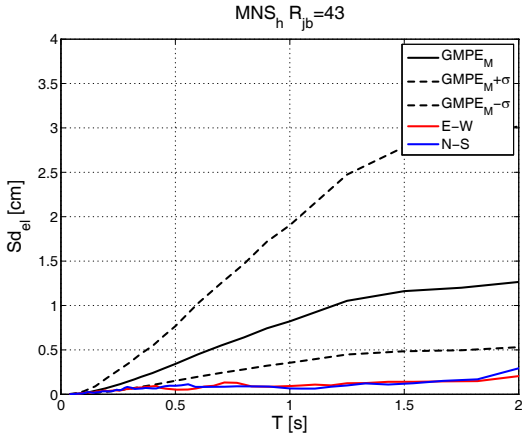

Figure 131. Comparison of the elastic displacement spectra for the horizontal components, Sd_{el}, at MNS station with the median prediction and $\pm\sigma$ bands according to De Luca et al. 2012.

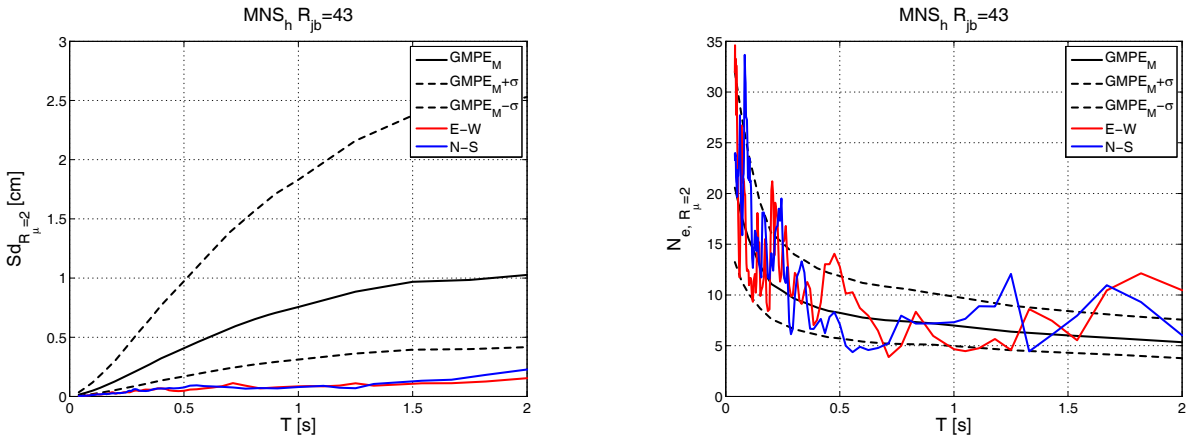

Figure 132. Comparison of the inelastic spectra in terms of displacements, $Sd_{R_\mu=i}$ (on the left) and equivalent number of cycles, $N_{e,\,R_\mu=i}$ (on the left) for R_μ equal to 2, for the horizontal components, at MNS station with the median prediction and $\pm\sigma$ bands according to De Luca et al. 2012.

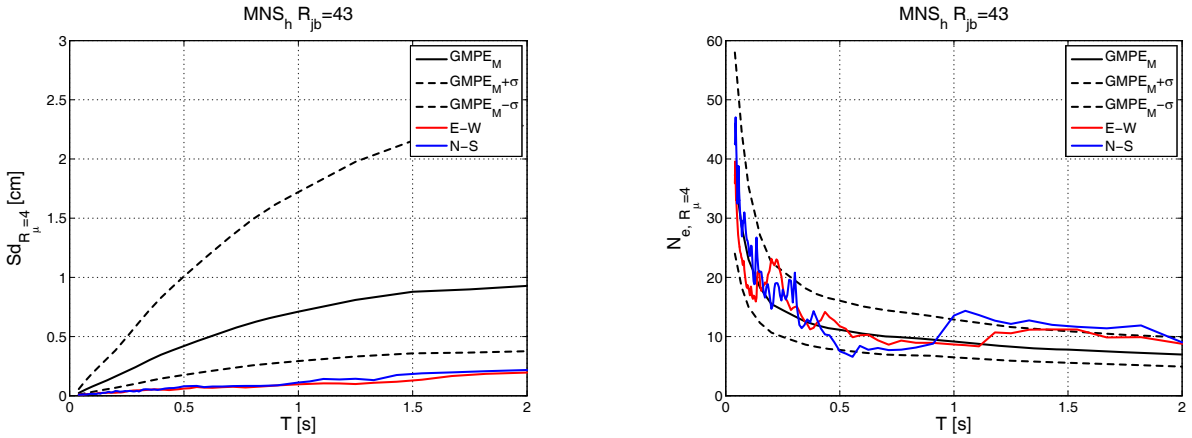

Figure 133. Comparison of the inelastic spectra in terms of displacements, $Sd_{R_\mu=i}$ (on the left) and equivalent number of cycles, $N_{e,\,R_\mu=i}$ (on the left) for R_μ equal to 4, for the horizontal components, at MNS station with the median prediction and $\pm\sigma$ bands according to De Luca et al. 2012.

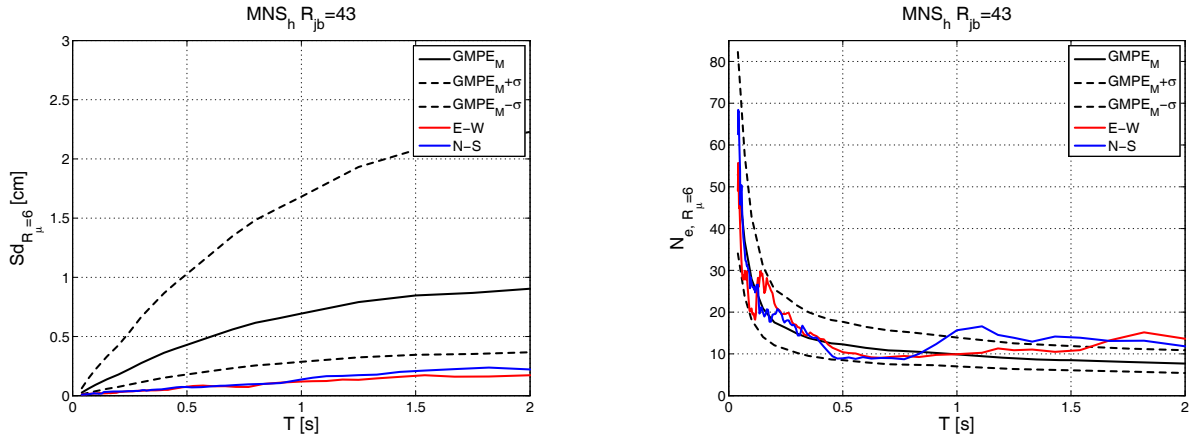

Figure 134. Comparison of the inelastic spectra in terms of displacements, $Sd_{R_\mu=i}$ (on the left) and equivalent number of cycles, $N_{e,R_\mu=i}$ (on the left) for R_μ equal to 6, for the horizontal components, at MNS station with the median prediction and $\pm\sigma$ bands according to De Luca et al. 2012.

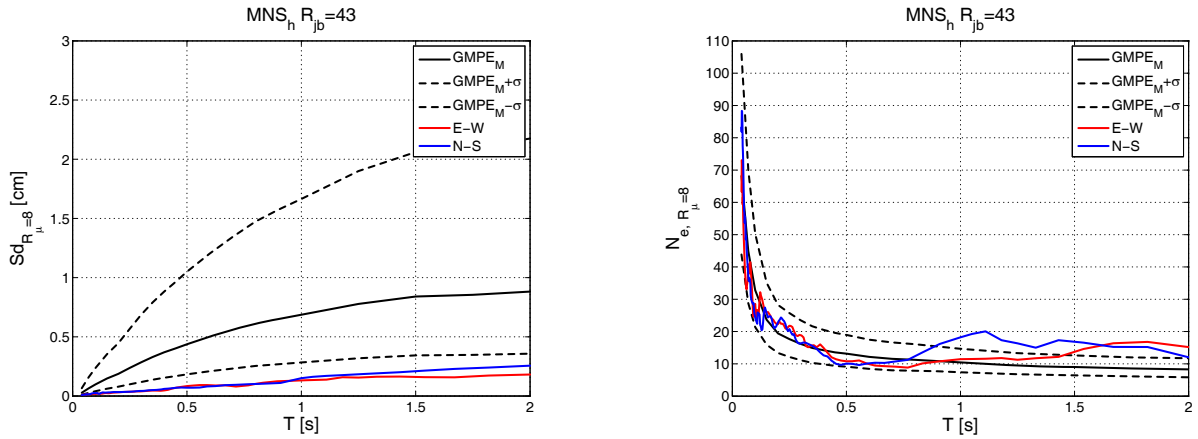

Figure 135. Comparison of the inelastic spectra in terms of displacements, $Sd_{R_\mu=i}$ (on the left) and equivalent number of cycles, $N_{e,R_\mu=i}$ (on the left) for R_μ equal to 8, for the horizontal components, at MNS station with the median prediction and $\pm\sigma$ bands according to De Luca et al. 2012.

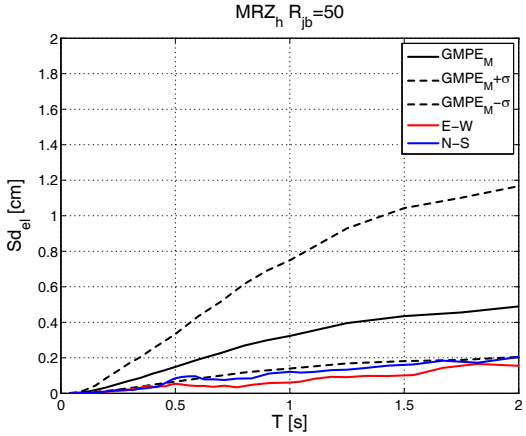

Figure 136. Comparison of the elastic displacement spectra for the horizontal components, Sd_{el}, at MRZ station with the median prediction and $\pm\sigma$ bands according to De Luca et al. 2012.

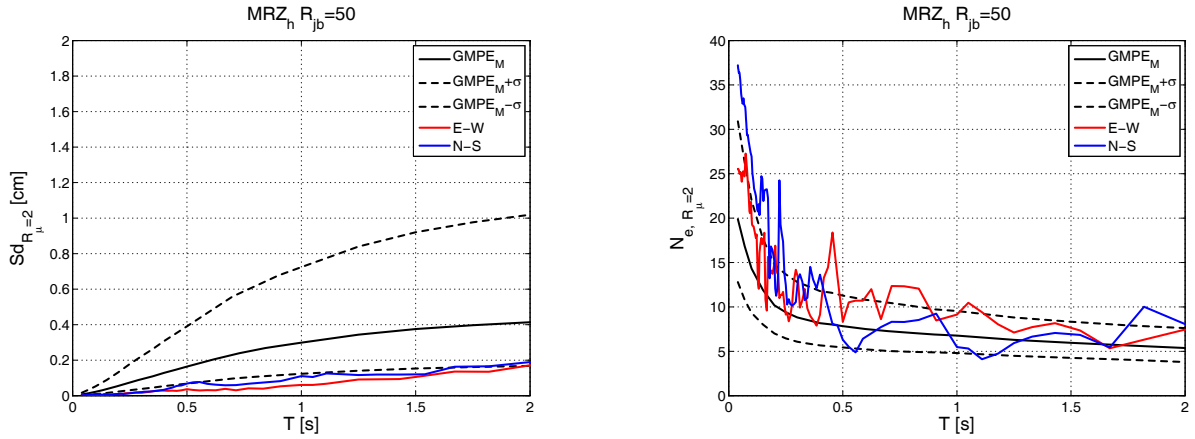

Figure 137. Comparison of the inelastic spectra in terms of displacements, $Sd_{R_\mu=i}$ (on the left) and equivalent number of cycles, $N_{e,R_\mu=i}$ (on the left) for R_μ equal to 2, for the horizontal components, at MRZ station with the median prediction and $\pm\sigma$ bands according to De Luca et al. 2012.

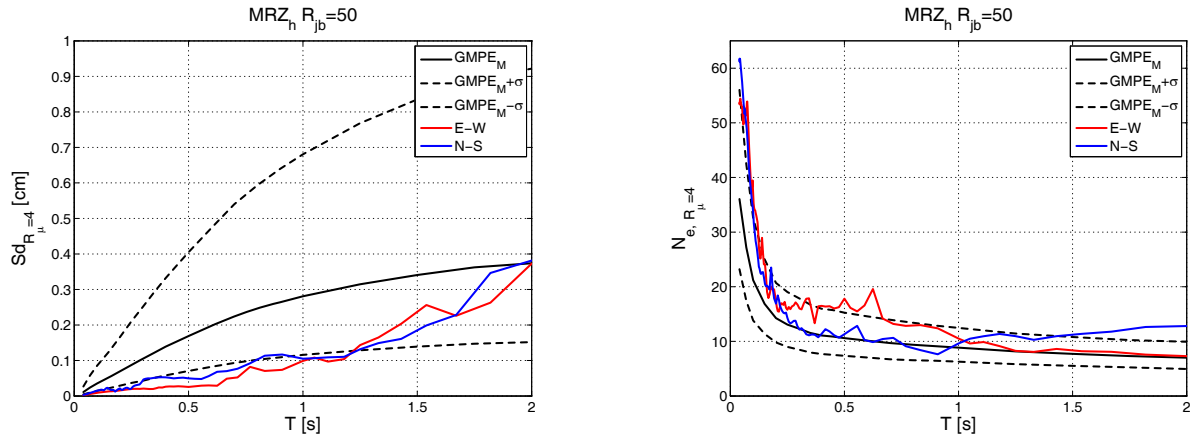

Figure 138. Comparison of the inelastic spectra in terms of displacements, $Sd_{R_\mu=i}$ (on the left) and equivalent number of cycles, $N_{e,R_\mu=i}$ (on the left) for R_μ equal to 4, for the horizontal components, at MRZ station with the median prediction and $\pm\sigma$ bands according to De Luca et al. 2012.

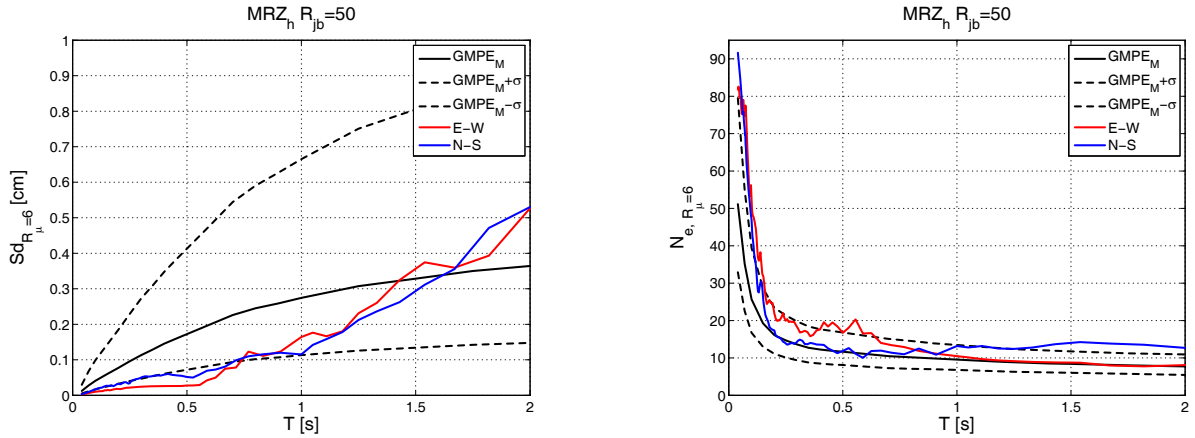

Figure 139. Comparison of the inelastic spectra in terms of displacements, $Sd_{R_\mu=i}$ (on the left) and equivalent number of cycles, $N_{e,R_\mu=i}$ (on the left) for R_μ equal to 6, for the horizontal components, at MRZ station with the median prediction and $\pm\sigma$ bands according to De Luca et al. 2012.

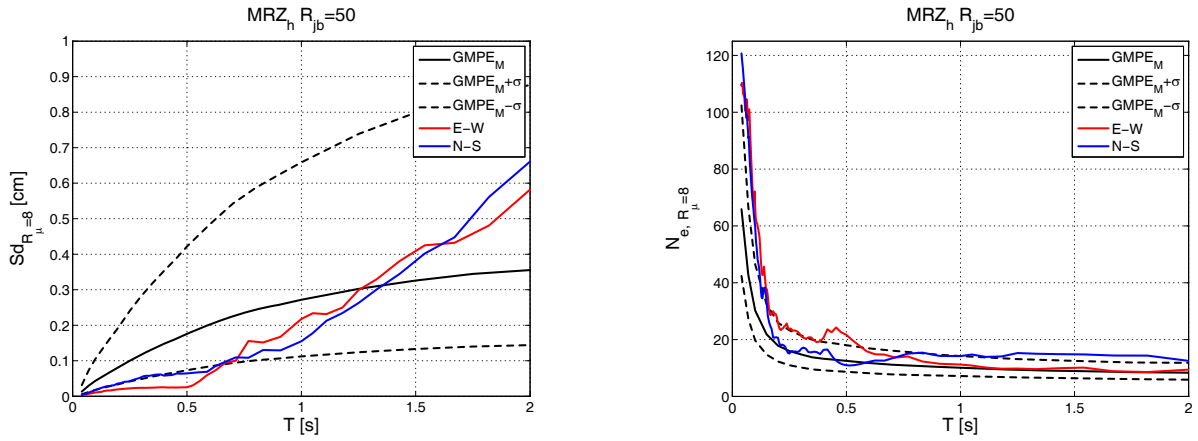

Figure 140. Comparison of the inelastic spectra in terms of displacements, $Sd_{R_\mu=i}$ (on the left) and equivalent number of cycles, $N_{e,R_\mu=i}$ (on the left) for R_μ equal to 8, for the horizontal components, at MRZ station with the median prediction and $\pm\sigma$ bands according to De Luca et al. 2012.

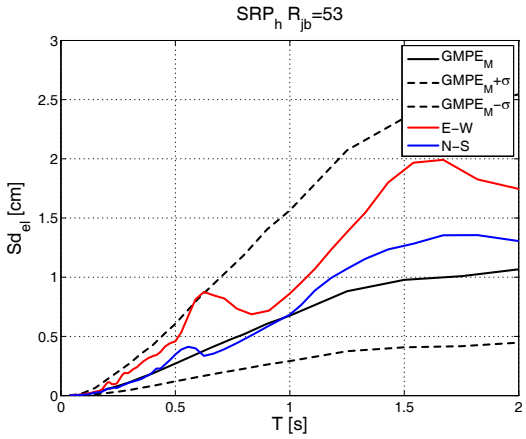

Figure 141. Comparison of the elastic displacement spectra for the horizontal components, Sd_{el}, at SRP station with the median prediction and $\pm\sigma$ bands according to De Luca et al. 2012.

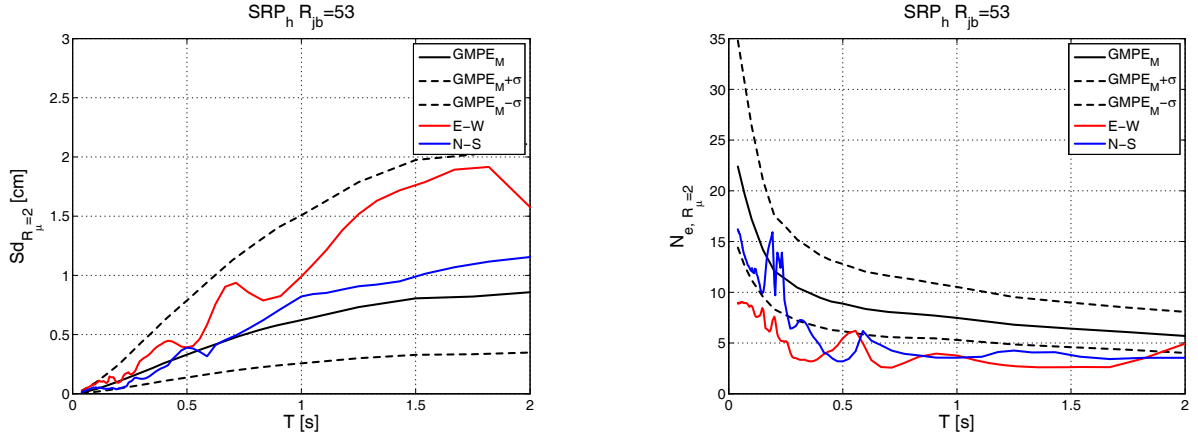

Figure 142. Comparison of the inelastic spectra in terms of displacements, $Sd_{R_\mu=i}$ (on the left) and equivalent number of cycles, $N_{e,R_\mu=i}$ (on the left) for R_μ equal to 2, for the horizontal components, at SRP station with the median prediction and $\pm\sigma$ bands according to De Luca et al. 2012.

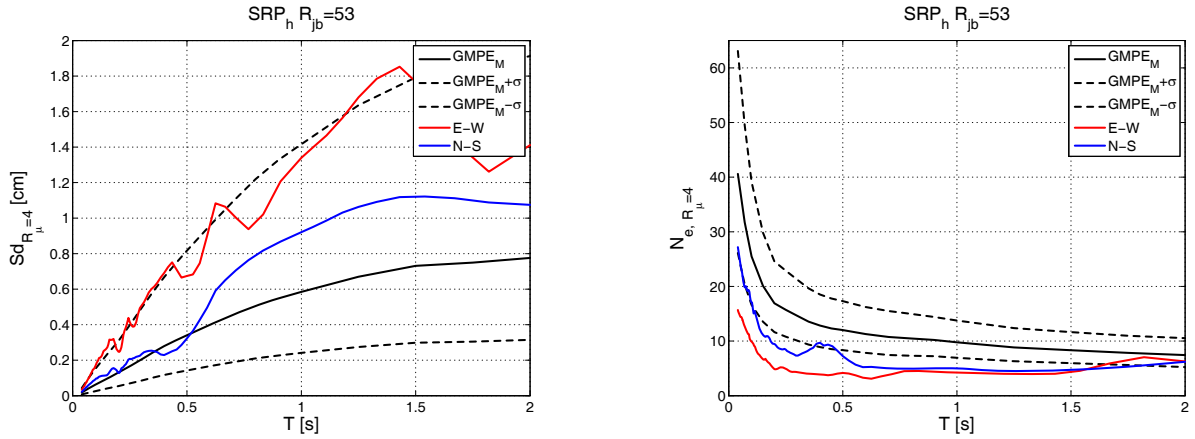

Figure 143. Comparison of the inelastic spectra in terms of displacements, $Sd_{R_\mu=i}$ (on the left) and equivalent number of cycles, $N_{e,R_\mu=i}$ (on the left) for R_μ equal to 4, for the horizontal components, at SRP station with the median prediction and $\pm\sigma$ bands according to De Luca et al. 2012.

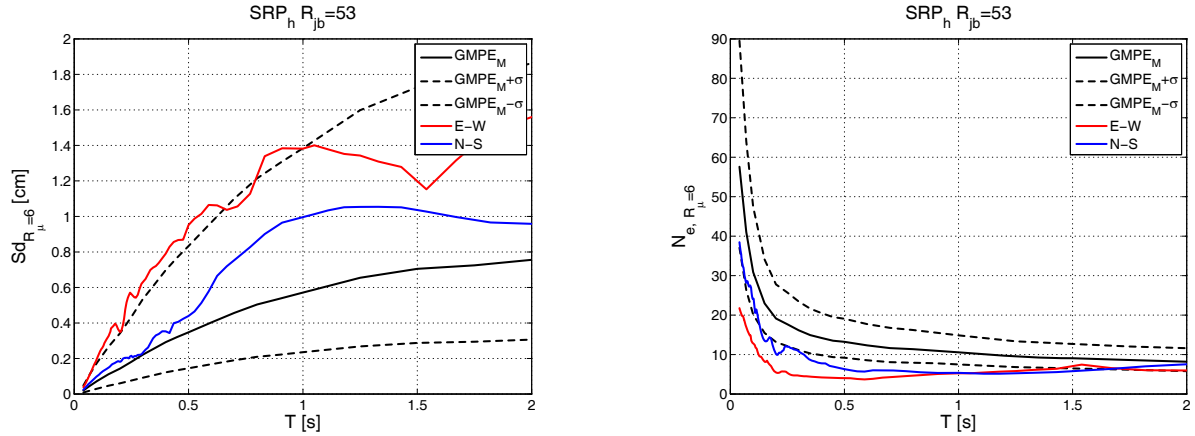

Figure 144. Comparison of the inelastic spectra in terms of displacements, $Sd_{R_\mu=i}$ (on the left) and equivalent number of cycles, $N_{e,R_\mu=i}$ (on the left) for R_μ equal to 6, for the horizontal components, at SRP station with the median prediction and $\pm\sigma$ bands according to De Luca et al. 2012.

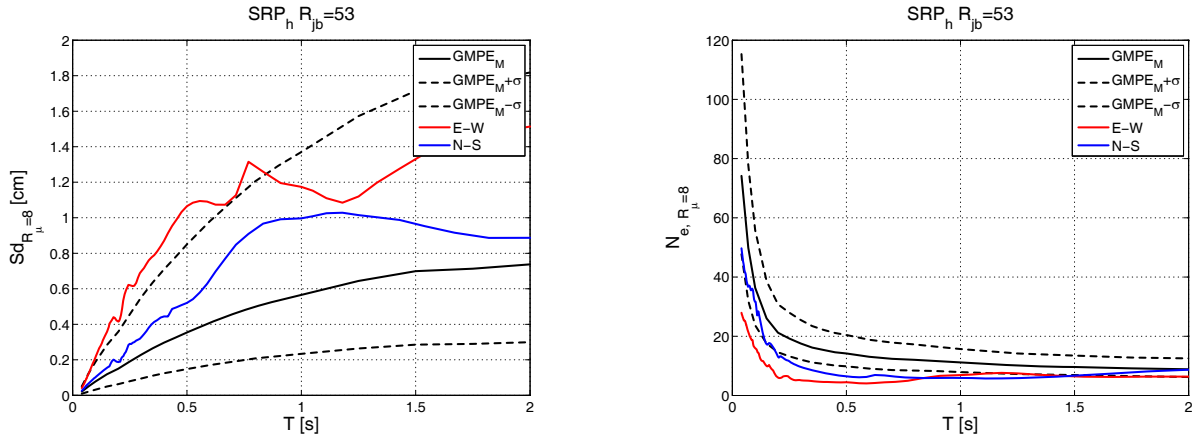

Figure 145. Comparison of the inelastic spectra in terms of displacements, $Sd_{R_\mu=i}$ (on the left) and equivalent number of cycles, $N_{e,R_\mu=i}$ (on the left) for R_μ equal to 8, for the horizontal components, at SRP station with the median prediction and $\pm\sigma$ bands according to De Luca et al. 2012.

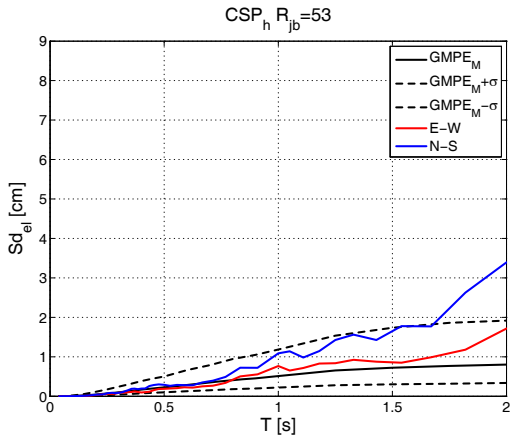

Figure 146. Comparison of the elastic displacement spectra for the horizontal components, Sd_{el}, at CSP station with the median prediction and $\pm\sigma$ bands according to De Luca et al. 2012.

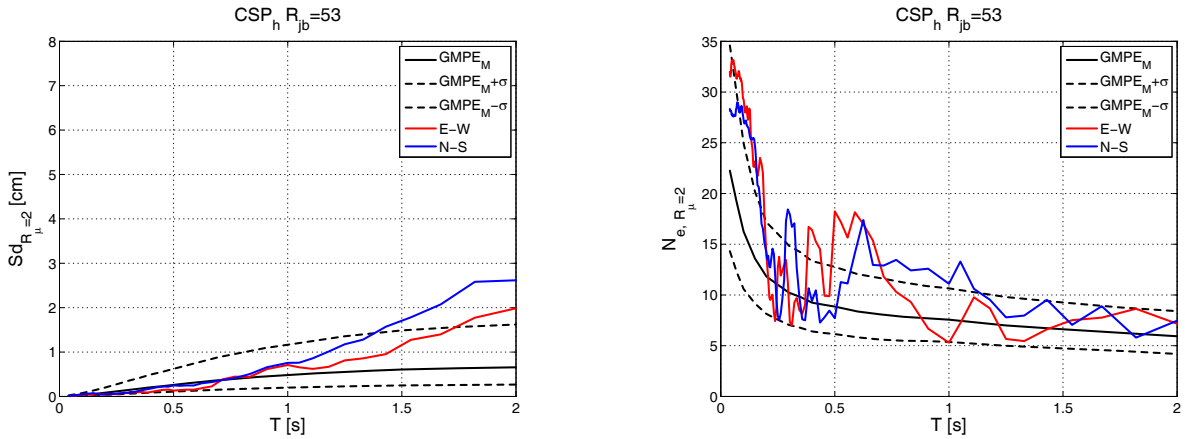

Figure 147. Comparison of the inelastic spectra in terms of displacements, $Sd_{R_\mu=i}$ (on the left) and equivalent number of cycles, $N_{e,R_\mu=i}$ (on the left) for R_μ equal to 2, for the horizontal components, at CSP station with the median prediction and $\pm\sigma$ bands according to De Luca et al. 2012.

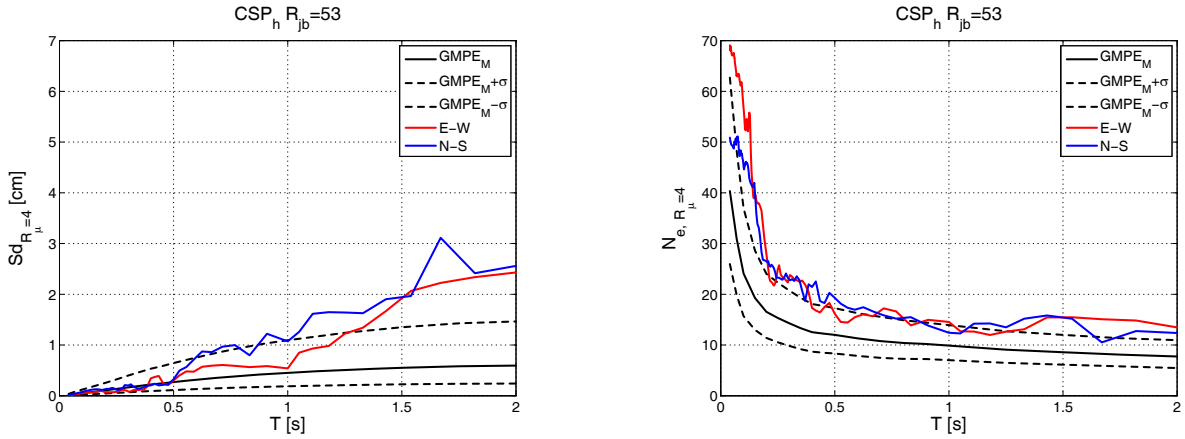

Figure 148. Comparison of the inelastic spectra in terms of displacements, $Sd_{R_\mu=i}$ (on the left) and equivalent number of cycles, $N_{e,R_\mu=i}$ (on the left) for R_μ equal to 4, for the horizontal components, at CSP station with the median prediction and $\pm\sigma$ bands according to De Luca et al. 2012.

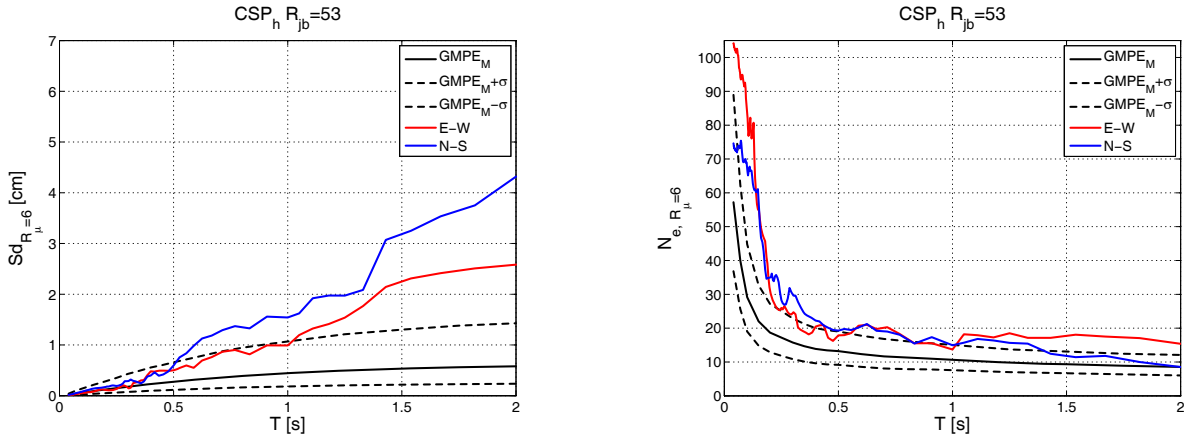

Figure 149. Comparison of the inelastic spectra in terms of displacements, $Sd_{R_\mu=i}$ (on the left) and equivalent number of cycles, $N_{e,R_\mu=i}$ (on the left) for R_μ equal to 6, for the horizontal components, at CSP station with the median prediction and $\pm\sigma$ bands according to De Luca et al. 2012.

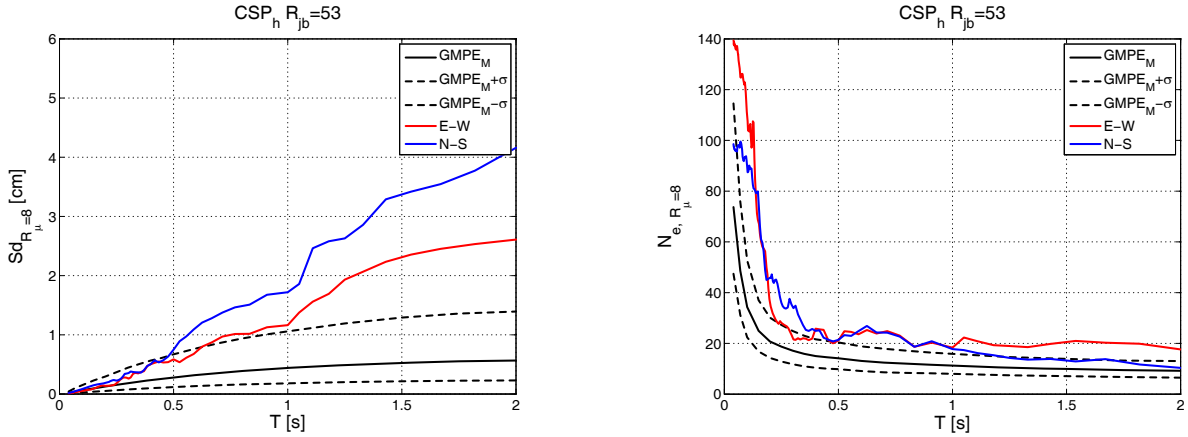

Figure 150. Comparison of the inelastic spectra in terms of displacements, $Sd_{R_\mu=i}$ (on the left) and equivalent number of cycles, $N_{e,R_\mu=i}$ (on the left) for R_μ equal to 8, for the horizontal components, at CSP station with the median prediction and $\pm\sigma$ bands according to De Luca et al. 2012.

12. Comparison of the data with De Luca et al (2012) inelastic GMPE predictions, Sd_{el}, Sd_{in} and N_E

In the following preliminary comparisons of the registered data with De Luca et al. (2012) GMPE median predictions and their $\pm\sigma$ bands (represented by the median plus and median minus one total standard deviation, $Median+\sigma$ and $Median-\sigma$, respectively) in terms of elastic displacements (Sd_{el}), inelastic displacements ($Sd_{R\mu=i}$) and equivalent number of cycles ($N_{e,\,R\mu=i}$) are provided for the geometric mean of the horizontal components of the registered signals. The predictions are made, preliminarily, for A soil class according to Eurocode 8 or EC8, (CEN, 2004), in analogy with the comparison shown in section 5.

$Sd_{R\mu=i}$ and $N_{e,\ R\mu=i}$ are evaluated on the same nonlinear SDOF employed in section 10 with strength reduction factor R_μ equal to 2, 4, 6, and 8.

In Figure 151 to 249, the geometrical mean of the horizontal component of the data and the median estimates $\pm\sigma$ of the prediction equations are shown for each period (T) and each value of R_μ considered. The geometric mean of the horizontal components of the registered data show a generally good agreement with the predictions. It is worth to note that the range of validity of the prediction equations is 0 - 200km; outside this range the prediction is extrapolated.

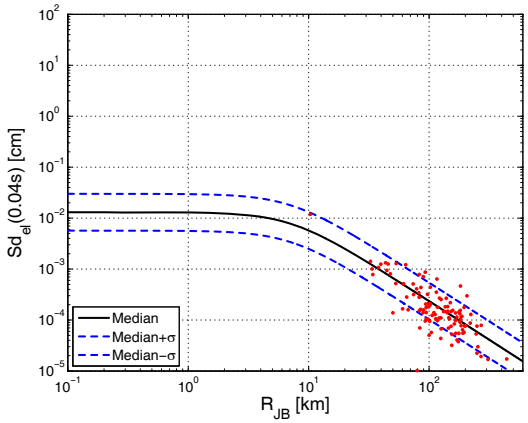

Figure 150. Comparison of the geometric mean of the horizontal components of Sd_{el} of the registered data with the median and $\pm\sigma$ predictions according to De Luca et al. (2012) for T=0.04.

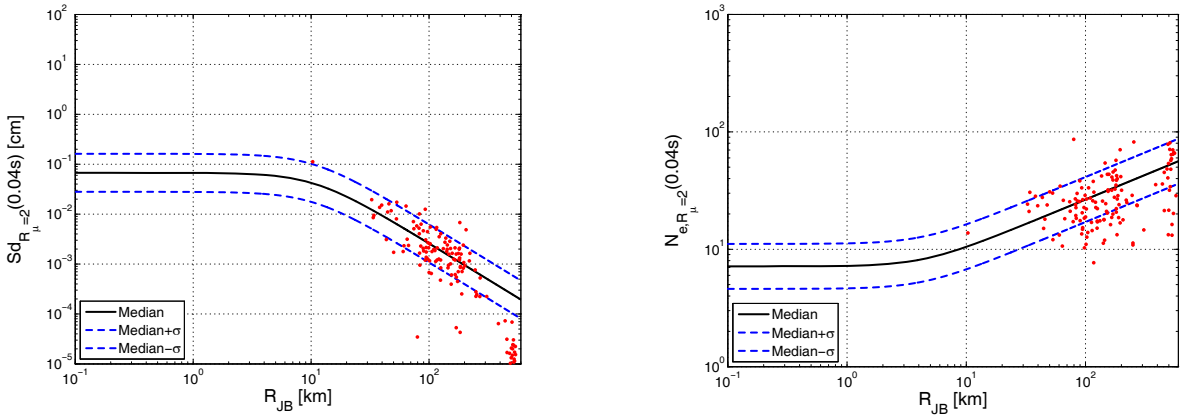

Figure 151. Comparison of the geometric mean of the horizontal components of $Sd_{R_\mu=i}$ on the left, and of $N_{e,\ R_\mu=i}$ on the right, of the registered data with the median and $\pm\sigma$ predictions according to De Luca et al. (2012) for T=0.04 and R_μ equal to 2.

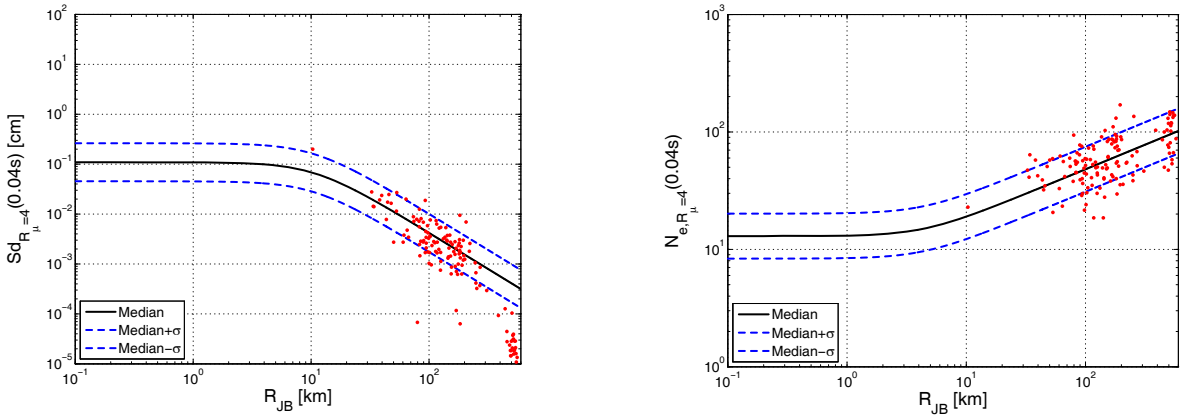

Figure 152. Comparison of the geometric mean of the horizontal components of $Sd_{R_\mu=i}$ on the left, and of $N_{e,\,R_\mu=i}$ on the right, of the registered data with the median and $\pm\sigma$ predictions according to De Luca et al. (2012) for T=0.04 and R_μ equal to 4.

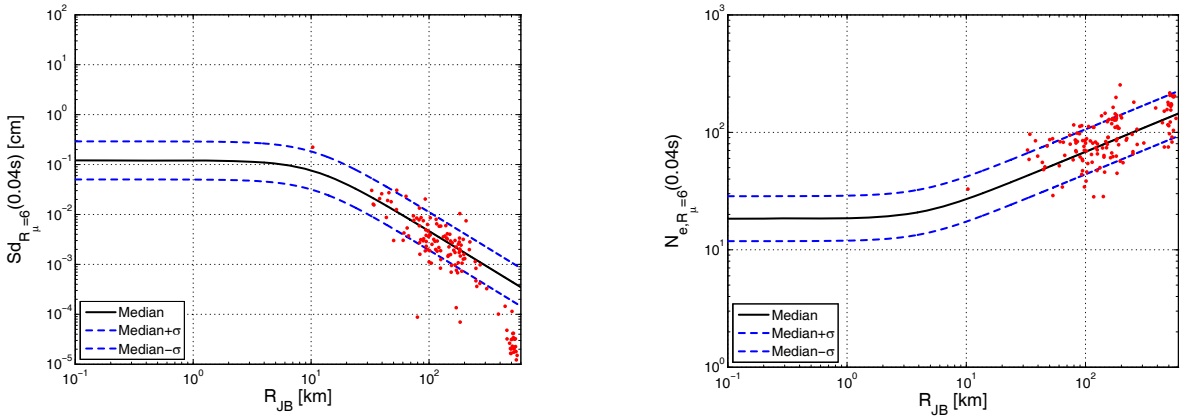

Figure 153. Comparison of the geometric mean of the horizontal components of $Sd_{R_\mu=i}$ on the left, and of $N_{e,\,R_\mu=i}$ on the right, of the registered data with the median and $\pm\sigma$ predictions according to De Luca et al. (2012) for T=0.04 and R_μ equal to 6.

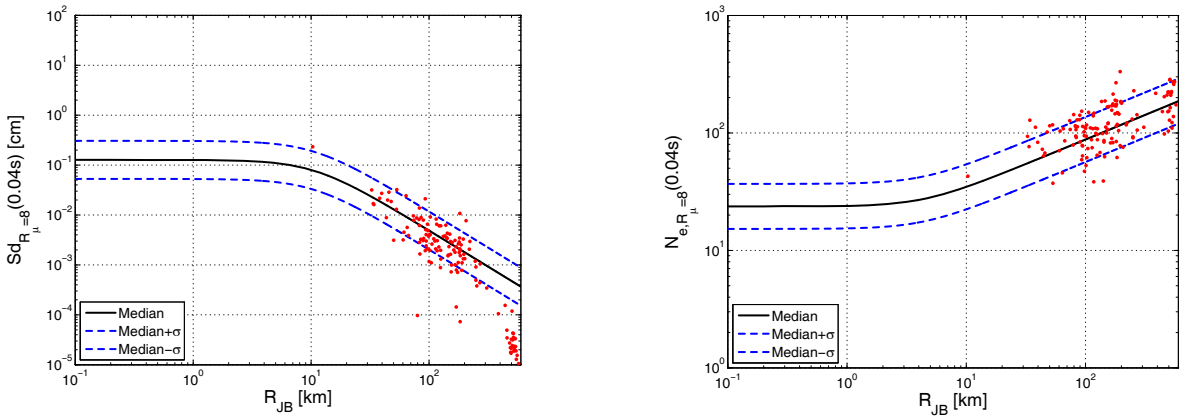

Figure 154. Comparison of the geometric mean of the horizontal components of $Sd_{R_\mu=i}$ on the left, and of $N_{e,\,R_\mu=i}$ on the right, of the registered data with the median and $\pm\sigma$ predictions according to De Luca et al. (2012) for T=0.04 and R_μ equal to 8.

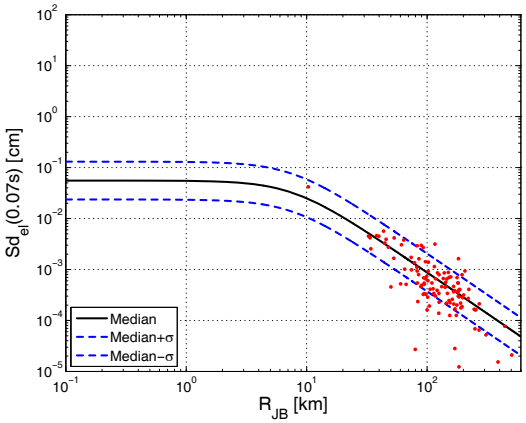

Figure 155. Comparison of the geometric mean of the horizontal components of Sd_{el} of the registered data with the median and $\pm\sigma$ predictions according to De Luca et al. (2012) for T=0.07.

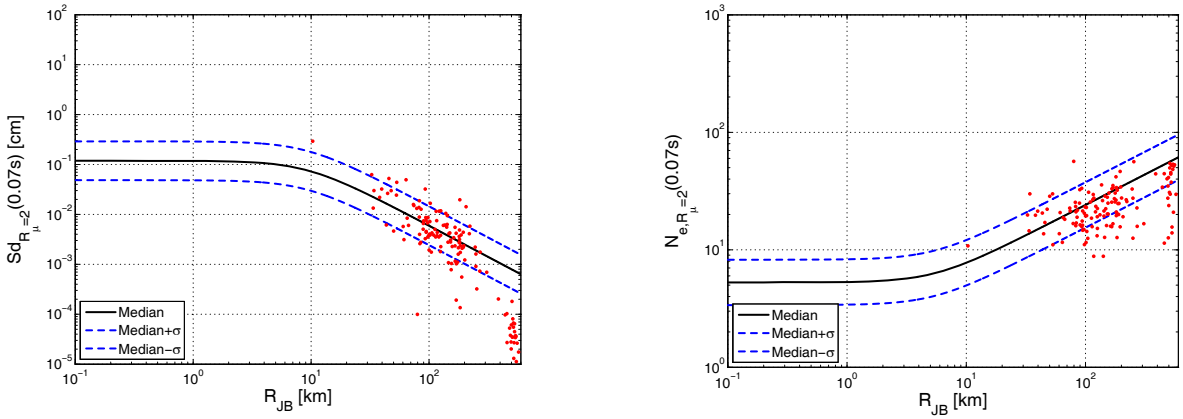

Figure 156. Comparison of the geometric mean of the horizontal components of $Sd_{R_\mu=i}$ on the left, and of $N_{e,\,R_\mu=i}$ on the right, of the registered data with the median and $\pm\sigma$ predictions according to De Luca et al. (2012) for T=0.07 and R_μ equal to 2.

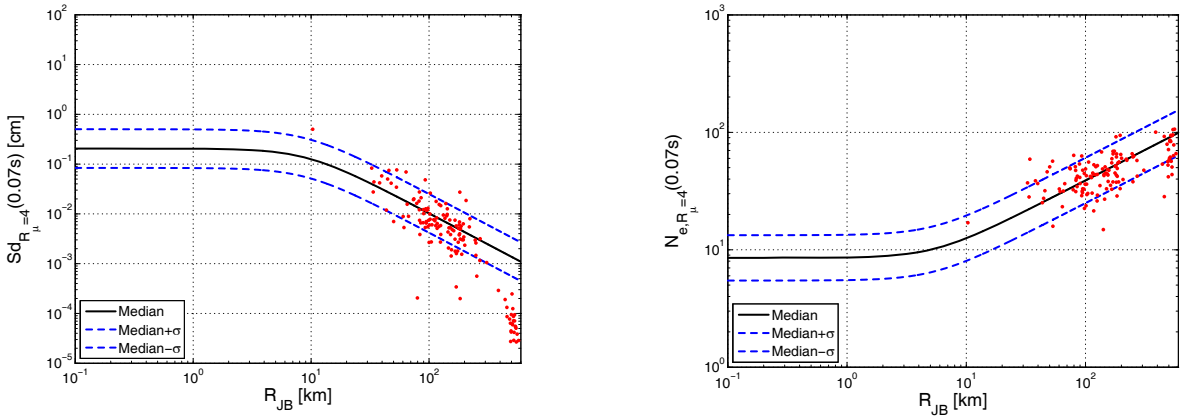

Figure 157. Comparison of the geometric mean of the horizontal components of $Sd_{R_\mu=i}$ on the left, and of $N_{e,\,R_\mu=i}$ on the right, of the registered data with the median and $\pm\sigma$ predictions according to De Luca et al. (2012) for T=0.07 and R_μ equal to 4.

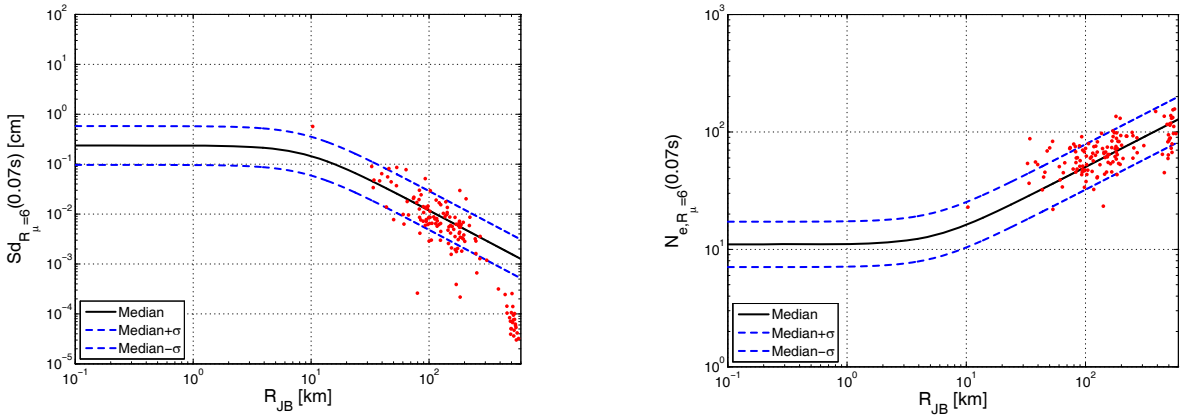

Figure 158. Comparison of the geometric mean of the horizontal components of $Sd_{R_\mu=i}$ on the left, and of $N_{e,\,R_\mu=i}$ on the right, of the registered data with the median and $\pm\sigma$ predictions according to De Luca et al. (2012) for T=0.07 and R_μ equal to 6.

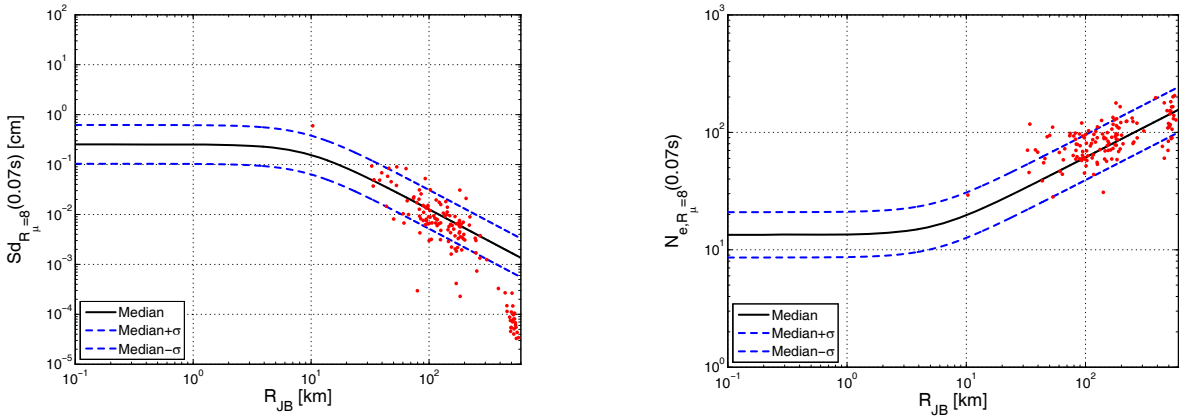

Figure 159. Comparison of the geometric mean of the horizontal components of $Sd_{R_\mu=i}$ on the left, and of $N_{e,\,R_\mu=i}$ on the right, of the registered data with the median and $\pm\sigma$ predictions according to De Luca et al. (2012) for T=0.07 and R_μ equal to 8.

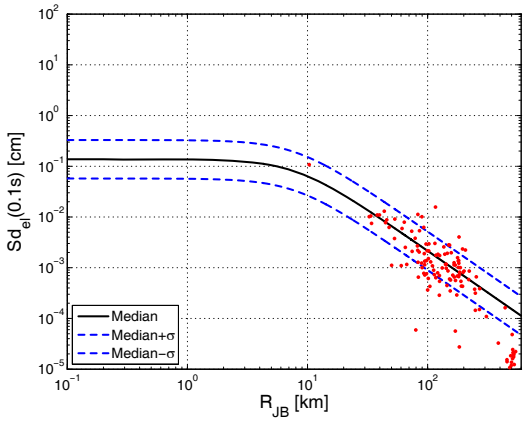

Figure 160. Comparison of the geometric mean of the horizontal components of Sd_{el} of the registered data with the median and $\pm\sigma$ predictions according to De Luca et al. (2012) for T=0.10.

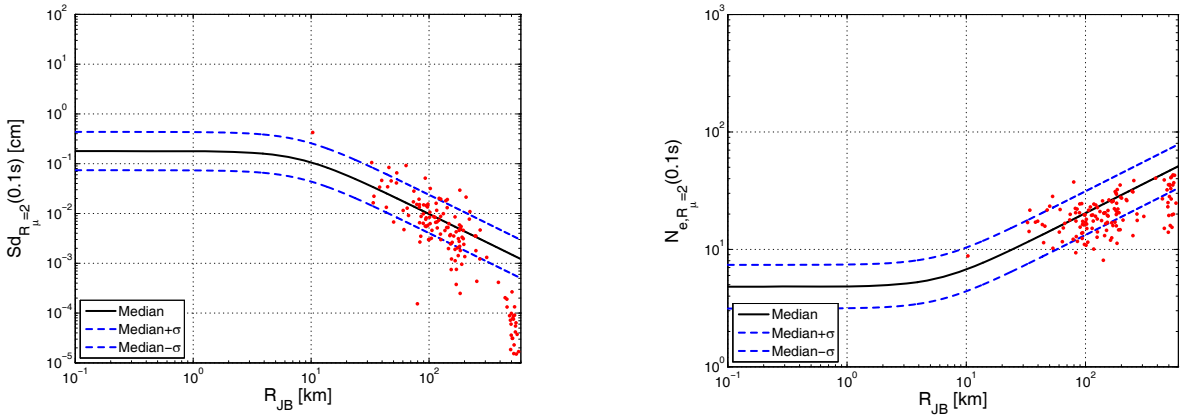

Figure 161. Comparison of the geometric mean of the horizontal components of $Sd_{R_\mu=i}$ on the left, and of $N_{e,\,R_\mu=i}$ on the right, of the registered data with the median and $\pm\sigma$ predictions according to De Luca et al. (2012) for T=0.10 and R_μ equal to 2.

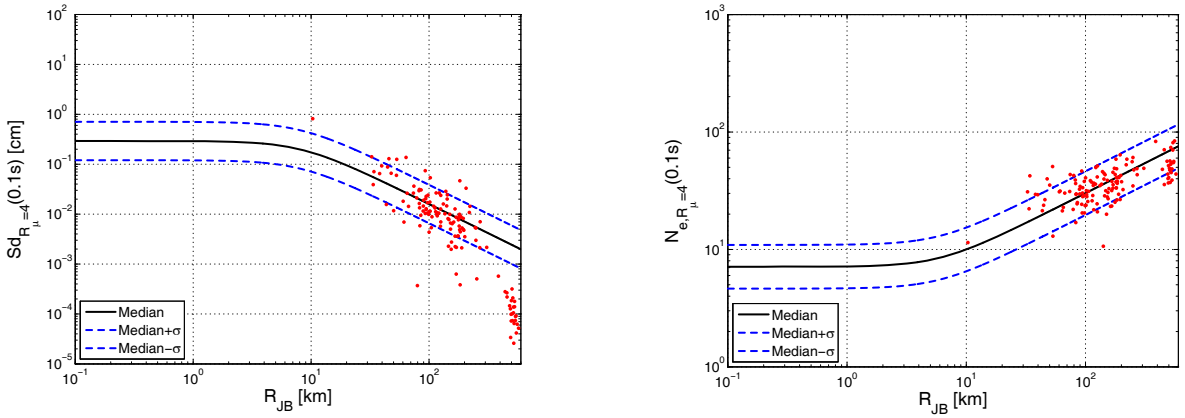

Figure 162. Comparison of the geometric mean of the horizontal components of $Sd_{R_\mu=i}$ on the left, and of $N_{e,\,R_\mu=i}$ on the right, of the registered data with the median and $\pm\sigma$ predictions according to De Luca et al. (2012) for T=0.10 and R_μ equal to 4.

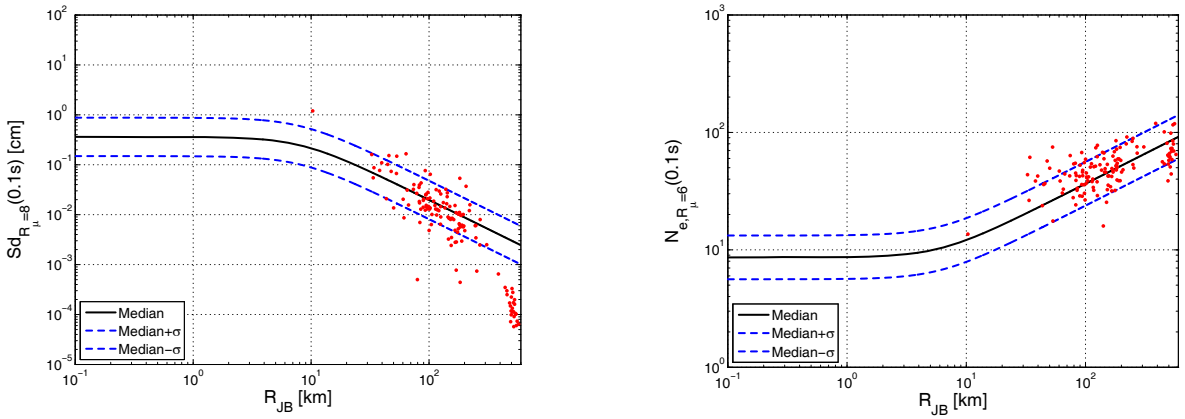

Figure 163. Comparison of the geometric mean of the horizontal components of $Sd_{R_\mu=i}$ on the left, and of $N_{e,\,R_\mu=i}$ on the right, of the registered data with the median and $\pm\sigma$ predictions according to De Luca et al. (2012) for T=0.10 and R_μ equal to 6.

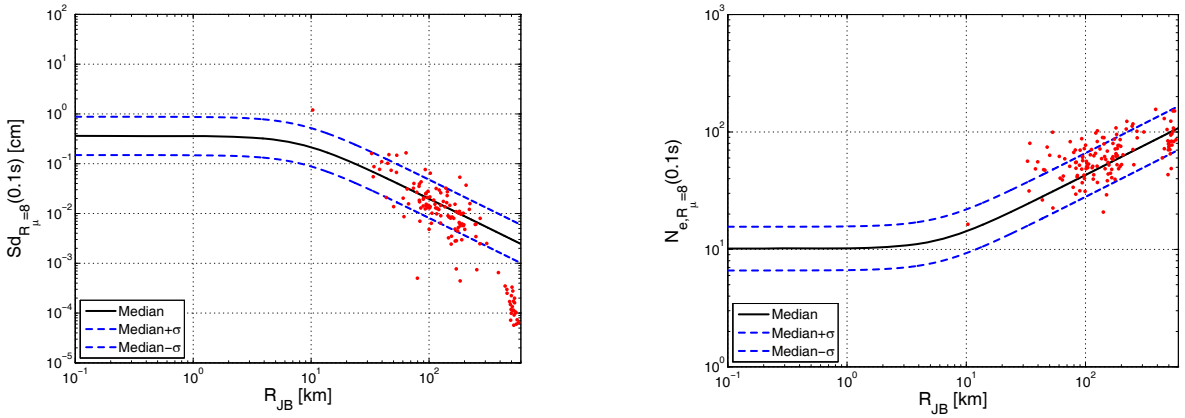

Figure 164. Comparison of the geometric mean of the horizontal components of $Sd_{R_\mu=i}$ on the left, and of $N_{e,R_\mu=i}$ on the right, of the registered data with the median and $\pm\sigma$ predictions according to De Luca et al. (2012) for T=0.10 and R_μ equal to 8.

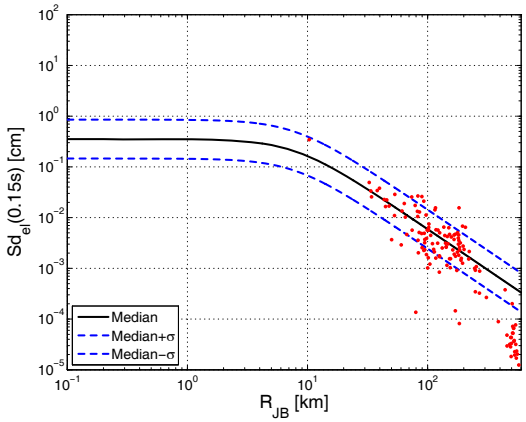

Figure 165. Comparison of the geometric mean of the horizontal components of Sd_{el} of the registered data with the median and $\pm\sigma$ predictions according to De Luca et al. (2012) for T=0.15.

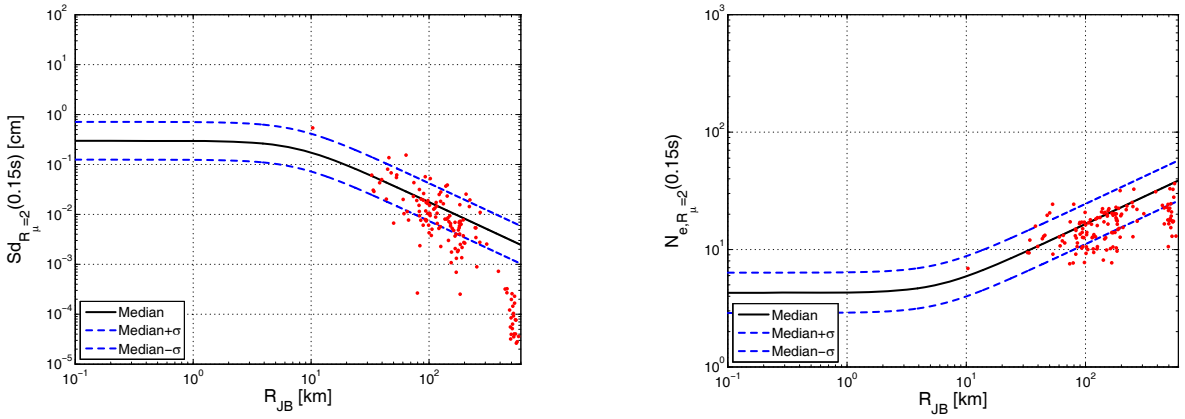

Figure 166. Comparison of the geometric mean of the horizontal components of $Sd_{R_\mu=i}$ on the left, and of $N_{e,R_\mu=i}$ on the right, of the registered data with the median and $\pm\sigma$ predictions according to De Luca et al. (2012) for T=0.15 and R_μ equal to 2.

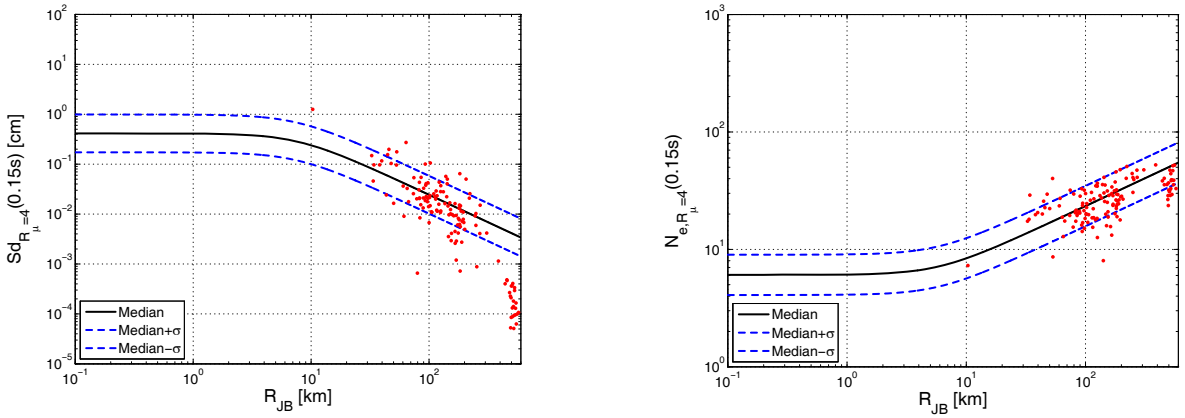

Figure 167. Comparison of the geometric mean of the horizontal components of $Sd_{R_\mu=i}$ on the left, and of $N_{e,\,R_\mu=i}$ on the right, of the registered data with the median and $\pm\sigma$ predictions according to De Luca et al. (2012) for T=0.15 and R_μ equal to 4.

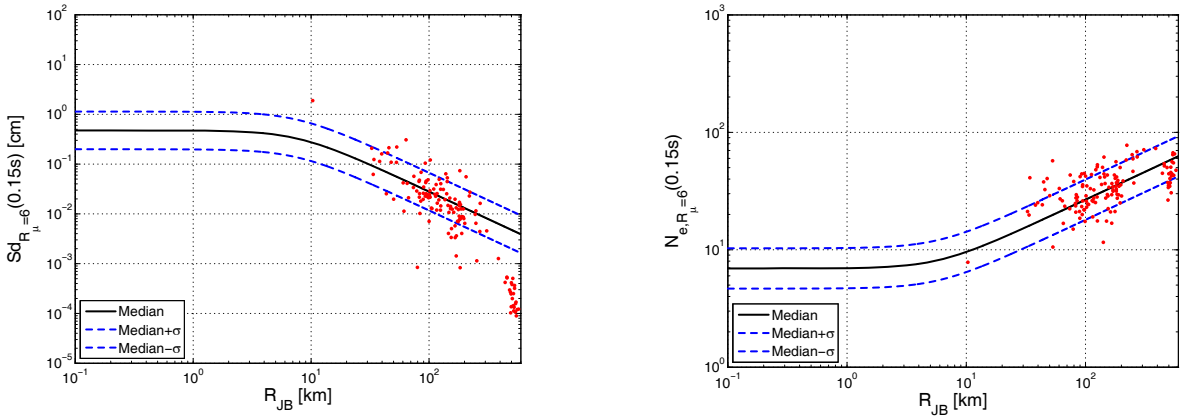

Figure 168. Comparison of the geometric mean of the horizontal components of $Sd_{R_\mu=i}$ on the left, and of $N_{e,\,R_\mu=i}$ on the right, of the registered data with the median and $\pm\sigma$ predictions according to De Luca et al. (2012) for T=0.15 and R_μ equal to 6.

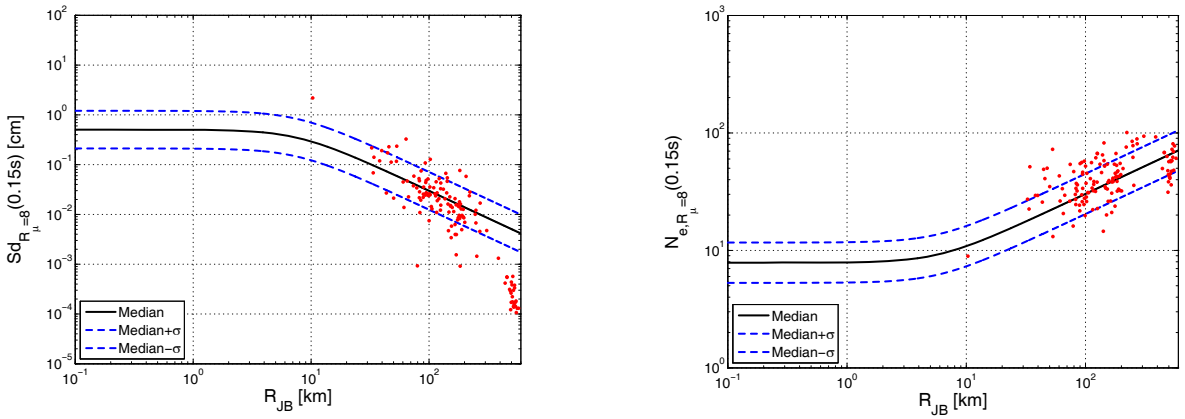

Figure 169. Comparison of the geometric mean of the horizontal components of $Sd_{R_\mu=i}$ on the left, and of $N_{e,\,R_\mu=i}$ on the right, of the registered data with the median and $\pm\sigma$ predictions according to De Luca et al. (2012) for T=0.15 and R_μ equal to 8.

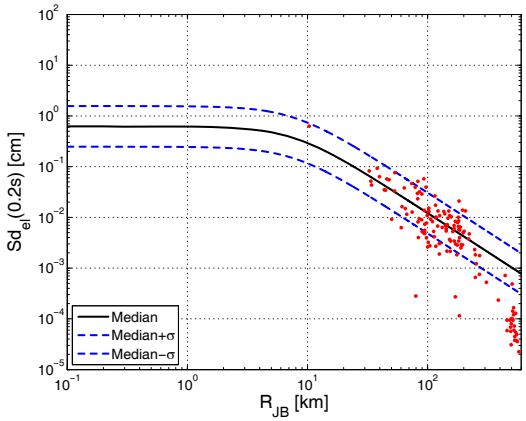

Figure 170. Comparison of the geometric mean of the horizontal components of Sd_{el} of the registered data with the median and $\pm\sigma$ predictions according to De Luca et al. (2012) for T=0.20.

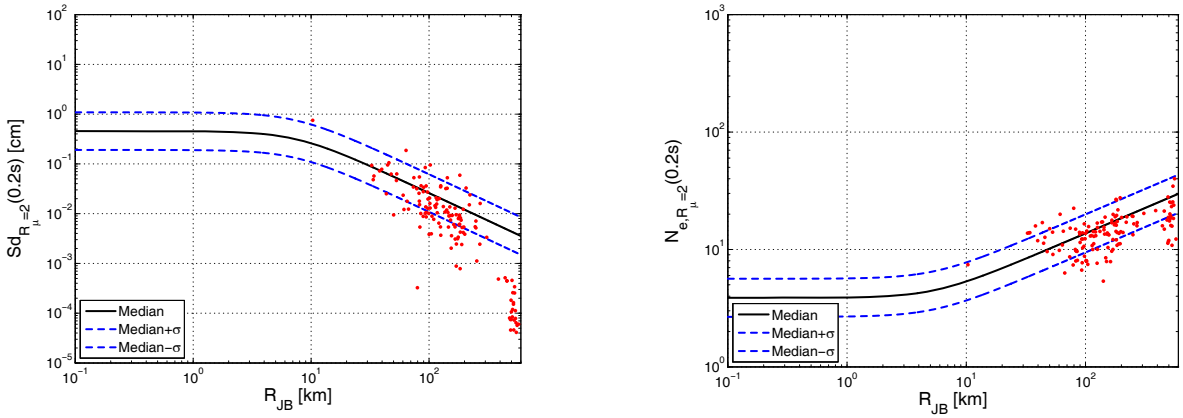

Figure 171. Comparison of the geometric mean of the horizontal components of $Sd_{R_\mu=i}$ on the left, and of $N_{e,\,R_\mu=i}$ on the right, of the registered data with the median and $\pm\sigma$ predictions according to De Luca et al. (2012) for T=0.20 and R_μ equal to 2.

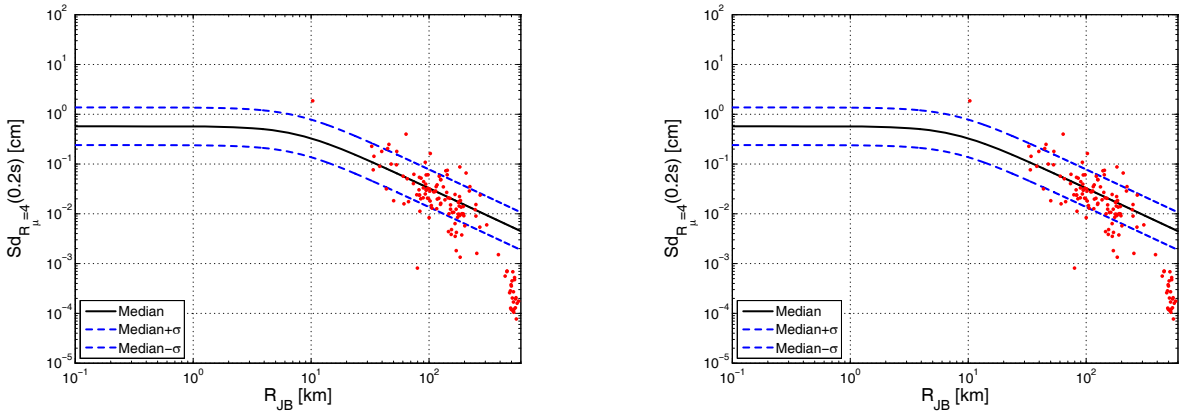

Figure 172. Comparison of the geometric mean of the horizontal components of $Sd_{R_\mu=i}$ on the left, and of $N_{e,\,R_\mu=i}$ on the right, of the registered data with the median and $\pm\sigma$ predictions according to De Luca et al. (2012) for T=0.20 and R_μ equal to 4.

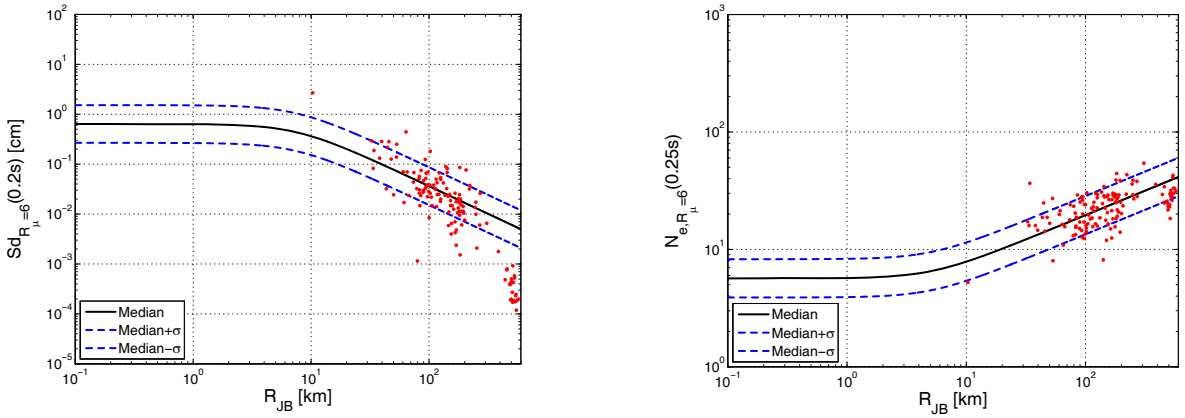

Figure 173. Comparison of the geometric mean of the horizontal components of $Sd_{R_\mu=i}$ on the left, and of $N_{e,\,R_\mu=i}$ on the right, of the registered data with the median and $\pm\sigma$ predictions according to De Luca et al. (2012) for T=0.20 and R_μ equal to 6.

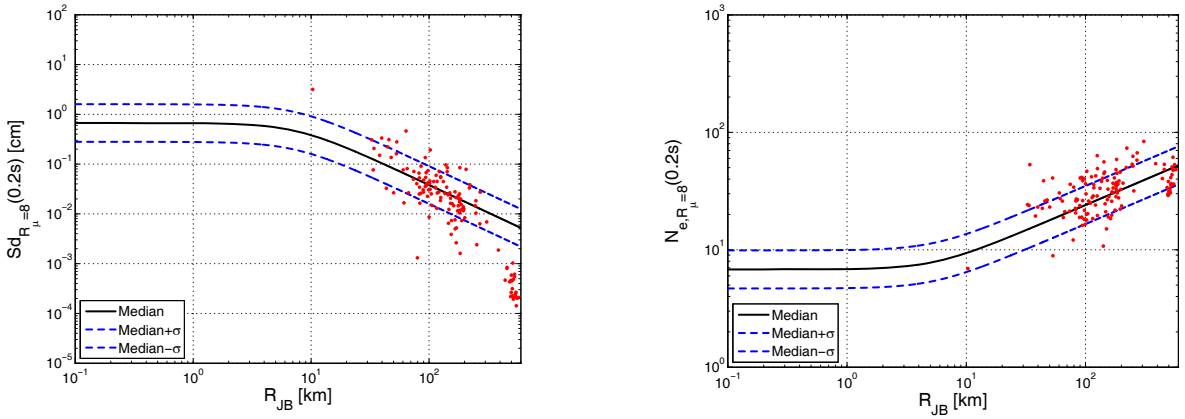

Figure 174. Comparison of the geometric mean of the horizontal components of $Sd_{R_\mu=i}$ on the left, and of $N_{e,\,R_\mu=i}$ on the right, of the registered data with the median and $\pm\sigma$ predictions according to De Luca et al. (2012) for T=0.20 and R_μ equal to 8.

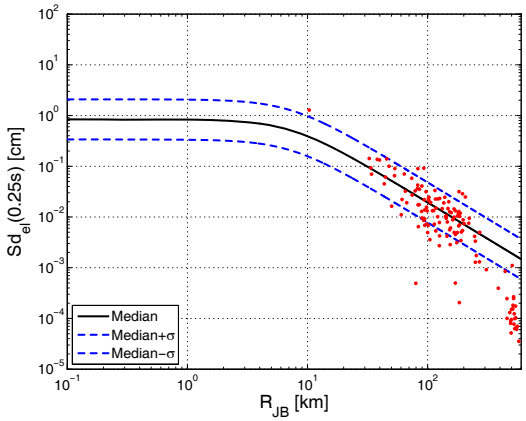

Figure 175. Comparison of the geometric mean of the horizontal components of Sd_{el} of the registered data with the median and $\pm\sigma$ predictions according to De Luca et al. (2012) for T=0.25.

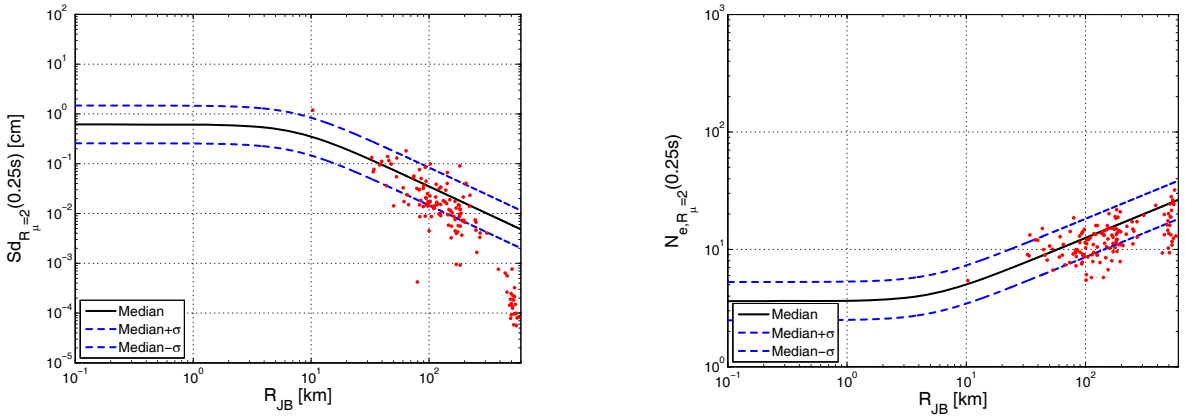

Figure 176. Comparison of the geometric mean of the horizontal components of $Sd_{R_\mu=i}$ on the left, and of $N_{e,\,R_\mu=i}$ on the right, of the registered data with the median and $\pm\sigma$ predictions according to De Luca et al. (2012) for T=0.25 and R_μ equal to 2.

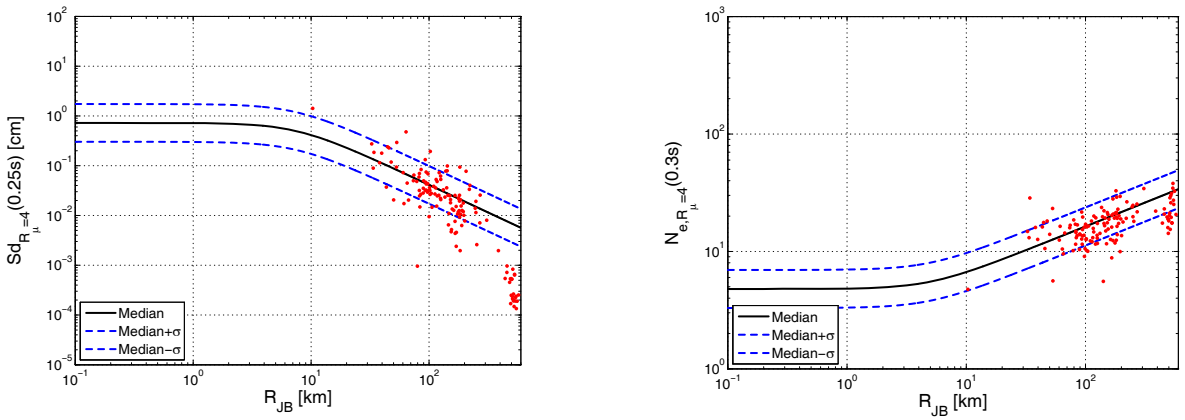

Figure 177. Comparison of the geometric mean of the horizontal components of $Sd_{R_\mu=i}$ on the left, and of $N_{e,\,R_\mu=i}$ on the right, of the registered data with the median and $\pm\sigma$ predictions according to De Luca et al. (2012) for T=0.25 and R_μ equal to 4.

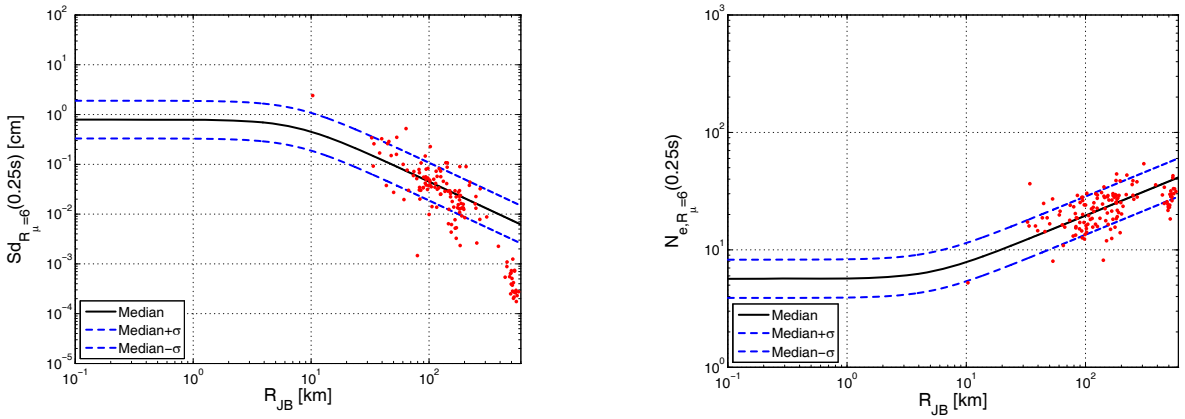

Figure 178. Comparison of the geometric mean of the horizontal components of $Sd_{R_\mu=i}$ on the left, and of $N_{e,\,R_\mu=i}$ on the right, of the registered data with the median and $\pm\sigma$ predictions according to De Luca et al. (2012) for T=0.25 and R_μ equal to 6.

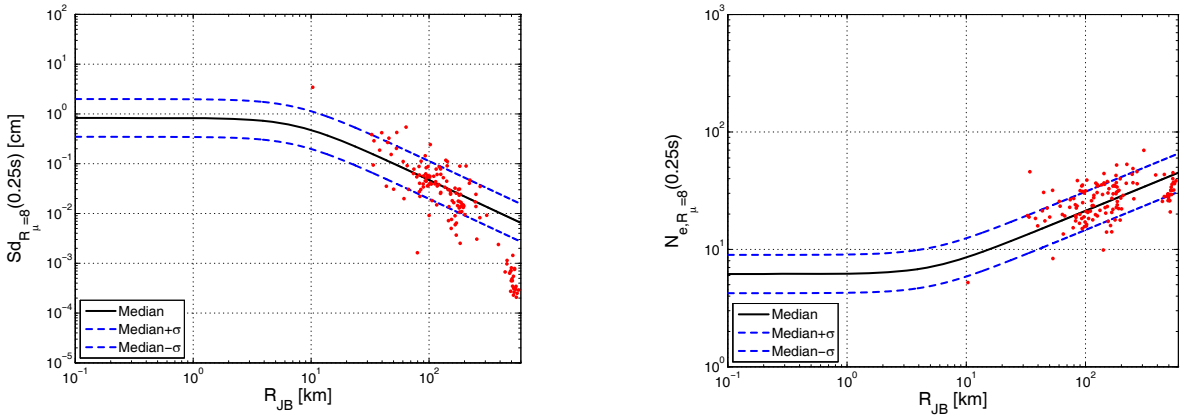

Figure 179. Comparison of the geometric mean of the horizontal components of $Sd_{R_\mu=i}$ on the left, and of $N_{e,\,R_\mu=i}$ on the right, of the registered data with the median and $\pm\sigma$ predictions according to De Luca et al. (2012) for T=0.25 and R_μ equal to 8.

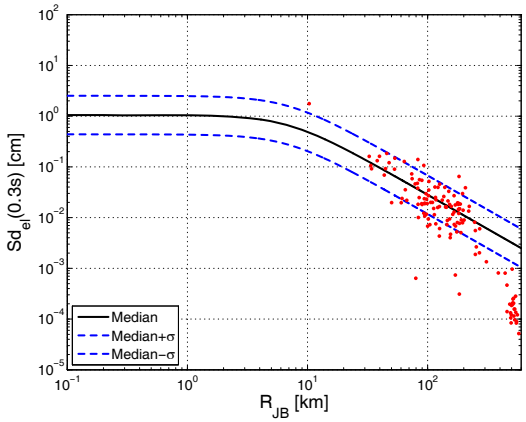

Figure 180. Comparison of the geometric mean of the horizontal components of Sd_{el} of the registered data with the median and $\pm\sigma$ predictions according to De Luca et al. (2012) for T=0.30.

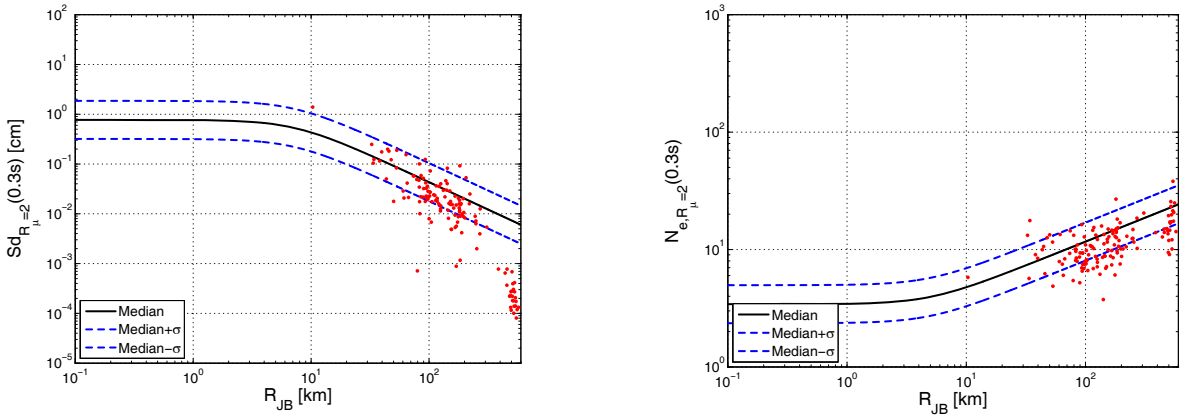

Figure 181. Comparison of the geometric mean of the horizontal components of $Sd_{R_\mu=i}$ on the left, and of $N_{e,\,R_\mu=i}$ on the right, of the registered data with the median and $\pm\sigma$ predictions according to De Luca et al. (2012) for T=0.30 and R_μ equal to 2.

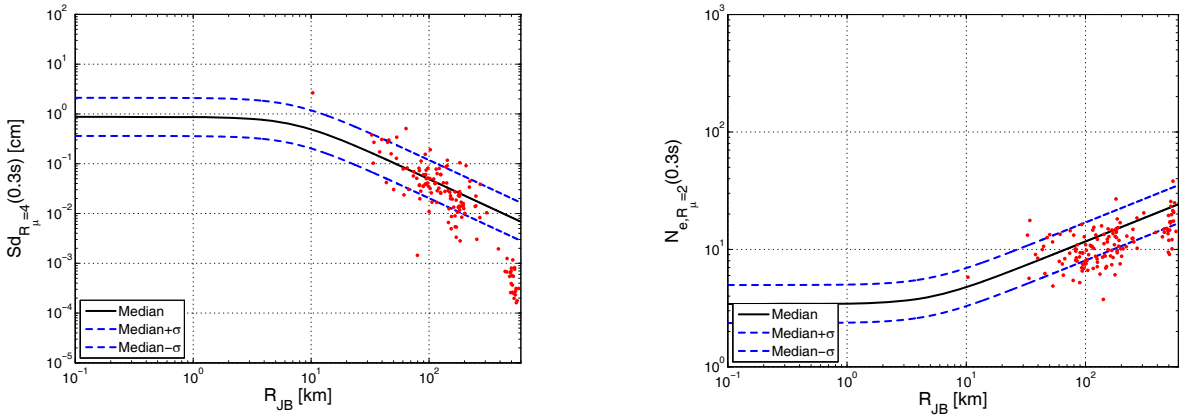

Figure 182. Comparison of the geometric mean of the horizontal components of $Sd_{R_\mu=i}$ on the left, and of $N_{e,\,R_\mu=i}$ on the right, of the registered data with the median and $\pm\sigma$ predictions according to De Luca et al. (2012) for T=0.30 and R_μ equal to 4.

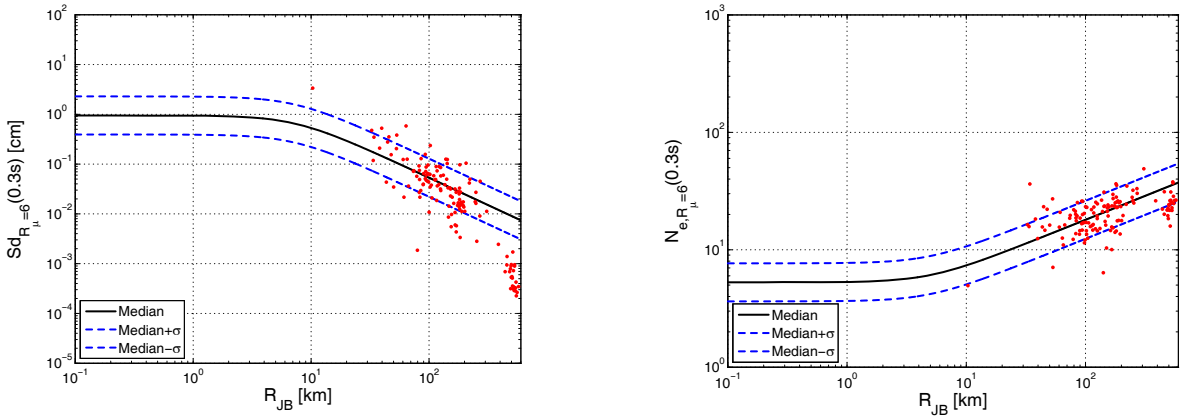

Figure 183. Comparison of the geometric mean of the horizontal components of $Sd_{R_\mu=i}$ on the left, and of $N_{e,\,R_\mu=i}$ on the right, of the registered data with the median and $\pm\sigma$ predictions according to De Luca et al. (2012) for T=0.30 and R_μ equal to 6.

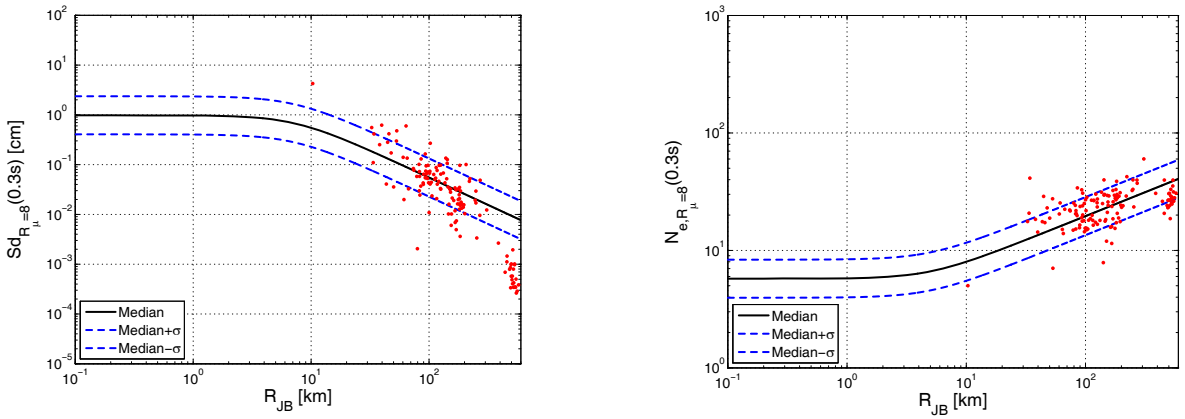

Figure 184. Comparison of the geometric mean of the horizontal components of $Sd_{R_\mu=i}$ on the left, and of $N_{e,\,R_\mu=i}$ on the right, of the registered data with the median and $\pm\sigma$ predictions according to De Luca et al. (2012) for T=0.30 and R_μ equal to 8.

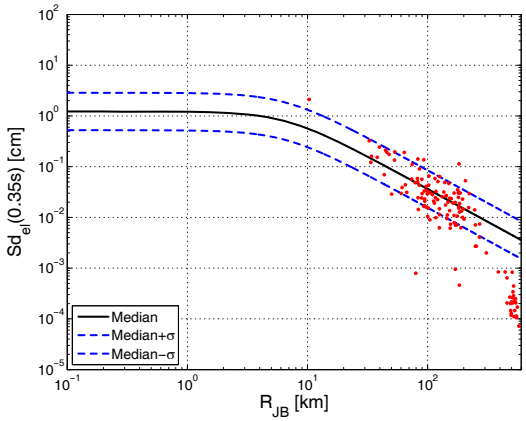

Figure 185. Comparison of the geometric mean of the horizontal components of Sd_{el} of the registered data with the median and $\pm\sigma$ predictions according to De Luca et al. (2012) for T=0.35.

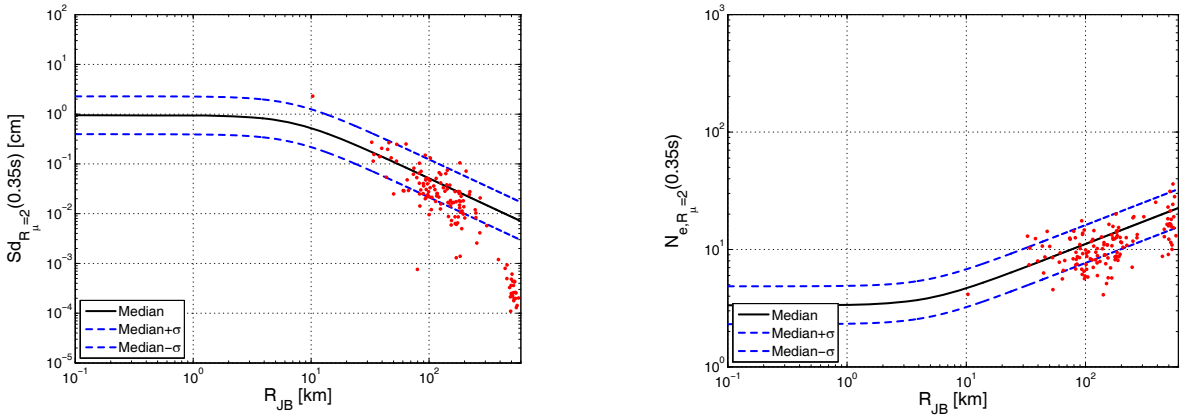

Figure 186. Comparison of the geometric mean of the horizontal components of $Sd_{R_\mu=i}$ on the left, and of $N_{e,\,R_\mu=i}$ on the right, of the registered data with the median and $\pm\sigma$ predictions according to De Luca et al. (2012) for T=0.35 and R_μ equal to 2.

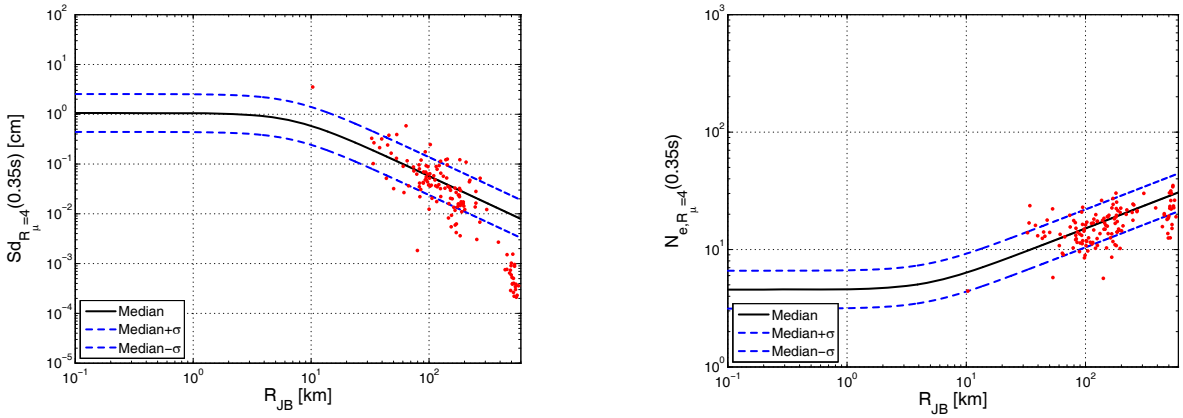

Figure 187. Comparison of the geometric mean of the horizontal components of $Sd_{R_\mu=i}$ on the left, and of $N_{e,\,R_\mu=i}$ on the right, of the registered data with the median and $\pm\sigma$ predictions according to De Luca et al. (2012) for T=0.35 and R_μ equal to 4.

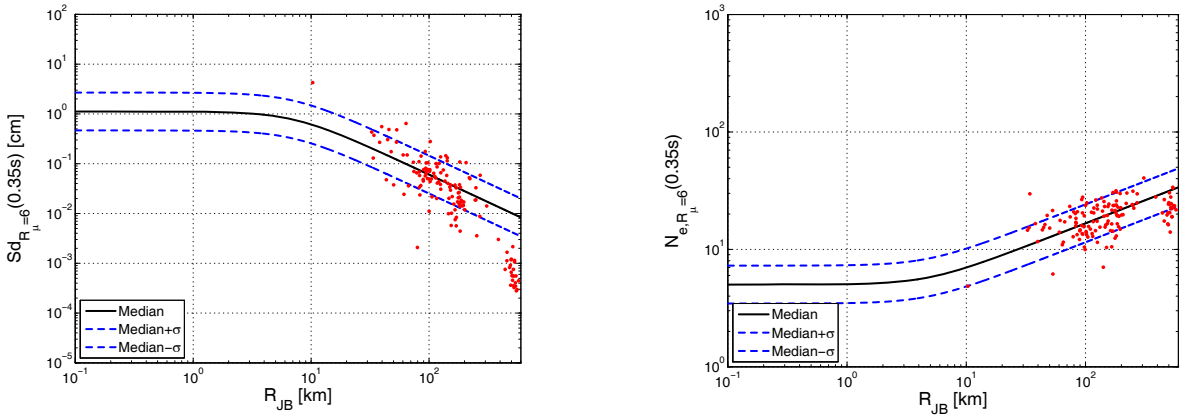

Figure 188. Comparison of the geometric mean of the horizontal components of $Sd_{R_\mu=i}$ on the left, and of $N_{e,\,R_\mu=i}$ on the right, of the registered data with the median and $\pm\sigma$ predictions according to De Luca et al. (2012) for T=0.35 and R_μ equal to 6.

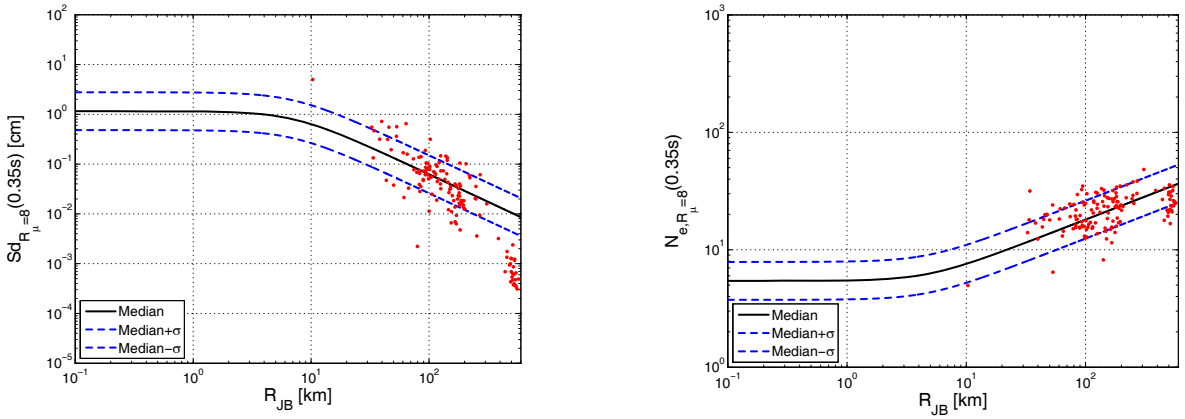

Figure 189. Comparison of the geometric mean of the horizontal components of $Sd_{R_\mu=i}$ on the left, and of $N_{e,\,R_\mu=i}$ on the right, of the registered data with the median and $\pm\sigma$ predictions according to De Luca et al. (2012) for T=0.35 and R_μ equal to 8.

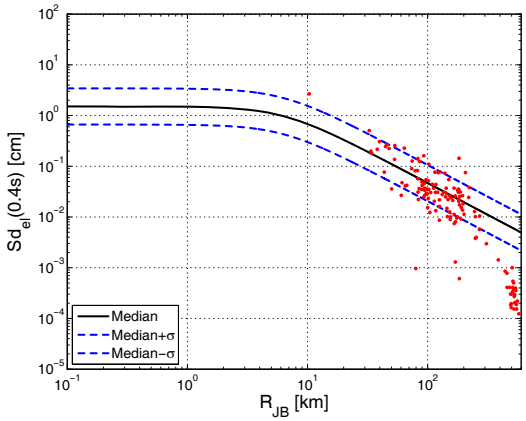

Figure 190. Comparison of the geometric mean of the horizontal components of Sd_{el} of the registered data with the median and $\pm\sigma$ predictions according to De Luca et al. (2012) for T=0.40.

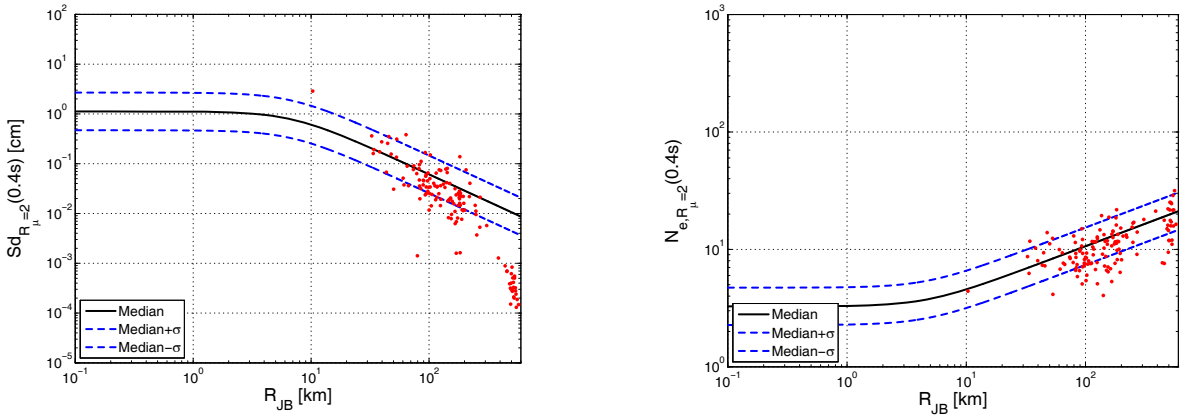

Figure 191. Comparison of the geometric mean of the horizontal components of $Sd_{R_\mu=i}$ on the left, and of $N_{e,\,R_\mu=i}$ on the right, of the registered data with the median and $\pm\sigma$ predictions according to De Luca et al. (2012) for T=0.40 and R_μ equal to 2.

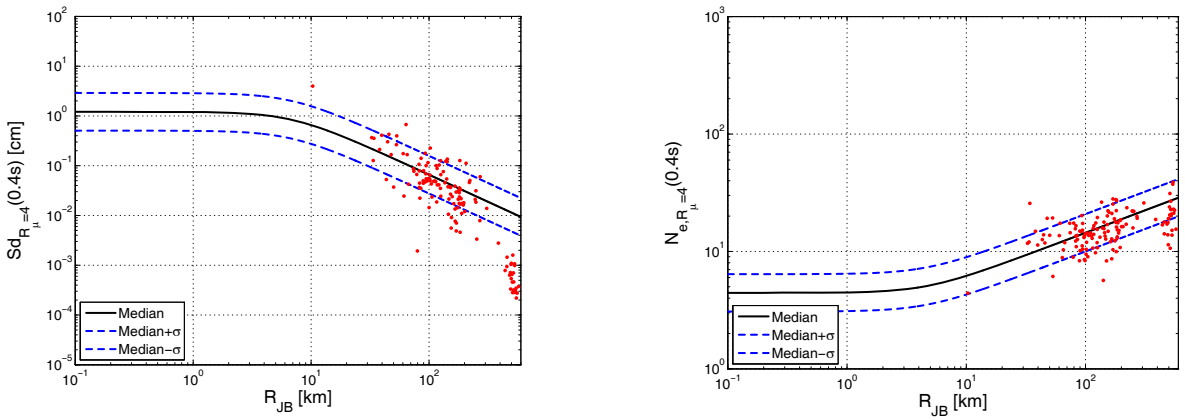

Figure 192. Comparison of the geometric mean of the horizontal components of $Sd_{R_\mu=i}$ on the left, and of $N_{e,\,R_\mu=i}$ on the right, of the registered data with the median and $\pm\sigma$ predictions according to De Luca et al. (2012) for T=0.40 and R_μ equal to 4.

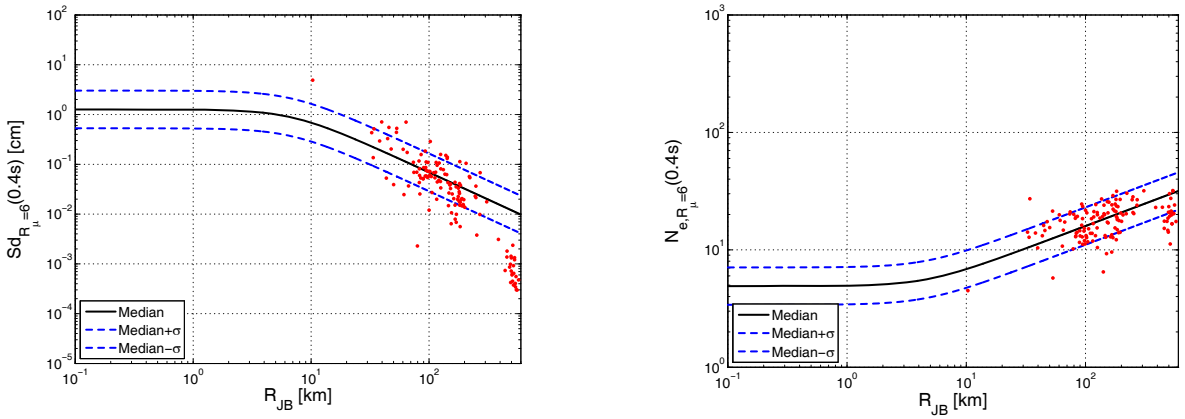

Figure 193. Comparison of the geometric mean of the horizontal components of $Sd_{R_\mu=i}$ on the left, and of $N_{e,\,R_\mu=i}$ on the right, of the registered data with the median and $\pm\sigma$ predictions according to De Luca et al. (2012) for T=0.40 and R_μ equal to 6.

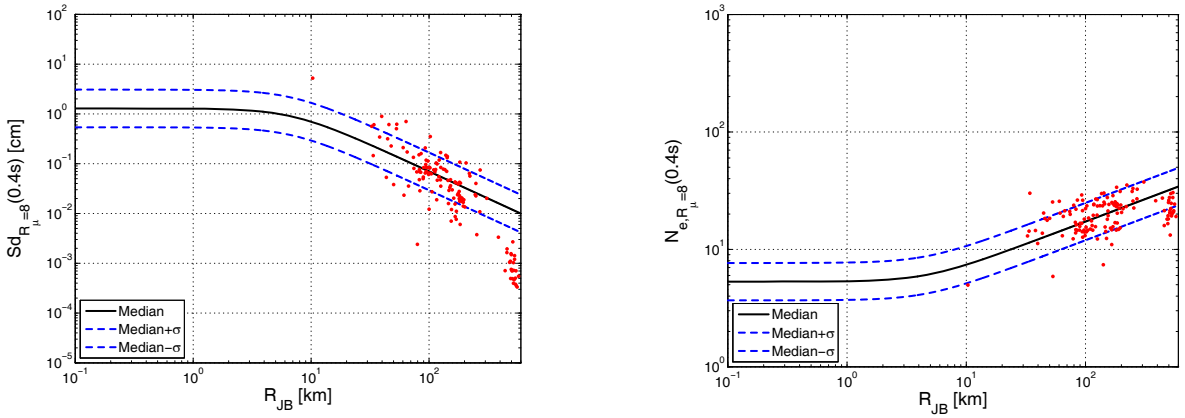

Figure 194. Comparison of the geometric mean of the horizontal components of $Sd_{R_\mu=i}$ on the left, and of $N_{e,\,R_\mu=i}$ on the right, of the registered data with the median and $\pm\sigma$ predictions according to De Luca et al. (2012) for T=0.40 and R_μ equal to 8.

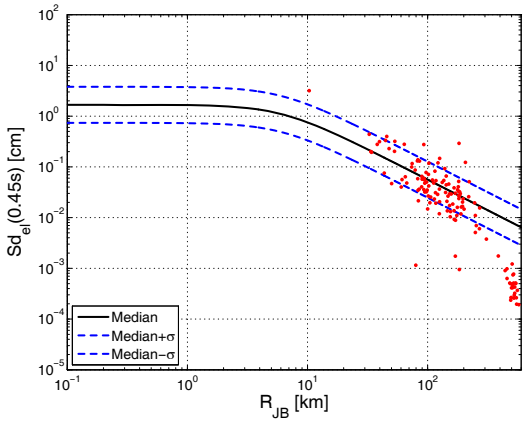

Figure 195. Comparison of the geometric mean of the horizontal components of Sd_{el} of the registered data with the median and $\pm\sigma$ predictions according to De Luca et al. (2012) for T=0.45.

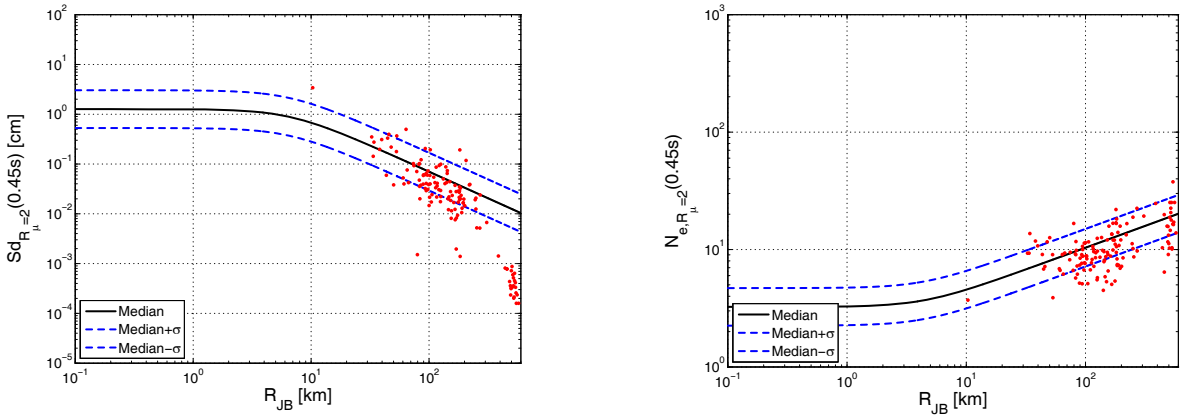

Figure 196. Comparison of the geometric mean of the horizontal components of $Sd_{R_\mu=i}$ on the left, and of $N_{e,\,R_\mu=i}$ on the right, of the registered data with the median and $\pm\sigma$ predictions according to De Luca et al. (2012) for T=0.45 and R_μ equal to 2.

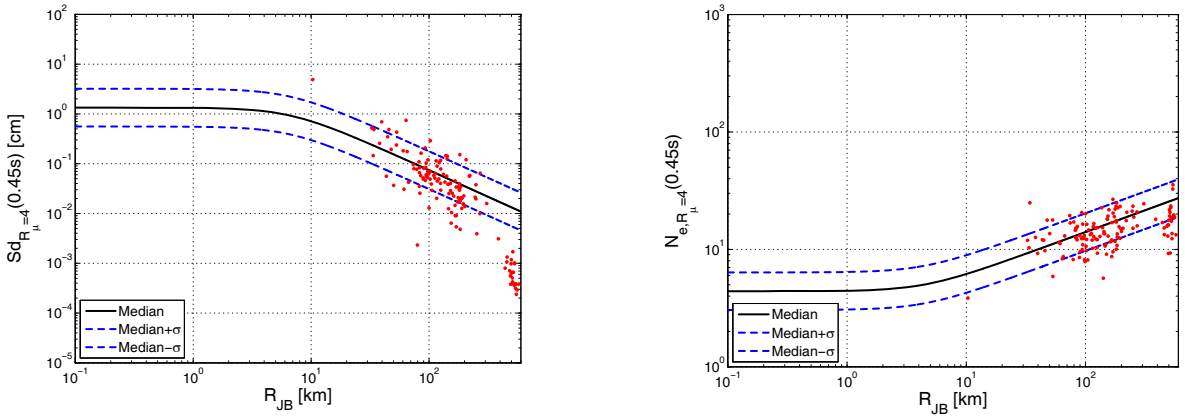

Figure 197. Comparison of the geometric mean of the horizontal components of $Sd_{R_\mu=i}$ on the left, and of $N_{e,\,R_\mu=i}$ on the right, of the registered data with the median and $\pm\sigma$ predictions according to De Luca et al. (2012) for T=0.45 and R_μ equal to 4.

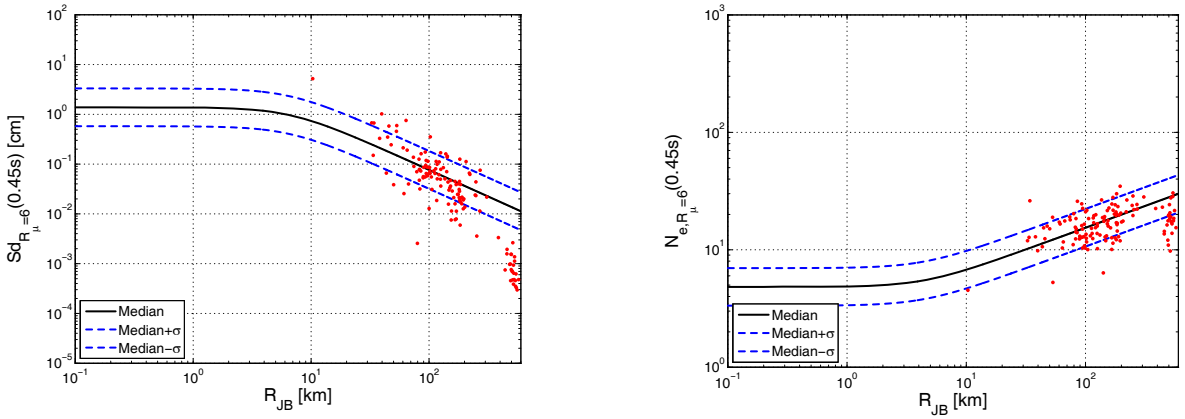

Figure 198. Comparison of the geometric mean of the horizontal components of $Sd_{R_\mu=i}$ on the left, and of $N_{e,\,R_\mu=i}$ on the right, of the registered data with the median and $\pm\sigma$ predictions according to De Luca et al. (2012) for T=0.45 and R_μ equal to 6.

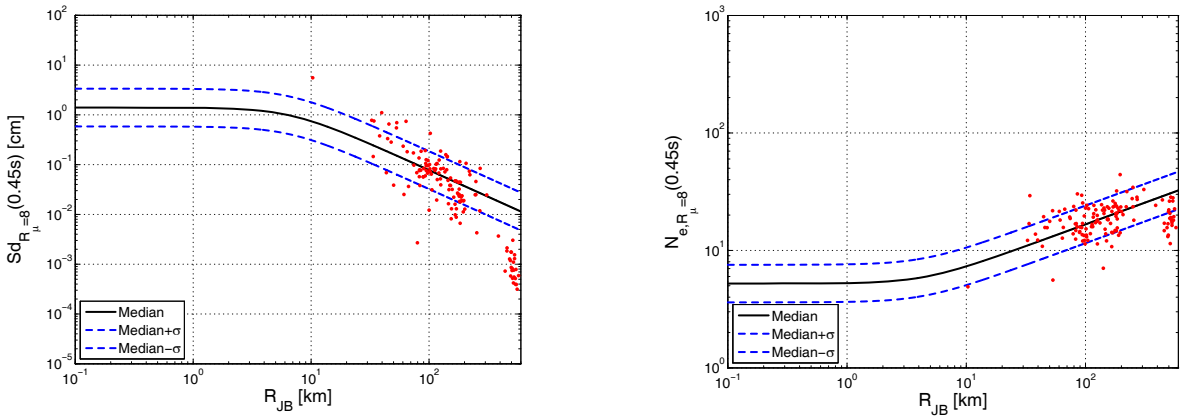

Figure 199. Comparison of the geometric mean of the horizontal components of $Sd_{R_\mu=i}$ on the left, and of $N_{e,\,R_\mu=i}$ on the right, of the registered data with the median and $\pm\sigma$ predictions according to De Luca et al. (2012) for T=0.45 and R_μ equal to 8.

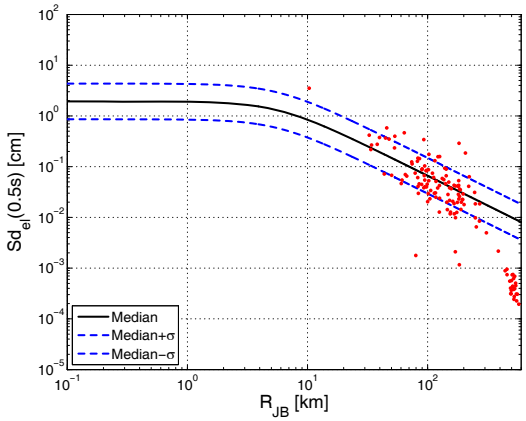

Figure 200. Comparison of the geometric mean of the horizontal components of Sd_{el} of the registered data with the median and $\pm\sigma$ predictions according to De Luca et al. (2012) for T=0.50.

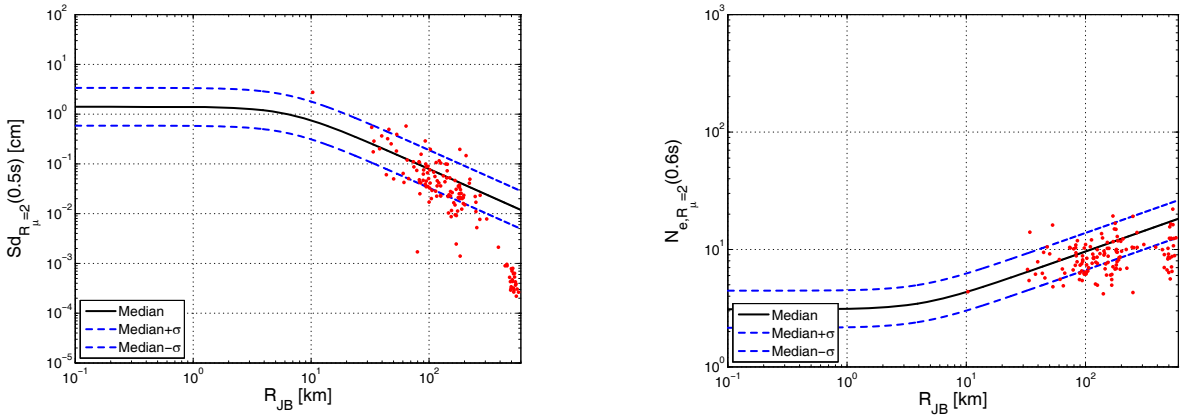

Figure 201. Comparison of the geometric mean of the horizontal components of $Sd_{R_\mu=i}$ on the left, and of $N_{e,\,R_\mu=i}$ on the right, of the registered data with the median and $\pm\sigma$ predictions according to De Luca et al. (2012) for T=0.50 and R_μ equal to 2.

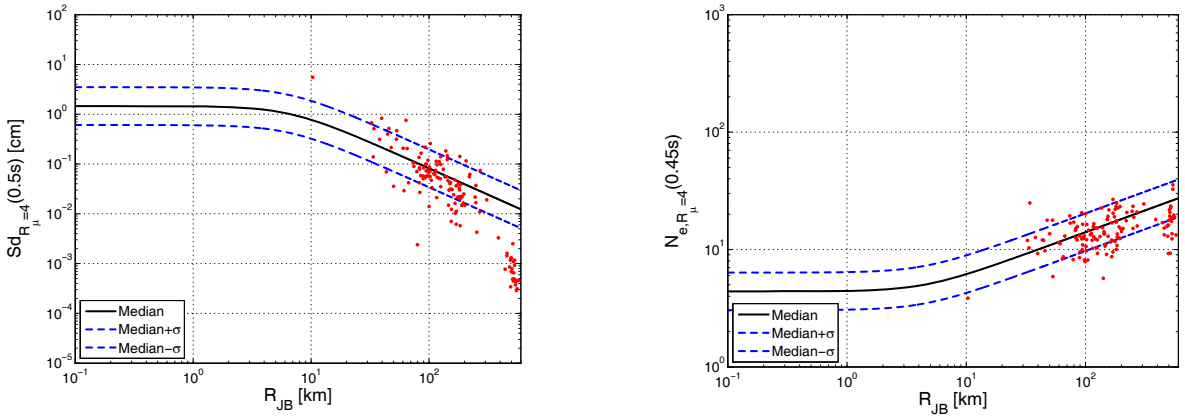

Figure 202. Comparison of the geometric mean of the horizontal components of $Sd_{R_\mu=i}$ on the left, and of $N_{e,\,R_\mu=i}$ on the right, of the registered data with the median and $\pm\sigma$ predictions according to De Luca et al. (2012) for T=0.50 and R_μ equal to 4.

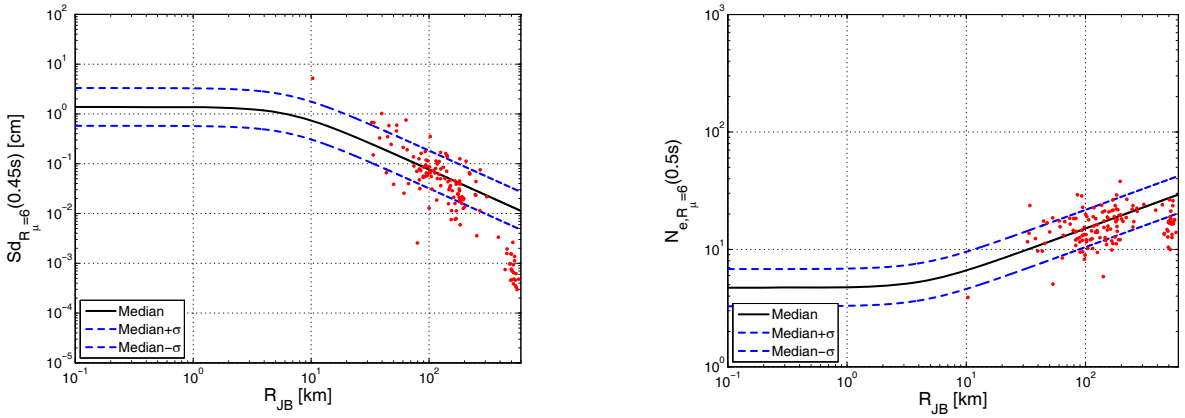

Figure 203. Comparison of the geometric mean of the horizontal components of $Sd_{R_\mu=i}$ on the left, and of $N_{e,\,R_\mu=i}$ on the right, of the registered data with the median and $\pm\sigma$ predictions according to De Luca et al. (2012) for T=0.50 and R_μ equal to 6.

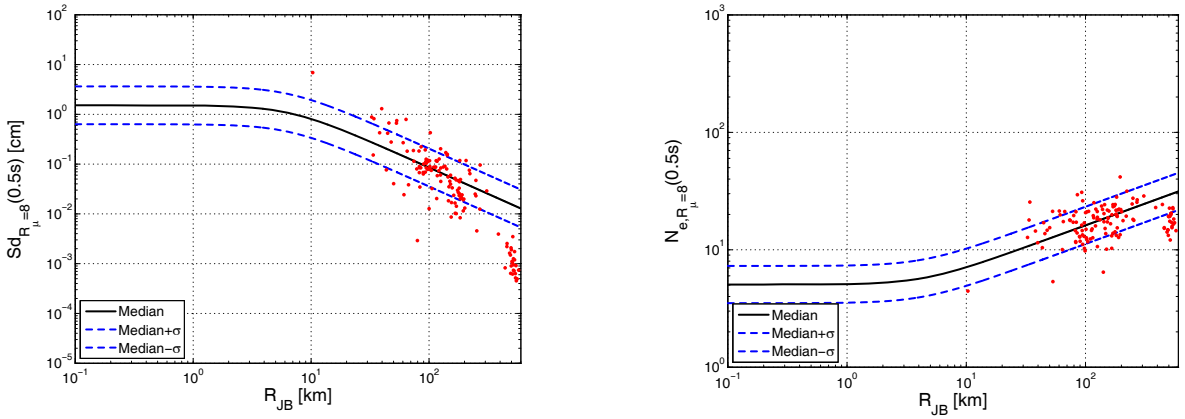

Figure 204. Comparison of the geometric mean of the horizontal components of $Sd_{R_\mu=i}$ on the left, and of $N_{e,\,R_\mu=i}$ on the right, of the registered data with the median and $\pm\sigma$ predictions according to De Luca et al. (2012) for T=0.50 and R_μ equal to 8.

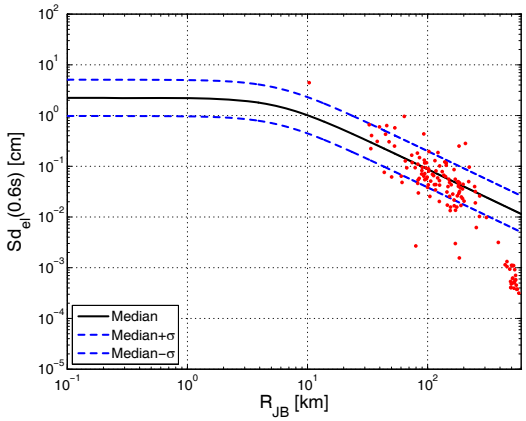

Figure 205. Comparison of the geometric mean of the horizontal components of Sd_{el} of the registered data with the median and $\pm\sigma$ predictions according to De Luca et al. (2012) for T=0.60.

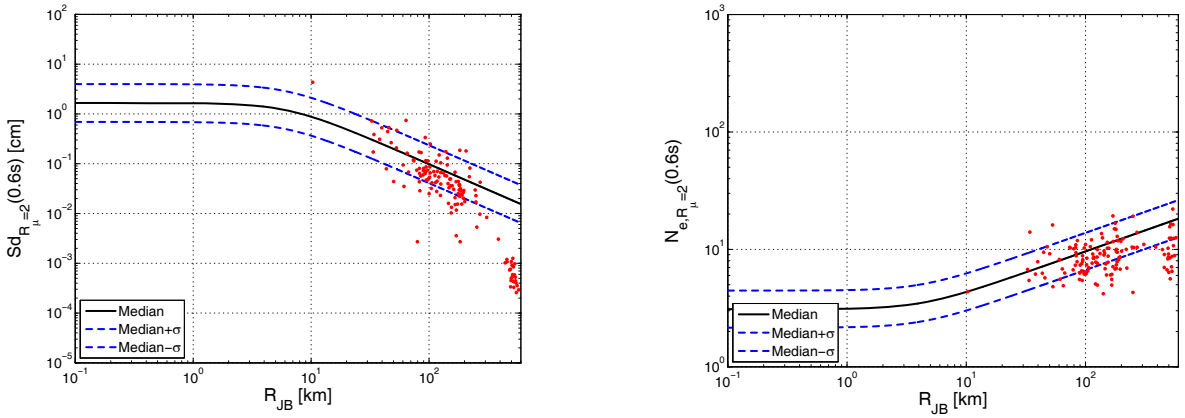

Figure 206. Comparison of the geometric mean of the horizontal components of $Sd_{R_\mu=i}$ on the left, and of $N_{e,\,R_\mu=i}$ on the right, of the registered data with the median and $\pm\sigma$ predictions according to De Luca et al. (2012) for T=0.60 and R_μ equal to 2.

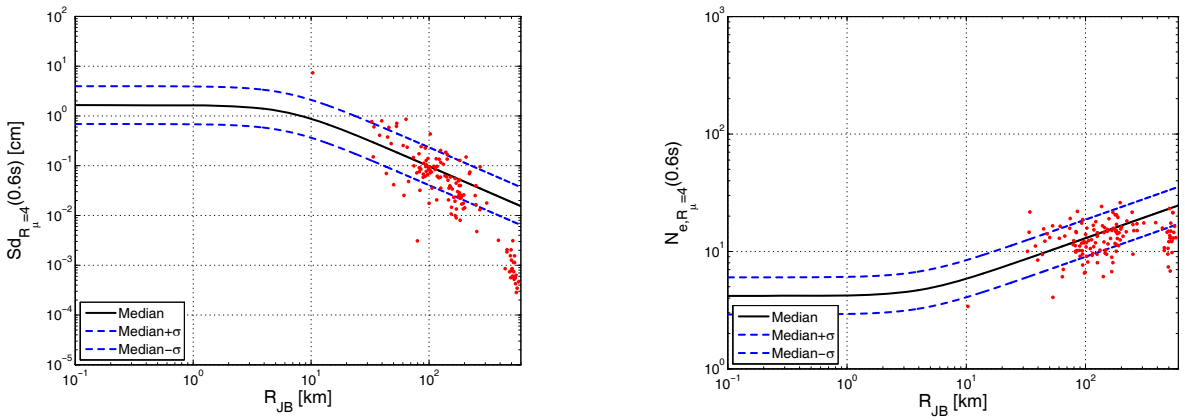

Figure 207. Comparison of the geometric mean of the horizontal components of $Sd_{R_\mu=i}$ on the left, and of $N_{e,\,R_\mu=i}$ on the right, of the registered data with the median and $\pm\sigma$ predictions according to De Luca et al. (2012) for T=0.60 and R_μ equal to 4.

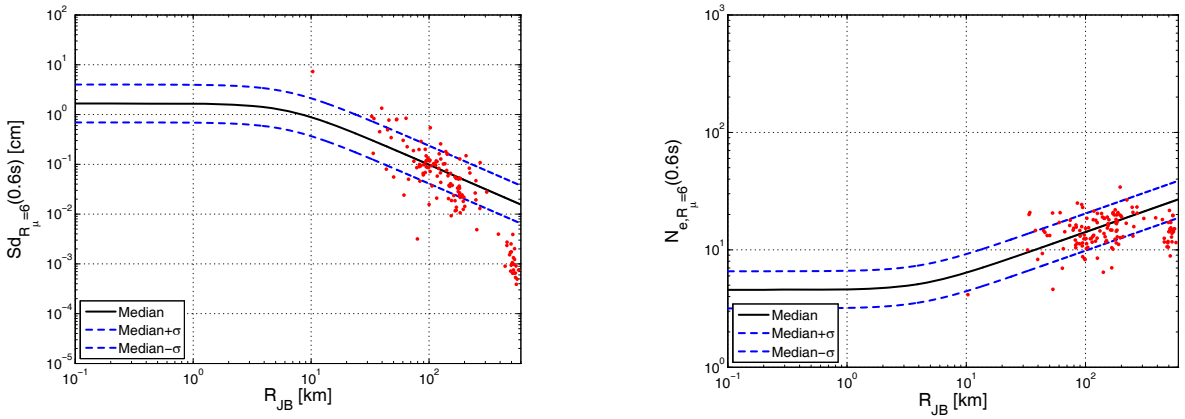

Figure 208. Comparison of the geometric mean of the horizontal components of $Sd_{R_\mu=i}$ on the left, and of $N_{e,\,R_\mu=i}$ on the right, of the registered data with the median and $\pm\sigma$ predictions according to De Luca et al. (2012) for T=0.60 and R_μ equal to 6.

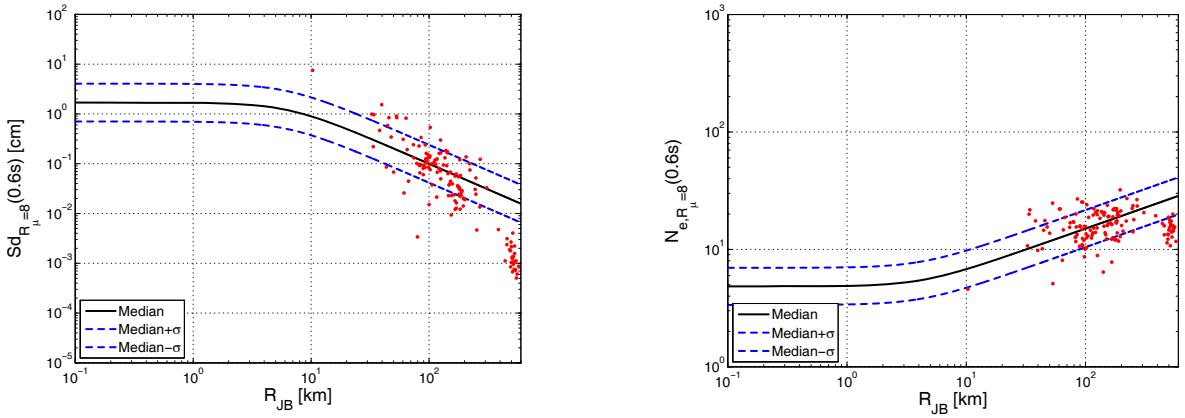

Figure 209. Comparison of the geometric mean of the horizontal components of $Sd_{R_\mu=i}$ on the left, and of $N_{e,\,R_\mu=i}$ on the right, of the registered data with the median and $\pm\sigma$ predictions according to De Luca et al. (2012) for T=0.60 and R_μ equal to 8.

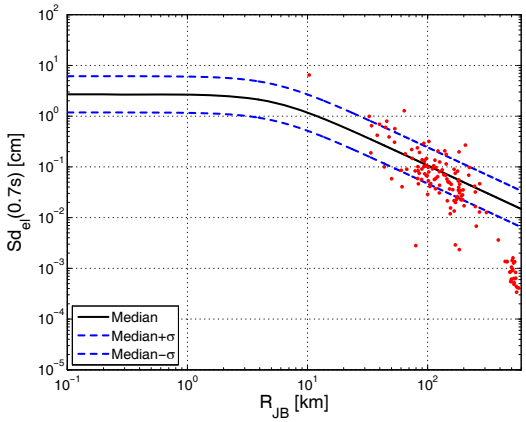

Figure 210. Comparison of the geometric mean of the horizontal components of Sd_{el} of the registered data with the median and $\pm\sigma$ predictions according to De Luca et al. (2012) for T=0.70.

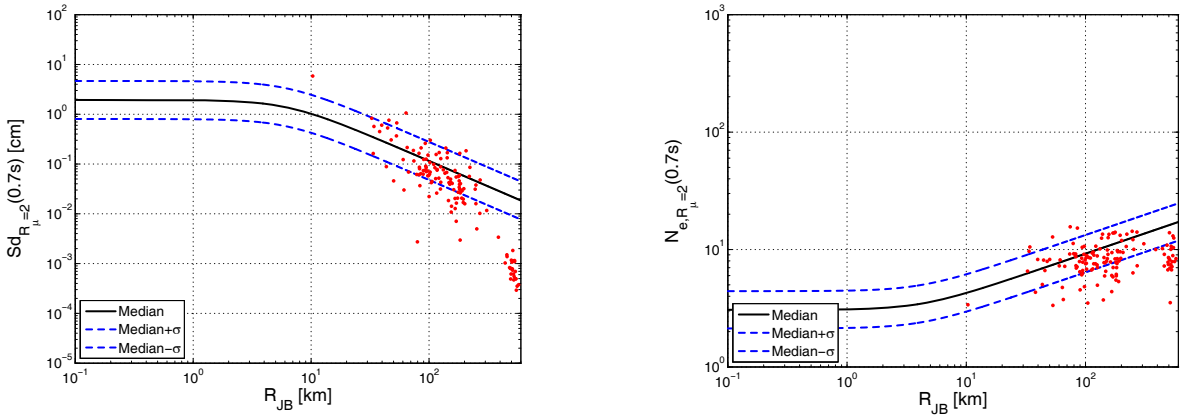

Figure 211. Comparison of the geometric mean of the horizontal components of $Sd_{R_\mu=i}$ on the left, and of $N_{e,\,R_\mu=i}$ on the right, of the registered data with the median and $\pm\sigma$ predictions according to De Luca et al. (2012) for T=0.70 and R_μ equal to 2.

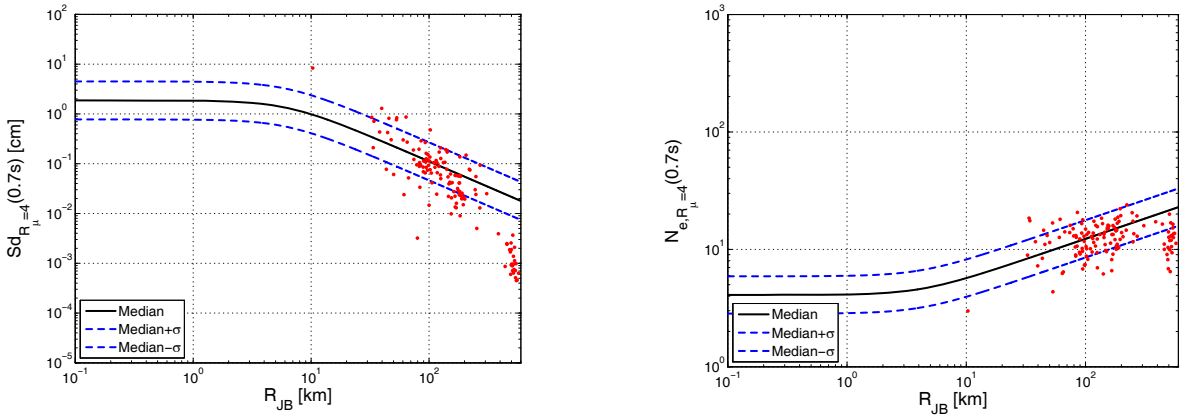

Figure 212. Comparison of the geometric mean of the horizontal components of $Sd_{R_\mu=i}$ on the left, and of $N_{e,\,R_\mu=i}$ on the right, of the registered data with the median and $\pm\sigma$ predictions according to De Luca et al. (2012) for T=0.70 and R_μ equal to 4.

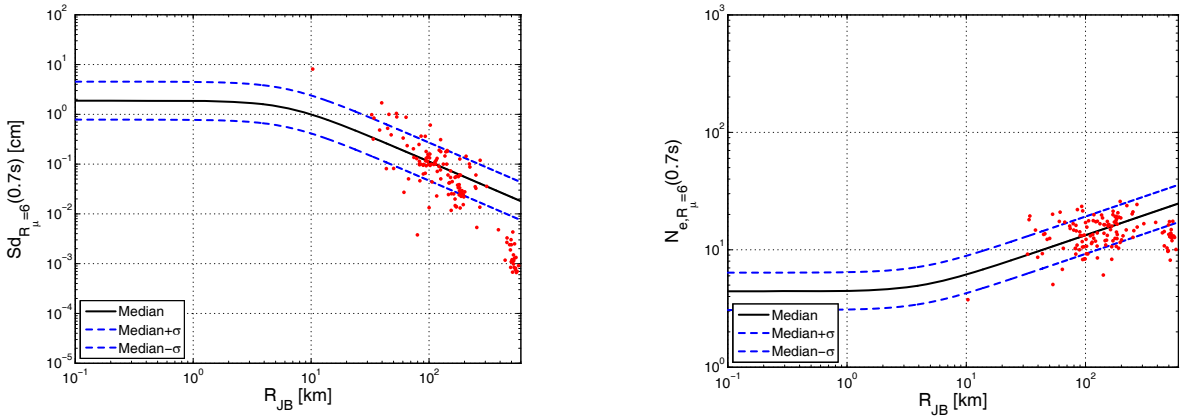

Figure 213. Comparison of the geometric mean of the horizontal components of $Sd_{R_\mu=i}$ on the left, and of $N_{e,\,R_\mu=i}$ on the right, of the registered data with the median and $\pm\sigma$ predictions according to De Luca et al. (2012) for T=0.70 and R_μ equal to 6.

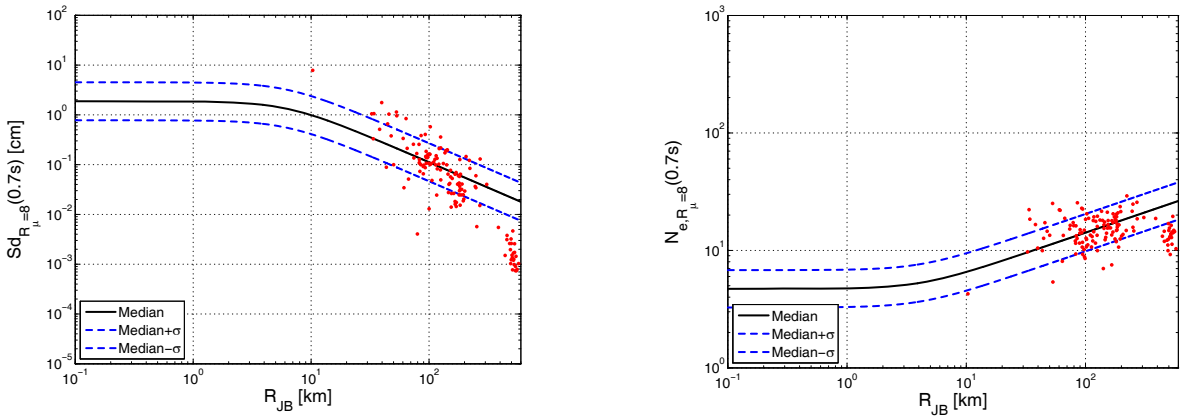

Figure 214. Comparison of the geometric mean of the horizontal components of $Sd_{R_\mu=i}$ on the left, and of $N_{e,\,R_\mu=i}$ on the right, of the registered data with the median and $\pm\sigma$ predictions according to De Luca et al. (2012) for T=0.70 and R_μ equal to 8.

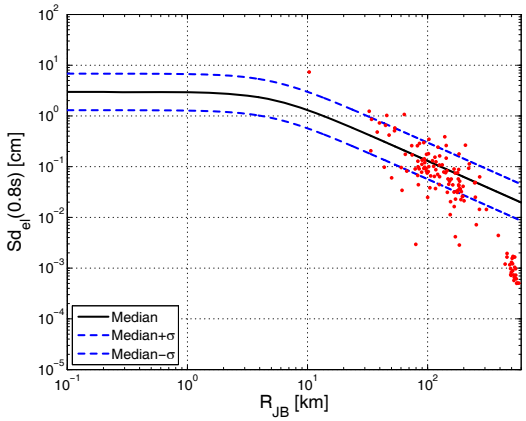

Figure 215. Comparison of the geometric mean of the horizontal components of Sd_{el} of the registered data with the median and $\pm\sigma$ predictions according to De Luca et al. (2012) for T=0.80.

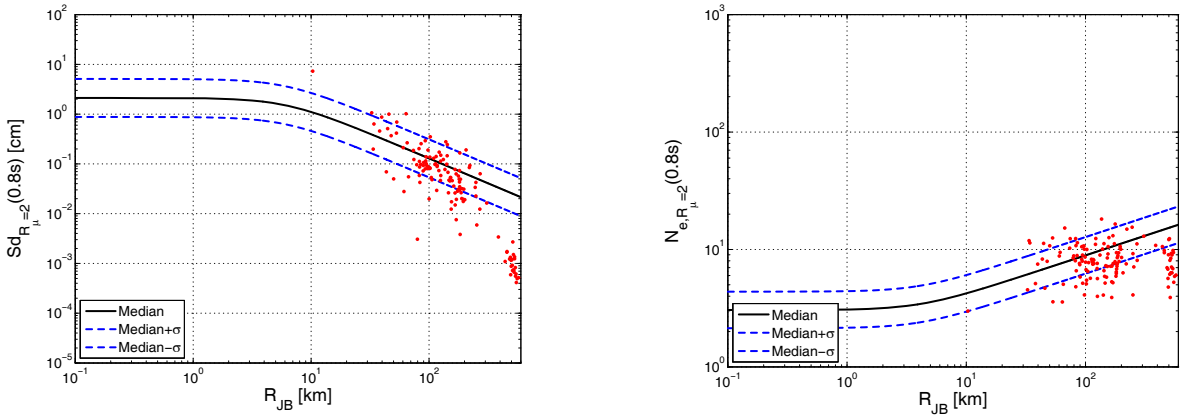

Figure 216. Comparison of the geometric mean of the horizontal components of $Sd_{R_\mu=i}$ on the left, and of $N_{e,\,R_\mu=i}$ on the right, of the registered data with the median and $\pm\sigma$ predictions according to De Luca et al. (2012) for T=0.80 and R_μ equal to 2.

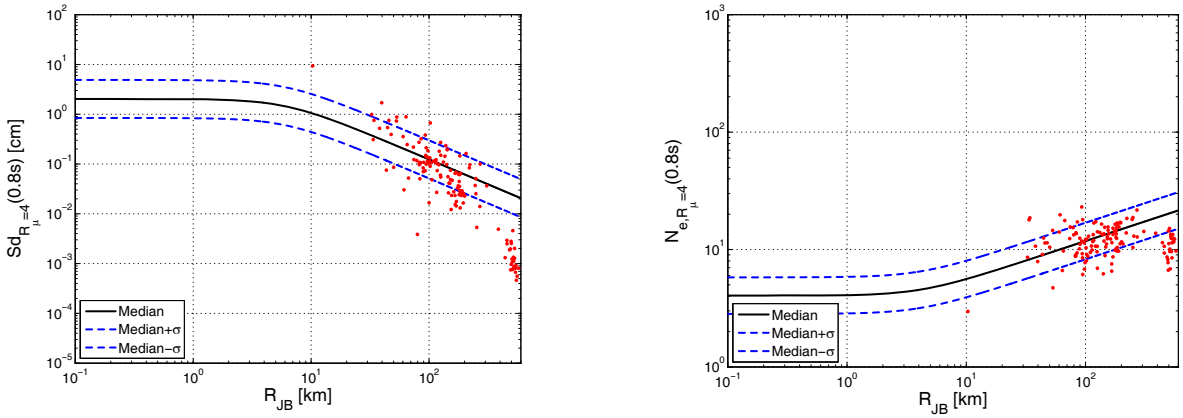

Figure 217. Comparison of the geometric mean of the horizontal components of $Sd_{R_\mu=i}$ on the left, and of $N_{e,\,R_\mu=i}$ on the right, of the registered data with the median and $\pm\sigma$ predictions according to De Luca et al. (2012) for T=0.80 and R_μ equal to 4.

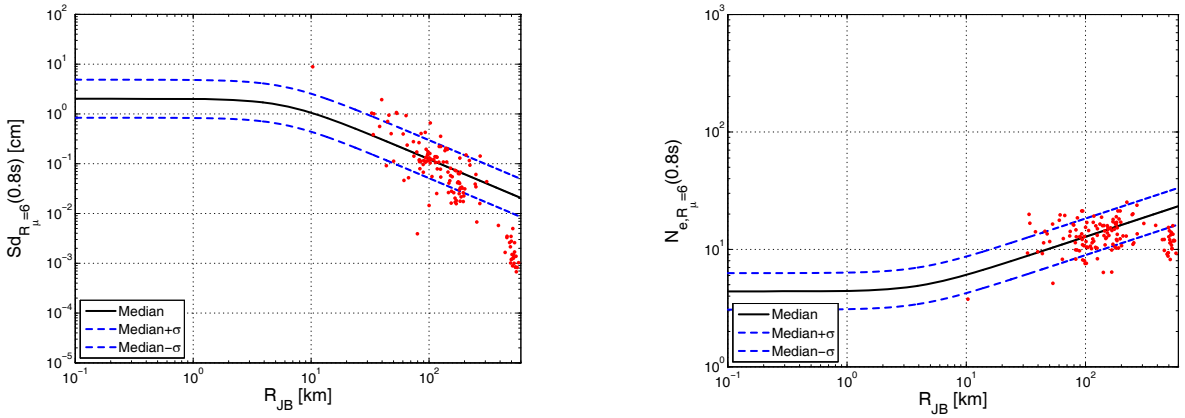

Figure 218. Comparison of the geometric mean of the horizontal components of $Sd_{R_\mu=i}$ on the left, and of $N_{e,\,R_\mu=i}$ on the right, of the registered data with the median and $\pm\sigma$ predictions according to De Luca et al. (2012) for T=0.80 and R_μ equal to 6.

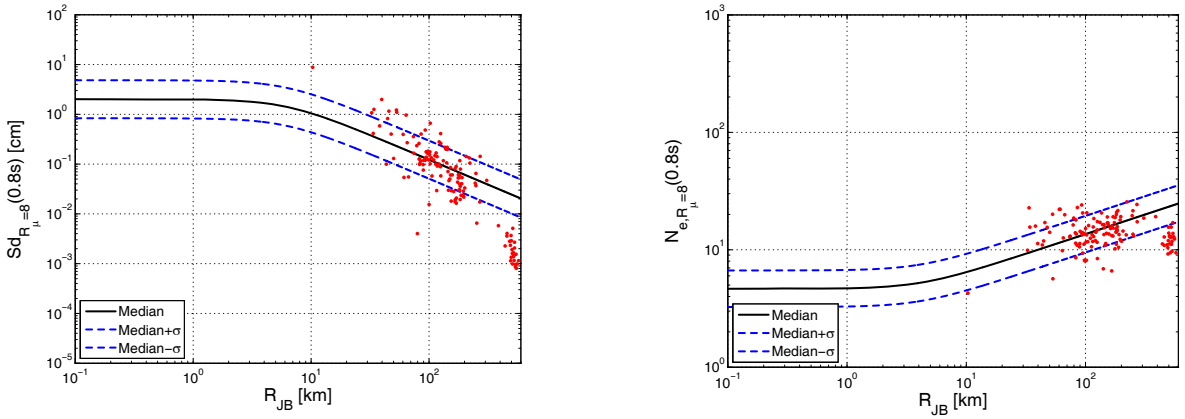

Figure 219. Comparison of the geometric mean of the horizontal components of $Sd_{R_\mu=i}$ on the left, and of $N_{e,\,R_\mu=i}$ on the right, of the registered data with the median and $\pm\sigma$ predictions according to De Luca et al. (2012) for T=0.80 and R_μ equal to 8.

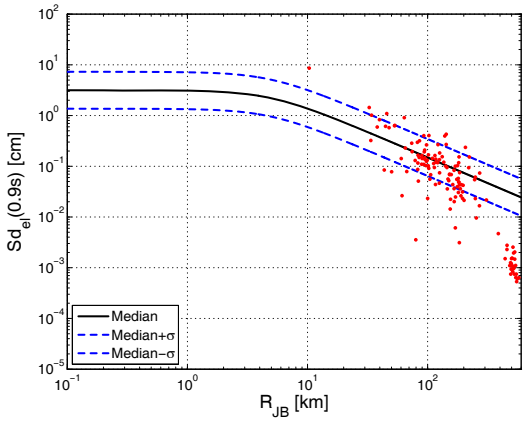

Figure 220. Comparison of the geometric mean of the horizontal components of Sd_{el} of the registered data with the median and $\pm\sigma$ predictions according to De Luca et al. (2012) for T=0.90.

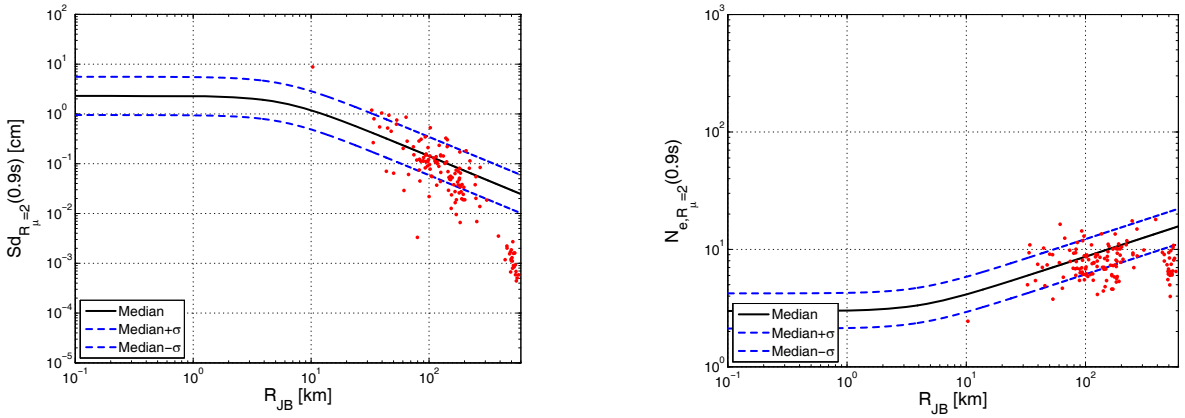

Figure 221. Comparison of the geometric mean of the horizontal components of $Sd_{R_\mu=i}$ on the left, and of $N_{e,\,R_\mu=i}$ on the right, of the registered data with the median and $\pm\sigma$ predictions according to De Luca et al. (2012) for T=0.90 and R_μ equal to 2.

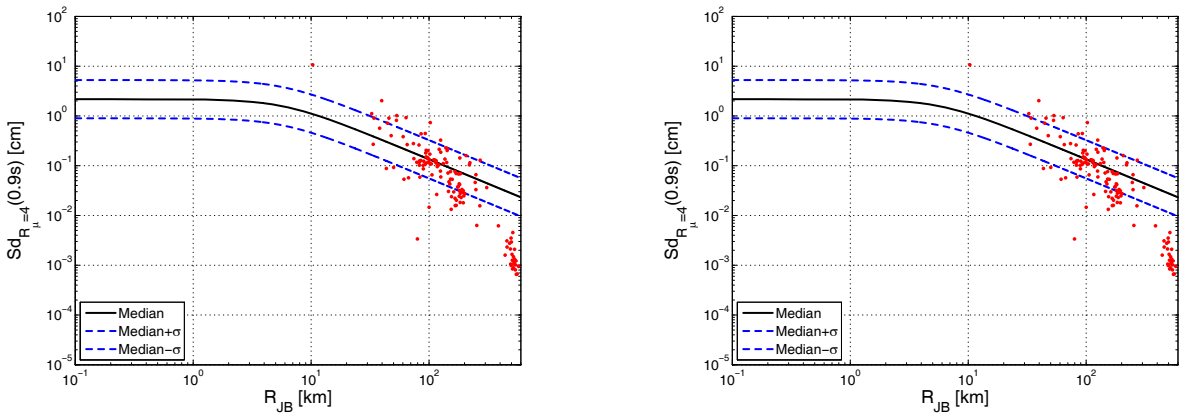

Figure 222. Comparison of the geometric mean of the horizontal components of $Sd_{R_\mu=i}$ on the left, and of $N_{e,\,R_\mu=i}$ on the right, of the registered data with the median and $\pm\sigma$ predictions according to De Luca et al. (2012) for T=0.90 and R_μ equal to 4.

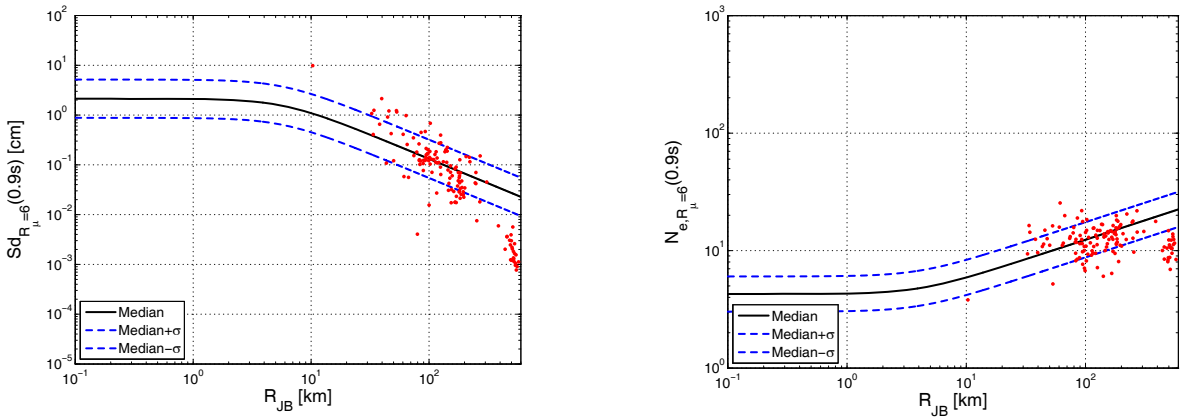

Figure 223. Comparison of the geometric mean of the horizontal components of $Sd_{R_\mu=i}$ on the left, and of $N_{e,\,R_\mu=i}$ on the right, of the registered data with the median and $\pm\sigma$ predictions according to De Luca et al. (2012) for T=0.90 and R_μ equal to 6.

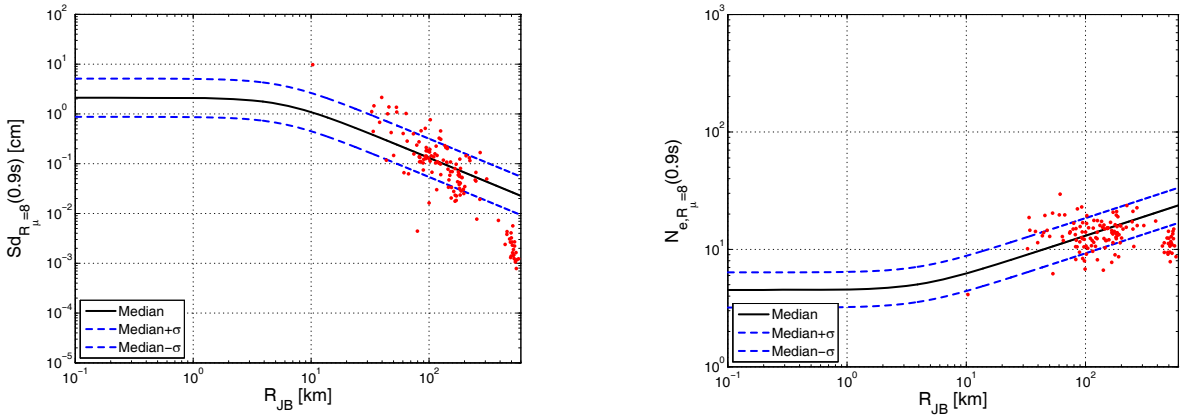

Figure 224. Comparison of the geometric mean of the horizontal components of $Sd_{R_\mu=i}$ on the left, and of $N_{e,\,R_\mu=i}$ on the right, of the registered data with the median and $\pm\sigma$ predictions according to De Luca et al. (2012) for T=0.90 and R_μ equal to 8.

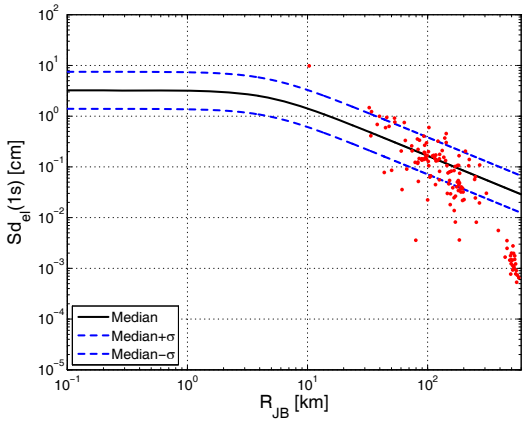

Figure 225. Comparison of the geometric mean of the horizontal components of Sd_{el} of the registered data with the median and $\pm\sigma$ predictions according to De Luca et al. (2012) for T=1.00.

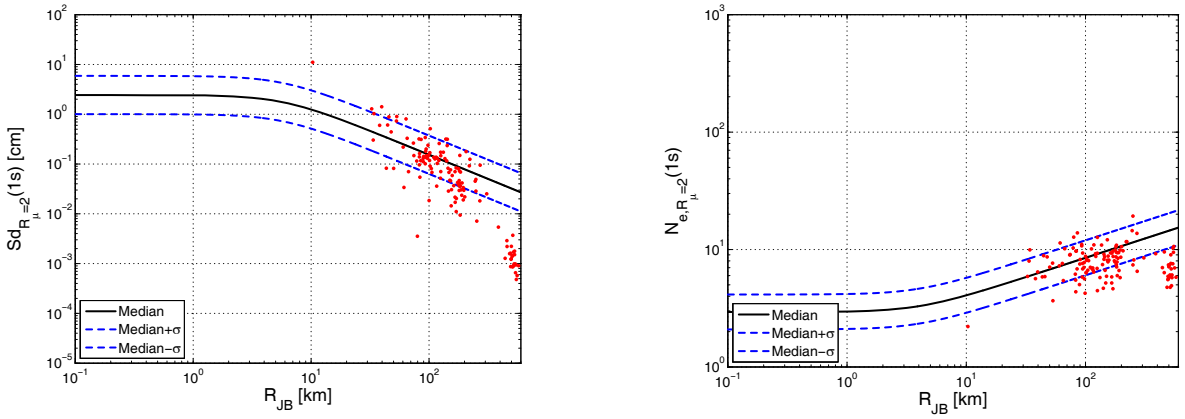

Figure 226. Comparison of the geometric mean of the horizontal components of $Sd_{R_\mu=i}$ on the left, and of $N_{e,\,R_\mu=i}$ on the right, of the registered data with the median and $\pm\sigma$ predictions according to De Luca et al. (2012) for T=1.00 and R_μ equal to 2.

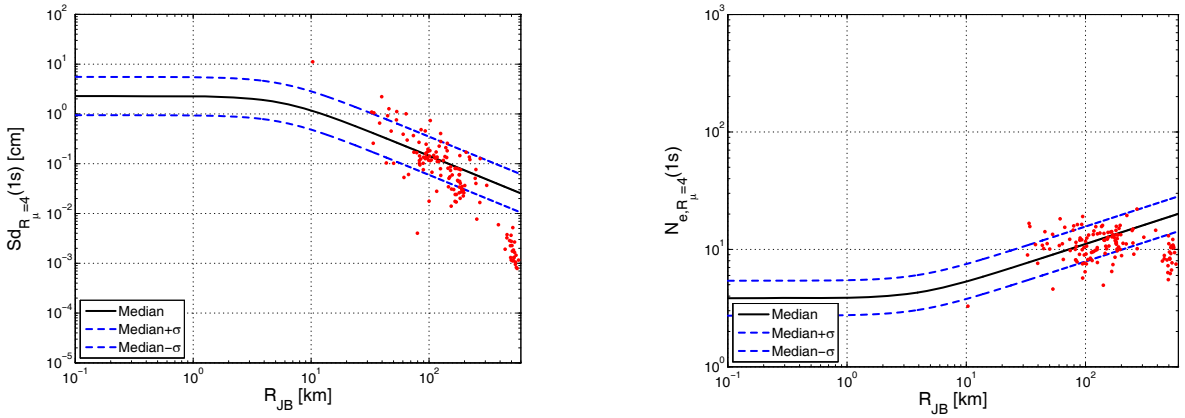

Figure 227. Comparison of the geometric mean of the horizontal components of $Sd_{R_\mu=i}$ on the left, and of $N_{e,\,R_\mu=i}$ on the right, of the registered data with the median and $\pm\sigma$ predictions according to De Luca et al. (2012) for T=1.00 and R_μ equal to 4.

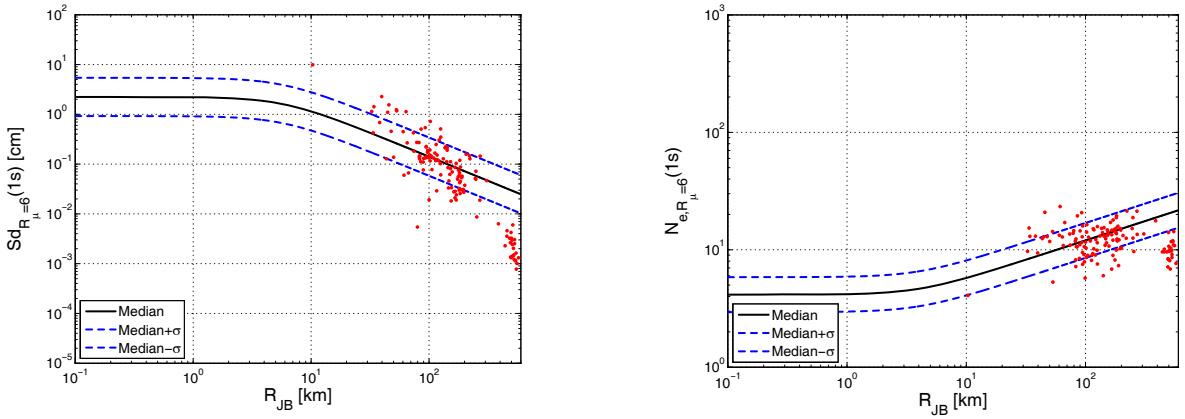

Figure 228. Comparison of the geometric mean of the horizontal components of $Sd_{R_\mu=i}$ on the left, and of $N_{e,\,R_\mu=i}$ on the right, of the registered data with the median and $\pm\sigma$ predictions according to De Luca et al. (2012) for T=1.00 and R_μ equal to 6.

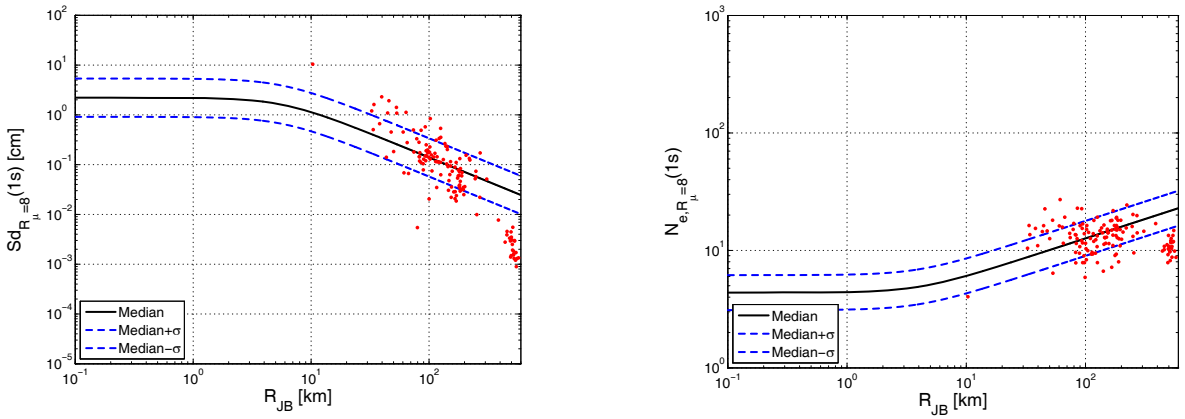

Figure 229. Comparison of the geometric mean of the horizontal components of $Sd_{R_\mu=i}$ on the left, and of $N_{e,\,R_\mu=i}$ on the right, of the registered data with the median and $\pm\sigma$ predictions according to De Luca et al. (2012) for T=1.00 and R_μ equal to 8.

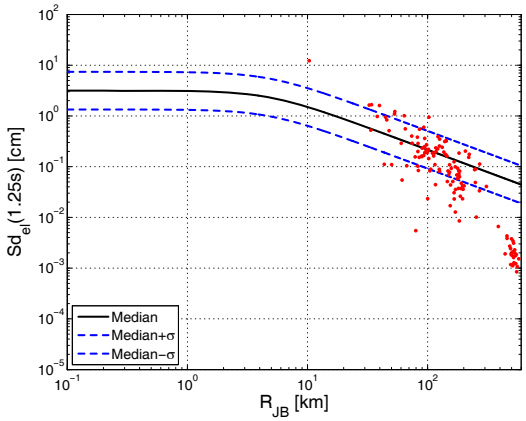

Figure 230. Comparison of the geometric mean of the horizontal components of Sd_{el} of the registered data with the median and $\pm\sigma$ predictions according to De Luca et al. (2012) for T=1.25.

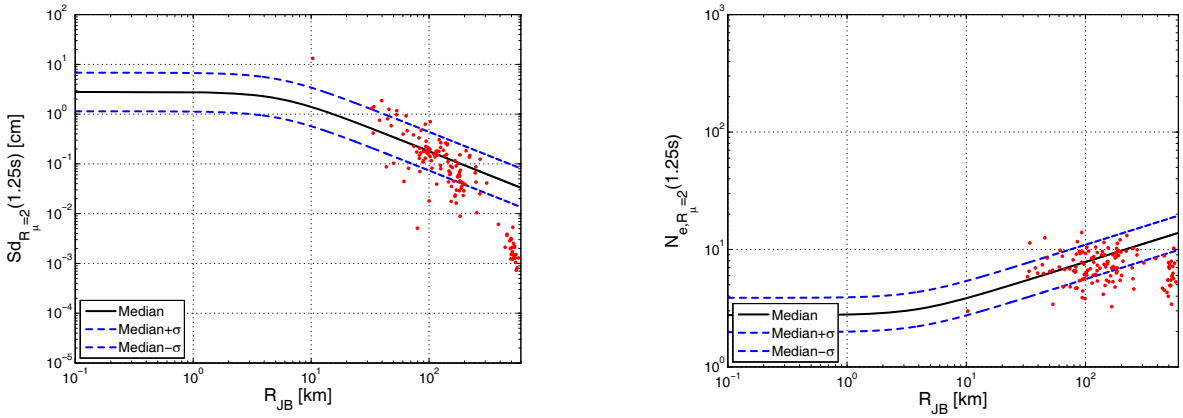

Figure 231. Comparison of the geometric mean of the horizontal components of $Sd_{R_\mu=i}$ on the left, and of $N_{e,\,R_\mu=i}$ on the right, of the registered data with the median and $\pm\sigma$ predictions according to De Luca et al. (2012) for T=1.25 and R_μ equal to 2.

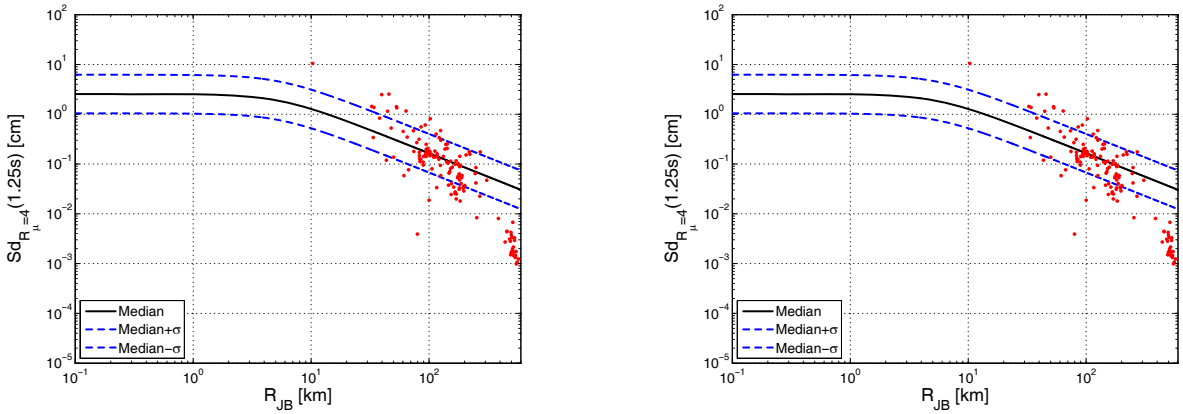

Figure 232. Comparison of the geometric mean of the horizontal components of $Sd_{R_\mu=i}$ on the left, and of $N_{e,\,R_\mu=i}$ on the right, of the registered data with the median and $\pm\sigma$ predictions according to De Luca et al. (2012) for T=1.25 and R_μ equal to 4.

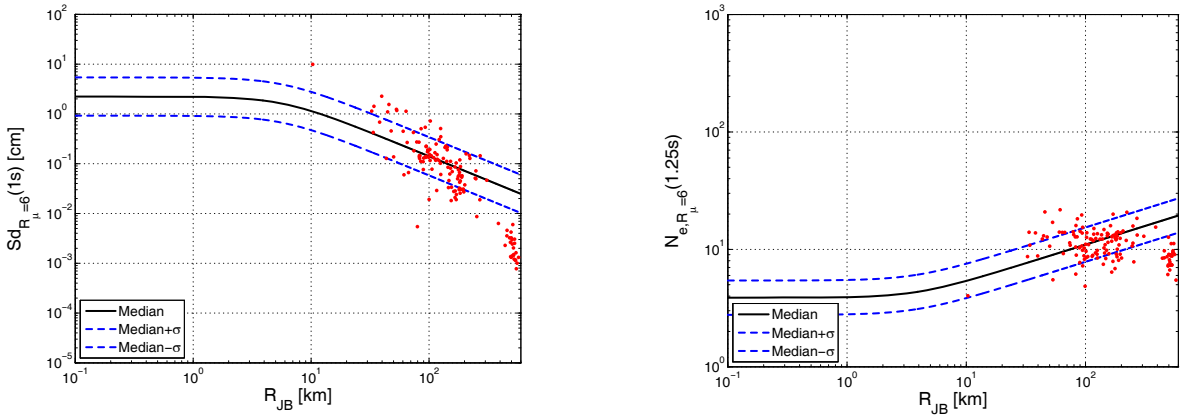

Figure 233. Comparison of the geometric mean of the horizontal components of $Sd_{R_\mu=i}$ on the left, and of $N_{e,\,R_\mu=i}$ on the right, of the registered data with the median and $\pm\sigma$ predictions according to De Luca et al. (2012) for T=1.25 and R_μ equal to 6.

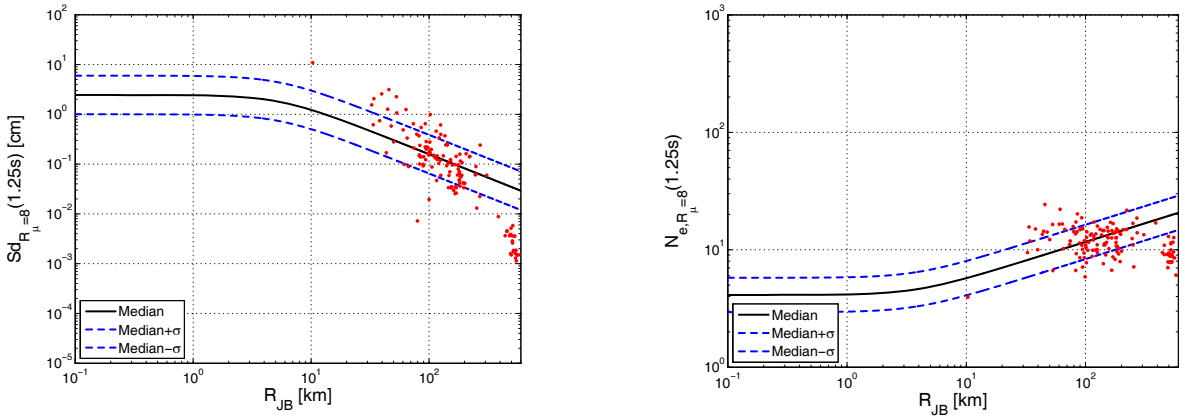

Figure 234. Comparison of the geometric mean of the horizontal components of $Sd_{R_\mu=i}$ on the left, and of $N_{e,\,R_\mu=i}$ on the right, of the registered data with the median and $\pm\sigma$ predictions according to De Luca et al. (2012) for T=1.25 and R_μ equal to 8.

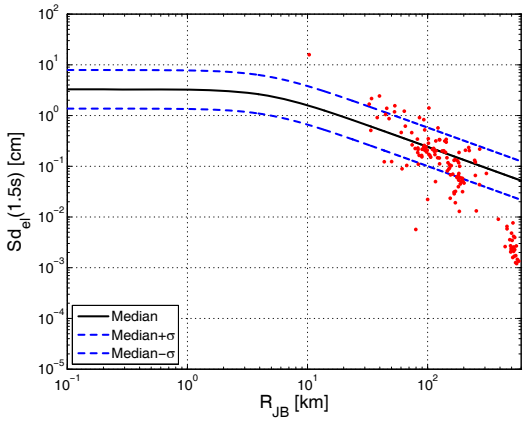

Figure 235. Comparison of the geometric mean of the horizontal components of Sd_{el} of the registered data with the median and $\pm\sigma$ predictions according to De Luca et al. (2012) for T=1.50.

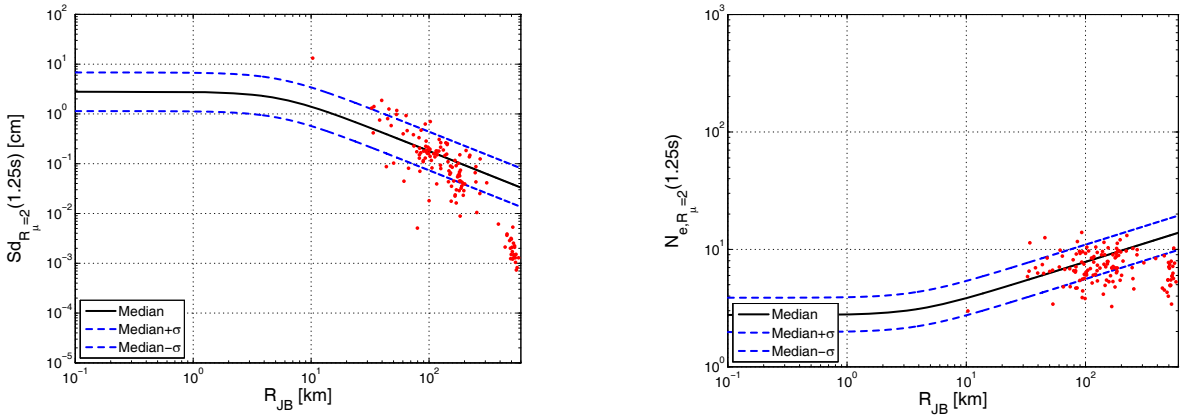

Figure 236. Comparison of the geometric mean of the horizontal components of $Sd_{R_\mu=i}$ on the left, and of $N_{e,\,R_\mu=i}$ on the right, of the registered data with the median and $\pm\sigma$ predictions according to De Luca et al. (2012) for T=1.50 and R_μ equal to 2.

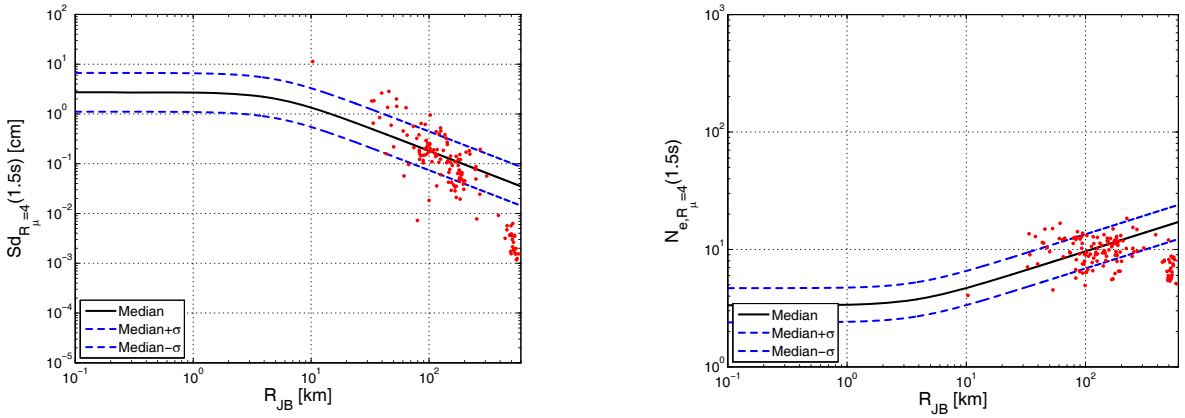

Figure 237. Comparison of the geometric mean of the horizontal components of $Sd_{R_\mu=i}$ on the left, and of $N_{e,\,R_\mu=i}$ on the right, of the registered data with the median and $\pm\sigma$ predictions according to De Luca et al. (2012) for T=1.50 and R_μ equal to 4.

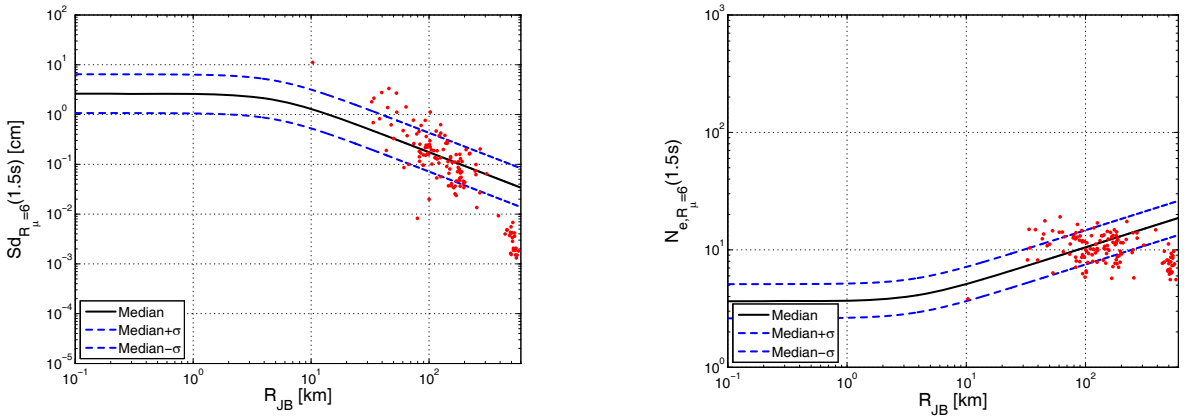

Figure 238. Comparison of the geometric mean of the horizontal components of $Sd_{R_\mu=i}$ on the left, and of $N_{e,\,R_\mu=i}$ on the right, of the registered data with the median and $\pm\sigma$ predictions according to De Luca et al. (2012) for T=1.50 and R_μ equal to 6.

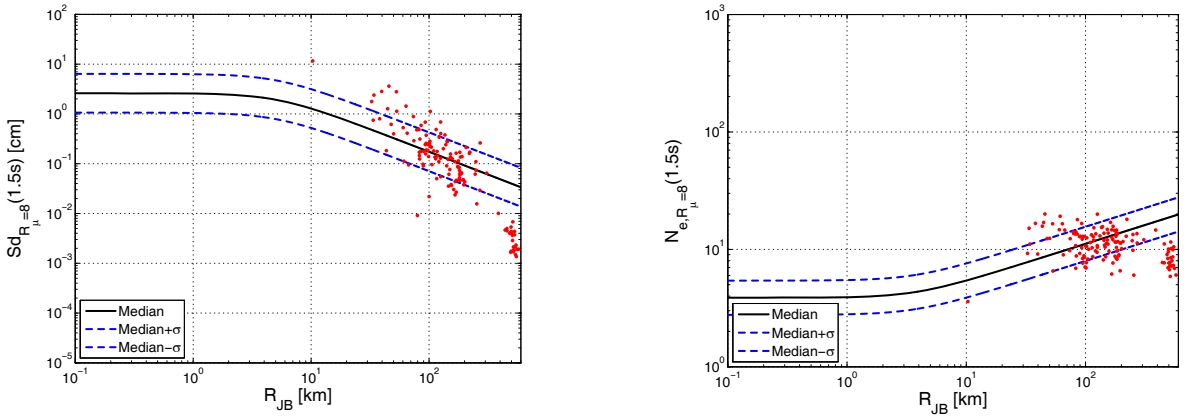

Figure 239. Comparison of the geometric mean of the horizontal components of $Sd_{R_\mu=i}$ on the left, and of $N_{e,\,R_\mu=i}$ on the right, of the registered data with the median and $\pm\sigma$ predictions according to De Luca et al. (2012) for T=1.50 and R_μ equal to 8.

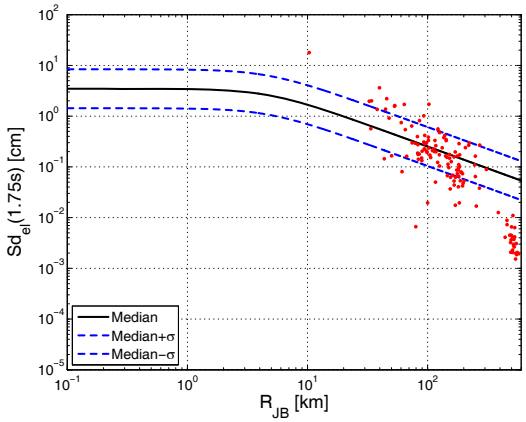

Figure 240. Comparison of the geometric mean of the horizontal components of Sd_{el} of the registered data with the median and $\pm\sigma$ predictions according to De Luca et al. (2012) for T=1.75.

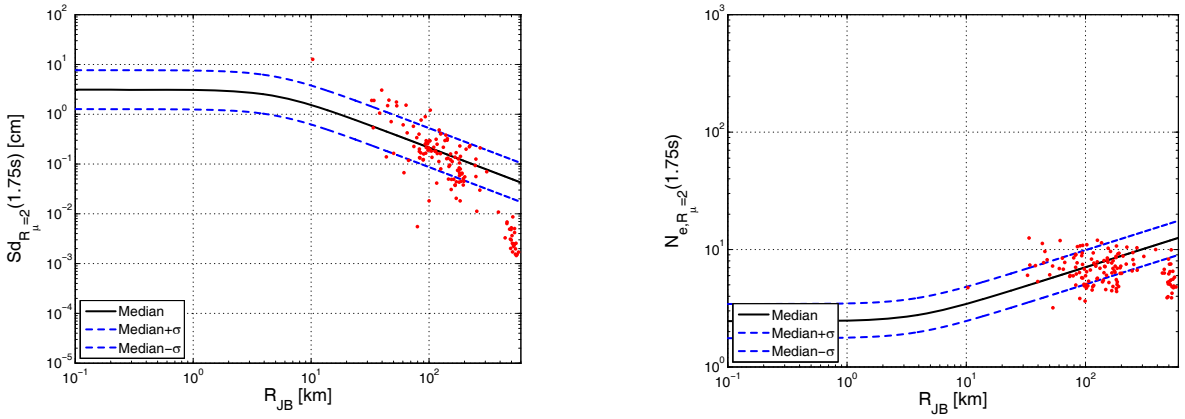

Figure 241. Comparison of the geometric mean of the horizontal components of $Sd_{R_\mu=i}$ on the left, and of $N_{e,\,R_\mu=i}$ on the right, of the registered data with the median and $\pm\sigma$ predictions according to De Luca et al. (2012) for T=1.75 and R_μ equal to 2.

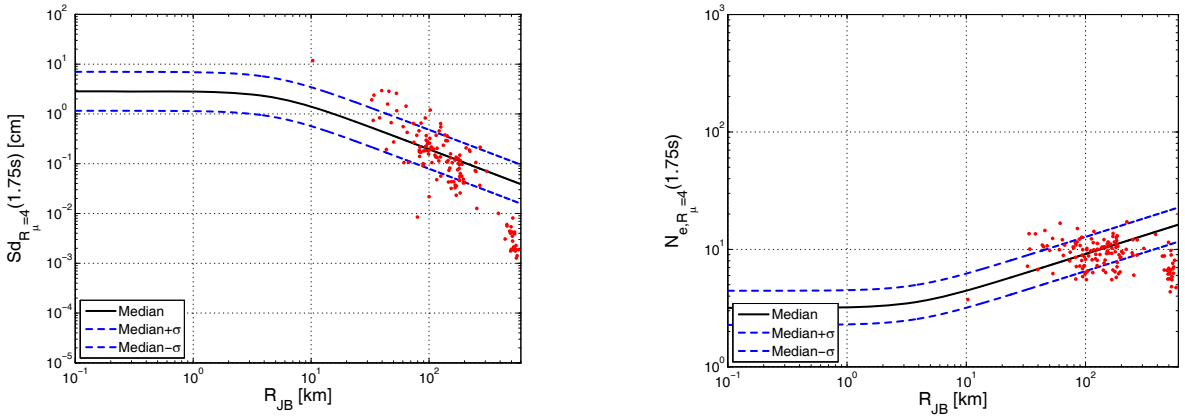

Figure 242. Comparison of the geometric mean of the horizontal components of $Sd_{R_\mu=i}$ on the left, and of $N_{e,\,R_\mu=i}$ on the right, of the registered data with the median and $\pm\sigma$ predictions according to De Luca et al. (2012) for T=1.75 and R_μ equal to 4.

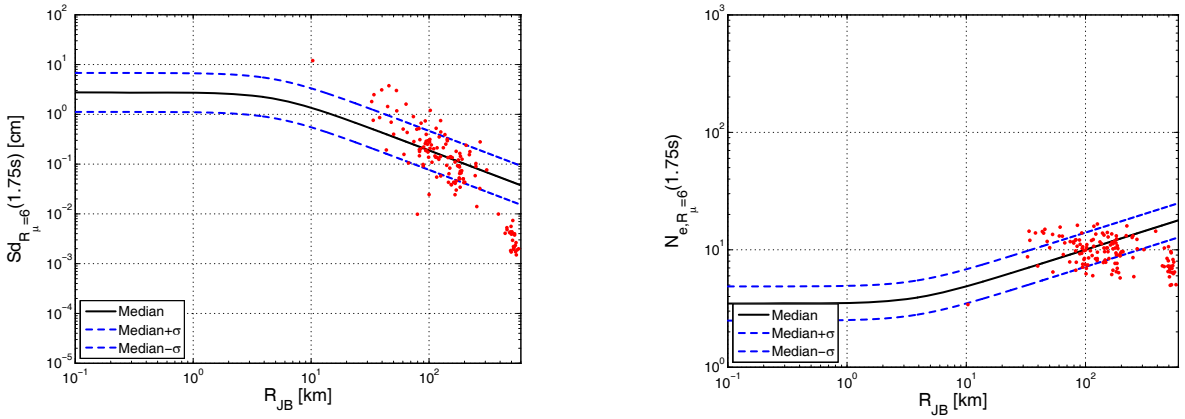

Figure 243. Comparison of the geometric mean of the horizontal components of $Sd_{R_\mu=i}$ on the left, and of $N_{e,\,R_\mu=i}$ on the right, of the registered data with the median and $\pm\sigma$ predictions according to De Luca et al. (2012) for T=1.75 and R_μ equal to 6.

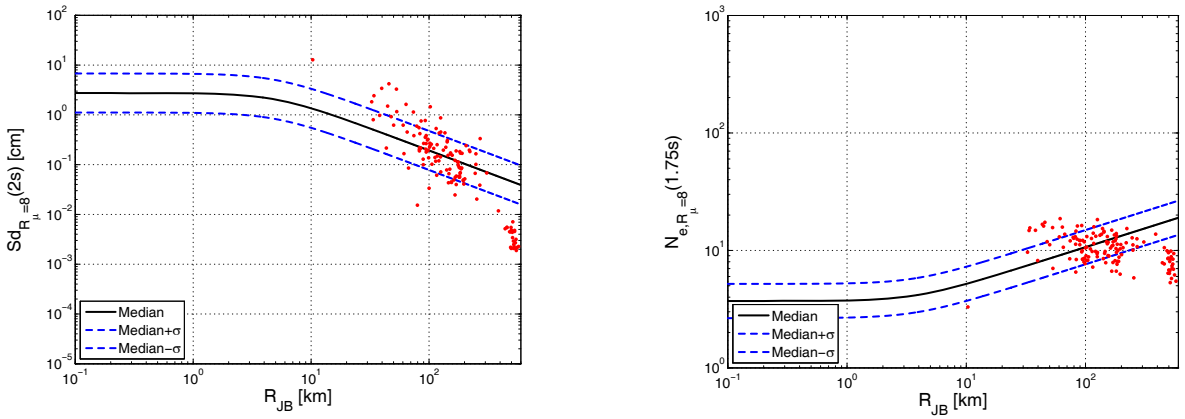

Figure 244. Comparison of the geometric mean of the horizontal components of $Sd_{R_\mu=i}$ on the left, and of $N_{e,\,R_\mu=i}$ on the right, of the registered data with the median and $\pm\sigma$ predictions according to De Luca et al. (2012) for T=1.75 and R_μ equal to 8.

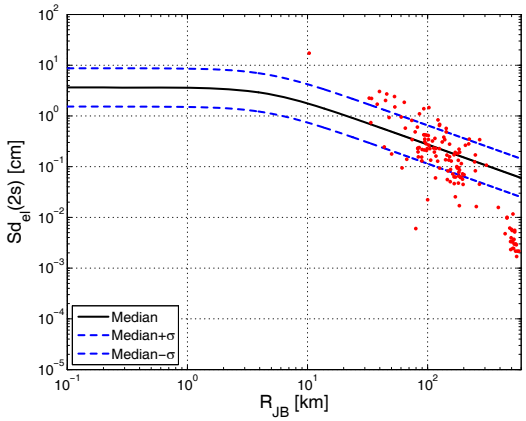

Figure 245. Comparison of the geometric mean of the horizontal components of Sd_{el} of the registered data with the median and $\pm\sigma$ predictions according to De Luca et al. (2012) for T=2.00.

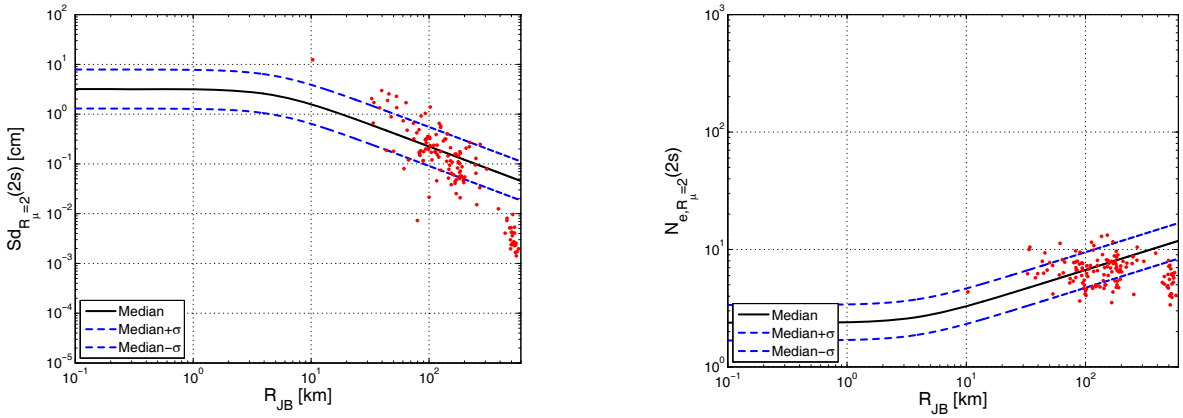

Figure 246. Comparison of the geometric mean of the horizontal components of $Sd_{R_\mu=i}$ on the left, and of $N_{e,\,R_\mu=i}$ on the right, of the registered data with the median and $\pm\sigma$ predictions according to De Luca et al. (2012) for T=2.00 and R_μ equal to 2.

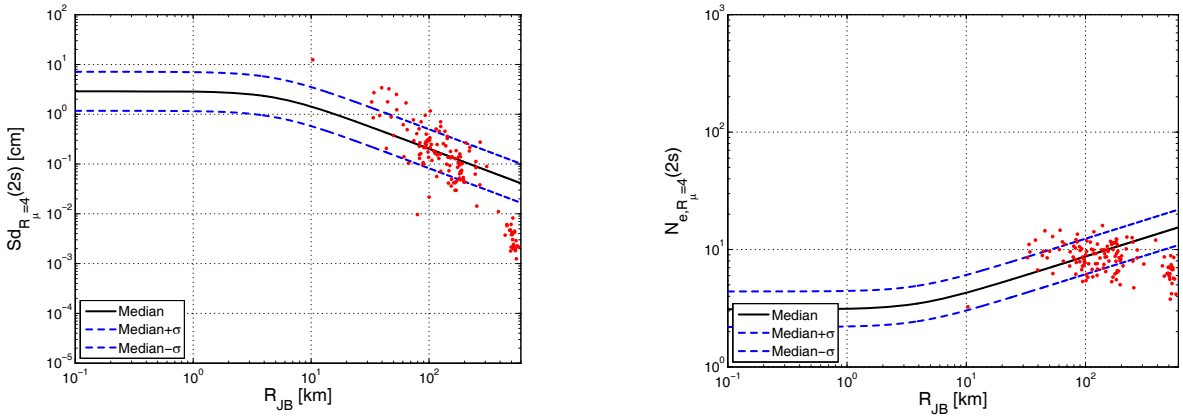

Figure 247. Comparison of the geometric mean of the horizontal components of $Sd_{R_\mu=i}$ on the left, and of $N_{e,\,R_\mu=i}$ on the right, of the registered data with the median and $\pm\sigma$ predictions according to De Luca et al. (2012) for T=2.00 and R_μ equal to 4.

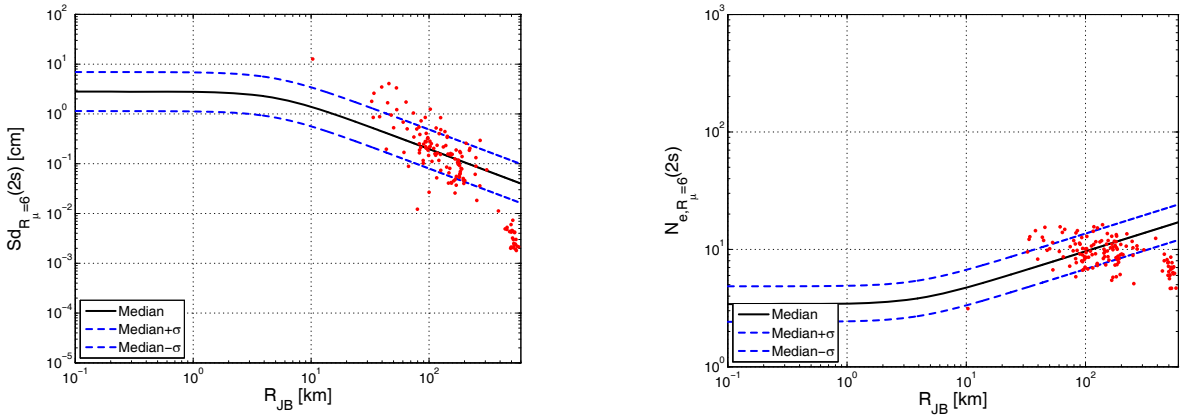

Figure 248. Comparison of the geometric mean of the horizontal components of $Sd_{R_\mu=i}$ on the left, and of $N_{e,\,R_\mu=i}$ on the right, of the registered data with the median and $\pm\sigma$ predictions according to De Luca et al. (2012) for T=2.00 and R_μ equal to 6.

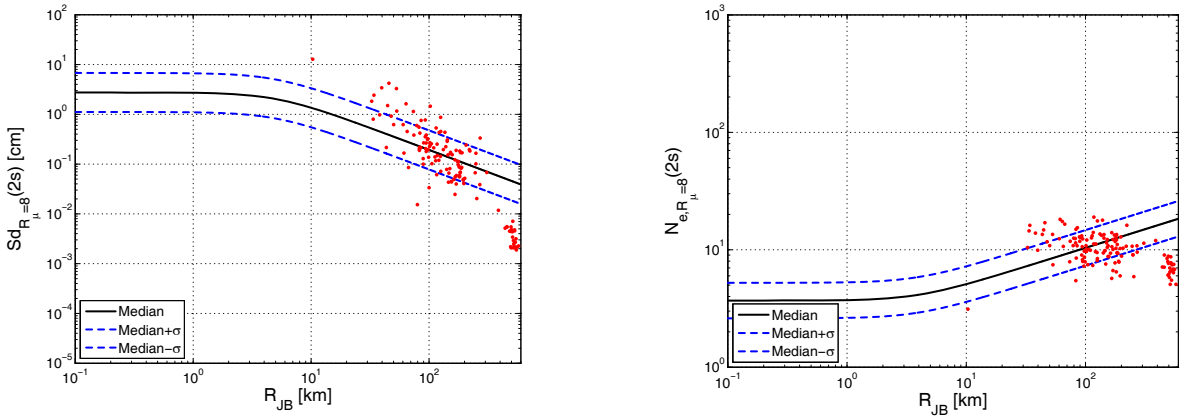

Figure 249. Comparison of the geometric mean of the horizontal components of $Sd_{R_\mu=i}$ on the left, and of $N_{e,\,R_\mu=i}$ on the right, of the registered data with the median and $\pm\sigma$ predictions according to De Luca et al. (2012) for T=2.00 and R_μ equal to 8.

Appendix

Table A1. Peak and integral parameters estimated on the uncorrected waveforms of the N-S component

Station ID	R_{epi}	Comp	PGA	PGV	I_A	I_D	H_{50}	Sd	Bd
	km		cm/s^2	cm/s	cm/s		cm	s	s
MRN	16	N	259.11	47.16	87.05	4.45	129.12	6.00	17.70
MDN	41	N	32.77	3.74	2.72	13.87	12.39	32.51	76.32
NVL	42	N	51.07	2.42	2.64	13.34	7.21	18.14	51.25
ZPP	43	N	22.84	4.40	2.87	17.84	15.77	51.66	114.29
ISD	47	N	16.48	1.81	0.95	19.90	7.11	58.23	123.50
CPC	49	N	33.21	7.07	3.28	8.73	15.93	32.51	91.32
ARG	53	N	16.90	2.50	1.18	17.45	1.30	33.64	122.63
SSU	54	N	16.44	1.70	0.90	20.13	7.03	32.03	81.34
MDC	56	N	38.90	5.37	3.14	9.38	13.16	68.25	111.77
MNS	58	N	16.43	0.57	0.49	32.39	5.66	15.96	58.57
MRZ	61	N	3.48	0.63	0.04	12.14	1.23	38.05	67.23
SRP	64	N	24.05	2.64	0.80	7.85	10.60	43.95	79.17
CSP	64	N	15.21	5.10	1.70	13.68	7.82	54.70	112.42
PVF	72	N	4.83	1.14	0.09	9.84	2.92	51.01	110.70
TGG	73	N	5.95	0.25	0.09	37.28	0.61	28.53	94.24
PAR	76	N	6.00	0.91	0.11	13.14	10.26	52.68	93.27
ALF	78	N	26.87	3.63	1.62	10.39	2.80	57.18	117.23
LNG	80	N	5.81	0.69	0.14	21.55	3.09	50.03	106.85
FRE1	87	N	6.60	0.80	0.17	19.48	3.24	28.83	64.24
BRH	88	N	11.24	1.05	0.31	16.14	2.70	39.27	93.92
FRN	93	N	0.00	0.00	0.00	21.89	1.77	138.06	153.12
MDG	94	N	10.44	0.93	0.15	9.94	0.00	35.94	69.54
MRR	97	N	7.09	0.40	0.09	18.58	3.11	26.84	53.85
MDT	97	N	8.16	1.09	0.23	16.17	1.24	41.77	96.59
BSZ	98	N	1.84	0.49	0.01	8.46	1.76	44.36	63.07
SMP	98	N	5.41	0.76	0.08	12.43	2.10	33.26	75.70
GAI	99	N	13.27	1.08	0.34	14.64	0.83	20.71	53.91
PTV	100	N	10.84	1.46	0.43	17.12	2.58	75.27	117.87
CST	101	N	10.52	0.66	0.22	19.84	4.48	37.41	100.68
PIT	105	N	4.05	0.44	0.04	12.62	1.19	35.99	67.72
BRB	105	N	4.38	0.52	0.04	12.30	1.24	44.22	73.10
MLC	106	N	10.47	0.45	0.30	39.93	1.58	27.91	75.09
SNZ1	109	N	11.91	1.20	0.27	11.60	4.26	71.09	114.00
BRR	109	N	5.57	0.31	0.05	19.55	5.28	28.53	70.33
PZS	110	N	4.07	0.64	0.06	15.06	1.44	25.23	67.03
CNF	111	N	2.72	0.47	0.02	9.09	2.85	34.44	65.13
MLD	111	N	20.04	1.66	0.72	13.47	1.43	23.55	48.84
PRM	111	N	2.61	0.49	0.02	11.28	1.25	58.89	118.43
BGL	114	N	4.02	0.49	0.04	12.02	1.53	30.00	65.95
CVT	115	N	6.57	0.63	0.08	12.68	2.23	33.52	50.92
DCM	115	N	3.39	0.73	0.03	6.49	1.61	35.61	61.76
FVZ	116	N	4.19	0.42	0.04	13.76	1.74	29.27	64.14

Station ID	R_{epi}	Comp	PGA	PGV	I_A	I_D	H_{50}	Sd	Bd
	km		cm/s^2	cm/s	cm/s		cm	s	s
VGL	117	N	8.71	0.63	0.20	22.80	1.98	30.73	66.77
BGN	118	N	3.20	0.48	0.02	8.17	1.96	26.90	49.86
RNC	119	N	2.64	0.59	0.02	8.49	2.16	40.26	115.63
STS	119	N	4.34	0.65	0.07	15.14	1.35	26.57	50.44
CES	120	N	11.06	2.16	0.40	10.51	5.66	76.34	114.11
FIE	122	N	1.16	0.49	0.01	7.33	0.64	52.11	86.00
PNM	124	N	2.93	0.23	0.02	21.91	0.90	30.34	64.33
AUL	128	N	4.87	0.53	0.06	14.66	2.27	27.38	74.43
RVR	131	N	3.56	0.48	0.04	14.95	1.76	34.28	63.82
TVR	133	N	2.26	0.56	0.02	9.60	1.43	60.94	115.80
BDG	134	N	8.31	0.66	0.09	10.68	1.88	33.29	69.74
BBN	135	N	2.20	0.40	0.01	10.58	0.51	33.47	69.62
CNG	136	N	8.61	0.88	0.20	16.58	1.29	34.59	76.20
FLP	137	N	11.93	0.28	0.28	52.01	2.38	29.28	58.50
VRL	141	N	4.00	0.41	0.02	9.25	1.36	24.61	62.47
RIM	142	N	7.13	0.86	0.20	20.06	3.46	38.14	70.55
LSP	145	N	1.87	0.16	0.01	11.59	0.63	36.94	55.54
FGV	146	N	0.90	0.34	0.00	7.91	1.41	41.27	57.38
SNM	146	N	2.11	0.97	0.03	10.67	0.63	60.73	100.72
PNN	146	N	6.40	0.97	0.14	13.63	2.70	55.17	111.38
BDT	154	N	4.90	0.53	0.05	12.71	1.88	38.36	87.01
SEL	158	N	4.21	0.50	0.02	5.02	1.69	25.28	57.58
POR	161	N	4.61	0.66	0.08	17.15	2.42	64.19	109.97
CTL	163	N	6.16	0.66	0.15	23.14	1.42	46.33	107.68
SSG	165	N	3.09	0.52	0.06	23.24	2.04	44.93	108.45
SNS	165	N	4.30	0.73	0.09	18.61	2.69	43.12	103.41
ARO	168	N	1.74	0.33	0.01	10.93	1.03	44.02	62.45
TGL	169	N	2.42	0.16	0.01	21.11	0.43	34.89	63.34
BRA	171	N	2.05	0.14	0.02	34.46	0.63	39.84	102.45
CTS	174	N	4.08	0.91	0.10	16.51	0.91	63.12	106.78
MOV	176	N	7.31	0.36	0.08	17.69	0.85	27.74	74.91
LEC	176	N	1.12	0.11	0.00	19.03	2.91	33.85	64.24
PSR	178	N	3.43	0.34	0.04	21.70	0.20	37.77	84.77
CLA	179	N	0.75	0.09	0.00	18.80	0.38	33.99	56.81
SPI	182	N	4.42	0.30	0.04	19.01	0.82	45.67	84.82
RNS	187	N	1.68	0.15	0.01	17.64	0.48	37.96	61.09
GNV	192	N	3.22	0.29	0.02	13.75	0.30	31.03	66.00
SEM	192	N	1.85	0.10	0.01	30.73	1.19	40.06	81.04
MNT	192	N	0.09	0.08	0.00	3.17	0.28	56.57	64.55
PRAD	196	N	1.25	0.13	0.01	20.12	1.06	44.30	87.69
MAJ	196	N	2.87	0.36	0.04	21.97	0.03	44.07	82.91
FDS	197	N	0.90	0.09	0.00	28.96	0.28	58.69	106.54
UMB	202	N	1.02	0.14	0.00	19.81	0.44	68.38	106.82
AVS	204	N	1.24	0.20	0.00	12.32	0.43	33.27	58.00
OVD	204	N	1.98	0.22	0.01	16.84	1.02	40.39	67.74
GEDE	207	N	3.26	0.29	0.05	32.67	0.64	47.92	131.62
GESC	208	N	3.25	0.28	0.03	22.89	0.40	50.24	106.13

Station ID	R_{epi}	Comp	PGA	PGV	I_A	I_D	H_{50}	Sd	Bd
	km		cm/s^2	cm/s	cm/s		cm	s	s
TLM2	209	N	2.10	0.16	0.02	34.64	0.88	47.66	104.64
CESC	209	N	2.56	0.13	0.01	27.67	0.41	46.12	104.57
CARC	210	N	12.05	1.00	0.55	28.82	0.52	44.88	103.77
CVF	210	N	2.13	0.15	0.02	34.06	2.60	41.76	64.97
TRI	212	N	0.10	0.14	0.00	3.61	0.06	65.75	100.23
DST2	212	N	1.78	0.18	0.01	19.03	0.54	39.50	103.77
VINO	213	N	2.51	0.37	0.02	13.60	0.87	60.20	252.42
MASA	216	N	3.04	0.18	0.03	31.84	0.49	43.96	104.37
SDV	218	N	1.12	0.13	0.00	13.89	0.35	46.46	105.68
SAS	220	N	1.49	0.13	0.00	14.15	0.28	33.62	63.66
MOGG	224	N	1.04	0.11	0.00	20.18	0.46	52.12	102.39
STOL	225	N	4.23	0.21	0.10	72.33	0.39	46.10	100.71
DRN	227	N	1.56	0.12	0.01	32.90	0.41	44.99	82.49
AUP	231	N	1.63	0.15	0.01	19.57	0.34	47.14	75.30
ANB	237	N	7.03	0.76	0.17	19.41	2.59	28.58	64.41
TLN	252	N	1.73	0.28	0.02	22.99	1.04	56.35	94.97
MCT	255	N	3.00	0.50	0.05	19.15	1.39	57.64	94.71
TNS	282	N	1.40	0.18	0.01	20.18	0.72	36.06	68.84
TNO	286	N	1.18	0.36	0.01	14.09	0.39	53.31	71.83
CSC	286	N	0.61	0.11	0.00	19.91	0.81	65.80	117.07
RQT	291	N	0.65	0.03	0.00	45.34	0.10	32.45	37.41
PNR	309	N	0.44	0.07	0.00	35.12	0.27	67.10	111.84
SBT	311	N	1.64	0.55	0.01	10.46	1.13	52.57	66.00
SDM	353	N	0.36	0.11	0.00	15.96	0.29	65.12	113.29
MTC	442	N	0.12	0.02	0.00	25.90	0.06	67.75	107.13
SNN	503	N	0.21	0.01	0.00	44.23	0.02	63.90	98.27
BENI	521	N	0.05	0.01	0.00	17.94	0.03	36.93	55.27
NAPI	522	N	0.06	0.01	0.00	12.27	0.04	45.46	61.41
SSB3	549	N	0.04	0.01	0.00	11.81	0.02	40.92	57.82
RSF3	557	N	0.03	0.01	0.00	10.05	0.02	41.58	58.46
MNT3	560	N	0.03	0.01	0.00	14.85	0.01	40.87	59.40
LIO3	564	N	0.02	0.01	0.00	6.46	0.01	39.81	59.13
NSC3	565	N	0.03	0.01	0.00	12.93	0.01	42.78	59.54
AND3	568	N	0.04	0.01	0.00	12.17	0.02	44.03	60.31
CLT3	575	N	0.12	0.01	0.00	28.41	0.02	42.87	61.34
SNR3	579	N	0.04	0.01	0.00	20.28	0.02	43.56	61.46
CMP3	582	N	0.05	0.01	0.00	17.28	0.01	43.69	62.38
RDM3	584	N	0.05	0.02	0.00	9.54	0.03	46.96	53.78
COL3	591	N	0.03	0.01	0.00	16.56	0.02	46.48	63.50
VDS3	591	N	0.05	0.01	0.00	19.75	0.01	46.15	55.67
SFL3	594	N	0.02	0.00	0.00	17.27	0.01	48.35	64.34
PST3	598	N	0.02	0.01	0.00	12.45	0.01	48.35	64.52
BEL3	604	N	0.02	0.01	0.00	12.97	0.01	45.47	64.68
AVG3	605	N	0.03	0.01	0.00	9.95	0.02	45.45	66.24
CGG3	614	N	0.03	0.01	0.00	10.87	0.01	49.57	67.10
SRN3	616	N	0.02	0.01	0.00	22.11	0.01	49.17	66.96
STN3	622	N	0.02	0.01	0.00	9.11	0.01	48.10	68.22

Station ID	R_{epi}	Comp	PGA	PGV	I_A	I_D	H_{50}	Sd	Bd
	km		cm/s^2	cm/s	cm/s		cm	s	s
PGN3	626	N	0.02	0.01	0.00	8.47	0.01	52.64	68.45
MRN3	636	N	0.02	0.01	0.00	15.44	0.01	49.25	67.52
VGG3	653	N	0.02	0.01	0.00	4.01	0.01	50.49	65.54

Table A2. Peak and integral parameters estimated on the uncorrected waveforms of the E-W component

Station ID	R_{epi}	Comp	PGA	PGV	I_A	I_D	H_{50}	Sd	Bd
	km		cm/s^2	cm/s	cm/s		cm	s	s
MRN	16	E	256.13	29.61	71.72	5.91	82.08	5.69	17.82
MDN	41	E	36.32	6.74	3.59	9.17	14.42	31.88	83.83
NVL	42	E	47.46	2.86	2.79	12.84	7.71	17.99	57.51
ZPP	43	E	15.79	3.25	1.61	19.63	9.10	63.24	127.04
ISD	47	E	13.05	2.06	0.97	22.60	7.71	67.68	129.08
CPC	49	E	24.52	4.67	2.12	11.58	12.77	36.26	81.64
ARG	53	E	23.81	3.89	1.47	9.89	1.33	44.85	94.86
SSU	54	E	22.25	2.03	1.17	16.17	9.65	30.75	71.06
MDC	56	E	24.42	4.41	2.39	13.86	10.06	92.39	122.08
MNS	58	E	17.74	0.73	0.47	22.45	6.44	15.70	53.79
MRZ	61	E	3.21	0.46	0.03	11.41	0.83	38.84	66.94
SRP	64	E	40.75	3.96	1.31	5.05	6.15	40.04	96.60
CSP	64	E	10.49	3.92	0.92	13.94	11.51	63.25	121.19
PVF	72	E	3.49	0.95	0.07	12.57	2.47	71.03	106.85
TGG	73	E	9.53	0.38	0.22	38.03	0.77	24.62	70.76
PAR	76	E	7.72	1.11	0.15	10.59	11.33	48.54	96.93
ALF	78	E	33.05	4.05	1.87	8.71	3.93	62.39	116.21
LNG	80	E	4.62	0.93	0.12	17.79	2.86	59.86	105.59
FRE1	87	E	9.07	0.72	0.21	19.86	3.68	30.87	64.12
BRH	88	E	12.95	1.63	0.42	12.57	2.02	42.66	73.58
FRN	93	E	7.94	0.74	0.20	20.79	1.64	38.60	107.09
MDG	94	E	9.17	0.74	0.14	13.03	2.81	40.03	83.13
MRR	97	E	6.34	0.46	0.10	20.99	3.22	29.05	56.20
MDT	97	E	8.41	1.04	0.23	16.68	1.26	41.84	99.80
BSZ	98	E	1.53	0.35	0.01	9.62	2.71	48.14	62.63
SMP	98	E	4.07	0.55	0.05	14.94	1.83	31.67	79.12
GAI	99	E	23.76	0.94	0.68	18.99	0.61	16.67	49.35
PTV	100	E	9.71	1.49	0.42	18.01	1.81	77.71	117.13
CST	101	E	9.77	0.61	0.24	25.02	4.31	41.78	94.21
PIT	105	E	2.75	0.39	0.03	17.11	1.16	34.50	68.21
BRB	105	E	3.40	0.50	0.04	16.11	1.64	40.98	73.19
MLC	106	E	15.64	0.54	0.42	31.25	1.74	22.59	55.92
SNZ1	109	E	10.83	0.96	0.29	17.42	3.13	84.62	115.08
BRR	109	E	5.89	0.52	0.07	15.07	6.80	24.30	68.56
PZS	110	E	4.51	0.61	0.05	11.91	1.59	29.95	67.40
CNF	111	E	2.37	0.45	0.02	12.67	2.29	34.02	65.73
MLD	111	E	22.34	1.69	0.75	12.39	1.49	21.24	48.74
PRM	111	E	3.37	0.47	0.02	9.67	1.29	51.38	96.17
BGL	114	E	6.49	1.03	0.06	5.66	1.93	25.85	65.55

Station ID	R_{epi}	Comp	PGA	PGV	I_A	I_D	H_{50}	Sd	Bd
	km		cm/s^2	cm/s	cm/s		cm	s	s
CVT	115	E	8.30	0.68	0.14	15.48	1.00	25.23	51.08
DCM	115	E	1.83	0.39	0.01	11.27	2.46	40.63	63.43
FVZ	116	E	4.10	0.32	0.04	19.39	1.05	31.00	65.10
VGL	117	E	0.17	0.07	0.00	4.33	0.04	37.17	89.53
BGN	118	E	2.31	0.28	0.01	13.12	1.35	31.84	50.08
RNC	119	E	2.02	0.35	0.01	11.77	1.77	61.92	108.00
STS	119	E	4.94	0.70	0.05	9.24	1.03	31.16	50.78
CES	120	E	10.71	2.36	0.60	14.83	8.49	72.97	113.01
FIE	122	E	1.66	0.36	0.01	7.61	1.04	37.12	58.46
PNM	124	E	2.91	0.21	0.03	29.20	0.93	32.31	65.19
AUL	128	E	4.37	0.66	0.08	17.21	1.96	29.81	74.51
RVR	131	E	6.98	0.66	0.07	9.65	2.21	33.46	63.27
TVR	133	E	2.35	0.54	0.02	9.18	1.75	58.61	112.84
BDG	134	E	6.05	0.57	0.08	15.15	1.77	32.71	85.19
BBN	135	E	2.58	0.54	0.02	8.05	0.55	35.18	67.67
CNG	136	E	8.43	0.73	0.16	15.83	1.67	39.64	76.36
FLP	137	E	15.13	0.29	0.29	41.06	2.14	32.04	62.13
VRL	141	E	3.26	0.34	0.03	15.75	1.27	29.87	63.75
RIM	142	E	5.95	0.86	0.14	17.66	3.49	35.10	69.29
LSP	145	E	1.45	0.28	0.01	9.78	0.87	34.64	56.18
FGV	146	E	1.28	0.35	0.01	7.12	2.62	33.16	56.14
SNM	146	E	3.49	1.19	0.08	11.40	0.81	65.00	99.67
PNN	146	E	5.96	0.84	0.17	20.75	2.44	52.31	112.51
BDT	154	E	2.62	0.41	0.03	18.21	1.41	48.99	88.69
SEL	158	E	2.75	0.30	0.01	7.73	1.55	32.98	60.41
POR	161	E	4.01	0.71	0.09	19.60	3.33	61.95	109.63
CTL	163	E	6.84	0.91	0.21	20.72	1.07	50.49	107.00
SSG	165	E	4.35	0.70	0.07	13.40	2.51	50.43	107.99
SNS	165	E	4.73	0.79	0.10	17.43	3.05	40.79	103.37
ARO	168	E	1.67	0.25	0.01	14.18	0.89	37.56	62.47
TGL	169	E	2.60	0.24	0.02	16.92	0.41	32.15	64.03
BRA	171	E	2.31	0.13	0.02	35.31	0.92	42.70	93.22
CTS	174	E	3.49	0.91	0.06	12.35	0.69	72.58	106.28
MOV	176	E	3.49	0.28	0.03	17.44	0.71	42.48	77.07
LEC	176	E	1.15	0.12	0.00	16.37	2.36	29.05	63.71
PSR	178	E	3.28	0.27	0.03	24.45	0.21	52.27	85.26
CLA	179	E	0.77	0.10	0.00	11.70	0.37	37.10	56.87
SPI	182	E	2.64	0.37	0.04	22.77	0.77	46.18	85.07
RNS	187	E	2.41	0.17	0.01	13.90	0.54	40.84	61.94
GNV	192	E	3.36	0.29	0.02	15.39	0.40	34.55	67.97
SEM	192	E	2.55	0.14	0.02	28.86	1.03	33.53	75.85
MNT	192	E	0.40	0.08	0.00	12.90	0.20	29.06	38.76
PRAD	196	E	1.13	0.10	0.00	22.28	1.05	48.56	87.28
MAJ	196	E	2.56	0.33	0.03	23.35	0.29	42.36	82.95
FDS	197	E	0.93	0.13	0.00	20.24	0.33	56.80	107.36
UMB	202	E	0.82	0.20	0.00	16.01	0.48	62.41	106.32
AVS	204	E	1.36	0.24	0.01	12.37	0.51	31.51	57.94

Station ID	R_{epi}	Comp	PGA	PGV	I_A	I_D	H_{50}	Sd	Bd
	km		cm/s^2	cm/s	cm/s		cm	s	s
OVD	204	E	2.46	0.23	0.01	15.22	1.01	40.14	68.20
GEDE	207	E	2.77	0.36	0.04	24.91	0.77	50.54	134.50
GESC	208	E	3.24	0.27	0.04	25.75	0.48	52.56	104.85
TLM2	209	E	2.21	0.18	0.03	43.15	0.82	43.39	104.93
CESC	209	E	5.34	0.29	0.07	29.17	0.87	40.41	90.95
CARC	210	E	10.53	0.81	0.61	44.49	0.59	41.99	103.72
CVF	210	E	2.69	0.20	0.02	22.74	2.42	33.15	64.97
TRI	212	E	0.09	0.06	0.00	7.65	0.07	69.90	106.94
DST2	212	E	1.63	0.13	0.01	29.42	0.53	44.49	104.26
VINO	213	E	2.33	0.27	0.02	20.80	0.80	70.88	261.96
MASA	216	E	2.57	0.15	0.02	33.11	0.44	47.33	103.78
SDV	218	E	0.85	0.10	0.00	27.83	0.37	52.54	106.58
SAS	220	E	1.30	0.12	0.00	14.47	0.31	45.98	64.53
MOGG	224	E	1.14	0.14	0.01	22.56	0.41	49.06	102.74
STOL	225	E	3.77	0.18	0.07	61.30	0.38	48.57	102.52
DRN	227	E	2.10	0.15	0.02	29.95	0.48	41.77	82.27
AUP	231	E	1.98	0.13	0.01	26.25	0.35	47.01	74.57
ANB	237	E	7.51	0.64	0.14	18.81	2.30	30.67	64.06
TLN	252	E	2.62	0.43	0.03	19.21	1.66	53.79	94.84
MCT	255	E	3.30	0.43	0.06	27.04	1.79	60.45	94.60
TNS	282	E	1.19	0.17	0.01	22.72	0.66	36.36	68.98
TNO	286	E	1.01	0.32	0.01	15.38	0.40	47.99	71.94
CSC	286	E	0.63	0.17	0.00	13.55	0.71	61.33	122.54
RQT	291	E	0.60	0.05	0.00	24.95	0.11	33.05	37.14
PNR	309	E	0.57	0.08	0.00	26.06	0.34	55.03	93.24
SBT	311	E	1.81	0.51	0.02	12.58	1.07	51.31	66.00
SDM	353	E	0.49	0.13	0.00	14.53	0.43	60.65	88.80
MTC	442	E	0.14	0.05	0.00	11.72	0.07	64.16	107.14
SNN	503	E	0.33	0.02	0.00	32.47	0.02	62.16	88.80
BENI	521	E	0.06	0.01	0.00	17.09	0.04	37.42	54.82
NAPI	522	E	0.04	0.01	0.00	11.42	0.03	47.96	61.41
SSB3	549	E	0.03	0.01	0.00	9.78	0.02	41.88	58.06
RSF3	557	E	0.03	0.01	0.00	11.65	0.02	42.13	58.46
MNT3	560	E	0.02	0.00	0.00	17.72	0.01	43.29	59.42
LIO3	564	E	0.02	0.01	0.00	10.75	0.02	38.59	59.34
NSC3	565	E	0.02	0.01	0.00	12.44	0.02	42.31	59.58
AND3	568	E	0.05	0.01	0.00	13.34	0.03	42.53	60.27
CLT3	575	E	0.16	0.01	0.00	20.24	0.02	42.36	61.36
SNR3	579	E	0.03	0.01	0.00	11.73	0.01	42.76	61.46
CMP3	582	E	0.04	0.01	0.00	18.63	0.01	44.97	62.33
RDM3	584	E	0.06	0.02	0.00	7.68	0.04	46.64	55.48
COL3	591	E	0.06	0.01	0.00	12.64	0.02	45.91	63.50
VDS3	591	E	0.05	0.01	0.00	25.72	0.01	45.88	63.22
SFL3	594	E	0.03	0.01	0.00	12.78	0.02	45.66	64.26
PST3	598	E	0.03	0.00	0.00	24.89	0.01	47.83	64.50
BEL3	604	E	0.05	0.01	0.00	11.86	0.03	44.77	57.50
AVG3	605	E	0.03	0.01	0.00	8.89	0.02	47.63	66.30

Station ID	R_{epi}	Comp	PGA	PGV	I_A	I_D	H_{50}	Sd	Bd
	km		cm/s^2	cm/s	cm/s		cm	s	s
CGG3	614	E	0.05	0.01	0.00	18.67	0.01	48.58	67.04
SRN3	616	E	0.02	0.00	0.00	18.91	0.01	47.29	66.66
STN3	622	E	0.02	0.01	0.00	10.02	0.01	48.91	68.24
PGN3	626	E	0.01	0.01	0.00	10.86	0.01	51.41	68.46
MRN3	636	E	0.02	0.01	0.00	8.23	0.01	50.20	67.52
VGG3	653	E	0.01	0.00	0.00	10.70	0.01	47.69	65.54

Table A3. Peak and integral parameters estimated on the uncorrected waveforms of the Z component.

Station name	R_{epi}	Comp	PGA	PGV	I_A	I_D	H_{50}	Sd	Bd
	km		cm/s^2	cm/s	cm/s		cm	s	s
MRN	16	Z	303.30	5.96	49.93	17.26	16.25	5.77	11.85
MDN	41	Z	28.74	1.62	1.33	17.74	5.42	24.92	79.41
NVL	42	Z	28.72	0.98	0.93	20.71	1.69	20.61	44.91
ZPP	43	Z	19.64	2.04	0.90	13.93	4.69	49.74	89.14
ISD	47	Z	8.95	1.04	0.23	15.37	2.43	88.64	130.51
CPC	49	Z	11.24	1.18	0.31	14.69	1.92	62.95	122.43
ARG	53	Z	10.11	1.08	0.20	11.68	1.19	42.76	124.78
SSU	54	Z	11.39	1.23	0.35	15.78	2.49	32.79	67.38
MDC	56	Z	11.65	2.39	0.44	9.81	3.95	79.41	128.67
MNS	58	Z	10.41	0.51	0.15	18.03	3.43	21.27	58.83
MRZ	61	Z	2.33	0.69	0.02	9.20	0.99	49.38	68.41
SRP	64	Z	7.76	0.37	0.16	35.36	3.73	74.90	126.28
CSP	64	Z	6.63	1.89	0.33	16.56	1.29	66.20	126.62
PVF	72	Z	2.94	1.19	0.06	11.29	2.11	76.78	112.24
TGG	73	Z	10.90	0.44	0.25	33.57	0.83	21.66	59.93
PAR	76	Z	3.49	0.38	0.04	16.47	1.81	73.44	101.00
ALF	78	Z	7.29	1.15	0.18	13.55	1.14	101.57	124.80
LNG	80	Z	3.50	0.53	0.06	19.12	1.69	63.05	107.45
FRE1	87	Z	3.03	0.55	0.03	12.69	1.89	52.11	66.74
BRH	88	Z	4.11	1.14	0.11	14.26	1.01	54.75	122.84
FRN	93	Z	3.73	0.35	0.06	26.90	1.18	59.90	122.52
MDG	94	Z	4.30	0.81	0.05	9.59	1.39	55.33	109.16
MRR	97	Z	2.80	0.45	0.03	12.30	1.61	36.87	57.97
MDT	97	Z	5.21	0.76	0.09	14.51	0.98	54.32	108.24
BSZ	98	Z	1.44	0.40	0.01	10.21	1.20	50.45	63.37
SMP	98	Z	2.44	0.29	0.02	16.15	0.94	45.91	82.99
GAI	99	Z	11.90	0.54	0.20	19.87	0.60	22.94	50.58
PTV	100	Z	7.31	0.90	0.17	16.14	1.00	97.52	121.06
CST	101	Z	4.87	0.41	0.06	19.96	1.55	64.69	101.14
PIT	105	Z	1.46	0.32	0.01	14.01	0.73	41.86	69.17
BRB	105	Z	3.14	0.43	0.03	13.89	0.80	55.83	74.46
MLC	106	Z	6.53	0.30	0.10	31.44	1.67	28.77	70.84
SNZ1	109	Z	2.69	0.38	0.03	21.37	0.94	91.04	119.78
BRR	109	Z	2.66	0.23	0.02	20.70	2.24	42.79	89.72
PZS	110	Z	1.96	0.38	0.02	17.01	0.81	41.23	70.84
CNF	111	Z	1.52	0.28	0.01	14.06	1.36	42.19	66.70

Station name	R_{epi}	Comp	PGA	PGV	I_A	I_D	H_{50}	Sd	Bd
	km		cm/s^2	cm/s	cm/s		cm	s	s
MLD	111	Z	10.42	0.69	0.15	12.82	0.97	33.00	51.25
PRM	111	Z	1.87	0.57	0.02	11.63	0.96	74.13	115.44
BGL	114	Z	1.89	0.23	0.01	18.76	0.02	37.94	66.34
CVT	115	Z	0.07	0.09	0.00	2.44	0.74	66.64	73.55
DCM	115	Z	1.53	0.47	0.01	8.52	0.88	45.93	64.24
FVZ	116	Z	3.43	0.42	0.03	11.40	1.46	30.89	66.43
VGL	117	Z	3.55	0.26	0.04	29.41	0.90	32.38	67.35
BGN	118	Z	1.41	0.24	0.01	15.59	0.89	30.46	51.84
RNC	119	Z	1.78	0.44	0.01	7.83	1.33	64.33	115.50
STS	119	Z	3.16	0.46	0.03	13.21	0.84	41.37	51.56
CES	120	Z	2.21	1.09	0.06	14.62	1.50	99.35	118.59
FIE	122	Z	1.11	0.49	0.01	7.90	0.88	50.03	59.18
PNM	124	Z	1.35	0.14	0.01	24.05	0.47	42.24	66.07
AUL	128	Z	2.15	0.36	0.02	13.74	1.13	40.28	76.10
RVR	131	Z	2.71	0.36	0.02	16.03	1.22	48.78	65.30
TVR	133	Z	1.16	0.34	0.01	15.34	0.79	70.59	117.88
BDG	134	Z	2.74	0.25	0.02	16.03	1.35	47.99	112.59
BBN	135	Z	2.21	0.45	0.02	14.95	0.47	34.56	69.83
CNG	136	Z	5.24	0.68	0.08	13.46	1.61	39.91	78.11
FLP	137	Z	4.06	0.20	0.03	22.97	0.90	34.34	70.20
VRL	141	Z	2.06	0.22	0.01	18.85	0.77	32.94	64.12
RIM	142	Z	2.83	0.70	0.04	13.75	1.90	49.45	73.27
LSP	145	Z	1.23	0.21	0.00	11.40	0.44	36.60	56.36
FGV	146	Z	0.55	0.32	0.00	9.78	1.18	47.37	57.44
SNM	146	Z	1.58	0.50	0.02	15.34	0.63	67.70	102.51
PNN	146	Z	2.81	0.59	0.04	16.62	2.01	66.32	113.08
BDT	154	Z	1.48	0.40	0.01	15.62	0.81	65.30	96.99
SEL	158	Z	2.33	0.39	0.01	7.41	0.83	37.54	59.75
POR	161	Z	1.94	0.31	0.02	25.11	0.90	72.55	113.19
CTL	163	Z	2.42	0.24	0.02	26.02	1.32	60.14	111.59
SSG	165	Z	1.87	0.32	0.01	13.73	0.97	72.15	111.61
SNS	165	Z	1.64	0.31	0.02	22.96	1.22	65.64	107.15
ARO	168	Z	0.98	0.22	0.01	15.73	0.58	54.07	63.59
TGL	169	Z	1.88	0.22	0.01	10.71	0.41	39.07	64.67
BRA	171	Z	1.42	0.10	0.01	33.75	0.76	43.47	108.76
CTS	174	Z	1.94	0.35	0.03	30.52	0.58	68.77	110.40
MOV	176	Z	2.77	0.23	0.02	19.64	0.42	40.74	77.11
LEC	176	Z	0.81	0.11	0.00	16.95	1.50	39.08	65.03
PSR	178	Z	1.26	0.14	0.01	34.90	0.20	68.71	87.50
CLA	179	Z	0.60	0.10	0.00	12.34	0.40	37.81	56.84
SPI	182	Z	1.58	0.20	0.01	19.56	0.44	54.30	87.00
RNS	187	Z	1.44	0.12	0.00	14.78	0.44	45.03	63.44
GNV	192	Z	2.42	0.19	0.01	16.68	0.37	36.16	67.60
SEM	192	Z	1.91	0.12	0.01	20.55	0.69	39.15	80.43
MNT	192	Z	0.28	0.08	0.00	9.86	0.24	33.57	64.28
PRAD	196	Z	1.02	0.10	0.00	24.63	0.72	47.15	87.92
MAJ	196	Z	1.54	0.27	0.01	19.41	0.15	51.04	82.84

Station name	R_{epi}	Comp	PGA	PGV	I_A	I_D	H_{50}	Sd	Bd
	km		cm/s^2	cm/s	cm/s		cm	s	s
FDS	197	Z	0.64	0.09	0.00	21.79	0.22	65.94	108.43
UMB	202	Z	0.43	0.12	0.00	19.10	0.26	75.38	108.44
AVS	204	Z	0.93	0.14	0.00	15.82	0.41	36.10	58.00
OVD	204	Z	1.21	0.11	0.00	21.04	0.39	51.69	69.91
GEDE	207	Z	1.46	0.21	0.01	15.28	0.30	71.62	136.99
GESC	208	Z	1.21	0.15	0.01	29.35	0.23	58.08	108.08
TLM2	209	Z	1.03	0.09	0.00	22.81	0.34	58.57	106.34
CESC	209	Z	3.31	0.24	0.04	28.36	0.77	42.69	101.55
CARC	210	Z	4.60	0.30	0.10	45.42	0.43	48.41	106.40
CVF	210	Z	2.21	0.12	0.01	30.70	0.94	48.91	65.00
TRI	212	Z	0.10	0.06	0.00	7.06	0.07	71.68	106.91
DST2	212	Z	0.99	0.10	0.00	29.73	0.41	58.05	107.49
VINO	213	Z	1.80	0.21	0.01	24.36	0.65	75.24	271.66
MASA	216	Z	1.09	0.11	0.01	32.32	0.28	59.08	106.40
SDV	218	Z	0.73	0.12	0.00	16.91	0.36	64.78	106.98
SAS	220	Z	0.61	0.08	0.00	15.61	0.26	47.19	65.29
MOGG	224	Z	0.83	0.10	0.00	17.37	0.29	58.24	103.09
STOL	225	Z	1.77	0.09	0.01	39.41	0.21	48.69	99.70
DRN	227	Z	1.19	0.09	0.00	26.79	0.40	51.60	82.86
AUP	231	Z	0.74	0.07	0.00	27.97	0.21	48.54	62.11
ANB	237	Z	2.61	0.25	0.02	22.32	0.94	43.87	64.06
TLN	252	Z	0.96	0.28	0.01	12.70	0.55	71.47	94.99
MCT	255	Z	1.33	0.23	0.01	27.21	0.81	79.86	101.42
TNS	282	Z	0.89	0.08	0.00	24.27	0.30	52.55	69.00
TNO	286	Z	0.73	0.16	0.00	16.94	0.30	61.97	72.00
CSC	286	Z	0.48	0.14	0.00	9.10	0.43	77.07	123.42
RQT	291	Z	0.37	0.07	0.00	12.40	0.10	30.88	37.87
PNR	309	Z	0.41	0.07	0.00	16.43	0.16	71.11	111.89
SBT	311	Z	1.27	0.41	0.01	9.54	0.85	50.87	65.99
SDM	353	Z	0.52	0.16	0.00	14.41	0.42	62.38	88.75
MTC	442	Z	0.06	0.02	0.00	12.07	0.03	73.68	107.15
SNN	503	Z	0.15	0.01	0.00	41.12	0.02	66.23	98.42
BENI	521	Z	0.05	0.01	0.00	9.95	0.03	36.70	55.16
NAPI	522	Z	0.05	0.01	0.00	13.70	0.03	48.20	61.41
SSB3	549	Z	0.03	0.01	0.00	8.01	0.02	40.86	57.93
RSF3	557	Z	0.03	0.01	0.00	9.57	0.02	42.52	58.48
MNT3	560	Z	0.02	0.01	0.00	5.23	0.01	43.45	59.39
LIO3	564	Z	0.02	0.01	0.00	8.28	0.02	41.24	59.25
NSC3	565	Z	0.02	0.01	0.00	13.23	0.01	41.42	59.58
AND3	568	Z	0.04	0.01	0.00	12.31	0.02	45.57	60.15
CLT3	575	Z	0.07	0.01	0.00	12.53	0.02	46.62	61.31
SNR3	579	Z	0.02	0.00	0.00	15.25	0.01	47.41	61.46
CMP3	582	Z	0.02	0.01	0.00	7.72	0.01	46.60	62.39
RDM3	584	Z	0.02	0.01	0.00	6.95	0.02	48.22	62.66
COL3	591	Z	0.03	0.01	0.00	6.42	0.01	50.69	63.50
VDS3	591	Z	0.02	0.01	0.00	11.47	0.01	47.97	63.38
SFL3	594	Z	0.02	0.01	0.00	10.05	0.01	49.40	64.34

Station name	R_{epi}	Comp	PGA	PGV	I_A	I_D	H_{50}	Sd	Bd
	km		cm/s^2	cm/s	cm/s		cm	s	s
PST3	598	Z	0.02	0.00	0.00	12.66	0.01	48.19	64.52
BEL3	604	Z	0.03	0.01	0.00	7.90	0.01	48.30	65.71
AVG3	605	Z	0.02	0.01	0.00	8.98	0.01	48.38	66.30
CGG3	614	Z	0.02	0.01	0.00	11.53	0.01	53.31	67.10
SRN3	616	Z	0.01	0.01	0.00	8.92	0.01	50.77	67.14
STN3	622	Z	0.01	0.01	0.00	10.62	0.01	49.66	68.19
PGN3	626	Z	0.01	0.01	0.00	9.63	0.01	52.09	68.44
MRN3	636	Z	0.01	0.01	0.00	7.94	0.01	50.89	67.52
VGG3	653	Z	0.01	0.01	0.00	7.96	0.01	48.81	65.54

References

Bindi D, Pacor F, Luzi L, Puglia R, Massa M, Ameri G, Paolucci R, 2011. Ground motion prediction equations derived from the Italian strong motion database, Bulletin of Earthquake Engineering, 9(6), 1899-1920.

Chioccarelli E, Iervolino I. Near-source seismic demand and pulse-like records: a discussion for L'Aquila earthquake. Earthquake Engineering and Structural Dynamics 2010; 39(9):1039–1062

Clough R.W., Johnston S.B., 1966. Effect of stiffness degradation on earthquake ductility requirements. Proceedings of Japan Earthquake Engineering Symposium, Tokyo, Japan.

Comité Européen de Normalisation (CEN), 2004. Eurocode 8 – Design of Structures for earthquake resistance – Part 1: General rules, seismic actions and rules for buildings. EN 1998-1, CEN, Brussels.

Cosenza E, Manfredi G, Ramasco R, 1993: The Use of Damage Functionals in Earthquake Engineering: A Comparison between Different Methods. Earthquake Engineering and Structural Dynamics, 22 (10), 855-868.

CS.LL.PP; DM 14 Gennaio 2008: Norme tecniche per le costruzioni. *Gazzetta Ufficiale della Repubblica Italiana*, 29. 4/2/2008 (In Italian).

De Luca F, Ameri G, Iervolino I, Pacor F, Bindi D, 2012. Prediction equations for peak and cyclic engineering seismic response based on Italian data. Earthquake Spectra, (under review).

De Luca F., 2011. Records, capacity curve fits and reinforced concrete damage states within a performance based earthquake engineering framework. PhD thesis. Department of Structural Engineering, University of Naples Federico II. Advisors: G. Manfredi, I. Iervolino, G.M. Verderame. Available at http://wpage.unina.it/iuniervo/

Dolce M, Nicoletti M, Ammirati A, BInaconi R, Filippi L, Gorini A, Marcucci S, Palma F, Zambonelli E, Lavecchia G, de Nardins R, Brozzetti F, Boncio P, Cirillo D, Romano A, Costa G, Gallo A, Tiberi L, Zoppè G, Suhadolc P, Ponziani F, Formica A, 2012. The Emilia thrust earthquake of 20 May 2012 (Northern Italy): strong motion and geological observations – Report 1. Available at http://www.protezionecivile.gov.it/resources/cms/documents/Report_DPC_1_Emilia_EQSd.pdf

Gruppo di Lavoro (2004) Redazione della Mappa di Pericolosità Simica Prevista dall'Ordinanza PCM 3274 del 20 Marzo 2003, Rapporto conclusivo per il Dipartimento della Protezione Civile, INGV, Milano-Roma, 65pp. (in Italian)

Ibarra L.F., Medina R.A., Krawinkler H., 2005. Hysteretic models that incorporate strength and stiffness deterioration, Earthquake Engineering and Structural Dynamics, 34, 1489-1511.

Iervolino I, Chioccarelli E, Convertito V, 2011. Engineering design earthquakes from multimodal hazard disaggregation. Soil Dynamics and Earthquake Engineering, 31, 1212-1231.

Iervolino I., Galasso C., Cosenza C., 2010. REXEL :computer aided record selection fro code based seismic structural analysis, Bulletinf of Earthquake Engineering, 8, 339-362.

Iervolino I., Giorgio M., Galasso C., Manfredi G., 2010. Conditional hazard maps for secondary intensity measures, Bulletin of Seismological Society of America, 100(6), 3312-3319.

INGV Comunicato: aggiornamento del 01/06/2012 ore 05:48 UTC. Available at http://www.ingv.it/primo-piano/comunicazione/2012/05200508/

Joyner WB, Boore DM, 1981. Peak horizontal acceleration and velocity from strong-motion records including records from the1979 Imperial Valley, California, earthquake, Bulletin of Seismological Society of America 71, 2011–2038.

Lai C, Foti S, Rota M, 2009. Input sismico e stabilità geotecnica dei siti in costruzione. IUSS Press, Pavia, Italy.

Sabetta F, Pugliese A, 1996: Estimation of Response Spectra and Simulation of Nonstationary Earthquake Ground Motion. Bulletin of the Seismological Society of America, 86, 337-352.

Shahi S., Baker JW. An empirically calibrated framework for including the effects of near-fault directivity in probabilistic seismic hazard analysis. Bulletin of the Seismological Society of America 2011; 101(2):742-755.

Stucchi M, Meletti C, Montaldo V, Crowley H, Calvi GM, Boschi E. Seismic Hazard Assessment (2003-2009) for the Italian Building Code, Bulletin of the Seismological Society of America 2011; 101(4):1885-1911.